UNICA

UNIVERSITÀ
DEGLI STUDI
DI CAGLIARI

Ph.D. DEGREE IN
Innovation Sciences and Technologies

Cycle XXXVIII

TITLE OF THE Ph.D. THESIS

Processes and Materials for Space Exploration and Colonization

Scientific Disciplinary Sector(s)

09/ICHI-01/B

Ph.D. Student:	Mariano Casu
Supervisor	Prof. Roberto Orrù
Co-Supervisors	Prof. Antonio Mario Locci, Prof. Alessandro Concas

Final exam. Academic Year 2024/2025
Thesis defence session: February 2026

Acknowledgements

Abstract

Nowadays, Earth-based space exploration is extraordinarily challenging and still expensive, but significant efforts are being made to develop new space launchers according to the most cutting edge technologies. Indeed, more affordable and cost-efficient techniques are needed to guarantee both better performances and lower costs. In this regard, material research in the field of Ultra High Temperature Ceramics (UHTCs) is expected to contribute to the increase in performances of refractory parts that play an important role in rocket launchers and space vehicles. In this thesis work, new materials based on transition metal diborides are being synthesized, sintered and characterized according to innovative technologies, and their performance are being assessed in terms of mechanical properties and oxidation resistance. Research is focused on multicomponent transition metal borides (TMBs), from binary to quinary compositions. Mathematical modelling of the two key production techniques, called Self Propagating High-temperature Synthesis (SHS) and Spark Plasma Sintering (SPS), is also considered to give a valuable contribution for making the production of such materials more efficient.

Another crucial problem addressed in this Thesis, that highly affects the proposed space colonization of Mars, is that all payload mass shipped from Earth must escape the gravity field of our planet, and lifting propellant is a significant contributor to space exploration costs. The paradigm of *In Situ* Resource Utilization (ISRU) is a long-time established concept to minimize such costs. In this regard, instead of bringing the required materials from Earth, it is worth to study how to maximize the use of *in-situ* available resources such as regolith, Mars soil, for several applications. To this aim, regolith simulants are processed and tested in this Thesis to obtain useful products for possibly sustaining human presence on the red planet.

This Thesis is organized as follows. The general aspects of processes and materials for space exploration and colonization will be provided in the Introduction (**Chapter 1**). Information on UHTCs material synthesis and consolidation techniques, and a description of Mars regolith simulants available to the scientific community are also given in this Chapter.

The most important methods employed for the UHTCs processing (synthesis and consolidation) will be reported in **Chapter 2**, along with the precursors used for their synthesis. Subsequently, the

regolith simulants employed in this thesis as well as with the consolidation technologies adopted for their densification will be described.

The different studies involving UHTCs are reported in **Chapter 3**. In particular, the synthesis, sintering and characterization of multicomponent TMBs, are considered in **Sections 3.1-3.3**. The optimization of the SHS process is addressed in **Section 3.4**, while modelling activity regarding the densification mechanism of individual diborides by SPS is investigated in **Section 3.5**.

Chapter 4 is focused on ISRU technologies aimed to obtain bulk materials from Martian regolith for solar energy harvesting (**Section 4.1**), construction materials with high mechanical properties (**Section 4.3**) and complex parts via additive manufacturing (**Section 4.3**).

Finally, some concluding remarks on the investigated materials and processes are provided in **Chapter 5**.

Summary

Acknowledgements 1

Abstract 2

1. Introduction 8

1.1 General aspects 8

1.2 Ultra-High Temperature Ceramics 13

1.2.1 Synthesis 13

1.2.2 Sintering 17

1.3 In Situ Resource Utilization of Martian regoliths 20

1.3.1 Martian regolith simulants 20

1.3.2 Consolidation techniques 23

2. Experimental materials and methods 24

2.1 Ultra-High Temperature Ceramics 24

2.1.1 Powder synthesis 24

2.1.2 Powder consolidation 26

2.2 Martian regoliths 28

2.2.1 Martian soil simulants 28

2.2.2 Consolidation of Martian regolith simulants 30

3. Processes and Materials for the Space Exploration: Ultra-High Temperature Ceramics 31

3.1 W- and Mo-containing High Entropy Boride and effects of SiC addition. 31

3.1.1 Introduction 31

3.1.2 Materials and Methods 34

3.1.3 Results and Discussion 36

3.1.3.1 Synthesis and sintering 36

3.1.3.2 Mechanical properties 41

3.1.3.3 Oxidation behaviour of HEB_W and HEB_W-SiC samples 42

3.2 Zirconium-based binary borides 47

3.2.1 Introduction 47

3.2.2 Materials and Methods 50

3.2.3 Results and Discussion 52

3.2.3.1 Synthesis and sintering of ZrB_2-based solid solutions 52

3.2.3.2 Mechanical properties of ZHB and ZTB systems ____ 58
3.2.3.3 Oxidation resistance of ZHB and ZTB systems ____ 60

3.3 Niobium-based binary borides ____ 66

3.3.1 Introduction ____ 66
3.3.2 Materials and Methods ____ 68
3.3.3 Results and Discussion ____ 70
3.3.3.1 Synthesis and sintering of individual borides ____ 70
3.3.3.2 Synthesis and sintering of Nb-based solid solutions ____ 77
3.3.3.3 Mechanical properties ____ 84
3.3.3.4 Oxidation resistance ____ 86

3.4 Optimization of the SHS technique for the synthesis of metal boride ceramics ____ 98

3.4.1 Introduction ____ 98
3.4.2 Materials and Methods ____ 99
3.4.2.1 Thermodynamic analysis ____ 99
3.4.2.2 Experimental validation ____ 101
3.4.3 Results and Discussion ____ 102
3.4.4 Notation ____ 107

3.5 Constitutive modeling of Spark Plasma Sintering applied to transition metal diborides ____ 109

3.5.1 Introduction ____ 109
3.5.2 Mathematical model ____ 110
3.5.3 Results and Discussion ____ 118
3.5.3.1 Model fitting and mechanistic insights into densification behavior ____ 118
3.5.3.2 Apparent and intrinsic viscosity behavior ____ 129
3.5.3.3 Model validation ____ 135
3.5.4 Notation ____ 139

4. Processes and Materials for the Space Colonization: In-Situ Resource Utilization of Martian Regoliths ____ 143

4.1 Processing of Martian regoliths for their application as solar energy absorbers on Mars ____ 143

4.1.1 Introduction ____ 143
4.1.2 Materials and Methods ____ 144
4.1.3 Results and Discussion ____ 147
4.1.3.1 Initial characterization of the Martian regolith simulants ____ 147
4.1.3.2 Spark Plasma Sintering of the regolith simulants ____ 152
4.1.3.3 Compositional, microstructural and morphological characterization ____ 155
4.1.3.4 Optical properties characterization ____ 161

4.1.3.5 Optical properties discussion ____ 163

4.2 Enhanced properties of spark plasma sintered additive-free Martian soil simulants ____ 171

4.2.1 Introduction ____ 171

4.2.2 Materials and Methods ____ 174

4.2.3 Results and Discussion ____ 180

4.2.3.1 Initial characterization of the Martian regolith simulants ____ 180

4.2.3.2 Optimization of the sintering conditions ____ 183

4.2.3.3 Compositional, microstructural and morphological characterization ____ 186

4.2.3.3 Mechanical characterization ____ 193

4.3 Sintering of Mars regolith shaped using additive manufacturing methods ____ 197

4.3.1 Introduction ____ 197

4.3.2 Materials and methods ____ 200

4.3.2.1 Regolith and Martian saltwater simulants ____ 200

4.3.2.2 Wet processing ____ 203

4.3.2.3 Sintering and characterizations ____ 205

4.4.3 Results and Discussion ____ 207

4.3.3.1 Compositional optimization of the slurry ____ 207

4.3.3.2 Additive Manufacturing ____ 208

4.3.3.3 Thermogravimetric analyses ____ 210

4.3.3.4 Sintering conditions optimization ____ 211

4.3.3.5 Compositional characterization, thermal conductivity and mechanical properties ____ 215

5. Concluding Remarks ____ 223

List of Abbreviations ____ 226

List of Figures ____ 229

List of Tables ____ 240

References ____ 243

Appendices ____ 277

A. Rietveld Analysis Results ____ 277

A.a. Obtainment of W- and Mo-containing High Entropy Boride and SiC-reinforced composite. ____ 277

A.b Synthesis and sintering of ZrB_2-based solid solutions ____ 281

A.c Synthesis and sintering of NbB_2-based solid solutions ____ 285

A.d Processing of Martian regoliths for their application as solar energy absorbers on Mars ____ 295

B. Phase diagrams adapted from literature ____ 302

C. Details of the constitutive model of pressure-assisted powder consolidation by Spark Plasma Sintering applied to transition metal diborides **304**

C.a Plastic deformation of Body (1) 304

C.b Plastic deformation of Body (2) 309

C.c Derivation of stress–strain rate relation 309

C.d Duality between dissipation Φ and viscoplastic Ψ potentials 310

C.e Application to uniaxial pressing in a rigid cylindrical die and material viscosity functionality 313

C.f Constitutive parameter dependencies 314

1. Introduction

In this section, the general aspects of processes and materials for space exploration and colonization will be provided (**Section 1.1**), accompanied by subsequent information on UHTCs material synthesis and consolidation techniques (**Section 1.2**), as well as a description of Mars regolith simulants relevant for ISRU studies (**Section 1.3**).

1.1 General aspects

One of the most attractive challenges that currently drive research and human ambition is the exploration of space and near extraterrestrial bodies **[1]**. In the last decades, research and development of new technologies and solutions for the exploration and colonization of near extraterrestrial bodies saw an increase in the involved actors, which nowadays include not only space agencies of the major superpowers but also emerging space programs both from new geopolitical agents and private investors **[2,3]**.

One of the key areas of interest to enable space exploration and the future stable presence of astronauts on other planets is the development of reliable, efficient and capable space vehicles. In this regard, due to the extreme thermomechanical stresses encountered in the launch and atmosphere re-entry stages, other than in general in hypersonic flight, research continues on the development of effective thermal barrier systems **[4]**. Concurrently, propulsion systems also take benefit from the research of suitable materials capable of withstanding high thermomechanical stresses, especially for the design of the parts directly exposed to the hot exhaust gases, such as the engine nozzles **[5]**.

Past and present thermal barrier systems heavily rely on ablative materials (sacrificial materials that are consumed during the most violent stages of atmospheric re-entry) **[1]**. Currently, the space vehicle reusability approach, pioneered by NASA with the space shuttle program **[6]** and private company SpaceX (now leader in the commercial space sector with the Falcon 9, Falcon Heavy and Starship (under development) launchers **[7-9]**), is being adopted also by the other actors **[10]**. Consequently, the development of reusable space vehicles implies reusability also in the employed materials, that would need to resist to the environment, rather than being burned out **[4,11]**.

In principle, the class of so-called Ultra High Temperature Ceramics, UHTCs, fits this scope. These materials are often referred to compounds that have melting points above 3000 °C (see **Figure 1.1**) **[12]**. Alternatively, other definitions have been proposed, and some of them are application-oriented. For example, UHTCs are also indicated as ceramic materials that can be used for extended times at temperatures above 1650 °C **[13]**. From the chemical point of view, UHTCs are compounds in which boron, carbon, or nitrogen combine with the early transition metals (TMs) such as Ti, Zr, Hf, Nb, and Ta **[14]**. The generated strong covalent bonds result in compounds with high hardness, stiffness, and melting temperature **[15]**. Given the presence of some features of the metallic bond, these compounds also exhibit higher electrical and thermal conductivities than oxide ceramics **[5]**. It is the combination of metal and ceramic-like properties that allow UHTCs to withstand extreme temperatures, heat fluxes, radiation levels, mechanical loads, chemical reactivities, and other conditions that are typical of the proposed aerospace application **[5]**.

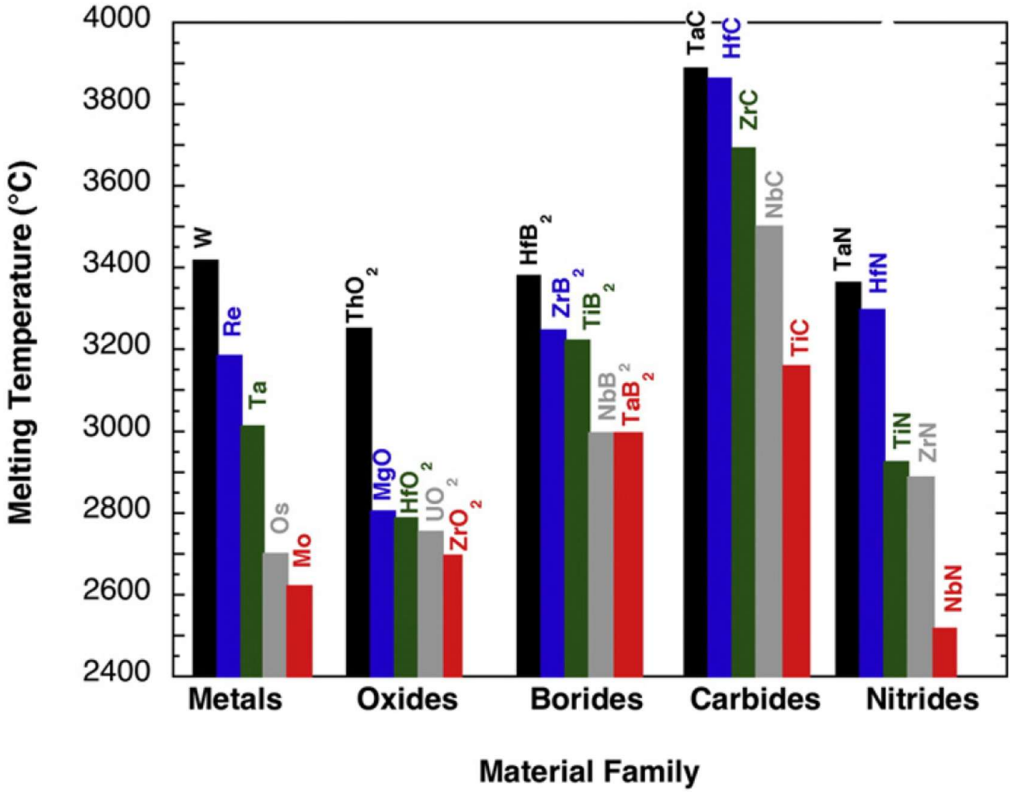

Figure 1.1 - Melting temperature of elements and compounds from different families of materials showing that very few materials have melting temperatures above 3000 °C. Taken from **Fahrenholtz et al. [12]**

In this framework, diboride-based UHTCs are investigated for their promising combination of thermal conductivity, strength at elevated temperature, and oxidation resistance **[5]**. These materials have been widely studied particularly in their simple transition metal diboride form (individual borides) **[16-20]**. However, in the past decade, due to the promising results obtained with equimolar quinary compositions, also called High-Entropy Borides (HEBs), where transition metal cations of the IV (Ti, Zr, Hf), V (especially Nb and Ta) and VI groups (mainly Mo and W), are combined, attention was also addressed to multicomponent solid solutions **[21-26]**.

The promising properties of HEBs, often superior to these of the individual constituents, were frequently attributed to the potential synergistic effects of the different cations, the so-called "cocktail effect" (**Figure 1.2**) **[21,22]**. However, efforts have been made to systematically identify the contribution of each metal constituent to the observed properties. In this regard, **Backman and collaborators [27-29]** investigated the role of metals of the different groups on the oxidation resistance of HEBs, suggesting that IV group metals present preferential oxidation, given the higher thermodynamic stability of the corresponding oxides. On the other hand, V group ones imply the presence of melted oxide phases during high temperature applications, because of the low melting point of their TM-oxides. Moreover, given the high volatility of VI group metal oxides, lower oxidation resistance of the related borides is expected. Indeed, large voids can be formed in the oxide layer on the surface of the UHTC parts, which instead should be as dense as possible, to hinder oxygen diffusion to the bulk **[27]**. Moreover, the role of complex mixed oxides (such as $Zr_6Nb_2O_{17}$ or $Hf_6Ta_2O_{17}$), potentially considered a positive feature **[27,30,31]**, is difficult to identify a priori, especially due to the lack of thermodynamic data **[29]**.

In this context, further studies on HEBs can corroborate these general theoretical considerations, for example combining IV group TMBs with only V or VI group ones (see **Section 3.1**). However, this approach could be challenging, due to the presence of 4-5 different metals whose single effect could be masked by the others. More simple and clearer trends can be identified when coupling only two transition metal borides to form binary solid solutions (see **Sections 3.2** and **3.3**). This would allow to identify more clearly the role of each transition metal in the observed oxidation behaviour.

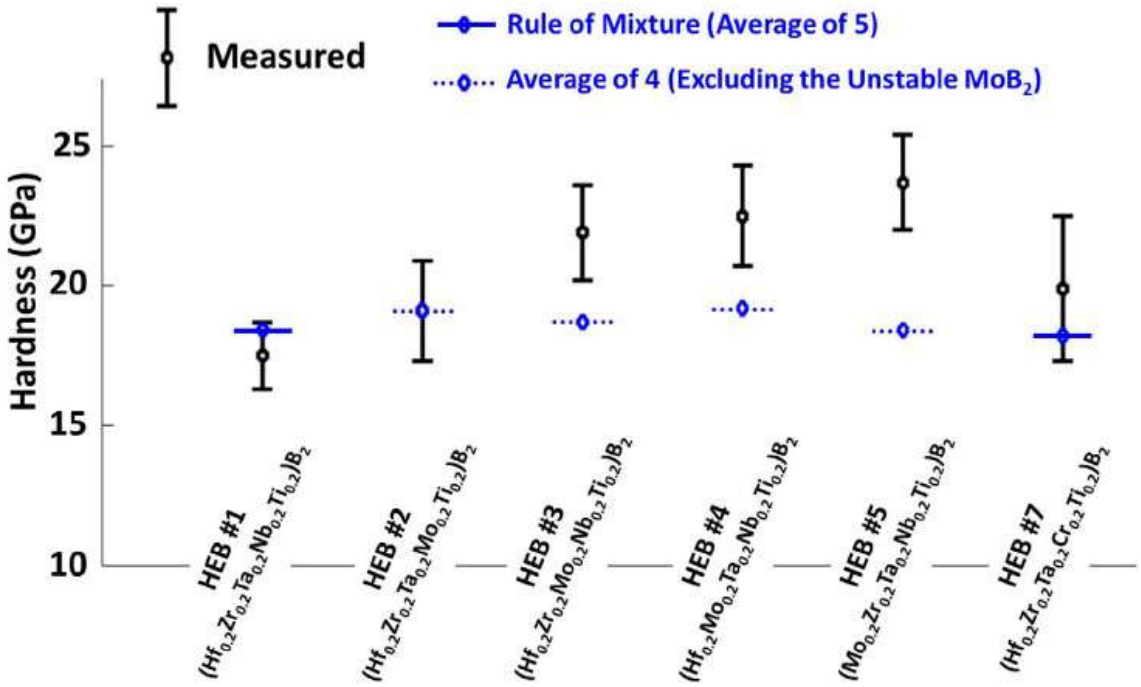

Figure 1.2 - Example of "cocktail effect": hardness values of HEB samples obtained by **Gild et al.**, compared to the average values of the related individual TMBs **[22]**

While these studies are aimed to address the needs of space launchers, crucial to reach Earth orbit and beyond, materials and chemical engineering research can give a valuable contribution also to the development of technologies to be applied for the achievement of a permanent human presence on Mars surface, which is the closest candidate for manned exploration in the foreseeable future other than the Moon. In this regard, while the Moon is already considered for human missions, ongoing space programs mostly target Mars for robotic explorations, being the manned ones expected to occur in the 2030s or later **[32-36]**. Nowadays, due to technological and economical constrains, limited payload can be launched to Low Earth Orbit and beyond. Earth-based space exploration is usually associated with high costs, since all launched mass needs to escape Earth's gravitational field relying on large amounts of propellant **[37-39]**. To mitigate excessive costs and meet technological challenges associated with long-term exploration missions or permanent colonization of the Red Planet, the *In-Situ* Resource Utilization (ISRU) approach represents the ideal solution. ISRU concept is based on the principle of maximizing the utilization of available space resources to obtain products and services which significantly reduce the mass, cost, and risk of near-

and long-term space exploration, allowing for the associated payload costs to be cut **[40]**. ISRU is particularly suitable in the case of Mars, which is more distant from Earth than the Moon, and presents a stronger gravitational field. Given the distance and the limited time windows availability, the most feasible short mission profile on Mars accounts for a total duration of about 400 to 650 days **[41-42]**, compared to the 30 days of Artemis III mission to the Moon **[43]**. On this basis, the degree of independence of a future permanent base is particularly underlined. Among the key aspects to be addressed for the development of permanent or long term human bases on Mars, the fabrication of sheltering constructions as well as *in-situ* surface power generation and storage are of the utmost importance **[38,44,45]**. To this aim, the materials proposed to satisfy these requirements need to be characterized for their mechanical, thermal/optical properties and, possibly, for their radiation shielding capability (**Figure 1.3**) **[45]**.

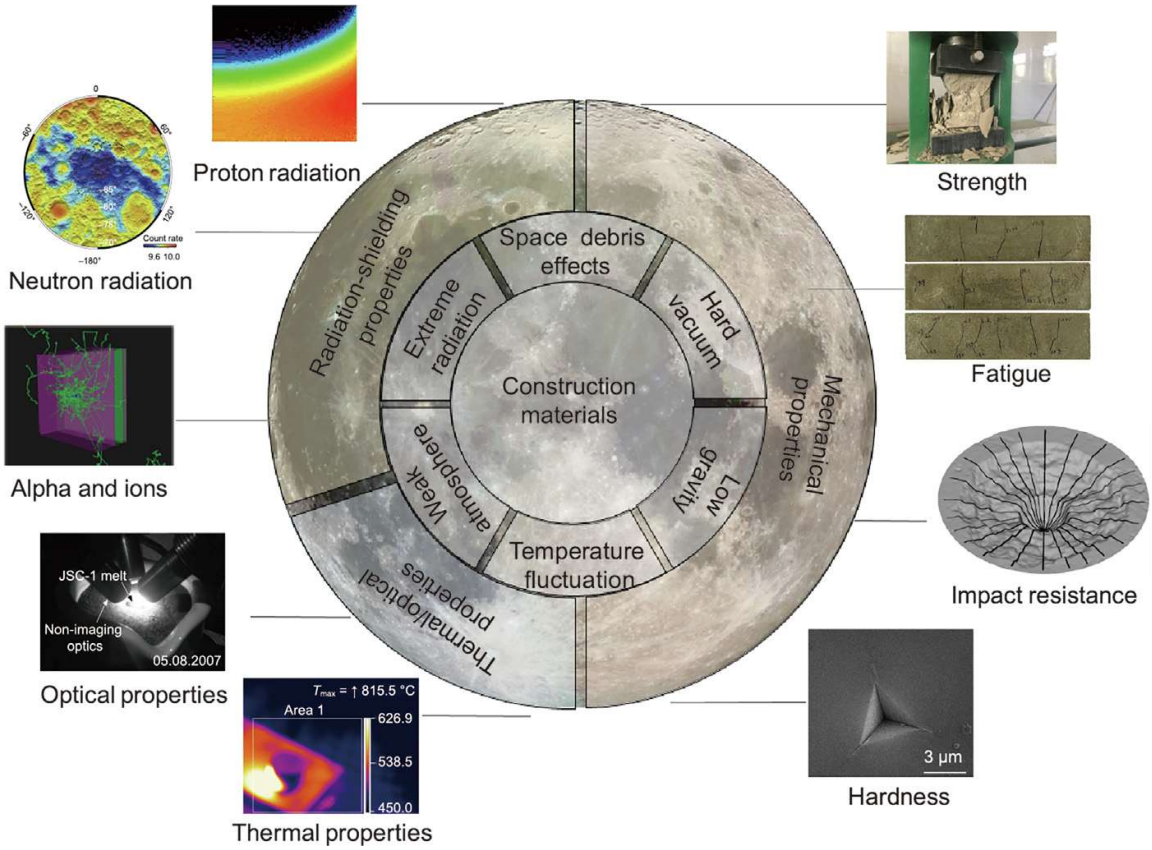

Figure 1.3 - Properties and characterization of regolith-based materials for construction on space. The moon is depicted, but the same consideration are valid also for Mars. Taken from **Zhou et al. [45].**

For these scopes, the most abundant and ubiquitous material available on the Martian surface is certainly represented by regolith **[37]**. The latter one typically shows a globally homogeneous basaltic nature with local to regional enrichments in secondary minerals, reflecting the geological history of the examined area. Given the complexity and energy requirements for the separation of different mineral phases, single metals or other elements, the direct utilization of regolith is then considered highly preferable **[37]**. Differently from Lunar soil, Martian regolith has not been yet brought to Earth, so that research work performed to date on this subject makes use of numerous regolith analogues produced so far **[37,46]**. The ones employed in this study will be described in detail in **Section 2.2.1**.

1.2 Ultra-High Temperature Ceramics

The state of the art on the synthesis and consolidation techniques proposed in the literature for the preparation of TMBs will be described in **Sections 1.2.1** and **1.2.2** respectively. Particular emphasis will be given to the two processing routes utilized in this work.

1.2.1 Synthesis

Several methods have been used to synthetize transition metal diborides. Borothermal (BR), carbothermal (CR) and borocarbothermal (BCR) reduction of metal oxides are certainly the techniques most widely employed to this purpose **[47,48]**. Other methods include Self-Propagating High-Temperature Synthesis (SHS) **[16,17,49-52]**, borohydride reduction (BHR) **[47,53]**, reduction of metal hydrides or chlorides by boron **[18,19,47,54]**, displacement reactions from carbide or nitride precursors **[47,55,56]** and sol-gel **[47,57]**. BR, BCR and CR of TM oxides take place according to the following reactions (1), (2), and (3) respectively **[47]**:

$$MeO_2 + \frac{10}{3}B \rightarrow MeB_2 + \frac{2}{3}B_2O_3 \quad (1)$$

$$MeO_2 + \frac{1}{2}B_4C + \frac{3}{2}C \rightarrow MeB_2 + 2CO \quad (2)$$

$$MeO_2 + B_2O_3 + 5C \rightarrow MeB_2 + 5CO \quad (3)$$

Since oxygen is bonded to the precursors, the resulting powders deriving from reactions (1), (2) and (3) typically contain it as impurity **[5]**. Moreover, when operating with reaction (1), boron oxide is also produced. Thanks to its high volatility, this compound can be removed by keeping the reacted powders at high temperatures (≥1300 K) for prolonged times (~hours) **[47,48]**. To avoid the associated energetic costs, carbon or boron carbide can be used as reducing agents instead of boron. With this strategy, gaseous CO is the obtained byproduct, which readily separates from the MeB_2 powders. Moreover, carbon containing reductants are less expensive than high purity boron **[47]**. Operating with carbon, however, can result in C impurities in the products. Other than the contaminants deriving from the employed reducing agents, transition metals or oxides usually contain other metals as impurities, deriving from the difficult separation of similar species. For example, commercial ZrB_2 is produced from naturally occurring zircon ores, which also contain small quantities of Hf **[47]**.

Regarding the energetic budget requested to make these reduction processes feasible, it is possible to state that reactions (1)-(3), but especially reaction (3), become thermodynamically favourable only at elevated temperatures, being usually strongly endothermic **[47]**. For example, **Figure 1.4** reports the standard free energy of reaction $\Delta G°_r$ of reactions (1), (2) and (3) for the case of ZrB_2, calculated basing on tabulated data **[58]**. It is possible to observe how reaction (1) represents the less endothermic one, followed by (2) and finally (3). Figure 1.4 also shows that the three synthesis pathways become thermodynamically favourable ($\Delta G°_r < 0$) only for T>1400K. For this reason, other than for B_2O_3 removal (reaction (1)), these reduction processes need to be carried out in furnace at high temperatures, for a sufficiently long time to complete the reactants conversion.

Other than the analysed reduction processes, **Figure 1.4** also reports how the direct reaction (DR) (4) between elemental transition metals and boron is thermodynamically favourable, presenting a strong exothermic character, with a $\Delta G°_r$ almost equivalent to the enthalpy of formation of MeB_2 (in the case of **Figure 1.4**, ZrB_2).

$$Me + 2B \rightarrow MeB_2 \quad (4)$$

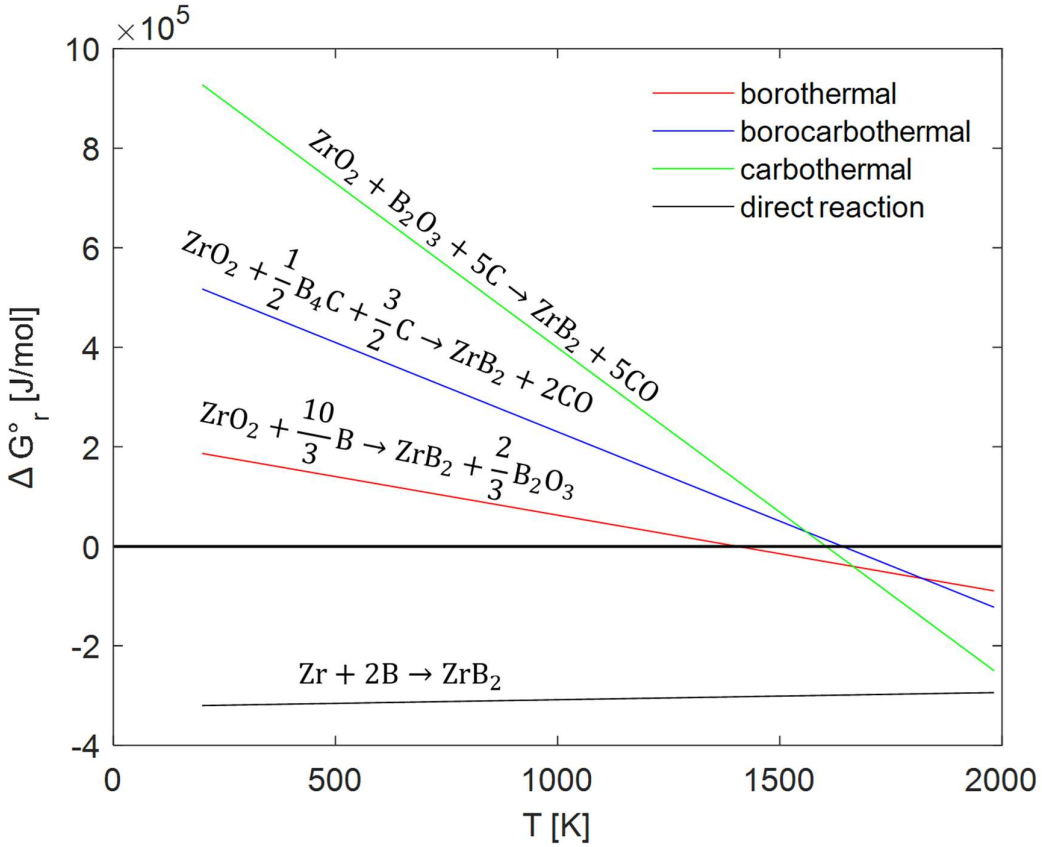

Figure 1.4 - Standard state Gibbs' free energy of formation as a function of temperature for the synthesis of ZrB_2, calculated from tabulated data **[58]**. Borothermal reaction: red solid line; borocarbothermal reaction: blue solid line; carbothermal reaction: green solid line; direct reaction: black solid line.

Due to the high enthalpy of formation of most TMBs (**Table 1.1**), it is possible to obtain them via combustion synthesis or Self-propagating High-Temperature Synthesis (SHS), starting from their elemental constituents. This process was successfully applied for the obtainment of IV group and V group transition metal borides **[16,17,49-52]**, as well as other UHTCs or UHTC-based materials **[59-62]**. Compared to the reduction of transition metal oxides (reactions (1)-(3)), starting from pure metals allows to better control impurity levels in the resulting ceramics **[47]**. During this process, the synthesis reaction self propagates in the form of a combustion wave across the powder reactant mixture, thus converting the reactants in the desired product in very short times (~seconds), once ignited **[63]**. The advantages of SHS are its rapidity, lack of external energy requirements other than ignition, possibility to obtain metastable phases due to the rapid cooling and the ability to expel

volatile impurities due to the high temperatures of the process **[63]**. Because of the short time scale of SHS, adiabatic considerations are commonly invoked in its theoretical analysis. For example, a well established empirical criterion to assure that a reaction is able to self propagate is that its adiabatic combustion temperature (T_a) exceeds ~1800 K **[63]**. For the case of TMBs, this requirement is by far overcome (see **Table 1.1**).

Table 1.1 – Enthalpy of formation and adiabatic combustion temperature of different IV and V group TMBs.

	TiB_2	**ZrB_2**	**HfB_2**	**NbB_2**	**TaB_2**
$\Delta H°_f$ (kJ/mol)	-323.8 **[58]**	-322.6 **[58]**	-336.0 **[58]**	-251.0 **[58]**	-209.2 **[58]**
T_a (K)	3190 **[63]**	3310 **[63]**	3523 **[62]**	2400 **[63]**	3370 **[63]**

However, the use of the direct reaction (4) presents some limitations, related to the cost of reduced metal compared to transition metal oxides. For instance, market price databases list approximate average costs of about 1.4 $/kg for TiO_2, while 5.9-6.3 $/kg for Ti, as of 2025 **[64]**.

Other than locally heated to make reaction (4) self-propagate, the starting mixture can be also mechanically activated once placed inside milling vials and shaken with ball milling devices until the synthesis process occurs **[65,66]**. However, when ball milling is employed to this aim, prolonged times can be required **[47]**. This could result in the presence of impurities deriving from the milling media, which can affect the properties of the resulting ceramics **[47]**. To overcome this problem, brittle hydrides or chlorides can be used as precursors for the mechanically activated synthesis of TMBs or TMB-based composites **[18,67]**.

Reactive synthesis processes can be also carried out concurrently with the powder consolidation step, in a process defined as Reactive Sintering, for instance in the Reactive Spark Plasma Sintering (RSPS) **[16,51,68,69]**. In this case, the powders undergo the reaction directly during the sintering experiment, so that the need of a two step (synthesis and then sintering) process is overcome. This route can also rely on different precursors, such as transition metal hydrides **[19]**. As a drawback,

the occurrence of highly exothermic reactions inside the closed powder containers during these processes might be not convenient for various reasons, including safety **[25,69,70]**.

Moving from the case of individual boride systems to the obtainment of multicomponent solid solutions, another problem needs to be addressed, which is the interdiffusion of different metal cations to form a homogeneous material, rather than a heterogeneous mixture of individual borides. As a possible solution, mechanical alloying was proposed to activate already synthetized individual TMBs. Long milling times, usually tens of hours, are needed **[21,22,71,72]**. Alternatively, reduction methods based on reaction (2) were employed **[26,73]**. SHS was also applied, but usually the total conversion of reactants to the desired composition was not attained **[24,25]**, most probably due to the very short processing times that are insufficient for completing the needed diffusion processes. To achieve the latter goal, subsequent thermal treatments, for example the ones needed for powder consolidation (which will be described in **Section 1.2.2**), are required to finally obtain the expected homogeneous solid solutions **[24,25,74]**.

Given the advantages of the SHS process, and the know-how acquired by our research group at the University of Cagliari, this synthesis route was employed, followed by a subsequent high-temperature consolidation step, for the fabrication of multicomponent UHTCs throughout this work. A possible alternative SHS route is proposed in **Section 3.4**, with the aim of mitigating the direct reaction disadvantages.

1.2.2 Sintering

Except for the attempts made to make the synthesis and consolidation in a single step (Reactive Sintering), Ultra-High Temperature Ceramics are commonly synthesized in powder form, using the techniques described in the previous section. However, their applications in the aerospace sector requires them as dense materials, for example for the fabrication of rocket engine nozzles, or thermal barrier protection systems **[12]**. Bulk components have to possess high densification levels, both to guarantee satisfactory mechanical properties (such hardness, which is heavily dependent on porosity), and hinder oxidation phenomena **[27]**. The occurrence of the latter is indeed made faster by the presence of pores, which facilitate the access of gaseous oxygen to the inner areas of the bulk material. However, it is well known that, due to their intrinsic characteristics, UHTCs are materials particularly hard to be densified **[12,19].** For this reason, advanced consolidation techniques are

needed to process UHTC powders, and specifically TMBs. Pressureless sintering (PLS), while still applicable to low-melting point materials such as regoliths, is seldom applicable for UHTCs, apart for some case studies, and usually in presence of sintering aids **[5]**. Other than that, ultra-fast sintering techniques such as Flash Sintering (FS) **[53,75]** and Arc Melting (ARM) **[76]** have been also employed for this scope. However, the high refractory character of such systems (melting point exceeding 3000 K **[12]**), usually requires the application of an external pressure, other than high temperatures, to obtain satisfactory densification levels during the sintering process **[5]**. In this regard, the most widely used techniques are certainly conventional Hot Pressing (HP) and Spark Plasma Sintering (SPS) **[5]**.

Similarly to pressureless sintering, conventional HP makes use of external heating elements as an energy source, with the powders confined in a closed sample holder, and a mechanical load concurrently applied along the axial direction **[77,78]**. With this technique, several UHTC-based systems have been successfully produced in bulk form **[54,79-81]**. Moreover, long processing times, of the order of hours, are usually needed to achieve a satisfactory densification level, mostly due to the low heating rates that are typically provided by external heating elements. This fact determines a high energy request for the fabrication process **[82]**.

Conversely, the SPS technology, also known as Field Assisted Sintering (FAST) or Pulsed Electric Current Sintering (PECS), is based on the direct heating of the sample by means of an electrical field, characterized by high intensity and low voltage. Powders are placed into a conductive die (usually made of graphite, which is high temperature resistant), and then exposed to a mechanical load and an electrical field, both applied in the axial direction. The generated electrical current can then produce heat primarily via the Joule effect **[77,78]**. A schematic representation of the SHS process is shown in **Figure 1.5**. If the powders are not electrically conductive, the electric current flows across the die and the generated heat is transmitted via conduction to the powders. However, if the powders themselves are conductive, heat can be also generated directly through them **[77,78]**. It is worth noting that while the role of Joule effect on powder densification is certain, other phenomena, such as plasma formation, electromigration, enhanced diffusion of materials at forming particle necks and high localized temperature at the contact area between particles are not excluded to take place **[77]**. However, the possible contribution of these phenomena is difficult to evaluate, being probably masked by the dominant Joule effect **[77,78]**.

Given the very localized heating, higher heating rates can be attained, and the densification of highly refractory materials such as the UHTCs can be completed in a matter of minutes. Moreover, being the temperatures and times involved in SPS densification milder, if compared to HP, grain growth can be limited, thus improving the properties of the resulting products **[77,78]**. The main drawbacks, common to all pressured-assisted techniques, are associated to the difficulty of complex shape design. However, due to the high electrical conductivity of UHTCs, the simple shapes produced via SPS can be post machined by EDM (Electrical Discharge Machining) to obtain more complex and precise shapes. In addition, it is important to state that in the last years, promising efforts have been made to combine 3D printing techniques with SPS **[83-86]**.

To avoid graphite degradation, SPS experiments are carried out in vacuum or inert atmosphere **[77]**, and a graphite felt placed on the outer surface of the die is usually employed to limit heat dissipation via irradiation.

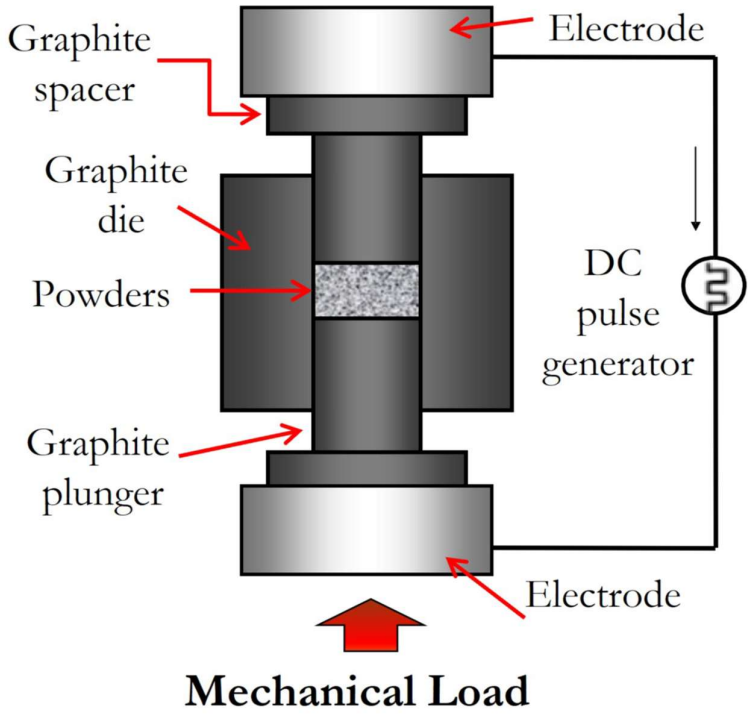

Figure 1.5 – Schematic of the SPS process.

1.3 In Situ Resource Utilization of Martian regoliths

In this Section, the state of the art on Martian regolith simulants developed and made available for the scientific community (**Section 1.3.1**) and consolidation techniques employed in literature to produce bulk materials (**Section 1.3.2**) will be described.

1.3.1 Martian regolith simulants

As anticipated in **Section 1.1**, no actual Martian regolith has ever been brought so far to Earth. For this reason, the scientific community relies on specifically crafted Martian regolith simulants, developed on Earth to mimic the actual material present on the planet. According to the insightful review recently published by **Karl et al. [37]**, these simulants can be differentiated into three generations. Indeed, the artificial simulants development reflects the growing knowledge of Mars, gained from remote research efforts by orbiters, landers and rovers **[87]**. In particular, thanks to the data collected by orbiter probes, human perception of this planet evolved from a red basalt sandbox to that of a heterogeneous celestial body with environments, both modern and ancient, as varied as those found on Earth **[88]**. For example, **Figure 1.6** reports the complex topography and elemental distribution observed on planet Mars **[89]**. Concurrently, simulant development has changed markedly over the years, becoming more complex and tailored to the diverse environments. **Figure 1.7** reports several examples of different regolith simulants.

As mentioned above and suggested by **Karl et al. [37]**, a generational approach can be used to classify such artificial regoliths. First-generation simulants are materials collected in single locations on Earth which are sufficiently similar, in terms of geology and/or chemical composition, to data collected for the Martian soil. The only process that these materials undergo, before being made available, is often grinding and sieving. These regoliths are therefore directly linked to the extraction site, which usually reflects Martian environments, such as deserts (Martian Mojave Simulant, MMS **[90]**) or volcanoes (Johnson Space Centre Mars-1A, JSC-Mars-1A **[91,92]**).

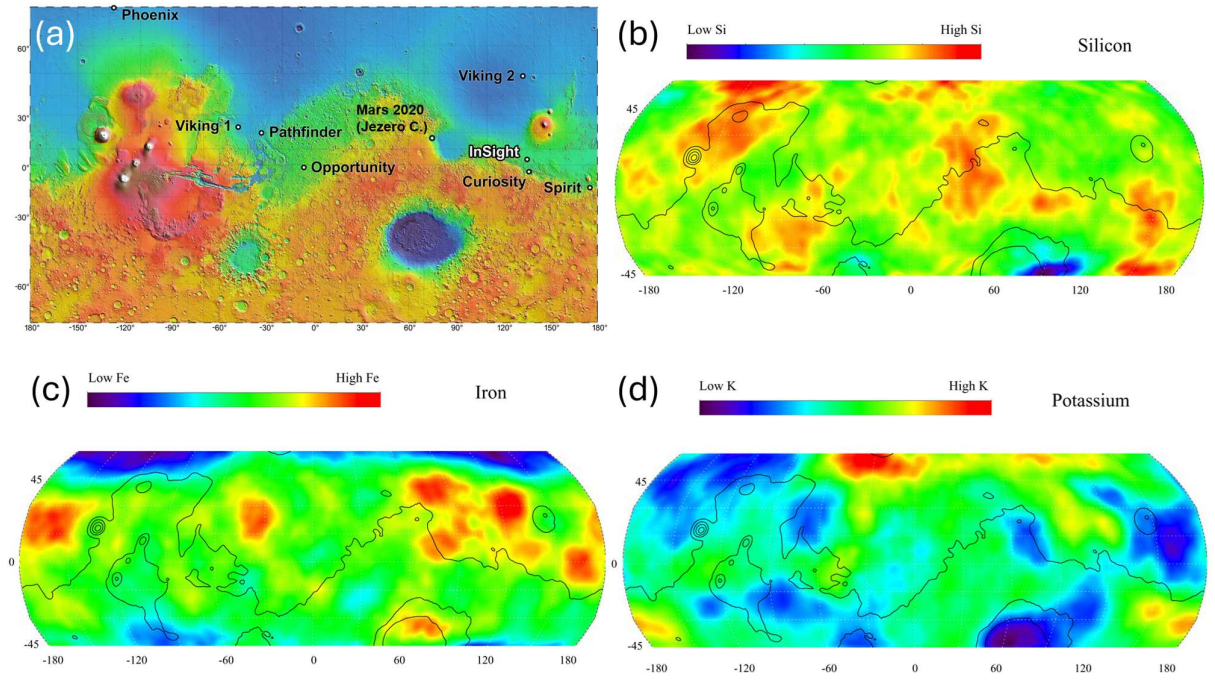

Figure 1.6 – Geological features of planet Mars. (a) Planet topography reporting the main mission landing sites and (b), (c), (d) elemental distribution of Si, Fe, K as detected by the Gamma Ray Spectrometer Suite of 2001 Mars Odyssey mission. Adapted from Jet Propulsion Laboratory Image Gallery, NASA/JPL-Caltech (a), NASA/JPL/University of Arizona (b), (c), (d) **[89]**.

Second-generation simulants are blends of different materials produced by directly mixing (often preliminary ground) different minerals. With this approach, it is possible to more closely reproduce the mineralogical distribution and elemental abundances observed on Mars. Third-generation materials follow the second-generation concept of mixing different minerals from diverse sources, and further enhance some physical properties (texture and particle size distribution, for example) **[37]**. Other than generational differences, a paradigm that has been developed especially for the third generation ones is the duality between global simulants (such as the Mars Global Simulant 1, MGS-1 **[93]**) and simulants crafted to replicate soil form specific areas such as the Jezero Crater (JEZ-1 **[94]**) or mineral deposits, present on Mars especially for clays (MGS-1C simulant, containing 40% montmorillonite **[95]**) or sulphur (MGS-1S, containing 41% gypsum **[96]**)**[37]**. The availability of such a variegated portfolio of different simulants is of the utmost importance, as it allows for a proper validation of different processing technologies with respect to different Martian terrains.

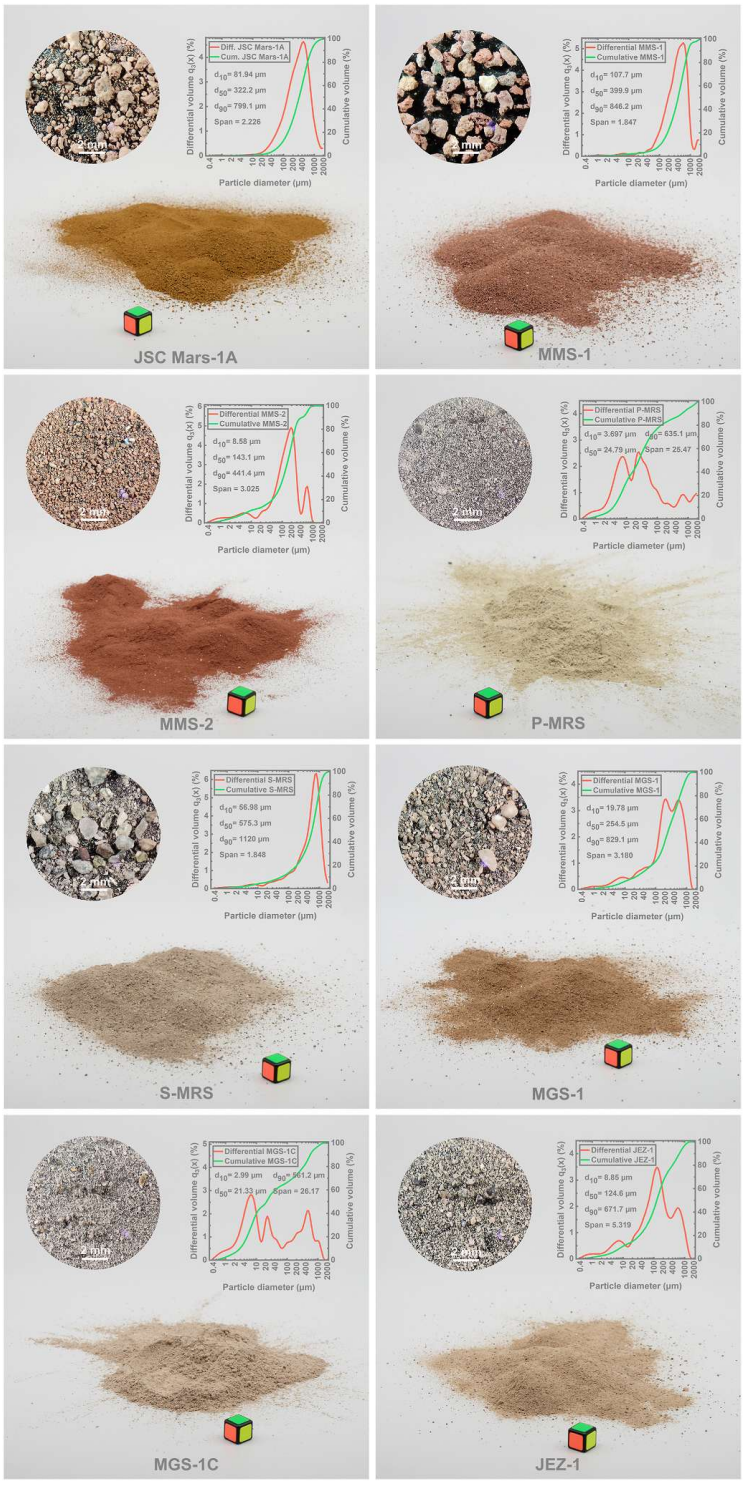

Figure 1.7 – Physical appearance and particle size distribution of numerous simulants available to a broad range of researchers. Taken from **Karl et al. [37]**.

1.3.2 Consolidation techniques

Consolidated regolith is considered the best option for the related applications investigated in this Thesis. For example, when considering it for thermal energy storage, bulk materials guarantee enhanced thermal conductivity and mechanical properties if compared to loose dust **[97,98]**. This holds also for the case of construction materials, either if the focus is on high performances or complex geometries, since adequate mechanical properties can be achieved only after reaching satisfactory densification levels.

Accordingly, different consolidation methods, previously applied to terrestrial processes, have been considered to convert loose Martian regolith into sintered bodies. They include pressureless sintering **[99,100]**, combustion synthesis-based processes **[101-103]**, impact compaction **[104]**, high-pressure consolidation **[104]**, solar sintering **[105]**, additive manufacturing **[99,106]**, and cold sintering **[107]**. The SPS technology, which has been successfully applied to process lunar regolith simulants **[108,109-111]**, was also very recently considered for the Martian ones **[112,113]**.

In general, the paradigm involved in the ISRU framework aims to the minimization of energy consumption, as well as binder/consolidation additives which may not be available *in situ*. Due to the relatively limited energy request associated with SPS, if compared to conventional HP or PLS **[82]**, this technique is expected to be highly applicable in contexts such as the proposed Martian outposts. Accordingly, it was chosen for investigations described in **Sections 4.1** and **4.2** of this thesis. Moreover, the operating conditions typical of the SPS setup, which requires high vacuum during experimental runs, simulate, more closely, the actual Martian atmosphere compared to air sintering. Furthermore, this technique also allows for the obtainment of adequate densification levels without employing additional binders. On the other hand, when additive manufacturing coupled with further consolidation and shape retention was considered in this work (**Section 4.3**), pressureless sintering was preferred.

2. Experimental materials and methods

In this Chapter, details on the methods employed for the UHTCs processing (synthesis in **Section 2.1.1** and consolidation in **Section 2.1.2**) will be reported. Then, the regolith simulant employed in this thesis will be described (**Section 2.2.1**), along with the consolidation techniques used for their densification (**Section 2.2.2**).

2.1 Ultra-High Temperature Ceramics

2.1.1 Powder synthesis

The SHS apparatus employed in this work consists of a stainless steel chamber (**Figure 2.1a**) connected with a controlled atmosphere system, consisting of a RV12 (Edwards Ltd, United Kingdom) vacuum pump, an argon inlet line and a pressure indicator. Prior to each experiment, the chamber is evacuated with the vacuum pump and then filled with Ar up to the pressure of 2 bar, to guarantee an adequate overpressure with respect to the external ambient air, avoiding oxygen infiltration inside the apparatus. To minimize the presence of atmospheric oxygen during the experiments, the system is flushed with Ar at least two times, before finally reaching the working pressure of 2 bar.

Prior to the SHS experiments, the reactant powders are placed in polymeric vials with agata spheres (ball to powders ratio, BPR=0.2) and mixed for 20 minutes in a SPEX 8000 (SPEX CertiPrep, USA) shaker mill device (if not specified differently in the following Chapters), with the aim of maximizing the homogenization of the different species. The resulting mixture was uniaxially pressed to form cylindrical pellets, which then can be placed in the reaction chamber (brown cylinder in **Figure 2.1a**).

To provide the energy necessary for the reaction ignition, a tungsten filament (R.D. Mathis, USA) is connected to a low-voltage / high-intensity DC circuit, which is closed for the time needed to ignite the reaction (few seconds) (**Figure 2.1b**). After the reaction is complete, the obtained products are mechanically treated for 1 h by ball milling (BPR=2) using the same SPEX 8000 device but employing stainless steel media. During this stage, some additives, in particular graphite, are in some cases introduced before the subsequent powder sintering step.

The precursors employed for the preparation of UHTC powders via SHS are listed in **Table 2.1**, along with the specific Sections where they will be employed.

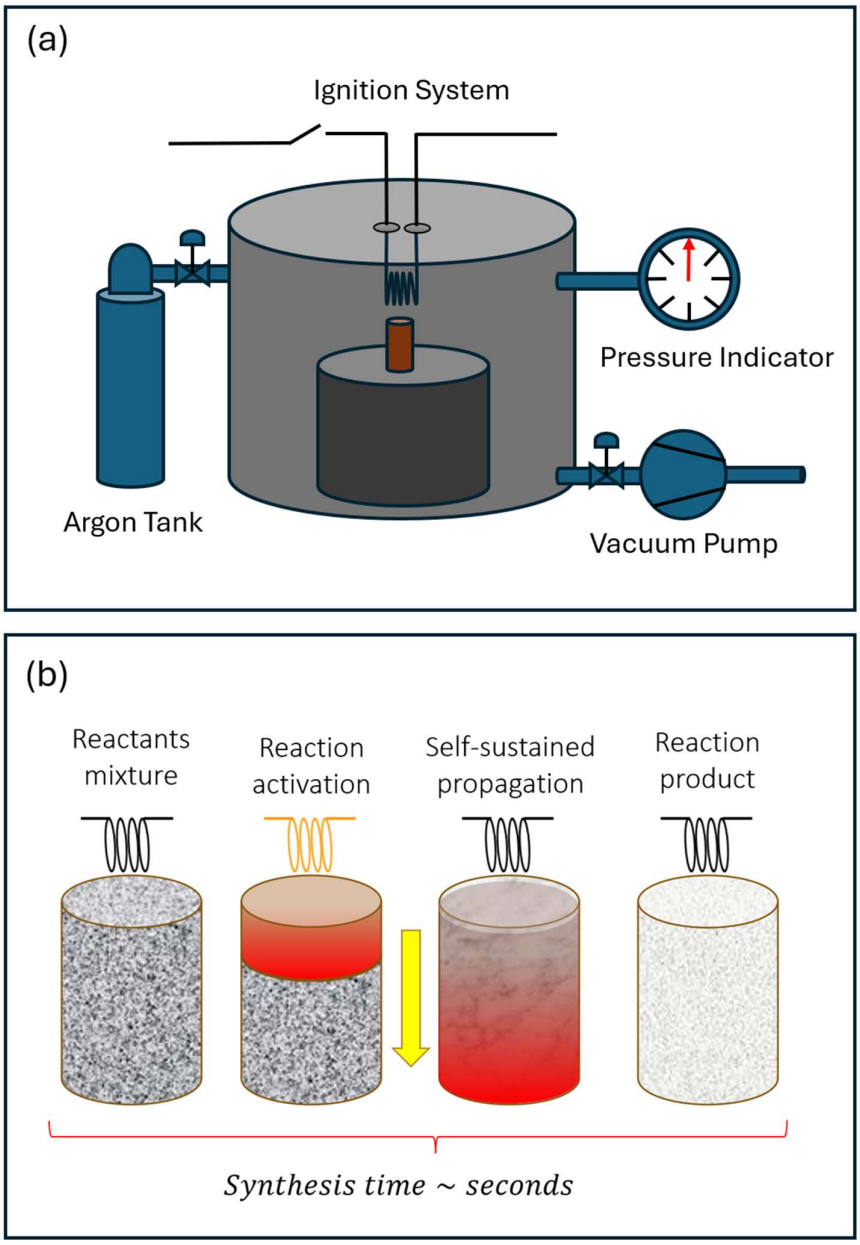

Figure 2.1 – Schematic of the SHS apparatus used in this work (a). Representation of the reacting pellet during the SHS process (b).

Table 2.1 – Precursors for the synthesis of Ultra High Temperature Ceramics by SHS employed in this work (n.r.: not reported by the producer).

Precursor	Particle Size	Purity	Product code	Supplier	Used in Sections
B	≤1µm	≥95 %	15580	Sigma Aldrich	3.1, 3.2, 3.3, 3.4, 3,5
Ti	325 Mesh (<44 µm)	99 %	10386	Alfa Aesar	3.1, 3.3, 3.4, 3.5
Zr	2–3 µm	n.r.	00847	Alfa Aesar	3.1, 3.2, 3.4
Hf	325 Mesh (<44 µm)	99.6 %	10201	Alfa Aesar	3.1, 3.2, 3.3, 3.4, 3.5
Nb	325 Mesh (<44 µm)	99.8%	10275	Alfa Aesar	3.3, 3.5
Ta	325 Mesh (<44 µm)	99.9 %	00337	Alfa Aesar	3.2
Mo	3–7 µm	99.95 %	10030	Alfa Aesar	3.1
W_{finer}	1–5 µm	99.9 %	10400	Alfa Aesar	3.1
$W_{coarser}$	325 Mesh (<44 µm)	99.9 %	39749	Alfa Aesar	3.1
TiO_2	n.r.	99%	232033	Sigma Aldrich	3.4
ZrO_2	325 Mesh (<44 µm)	99%	11395	Alfa Aesar	3.4
HfO_2	325 Mesh (<44 µm)	99%	11835	Alfa Aesar	3.4

2.1.2 Powder consolidation

In this work, the SPS equipment (515S model, Fuji Electronic Industrial Co., Ltd., Kanagawa, Japan) reported in **Figure 2.2** was employed, under vacuum conditions (about 20 Pa), for powder sintering. Variable amounts of powder, usually aiming to obtain a final height of the SPS samples of 3 mm, were placed inside cylindrical graphite dies (30 mm external diameter; 15 mm inside diameter; 30 mm height, if not differently specified in the following Sections) equipped with two punches (14.7

mm diameter, 20 mm height, if not differently specified in the following Sections), all made of AT101 graphite (ATAL, Italy), through which electric current and mechanical load are applied. Sintering experiments were carried out under temperature-controlled mode using an infrared pyrometer (CHINO, mod. IR-AHS2, Japan) focused on the lateral surface of the die. During the SPS runs, the heating rate (200 °C/min) and applied pressure (20 MPa) were kept constant, while the dwell temperature (T_D) and holding time (t_D) conditions adopted to produce the different bulk samples were varied depending to the investigated system. Graphite foils 0.13 mm wide (Alfa Aesar, Germany) were placed between the powders and the graphite equipment, to facilitate sample release after the experiments, while 3 mm thick graphite felt was employed to limit heat losses.

Given the beneficial effects observed in literature by the use of graphite as sintering aid, small amounts of this additive (Sigma Aldrich, cod. 282863, <20 µm particle size) were used in SPS experiments throughout this Thesis.

Figure 2.2 – The SPS 515S apparatus used in this work.

2.2 Martian regoliths

2.2.1 Martian soil simulants

The simulants used in this Thesis are JSC-Mars-1A, MMS, MGS-1, MGS-1C and JEZ-1. The first generation JSC-Mars-1A (Johnson Space Center Martian regolith simulant, <1mm class, Orbital Technologies Corporation, Madison, WI, USA) is a red/brown volcanic tephra mined from a quarry in the Pu'u Nene crater of the Mauna Kea volcano (near Hilo, Hawaii, USA) sieved to the <1 mm fraction **[91,92]**. The first generation MMS soil, provided by the Jet Propulsion Laboratory (Pasadena, USA), is a gray/brown basalt mined from the Saddleback Mountain in the Mojave Desert (near Boron, California, USA) **[90]**. As anticipated, third generation Mars Global (MGS-1) and Jezero Delta Crater (JEZ-1) simulants consist of blends of minerals of appropriate compositions and physical properties crafted to closely mimic the average Martian soil (MGS-1) or particular regions examined during recent exploration missions (JEZ-1, reflecting Jezero crater, see **Figure 1.6**) **[37,93,94]**. MGS-1C simulant is clay-enriched MGS-1, specifically crafted to simulate a clay-rich Martian terrain, albeit using montmorillonite (Na smectite) rather than nontronite and saponite (Fe/Mg smectites), which have been reported to dominate on the Martian crust but are rare on Earth **[106]**.

Table 2.2 reports the oxide constituents of the simulant batches employed in this work, in comparison to compositional findings collected for Gale crater, Meridiani Planum and Gusev crater. It can be observed how third generation simulants more closely mimic the composition of the actual Martian soil. Given the fact that MGS-1C, along with a different batch of MGS-1 was used in **Section 4.3**, specific oxide constituents of these two simulant batches will be provided directly in that Section.

As reported in **Karl et al. [37]**, the characterization of Martian regolith simulants is rather incomplete. To fill this literature gap, other than the oxide constituents reported in **Table 2.2**, the needed mineralogy, particle size distribution, thermal stability and other relevant properties will be measured and reported in **Chapter 4**, for the simulants employed in each Section.

Table 2.2 - Main oxide constituents (wt.%) of JSC Mars-1A, MMS, MGS-1, JEZ-1 simulants compared to average data collected on actual Martian regolith (in italics) on Gale crater **[114]**, Meridiani planum and Gusev crater **[115,116]**). (n.r.: not reported).

Oxides	**JSC-Mars-1A [92]**	**MMS [90]**	**MGS-1 [93]**	**JEZ-1 [94]**	***Gale* [114]**	***Meridiani* [115,116]**	***Gusev* [115,116]**
SiO_2	34.5 – 44	49.4	45.57	44.2	*43.16*	*46.14*	*46.32*
Al_2O_3	18.5 – 23.5	17.1	9.43	11.3	*9.16*	*9.39*	*10.14*
FeO	2.5 – 3.5	n.r.	16.85	9.5	*19.33 (Fe_xO_y tot.)*	*18.17 (Fe_xO_y tot.)*	*16.04 (Fe_xO_y tot.)*
Fe_2O_3	9 – 12	10.87	n.r.	n.r.			
MnO	0.2 – 0.3	0.17	0.1	0.1	*0.42*	*0.37*	*0.32*
MgO	2.5 – 3.5	6.08	16.5	25.9	*8.60*	*7.42*	*8.61*
CaO	5 – 6	10.45	4.03	3.5	*7.08*	*6.95*	*6.35*
Na_2O	2 – 2.5	3.28	3.66	1.9	*2.72*	*2.23*	*3.01*
K_2O	0.5 – 0.6	0.48	0.43	0.3	*0.5*	*0.49*	*0.44*
TiO_2	3 – 4	1.09	0.3	0.2	*1.05*	*1.03*	*0.87*
P_2O_5	0.7 – 0.9	0.17	0.37	0.6	*0.92*	*0.85*	*0.82*
Cr_2O_3	n.r.	0.05	0.12	0.3	*0.46*	*0.4*	*0.35*
SO_3	n.r.	0.1	2.63	2.1	*5.83*	*5.91*	*6.01*

2.2.2 Consolidation of Martian regolith simulants

In this Thesis, the SPS equipment described in **Section 2.1.2** was employed also to densify Martian regolith simulants. Cylindrical graphite dies (30.2 mm external diameter; 20.7 mm inside diameter; 48 mm height, if not differently specified in the following Sections) equipped with two punches (20.7 mm diameter, 34 mm height, if not differently specified in the following Sections) made of AT101 graphite (ATAL, Italy) were generally employed. SPS runs were conducted under temperature-controlled mode using a K-type thermocouple (T.C. Misure e Controlli, Turin, Italy) inserted in a small hole drilled on the external die surface. Electric current was applied to heat powders first from the room temperature to an intermediate level, 100°C below the maximum (T_D), at a rate of 50°C/min. Then, to reduce possible overshooting problems, the heating rate was lowered (10°C/min) until the T_D value was achieved. T_D, holding time (t_D) and applied pressure (P) conditions adopted to produce the different bulk samples were varied depending on the investigated system. Graphite foils 0.13 mm wide (Alfa Aesar, Germany) were placed between the powders and the graphite tools, to facilitate sample release after the experiments, while 3 mm thick graphite felt was employed to limit heat losses.

When additive manufacturing techniques were employed (**Section 4.3**), pressureless sintering experiments were carried out using a custom-built Al_2O_3 tube furnace inside an HT 1600 (LECO Instruments GmbH, Germany). Samples were heated from room temperature to a dwelling value in the range of 1150°C-1210°C with 3 h dwelling time and 1.7 K/min heating/cooling rates. Two-step treatments were performed by keeping an higher T_D for an additional hour. Further details on the pressureless sintering experiments can be found in **Section 4.3**.

3. Processes and Materials for the Space Exploration: Ultra-High Temperature Ceramics

In this Chapter, experimental and theoretical results related to the fabrication and characterization of metal diborides will be described and discussed. Specifically, Section **3.1** is focused on the study involving SiC-free and SiC-containing $(Ti_{0.2}Zr_{0.2}Hf_{0.2}Mo_{0.2}W_{0.2})B_2$. Investigation on Zr- and Nb-based binary systems will be then addressed in **Sections 3.2** and **3.3**, respectively. The possibility of partially replacing elemental precursors with cheaper metal oxides to make the SHS process economically more advantageous will be addressed in **Section 3.4**. Finally, a mathematical model on the consolidation of metal diborides by SPS will be described in **Section 3.5** along the obtained results.

3.1 W- and Mo-containing High Entropy Boride and effects of SiC addition.

3.1.1 Introduction

To better understand the role of VI group metals such as Mo and W on the overall properties of multi-component boride systems, and confirm the general trends proposed by Backman and Opila **[27]** on the oxidation resistance provided by IV and VI group transition metals in quinary HEBs, the first system investigated in this thesis is $(Ti_{0.2}Zr_{0.2}Hf_{0.2}Mo_{0.2}W_{0.2})B_2$, for the sake of brevity named HEB_W. In this context, several efforts were made in literature to synthesize this ceramic, often resulting in multiple phase products, mainly due to poor solubilization of Mo- or W-rich phases in the IV group element rich matrix **[22,117-121]**. To better visualize the state of the art, previous efforts to synthetize and sinter HEB_W-based ceramics are summarized in **Table 3.1**. The corresponding preparation routes, processing conditions, and final bulk samples' densities are also reported. It is interesting to observe how no previous data on $(Ti_{0.2}Zr_{0.2}Hf_{0.2}Mo_{0.2}W_{0.2})B_2$-SiC was available for this system.

The 6h high energy ball milling of different metal borides followed by SPS process performed by **Gild and coworkers [22]** resulted in a sample with a W-rich secondary phase, identified as $(Ti_{1.6}W_{2.4})B_4$. When the same authors combined BCR and SPS routes, a secondary (W,Mo)-rich phase was detected in the sintered materials **[118]**. Similarly, **Zhang et al. [117]** detected WB as an additional phase, along with the desired HEB, in the final product obtained by using the BR-SPS route. Starting from

HEB-based powders synthesized by BCR, secondary phases, including (W,Mo)B_2, were detected in the ceramic produced by PLS **[119]**.

Only few investigations succeeded in the obtainment of the single phase ($Ti_{0.2}Zr_{0.2}Hf_{0.2}Mo_{0.2}W_{0.2}$)$B_2$ ceramic **[26,120,121]**. For example, employing SPS on a mixture of metal borides previously treated by High-Energy Ball Milling (HEBM) resulted in samples containing a W-rich monoboride byproduct, ascribed to ($W_{0.78}Mo_{0.19}Ti_{0.02}Hf_{0.01}$)B. In contrast, no secondary phases were found when using the RSPS approach (multistep process, 2000°C/10min/50 MPa, as final condition) starting from elemental precursors co-milled for 50 min (ball to powder weight ratio, BPR=4) **[120]**. **Monteverde et al. [26]** combined the BCR route (HfO_2, ZrO_2, TiO_2, MoO_3, WO_3, B_4C, and carbon black, as raw materials) with the SPS process (2000°C/10min/50 MPa), resulting in a dense product, containing only some residual reactants (B_4C+C, about 2.5 vol.%) in addition to the expected HEB_W phase. The difficulties encountered in the synthesis of the pure HEB_W phase are likely due to the challenging solubilization of VI group metal borides in the main HEB phase. Therefore, it is expected that particular care needs to be taken in the synthesis step, aiming to the maximization of the conversion of the elemental reactants to the desired HEB_W phase, and in the subsequent SPS step, which was proven to be able to complete the conversion of secondary phases to form the complex quinary composition of HEBs systems **[24,25,74]**. In this regard, a strategy employed in this study to minimize the kinetic limitations ascribed to the VI group elements solubilization is the use of finer elemental powders in the SHS step. Indeed, this would lead to an increase of the superficial area of the precursor, thus extending the reaction interface during the SHS process. To further facilitate the conversion of unwanted secondary boride phases during the SPS step, small amounts of graphite as sintering additive are employed, given the beneficial effects associated to impurities reduction and abatement of kinetic limitation experienced with other HEB compositions **[23]**.

Apart from the difficulties associated with their fabrication, other crucial issues concerning pure HEBs are their scarce fracture toughness, and the limits of their oxidation resistance at high temperatures **[69,122-124]**. Specifically, as for the HEB_W system, which contains two VI group elements, criticalities on oxidation resistance are expected by the presence of two VI group elements (Mo and W), given their respective oxides high volatilities **[27]**. Following the positive effect obtained with the introduction of Si-containing additives (SiC, $MoSi_2$, $TaSi_2$, etc.) to simple individual borides, investigations focused on the fabrication and characterization of HEB-SiC systems have been recently conducted **[69,79,125-128].** For example, it was reported that the addition of 20 vol.% SiC

to $(Ti_{0.2}Zr_{0.2}Hf_{0.2}Nb_{0.2}Ta_{0.2})B_2$ powders produced by BCR favored sample consolidation, and the obtained product was characterized by a finer microstructure and superior fracture toughness with respect to the additive free system **[79,125].**

Table 3.1 - Density, composition, and mechanical properties of the bulk $(Ti_{0.2}Zr_{0.2}Hf_{0.2}Mo_{0.2}W_{0.2})B_2$-based products obtained in this work by SPS from coarser and finer W powders, with no graphite or in presence of 1wt.% of this additive. The corresponding values reported in the literature for the same HEB formulation are also included. BR: Borothermal reduction; BCR: Boro-Carbothermal Reduction; HEBM: High-Energy Ball Milling; PLS: Pressureless Sintering; RSPS: Reactive SPS; ρ_t= theoretical density of HEB; n.q.: not quantified; n.r.: not reported.

Precursors	**Fabrication method**	**Sintering conditions (T_D, t_d, P)**	**Secondary phases**	**ρ (%) (ρ_t, gcm^{-3})**	**HV (load,N) (GPa)**	**K_{IC} (MPa m$^{1/2}$)**	**Reference**
HfB_2, ZrB_2, TiB_2, W_2B_5, MoB_2	HEBM-SPS	2000°C/5min/30MPa	$(Ti_{1.6}W_{2.4})B_4$	n.r.	n.r.	n.r.	**[22]**
HfO_2, ZrO_2, TiO_2, MoO_3, WO_3, B_4C	BCR-SPS	2000°C/30min/80MPa	(W,Mo)-rich phase(n.q.)	n.r.	29.4±1.7 (1.96)	n.r.	**[118]**
Hf, Zr, Ti, Mo, W, B	HEBM-RSPS	Multistep 2000°C/10min/50 MPa	extra B(n.q.)	97.5 (8.56)	26.0±1.5 (1.96)	n.r.	**[120]**
HfO_2, ZrO_2, TiO_2, MoO_3, WO_3, B	BR-SPS	2000°C/10min/30 MPa	WB	n.r.	27.7±1.1 (1.96)	n.r.	**[117]**
HfO_2, ZrO_2, TiO_2, MoO_3, WO_3, B_4C, C black	BCR-SPS	2000°C/10min/50MPa	B_4C+C (2.5 vol.%)	96.5 (8.485)	n.r	n.r	**[26]**
HfO_2, ZrO_2, TiO_2, MoO_3, WO_3, B_4C, C black	BCR-PLS	2100°C/2h	Multiple phases	> 97.7	n.r	n.r	**[119]**
		2200°C/2h	$(W,Mo)B_2$(n.q.)	97.7 (8.40)	n.r	n.r	
H, Zr, Ti, Mo, coarse W, B	SHS-SPS	1950°C/20min/20MPa	$(W,Mo)B_2$(9 wt.%), TiO_2(2 wt.%)	96.6±0.7 (8.406)	26.2±1.4 (1)	2.32±0.55	**This work**
H, Zr, Ti, Mo, coarse W, B, graphite (1wt.%)	SHS-SPS	1950°C/20min/20MPa	None	98.6±0.1 (8.406)	26.4±0.7 (1)	2.14±0.42	**This work**
H, Zr, Ti, Mo, fine W, B	SHS-SPS	1950°C/20min/20MPa	$(W,Mo)B_2$(<1 wt.%), TiO_2(2 wt.%)	96.7±0.6 (8.406)	26.1±0.8 (1)	2.03±0.50	**This work**
H, Zr, Ti, Mo, fine W, B, graphite (1wt.%)	SHS-SPS	1950°C/20min/20MPa	None	98.5±0.7 (8.406)	26.8±0.9 (1)	1.54±0.66	**This work**
H, Zr, Ti, Mo, fine W, B, graphite (1wt.%), SiC (20 vol.%)	SHS-SPS	1950°C/20min/20MPa	None*	98.7±0.4 (8.406)	26.5±0.6 (1)	5.11±1.11	**This work**

(*) Except for the introduced SiC phase

The same HEB system, combined with different amounts (10, 20, 30 vol.%) of SiC, was also investigated by **Cheng et al. [128]**. Grain growth inhibition, powders consolidation enhancement, and improvement of mechanical properties (Vickers hardness and fracture toughness) were observed when SiC was added. More recently, bulk $(Ti_{0.2}Hf_{0.2}Nb_{0.2}Ta_{0.2}Mo_{0.2})B_2$ -27.7 vol.% SiC and $(Ti_{0.2}Zr_{0.2}Hf_{0.2}Ta_{0.2}Mo_{0.2})B_2$-27.4 vol.% SiC composites were produced SHS from elemental transition metals, B_4C and Si precursors followed by SPS **[69]**. The sintering behavior, mechanical properties and oxidation resistance at high temperatures clearly benefitted by the presence of SiC.

For these reasons, the influence on mechanical properties and oxidation resistance deriving from the introduction of SiC on the $(Ti_{0.2}Zr_{0.2}Hf_{0.2}Mo_{0.2}W_{0.2})B_2$ matrix is also examined in this study. The obtained results are finally compared with those relative to the SiC free system.

3.1.2 Materials and Methods

The synthesis of $(Ti_{0.2}Zr_{0.2}Hf_{0.2}Mo_{0.2}W_{0.2})B_2$ was carried out according to the following direct reaction:

$$0.2\mathrm{Ti} + 0.2\mathrm{Zr} + 0.2\mathrm{Hf} + 0.2\mathrm{Mo} + 0.2\mathrm{W} + 2.2\mathrm{B} \rightarrow \mathrm{Ti}_{0.2}\mathrm{Zr}_{0.2}\mathrm{Hf}_{0.2}\mathrm{Mo}_{0.2}\mathrm{W}_{0.2}\mathrm{B}_2 \qquad (4a)$$

which is an extended version of reaction 4 in **Section 1.2.1**. A 10 mol.% excess boron was employed, to take into account the borothermal reduction of oxide impurities present in the elemental powders, which need to be reduced to obtain a purer product after SHS **[23]**. Details on the employed reactants can be found in **Table 2.1**. In particular, coarser W powders (<44 µm) or finer W (1–5 µm) are used. Accordingly, the corresponding borides will be called from now on HEB_W_c and HEB_W_f respectively. The particle size of the initial W reactants was measured by laser light scattering analysis (CILAS 1180, France), to precisely characterize the two employed batches.

SHS experiments were carried out according to the details reported in **Section 2.1.1**. Milling and homogenization of the SHS product was performed according to the following three conditions:

a) Without any other additive (samples indicated as HEB_W_c_0C or HEB_W_f_0C)
b) Adding 1 wt.% graphite (Sigma-Aldrich, cod 282863, <20 µm) (samples indicated as HEB_W_c_1C or HEB_W_f_1C)

c) Adding 1 wt.% graphite and 20 vol% SiC (Alfa Aesar, cod. 014165, 99.8 % purity) only for the case of HEB_W_f to form a HEB-SiC composite (samples indicated as HEB_W_SiC)

The SPS conditions adopted to produce the different bulk samples were a dwell temperature (T_D) of 1950°C, heating rate of 200 °C/min, holding time (t_D) of 20 min, and an applied pressure (P) equal to 20 MPa. These conditions were adopted due to the success in the fabrication of other HEB composition in previous works **[23,24]**. About 4.2–4.3 g (SiC-free systems) or 3.7 g (HEB_W_ SiC) of powders were sintered in each experiment.

The obtained samples (discs of about 15 mm diameter and 3 mm height), were then ground to eliminate graphite impurities and characterized for their density, employing Archimedes' method using distilled water as immersing medium. The density value of 8.406 g/cm^3 for HEB_W was estimated according to the Rietveld's analysis results by using the following formula:

$$\rho_c = (Z \cdot M/V_c) \cdot (10^{24}/N_A) \quad (1)$$

where Z is the stoichiometry of each element, M the corresponding molar mass, V_c the volume of the lattice cell, and N_A the Avogadro constant. The density values of 3.21 g/cm^3 for SiC and 2.16 g/cm^3 for C were employed **[129]**, applying the rule of mixture whenever one or multiple additives were used **[130]**.

Phases identification in SHS and SPS products was performed by X- ray diffraction analysis (XRD) (rotating anode SmartLab Rigaku, Japan and Philips PW 1830, Netherlands) using Cu Kα radiation, over scattering angles 2θ from 20 to 110°, 0.05° and 15 s per each analysis step. The obtained XRD patterns were then analysed via MAUD program to quantify the detected phases and the microstructural parameters **[131]**. Rietveld refinement results are reported in **Appendix A.a**. A High-Resolution Scanning Electron Microscope (HRSEM) (mod. S4000, Hitachi, Tokyo, Japan), equipped with a UltraDry EDX Detector (Thermo Fisher Scientific, Waltham, MA, USA), was employed to characterize the morphology and elemental distribution in SHS powders and dense, polished samples.

The Vickers Hardness of the dense samples was estimated with a Micro Vickers Hardness Testers FUTURE-TECH FM-810 (Kawasaki, Kanagawa 210–0804, Japan) applying a 1N load for 15s, while

indentation fracture toughness was estimated observing the developed cracks with a scanning electron microscope (Quanta 400 of Field Electron and Ion Company, Hillsboro, Oregon, USA) and applying Evans and Charles formula **[132,133]**:

$$K_{IC} = 0.824\, L/c^{1.5} \quad (2)$$

where L is the applied load, and c the average crack length measured from the indentation centre.

Given the importance of the oxidation characterization of these HEB_W or HEB_W-based systems, oxidation behaviour was evaluated at different temperatures (in the interval 600-1300°C) with ramped oxidation experiments (hr=4°C/min) in a muffle furnace (LT 24/11/B410, Nabertherm, Lilienthal, Germany), followed with isotherms of 1h at the maximum temperature. The sample's mass variation after the experiments were recorded with a Ohaus Explorer Pro (Ohaus Corporation, NJ, USA) analytical balance (±0.0005 g precision), while XRD patterns were acquired on the samples' surfaces after oxidation, in the 2θ interval between 20°-80°. To examine the oxide scale morphology and composition, polished cross sections of the oxidised samples were characterized via SEM/EDX.

3.1.3 Results and Discussion

3.1.3.1 Synthesis and sintering

As reported in **Figure 3.1a**, **Figure 3.2a**, **Table A1a** and **Table A2a** during the SHS process individual borides as well as different solid solutions are produced using either the finer or coarser W as precursor. Apparently, the SHS process is too fast to achieve a satisfactory interdiffusion of the different transition metal borides to form only the desired solid solution, as also confirmed by the uneven elemental distribution in the powder products observed via SEM/EDX for the case of HEB_W_c (**Figure 3.2a**) and HEB_W_f (**Figure 3.2b**).

However, similar yields of the desired quinary boride phase HEB_W were observed in the powders produced starting from coarser ($d_{4,3}$=19.90±0.83 μm) and finer ($d_{4,3}$=7.24±0.27 μm) W powders, quantified to be 12 and 17 wt.% respectively (see **Table A1a** and **Table A2a**, **Figure 3.2a** and **3.3a**). Even if a slight effect of the reduction of the W particle size is present, the two products are still far from the desired composition.

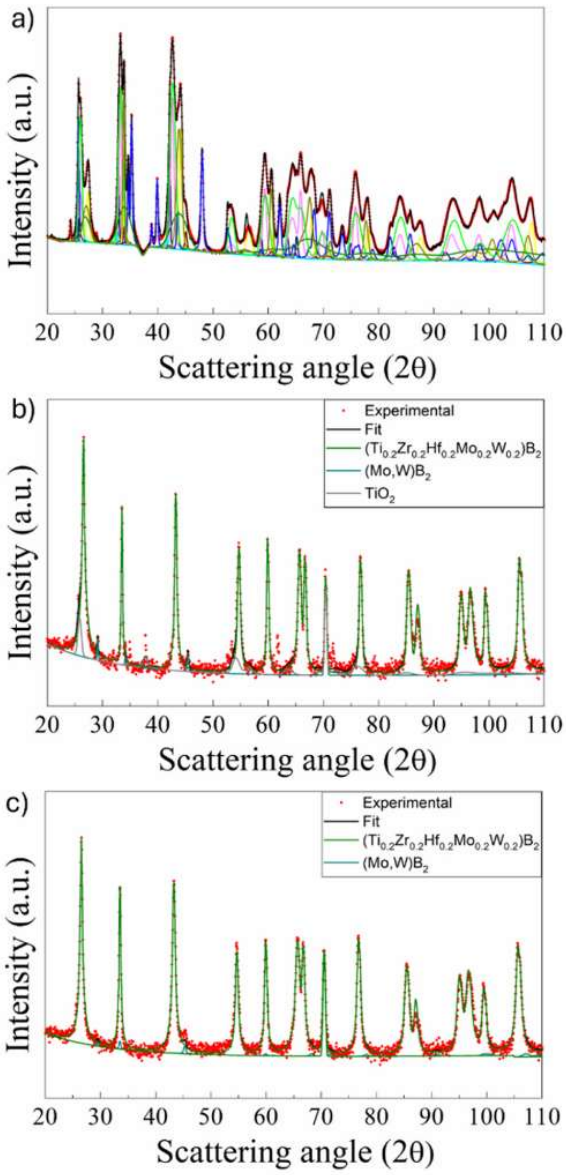

Figure 3.1 - XRD pattern and Rietveld refinement of (a) SHS milled powders from coarser W reactants and corresponding bulk samples obtained by SPS (b) with no graphite, and (c) with 1 wt.% C. Experimental: red dots; Best Fit: dark solid line; $(Ti_{0.2}Zr_{0.2}Hf_{0.2}Mo_{0.2}W_{0.2})B_2$: olive solid line; HfB_2 (COD #1510711): navy solid line; $(Ti_{0.5}Zr_{0.5})B_2$ (COD #1510845): magenta solid line; TiB_2 (COD #2002799): yellow solid line; WB_2 (COD #1510852): blue solid line; WB_4 (COD #2310108): wine solid line; ZrB_2 (COD #1510857): light blue solid line; $(Hf_{0.5}Ti_{0.5})B_2$ (COD #1510710): light green solid line; $(Ti_{0.5}Mo_{0.5})B_2$ (COD #1510760): dark yellow solid line); $(Mo,W)B_2$ (COD #1510765): cyan solid line; TiO_2 (COD #1010942): violet solid line.

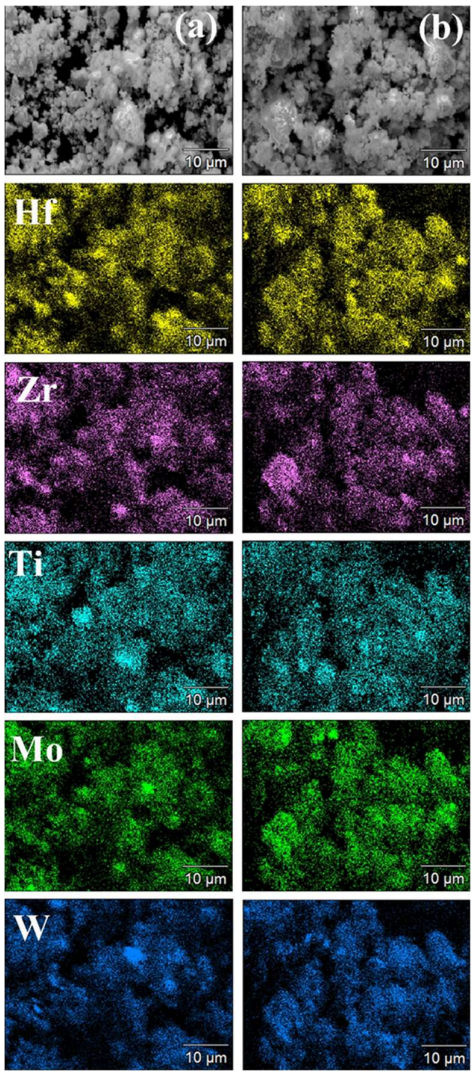

Figure 3.2 - SEM micrographs and corresponding EDX elemental maps of the 1h milled powders prepared by SHS from (a) coarse, and (b) fine W reactants.

When the ball milled SHS powders are processed in SPS at 1950°C/20min/20MPa, as reported in **Figure 3.1b** and **Table A1b** numerous secondary phases previously present disappear for the case of HEB_W_c_0C, where the HEB_W phase (89 wt.%) is accompanied by a nonnegligible 9 wt.% content of a Mo and W rich phase ascribed to $(Mo,W)B_2$ (**Table A1b**) as also evidenced by elemental maps in **Figure 3.4a**. For the case of HEB_W_f_0C, no other phases can be detected via XRD other than HEB_W (**Figure 3.2b** and **Table A2b**), however, looking at the EDX elemental maps reported for this

sample in **Figure 3.4b**, it is possible to identify some spots rich in Mo and W, testifying that even if the complete conversion is close, it is not yet achieved.

As reported in **Figure 3.1c**, **Figure 3.3c**, **Table A1c** and **Table A2c**, employing 1 wt.% C during SPS tests in both systems led to no other detectable phases other than the desired HEB_W (see also **Table A1c and A2c**). This finding was confirmed also by the elemental maps reported in **Figure 3.4c and 3.4d**, which testify the obtainment of the pure $Ti_{0.2}Zr_{0.2}Hf_{0.2}Mo_{0.2}W_{0.2}B_2$ composition.

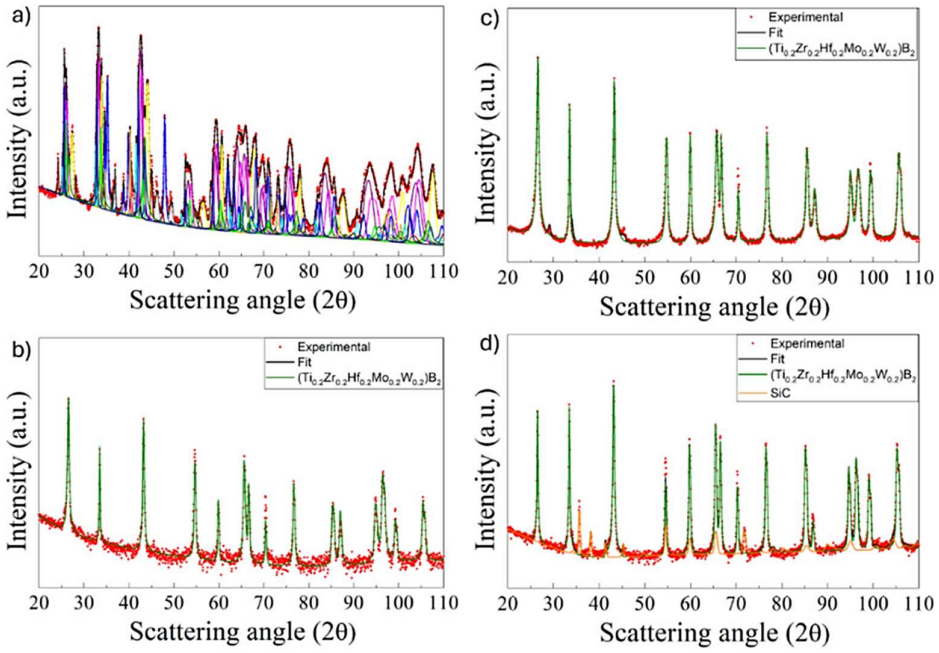

Figure 3.3 - XRD pattern and related Rietveld refinement of (a) SHS 1 h milled product from finer W powders and corresponding bulk samples obtained by SPS (b) with no graphite, (c) with 1 wt.% C, (d) with 1 wt.% C and 20 vol.% SiC. Experimental: red dots; Best Fit: dark solid line; $(Ti_{0.2}Zr_{0.2}Hf_{0.2}Mo_{0.2}W_{0.2})B_2$: olive solid line; $(Hf_{0.5}Zr_{0.5})B_2$ (PCD #1932158): purple solid line; HfB_2 (COD #1510711): navy solid line; $(Ti_{0.5}Zr_{0.5})B_2$ (COD #1510845): magenta solid line; TiB_2 (COD #2002799): yellow solid line; WB_2 (COD #1510852): blue solid line; WB_4 (COD #2310108): wine solid line; ZrB_2 (COD #1510857): light blue solid line; Mo (COD #4001308): pink solid line; $Mo_2B_{0.4026}$ (COD #1511521):light grey solid line; MoO_2 (COD #1548687):dark grey solid line; $Mo_{0.875}Zr_{125}$ (COD #1522701): light orange solid line; $(Hf_{0.5}Ti_{0.5})B_2$ (COD #1510710): light green solid line; SiC (COD # 9010158): orange solid line.

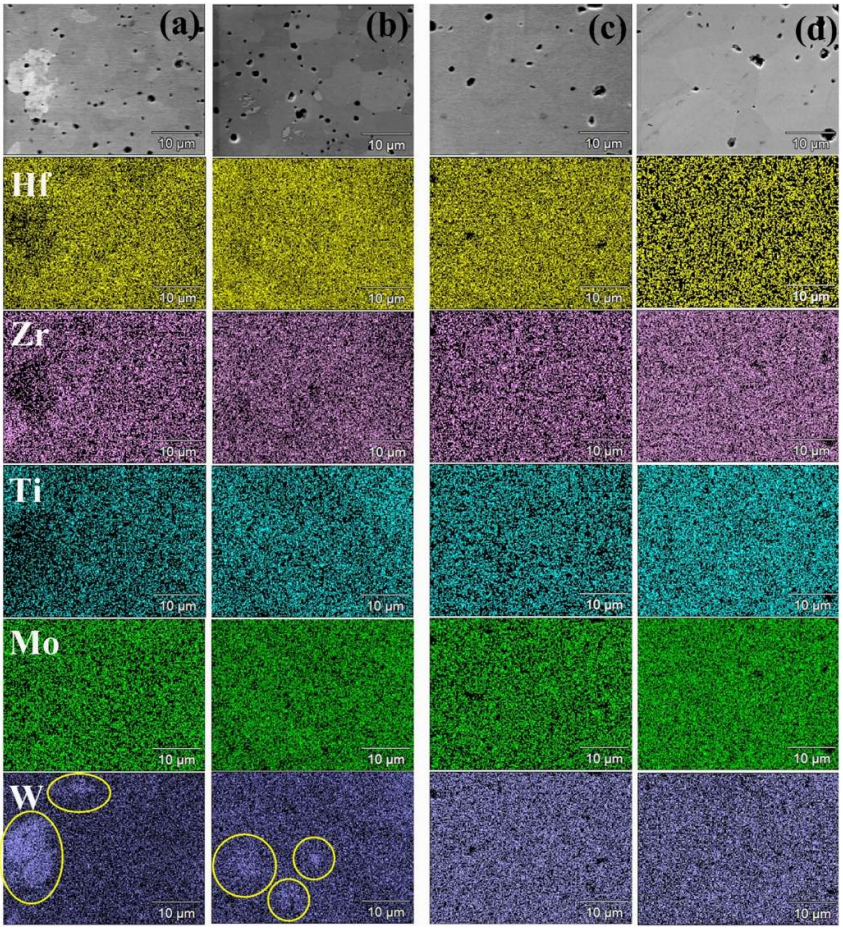

Figure 3.4 - Cross sectional SEM micrographs and related EDX elemental maps of HEB_W samples obtained by SPS from SHS powder with no graphite addition: (a) coarser, (b) finer W powders, and with 1 wt% graphite addition: (c) coarser, and (d) finer W powders.

Based on the results obtained for HEB_W_c and HEB_W_f, the precursors used for the HEB_W_f_1C system (fine W, 1 wt.% graphite) are also used for the preparation of the SiC containing HEB composite samples. Similarly to the monolithic HEB_W samples, the SPS conditions adopted were 1950 °C/20 min/20 MPa. The relative density of resulting composite was 98.7±0.4 %. As for product composition, the first issue to be checked was if the addition of SiC hindered, in some way, the conversion of secondary phases present in SHS powders (**Figure 3.3a**) into the desired solid solution. As reported in **Figure 3.3d** and **Table A3**, XRD analysis associated to the Rietveld refinement testifies that no other phases, other than the expected ones (HEB_W and SiC), were detected on this sample.

Also, the relative SiC content, was estimated to be 7 wt.% (**Table A3**), equivalent to about 21.5 vol.%, is in fair agreement to the amount initially added to SHS powders. SEM micrographs and corresponding EDX maps shown in **Figure 3.5** gives further evidence that a rather dense and homogeneously distributed HEB_W-SiC composite was produced.

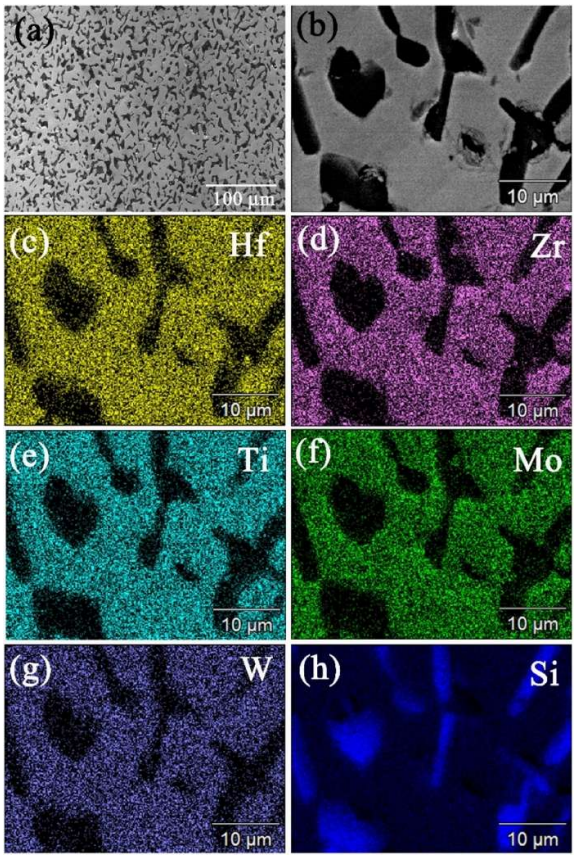

Figure 3.5 - Cross sectional SEM micrographs and related EDS elemental maps of HEB_W-SiC sample obtained by SPS: (a) general, (b) detailed views, and (c)-(h) related EDX elemental maps.

3.1.3.2 Mechanical properties

Analysing the outcomes of the SPS experiments carried out on HEB_W samples, shown in **Table 3.1**. It should be noted that no particular effect was displayed by the use of finer W and/or the addition of graphite on the Vickers hardness of samples fabricated in this work, with HV values in the range of 26.1–26.8 GPa. This is in agreement with the rather high densities obtained for all sintered samples presented in **Table 3.1**. Indeed, the obtained values are in line with results (26 GPa) reported

by **Qin et al. [120]**, obtained on HEB_W produced by RSPS from elemental powders preliminarily activated by HEBM. Superior hardness properties were obtained by **Gild et al. [118]** and **Zhang et al. [117]**, i.e. 29.4 and 27.7 GPa, respectively, but the samples presented non negligible secondary phases, which may affect the measured values.

Regarding the fracture toughness values also reported in **Table 3.1**, the monolithic high entropy borides possessed very low K_{IC}, i.e. 2.32 MPa $m^{0.5}$ at most. Moreover, the reduction of impurities thanks to the graphite addiction most probably removed all obstacles to crack propagation, further reducing the K_{IC} values in the purer samples. The introduction of SiC to the HEB_W matrix provided a marked improvement on the K_{IC} value, which increased up to 5.11 MPa $m^{0.5}$. This is strictly correlated to the obstacles to crack propagation caused by the dispersed silicon carbide phase into the composite sample.

3.1.3.3 Oxidation behaviour of HEB_W and HEB_W-SiC samples

Based on **Backman and Opila** studies **[27]**, the presence of two VI group metals (Mo, W) along with three IV group metals (Ti, Zr, Hf) is expected to affect the oxidation resistance of the HEB system investigated in this work. When TMBs are exposed to oxidising environments, a mass gain is usually recorded due to the incorporation of oxygen atoms to generate the corresponding metal oxides in solid state.

On the other hand, the opposite behaviour can be observed in **Figure 3.6** when considering the SiC-free HEB system (red line). Indeed, samples annealed at 800°C or higher temperatures manifested a progressive loss in their weight. This fact can be likely associated to the formation of highly volatile MoO_3 and WO_3 **[27]**. XRD analysis performed on the same sample's surfaces (**Figure 3.7a**) shows that no oxides are formed up to 600°C, In contrast, as temperature was raised to 700°C, XRD peaks ascribable to TiO_2, ZrO_2 and WO_3 were detected. As the temperature level was further increased at 1000°C and higher values, all reflections associated to tungsten oxide disappear, while Hf reacts with oxygen to form HfO_2. If the oxidation treatment is carried out at higher temperatures (1200°C), the mixed oxide phase $ZrTiO_2$ is also formed. SEM micrographies and related elemental maps, taken on the cross section of the oxidised samples are reported in **Figure 3.8**. It is confirmed that at 800°C (**Figure 3.8a**), Mo and W oxides are still present in the oxide scale, along with the other three IV group transition metals, albeit in a lower concentration for the case of Mo.

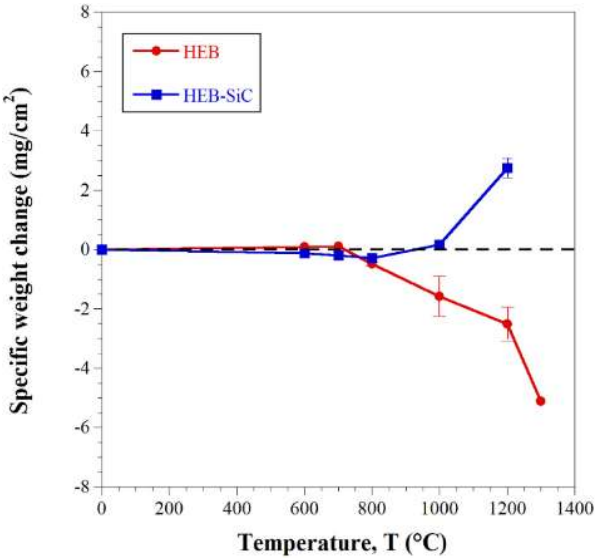

Figure 3.6 - Comparison of weight changes per surface area of additive free and SiC containing HEB_W samples during oxidation tests carried out in air furnace as a function of temperature (isotherm duration=1h).

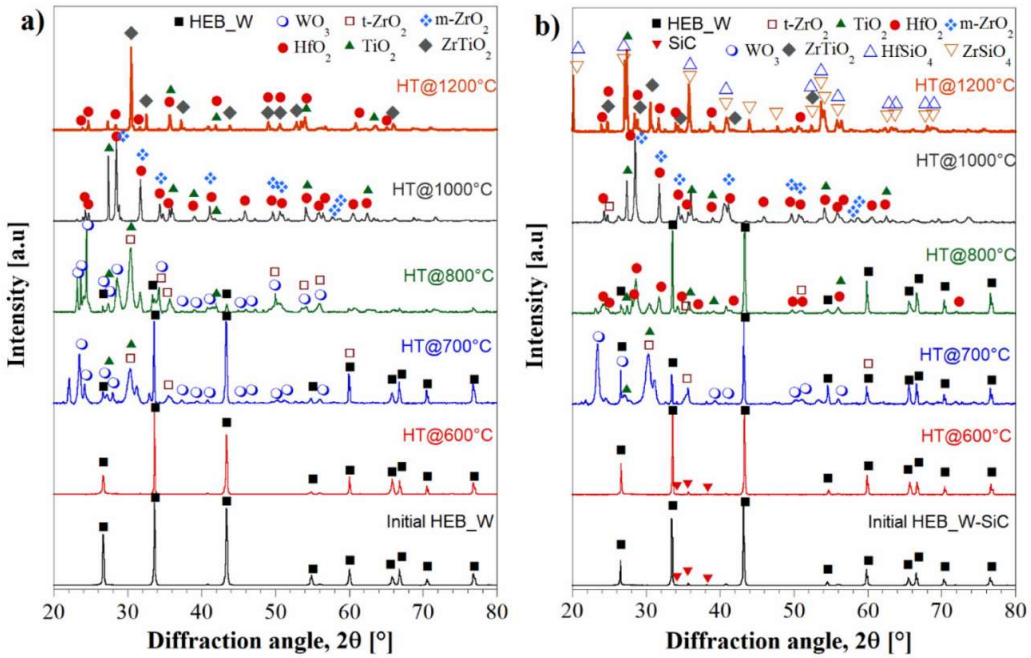

Figure 3.7 - XRD patterns of HEB_W (a) and HEB_W_SiC (b) samples after being heat treated in air furnace at different temperatures.

Examining the sample oxidised at 1000°C, a clear depletion of Mo and W can be observed in the superficial layers, along with a corresponding enrichment in Ti. This is a clear evidence of the volatilization of Mo and W oxides, which causes a significant degradation of the oxide scale, as can be observed already in the 1000°C condition. When the temperature is further augmented, the uppermost layer detaches from the sample, most probably due to the rising pressure exerted by the evolution of MoO_3 and WO_3 gases. This phenomenon can be considered highly detrimental, as Mo- and W-containing material is exposed to oxidation, causing an uncontrolled progression of the oxidation of HEB_W as testified by its growing mas loss observed for 1200 and 1300°C (**Figure 3.6**).

Based on the observations and considerations above, the Mo- and W- containing high entropy boride cannot be considered suitable for high temperature applications, confirming that the solubilization of VI group metals to form high entropy borides, can cause oxidation issues related to their oxides' volatility **[27]**. A solution is therefore needed to improve the oxidation resistance of this system.

The approach adopted in this work was then to introduce 20 vol.% SiC in the HEB_W_f_1C matrix. Other than improving the fracture toughness of the resulting composite, the idea is to obtain beneficial effects also in terms of prevention of the MoO_3 and WO_3 volatilization. Data reported in **Figure 3.6** shows that neither relevant gain nor loss was recorded in the mass of HEB_W_SiC system up to the oxidation temperature of 1000°C. For higher temperatures (1200°C), an increase in sample weight was observed. XRD data shown in **Figure 3.7b** evidence that apart from the presence of SiC, no differences can be observed in the patterns up to 700°C. However, as the annealing temperature was increased to 800°C, the intensity of HEB peaks is still high, in contrast with the additive free system, where the original phase is barely detected. At T=1000°C, no HEB phase can be found and the XRD patterns and both systems look very similar. However, when the temperature is raised to 1200°C, Hf- and Zr-silicate phases have been identified, which are expected to positively affect the oxidation resistance of the system.The effect of SiC at 1200°C is furtherly clarified when examining Figure **3.8c-3.8d**. It can be observed that while in the additive free HEB_W sample the volatilization of Mo and W oxides causes the collapse of the oxide scale, the SiC- containing sample was much less affected by the oxidation test.

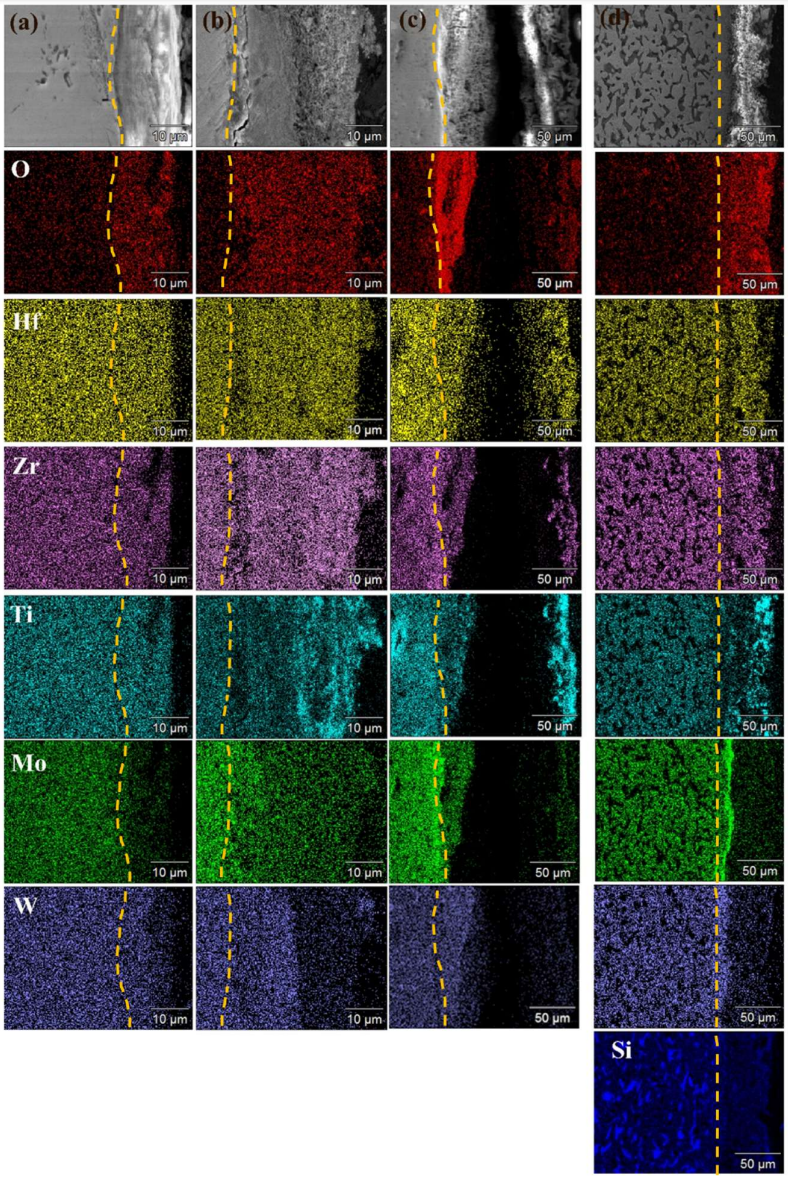

Figure 3.8 - Cross sectional SEM micrographs and related EDX elemental maps of SiC free samples after oxidation at (a) 800°C, (b) 1000°C, (c) 1200°C, and (d) HEB_W_SiC product heat treated in air furnace at 1200°C. A yellow dashed line has been added to indicate the boundary of the oxide scale.

In the latter case, the thinner formed oxide scale can be subdivided in two different layers, one (about 40-50 µm thick) is rich in IV group metals (Ti, Zr, Hf), the other (about 15-20 µm thick) in VI group ones (Mo and W). Given the quite uniform distribution of silicon across the two layers, it is then presumable that the first one is mainly composed of IV group metal oxides and silicates, while the inner one consists of Mo- and W-rich silicates (or borosilicates) which are responsible for the

protection of the material from the oxidation, causing a diffusion barrier for oxygen to reach the bulk material, as well as preventing the volatilization of Si-free Mo- and W-oxides.

It is important to state that the deep understanding of the oxidation mechanisms of the HEB_W here investigated and the effect of SiC involve both thermodynamic and kinetic considerations. In fact, several phenomena such as surface reaction, oxygen diffusion through the porous oxide scale and liquid boria, as well as permeation and evaporation of the latter are involved in oxidation of metal diborides such as the ones examined in this Section. **Parthasarathy et al. [134]** and, more recently, **Mogilevsky and Cinibulk [135]** provided, for the case of individual metal borides-based systems, an excellent schematization of the latter phenomena, as well as a mathematical model to describe them. However, when considering high entropy materials, the oxidation mechanism is made further complicated by the formation of several multicomponent phases, as confirmed in the present study by the various individual and mixed oxides detected by XRD analysis on the surface of the oxidized samples (**Figure 3.7**). One general insight which comes from this investigation is the fact that the use of VI group metals to form multi-component diborides needs to be handled with care, as their oxides volatility has proven to be a criticality in the oxidation resistance of HEB_W material, thus confirming the trends predicted by **Backman and Opila [27]**. However, the effect caused in this system by the combination of three different IV group metal (Ti, Zr, Hf) borides is still unresolved, and a similar situation could be expected if V group elements (Nb, Ta), which do not form volatile oxides, are employed for the fabrication of multicomponent TMBs. To address more clearly the effects of such elements, it would be advisable to study the behaviour of simpler multicomponent borides (binary and ternary). This approach would permit, taking also advantage of the information available in the literature for individual diboride systems, to better decouple the effects of the different constituents and their combination, with the ultimate goal of more thoroughly understand the consequences of the incorporation of each transition metal in complex compositions.

Results of this investigation were published in **Casu, M.**, Barbarossa, S., Locci, A. M., Cao, G., Cau, C., Caggiu, L., Garroni, S., Ferro, P., & Orrù, R. (2024). Processing and characterization of Ultra High Temperature High-Entropy $(Ti_{0.2}Zr_{0.2}Hf_{0.2}Mo_{0.2}W_{0.2})B_2$-based Ceramics: Effect of W granulometry, graphite, and SiC addition. *Journal of Alloys and Compounds*, *1007*, 176492. https://doi.org/10.1016/j.jallcom.2024.176492

3.2 Zirconium-based binary borides

3.2.1 Introduction

IV group transition metal borides TiB_2, ZrB_2 and HfB_2 represent the most studied individual TMBs **[47,136]**. Each one of these ceramics presents attractive properties but also some limitations. Indeed, dense HfB_2 shows rather good mechanical properties, with Vickers hardness up to 28 GPa, and Young's modulus is about 480 GPa **[12,47,137]**. This system also displays high oxidation resistance, thanks to the formation of a compact oxide scale which acts as a barrier to superficial oxygen diffusion up to about 1790°C. Correspondingly, a monoclinic to tetragonal phase transition occurs in HfO_2, which causes a drop in the oxidation resistance **[139-141]**. As a drawback, this ceramic possesses a high density (i.e. 11.21 g/cm^3 **[47]**), which hinders its applicability in the aerospace sector **[141]**, where this aspect plays a crucial role in materials choice. Moreover, Hf is listed among the critical-raw materials by the EU, with the unavoidable negative consequences for its supply and corresponding cost **[142]**. As for its cost, (about 3.800 $/kg as of 2025 **[143]**) it can be estimated to be two or even three orders of magnitude higher than those of Zr (about 18.86 $/kg for Zr-sponge **[144]**) or Ti (about 5.9-6.2 $/kg for Ti-sponge depending on purity **[64]**). The most economically convenient boride of the three metals is TiB_2, which is also a lightweight TMB, with a density of just 4.50 g/cm^3 **[47]**. Despite the good mechanical properties measured on dense samples (Vickers hardness up to 35 GPa and Young's modulus of about 560 GPa **[20,47]**), this material is flawed by a very modest oxidation resistance. This is caused by the rather porous and non protective oxide scale formed when exposing it to temperatures superior to 800°C **[20]**. Ti is also a critical raw material, due to the EU complete reliance on external imports of such metal **[142]**. Finally, ZrB_2 represents a compromise between density and performances of IV group TMBs. Indeed, its 6.09 g/cm^3 **[47]** density is more suitable for aerospace applications than that of HfB_2, while hardness values up to 23 GPa, Young's modulus of 526 GPa are reported for this system **[12,16,47]**. Furthermore, Zr is not listed as a critical raw material **[142]**. Its oxidation resistance, albeit superior to that of TiB_2, is flawed by the monoclinic to tetragonal phase transition that occurs to ZrO_2, at a much lower temperature (about 1120°C) than HfO_2, as reported above **[141]**. This phase transition causes severe thermomechanical stresses, that produce a characteristic porous, cracked and non protective oxide already at such temperatures, far from the proposed application **[138,139,145-**

147]. However, given the density lower than that of HfB_2 and the superior oxidation resistance if compared to TiB_2, ZrB_2 is considered the best base candidate for aerospace applications.

The development of ZrB_2-containing solid solutions can be then considered a strategy to enhance its advantages while limiting its drawbacks. To better understand the effect of the introduction of other TMBs into ZrB_2, the development of equimolar binary solid solutions is a straightforward choice, allowing to track the possible changes correspondingly introduced.

In this regard, the binary $(Zr_{0.5}Hf_{0.5})B_2$ solid solution was developed in this work. The particular aim was to verify if the oxidation resistance of the resulting material could be improved compared to ZrB_2. Given the complete solubility of ZrO_2 and HfO_2 (see the HfO_2-ZrO_2 phase diagram, **Figure B1** in **Appendix B [148]**), and the fact that HfO_2 presents the m→t phase transition only at 1790°C **[141]**, the phase transition temperature of the resulting equimolar solid solution is expected to be close to the average of those of ZrO_2 and HfO_2, i.e. about 1500°C (see **Figure B1**),with a consequent improvement of the oxidation resistance of the binary system, compared to ZrB_2.

The mutual solubility in the whole compositional range of ZrB_2 and HfB_2, prompts several authors to investigate the $(Zr_xHf_{1-x})B_2$ solid solution **[53,80,149,150]**. For instance, starting from ball milled ZrB_2, and HfB_2 powders, a nearly full dense $(Zr_{0.97}Hf_{0.03})B_2$ solid solution was obtained by a multistep hot pressing process (2150 °C) **[80]**. The same precursors were co-milled in different proportions for 3h (BPR=10) by **Sitler et al. [149,150]** and the resulting mixtures densified by Spark Plasma Sintering (5 kN, 1700 °C, 10 min) to obtain bulk $(Zr_{0.8}Hf_{0.2})B_2$ (ρ=82.9%), $(Zr_{0.5}Hf_{0.5})B_2$ (ρ=76.2%) and $(Zr_{0.2}Hf_{0.8})B_2$ (ρ=76.5%) solid solutions. **Belisario et al. [53]** employed flash sintering to produce $(Zr_{0.5}Hf_{0.5})B_2$ starting from powders synthesized either from carbothermal reduction (CR) or borohydride reduction (BHR). The second method led to higher samples' densities (rising from 70% to 95 %, when comparing CR and BHR), higher hardness (8.23 ± 0.10 and 23.01 ± 0.37 GPa, respectively), and oxidation resistance.

Let's consider now the combination of ZrB_2 and TaB_2 to form the corresponding binary system. In this regard, **Licheri et al. [16]** compares the mechanical properties of ZrB_2 and TaB_2 obtained via SHS-SPS or RSPS routes. Even if lower densification levels were achieved with TaB_2 (SHS-SPS: ρ=93.9%, RSPS: ρ=94.6%, compared to 98.5% and 95.6% respectively obtained for ZrB_2), this system was characterized by superior Vickers hardness (average of 18.0 GPa for TaB_2 versus 10.9 GPa for ZrB_2) and indentation fracture toughness (average of 4.0 MPa $m^{1/2}$ for TaB_2 versus 2.2 MPa $m^{1/2}$ for ZrB_2).

The Authors also report flexural strength values for the two systems, which however were heavily flawed by the residual porosity of the Ta-containing samples.

Recently, **Vorotilo et al. [151]**, attempted the fabrication of $(Zr_xTa_{1-x})B_2$ solid solutions with x=5÷100 by HP (1900°C, 50 MPa, 10 min) starting from powders obtained by SHS and processed by BM for 4h (BPR=6). Based on literature, experimental data and theoretical calculations, it was assessed that higher mechanical properties can be expected for the binary solid solutions, with respect to the individual constituents. For example, the authors estimated fracture toughness values for the solid solutions up to about 8.3 MPa $m^{1/2}$, considerably higher than the values of both ZrB_2 (3.28 MPa $m^{1/2}$) and TaB_2 (5.06 MPa $m^{1/2}$). Concurrently, an impressive nano-hardness value of 70 GPa was measured for the system containing 40 mol.% TaB_2 **[151]**. These interesting results need to be taken with caution, given the fact that all samples with a TaB_2 mol.% > 25–27 did not consist of a single pure solid solution, but were rather multiple-boride composites. Indeed, the authors were not able to fully solubilize TaB_2 to higher extents, despite that their thermodynamics calculations show that all solid solutions of ZrB_2 and TaB_2 are thermodynamically stable. Such discrepancies open the door for further studies. Nonetheless, findings observed by **Vorotilo et al. [151]** suggest that attractive mechanical properties can be obtained when part of ZrB_2 is replaced with TaB_2 to form solid solutions. Along this line, $(Zr_{0.5}Ta_{0.5})B_2$ is the second Zr-based binary solid solution studied in this Thesis, and the obtained results are discussed in this Section. The synthesis of $(Zr_xTa_{1-x})B_2$ solid solutions (x from 0 to 1) was also attempted by arc melting starting from ZrB_2, and TaB_2 precursors **[152]**. Based on the obtained results, it was concluded that the stable compositional range for this system was Ta ≤8 % mol. Consistently, a single phase $(Zr_{0.97}Ta_{0.03})B_2$ solid solution was obtained by **McClane et al. [80]** using a multistep program by HP (2150 °C) starting from ball milled ZrB_2, and Ta powders. Furthermore, Zr-rich $(Zr_xTa_{1-x})B_2$ products (x = 0.97 and 0.94) have been also prepared via a multistep reactive HP method (2200 °C) preceded by a hydride-based synthesis technique using ZrH_2, amorphous B, phenolic resin, and Ta_2H precursors **[54]**. The resulting products possessed relative densities of 99.2 and 99.0%, respectively, and consisted of the desired solid solutions with small amounts of ZrC and ZrO_2. The same processing route was also adopted for the preparation of $(Zr_{0.5}Ta_{0.5})B_2$ **[153]**, but the resulting 95.9% dense ceramic was not single-phase, with a core–shell microstructure, consisting of ZrB_2 cores surrounded by shells of $(Zr,Ta)B_2$ solid solutions. Based on the information provided above, the equimolar $(Zr,Ta)B_2$ solid solution was not obtained in the literature prior to this work (i.e. before 2023) as single boride phase.

The fabrication by SHS-SPS of single boride phase $(Zr_{0.5}Hf_{0.5})B_2$ and $(Zr_{0.5}Ta_{0.5})B_2$ solid solutions, from now on also identified as ZHB and ZTB for the sake of brevity, is described in this Thesis. The two-step approach was chosen for its effectiveness for the obtainment not only of standard MeB_2 (Me = Zr, Hf, Ta, and Ti) in bulk form **[16-17]** but also for the production of different dense quinary HEBs **[23-25]**, as also confirmed by **Section 3.1** in the present Thesis. Following the beneficial influence deriving from the introduction of small amounts of graphite to the SHS powders prior to SPS, to remove O-contaminants and concurrently improve sample consolidation, the effect of this additive will be also examined for the case of the two binary diboride systems above. The optimal sintered products will be finally characterized from the mechanical and oxidation points of view, to test if any improvement in these regards can be obtained by substituting 50 mol.% ZrB_2 with 50 mol%. of HfB_2 or TaB_2.

3.2.2 Materials and Methods

Reactants employed for the SHS synthesis of ZHB and ZTB systems are listed in **Table 2.1**, while details of the SHS methodology are reported in **Section 2.1.1**. As was done for the obtainment of HEB_W (**Section 3.1**), a 10 mol.% excess B in the direct reaction (4), modified to take into account the presence of two metal reactants, was employed to overcome the presence of oxide impurities in the elemental powders:

$$0.5\mathrm{Zr} + 0.5\mathrm{Me} + 2.2\mathrm{B} \rightarrow \mathrm{Zr}_{0.5}\mathrm{Me}_{0.5}\mathrm{B}_2;\ (\mathrm{Me{=}Hf,\ Ta}) \qquad (4b)$$

After SHS, particle size distribution of the homogenized products was evaluated by laser light scattering analysis (CILAS 1180, France). Additive free and 1 wt.% graphite containing mixtures were consolidated by SPS (see **Section 2.1.2**). The dwell temperature (T_D), heating rate (hr), holding time (t_D), and applied pressure (P) values during SPS runs were 1850 °C (1 wt.%C) or 1950 °C (0 wt.%C), about 200 °C/min, 20 min, and 20 MPa, respectively. The resulting sintered samples were cylindrical disks of about 15 mm diameter and 3 mm height. Phases identification in SHS and SPS products was carried out by X-ray diffraction using a SMARTLAB diffractometer with a rotating anode source of copper (λCu Kα = 1.54178 Å) working at 40 kV and 100 mA over a range of scattering angles 2ϑ from

20° to 80°, in steps of 0.05° with 15s acquisition time per angle step. The Rietveld method was used to estimate phases amount (wt.%) and the corresponding structural parameters by analysing the XRD patterns with the MAUD program **[131]**. Rietveld refinement results are reported in **Appendix A.b**. The Archimedes' method, using distilled water as immersion medium, was employed to determine the absolute density of SPS samples. The corresponding relative densities were calculated by considering the crystallographic values (ρ_c) of 9.10 and 8.59 g/cm3 for ZHB and ZTB, respectively, estimated according to Eq. (1), in **Section 3.1.2**. The presence of graphite (2.26 g/cm^3) in 1 wt.% C samples was also accounted for the evaluation of their theoretical densities, applying the rule of mixture when this additive was employed **[130]**. SHSed powders and sintered samples microstructures were examined by high resolution scanning electron microscopy (HRSEM) (mod. S4000, Hitachi, Tokyo, Japan) equipped with an UltraDry EDX Detector (Thermo Fisher Scientific, Waltham, MA, USA). Thermogravimetric analysis tests (NETZSCH, STA 409 PC Luxx Simultaneous DTA-TGA Instrument, Germany) were conducted under 0.1 L/min air flow to evaluate the mass changes ascribable to oxidation of the two binary TMBs. Specifically, the optimal products of both systems were subjected to non-isothermal (dynamic) experiments, consisting of slowly heating (2 °C/min) small parallelepiped sized pieces, from room temperature to 1450 °C. The resulting normalized weight changes, expressed as *mg/cm*^{2}, are compared with those relative to dense ZrB_2 **[16]**, TaB_2 **[16]**, and HfB_2 **[154]** ceramics produced by SHS-SPS or reactive SPS. Additional oxidation experiments on sintered samples were carried out in a muffle furnace in stagnant air (LT 24/11/B410, Nabertherm, Lilienthal, Germany). During these tests, samples were heated at a rate of 4 °C/min from room temperature to a maximum value, in the range of 600–1200 °C, followed by an isothermal step of 1h. The surface changes of heat-treated specimens were then examined by XRD and SEM.

The Young's modulus and hardness of the different samples were assessed using the micro-indentation technique. The evaluations were conducted utilizing the Open Platform equipment (CSM Instruments, Peseux, Switzerland), employing a Vickers indenter tip. The indentation process applied a 1 N load with a loading/unloading rate of 2 N/min, and the maximum load was sustained for 15 s. A minimum of 15 measurements were taken for each sample, and an automatic recording of the load-penetration depth curve was made for each indentation. Subsequently, the elastic modulus was determined using the Oliver and Pharr method, which relies on the indentation load-unloading curves **[155]**. Additionally, fracture toughness was evaluated using a load of 3 N in order

to make cracks propagate from the indent tips. Fracture toughness was then calculated based on the crack lengths according to widely used equations available in the literature **[132,133]**.

3.2.3 Results and Discussion

3.2.3.1 Synthesis and sintering of ZrB_2-based solid solutions

According to the high formation enthalpy of the two individual ZrB_2 and HfB_2 borides (-322.6 and -336.0 kJ/mol, respectively, **[58]**) the synthesis of ZHB from elemental powders showed a SHS character upon local ignition. The XRD pattern of the resulting powders is reported in **Figure 3.9**, while the results on phases' amount and microstructural parameters estimated by the Rietveld method are listed in **Table A4a**. Also in the case of this binary boride system, as observed for the HEB composition investigated in **Section 3.1**, a multiple-phase material is obtained via SHS: other than the expected $(Zr_{0.5}Hf_{0.5})B_2$ solid solution (21.3 wt.%), XRD analysis revealed the presence of also HfB_2 (31.2 wt.%), ZrB_2 (43.0 wt.%), and unreacted Zr (4.5 wt.%).

SEM/EDX observations of SHS powders agree with XRD outcomes. Elemental maps reported in **Figure 3.10** evidence a good but not homogeneous distribution of the two metallic constituents in the synthesized powders. Furthermore, O-contaminants are also detected on particles surface. These aspects suggests that the short duration of the SHS process, albeit advantageous for processing and energy saving reasons, is not sufficient to allow an effective interdiffusion of the two individual borides generated from the elemental reactants. As observed for the case of the HEB_W system (**Section 3.1**) and other HEB quinary metal diborides **[23-25]**, prolonged heat treatments at high temperatures are needed to complete the synthesis process. It is therefore expected that the subsequent consolidation step via SPS, carried out at high temperatures (≥1850 °C), will contribute to the conversion of secondary phases to form the desired equimolar solid solution.

The SHS powders were then milled for 1h (d10 = 0.18 ± 0.03 µm, d50 = 1.1 ± 0.1 µm, d90 = 7.3 ± 0.3 µm, and d43 = 2.6 ± 0.1 µm) either with no graphite or after being combined with 1 wt.% of this additive and then sintered via SPS. In the first case, the SPS process carried out at 1950 °C succeeded in obtaining a sample consisting of the desired solid solution, with no secondary diborides nor residual reactants. However, the densification level was modest (90%), and a significant content of impurities in the form of metal oxides (ZrO_2 and HfO_2), accounting to about 14.5 wt.% in total (see **Figure 3.9** and **Table A4b**) was detected.

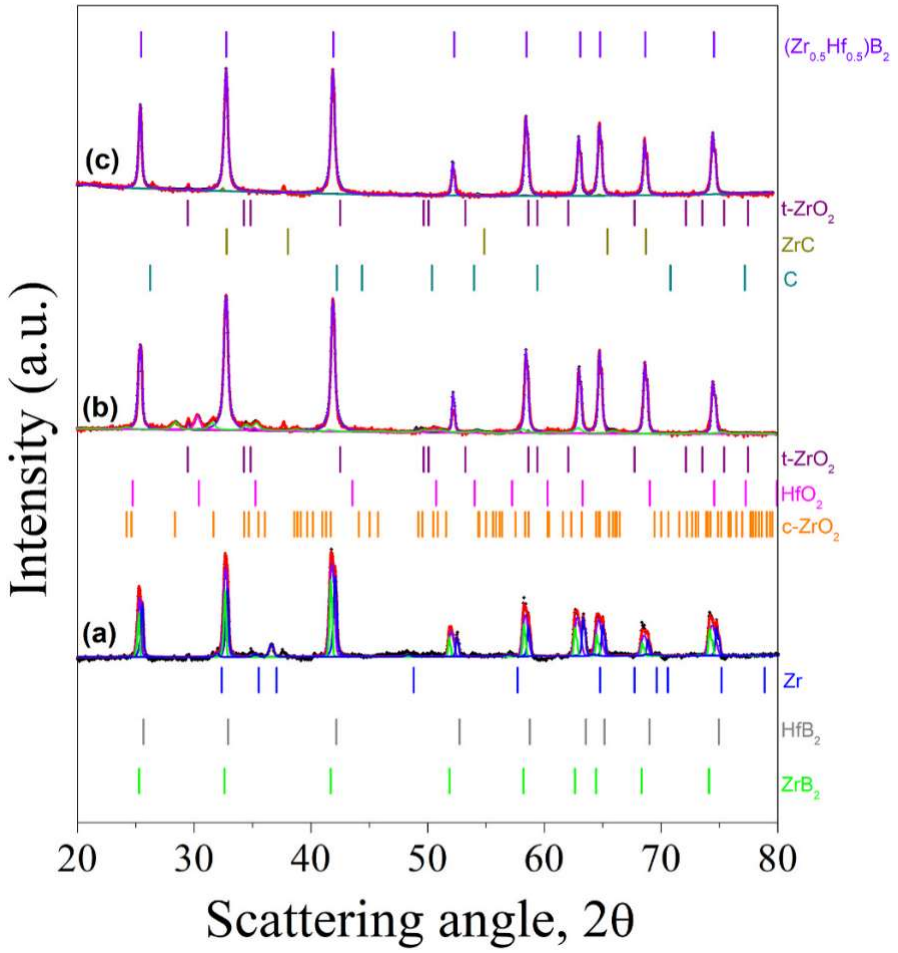

Figure 3.9 - XRD patterns of ZHB products: SHS powders (a), and SPS bulk samples obtained with no additive at T_D=1950 °C (b) and in presence of 1 wt.% graphite at T_D=1850 °C (c). Red dots are experimental data, the continuous lines are the calculated best fit.

Figure 3.11a evidences how in the corresponding SEM micrograph and the related elemental maps, various large pores, up to 4–5 µm sized, are present in these samples. Operating in presence of 1 wt.% C, a marked removal of oxide impurities (down to 2.1 wt.%) is achieved, along with the simultaneous increase of sample densification (up to 98% relative density), when SHS powders were processed at the lower temperature of 1850 °C by SPS. The dwelling temperature was lowered since in previous studies the presence of graphite was found to be beneficial not only for reducing

undesired oxides and improving samples consolidation, but also to enhance powders reactivity thus making the required SPS conditions milder **[156].**

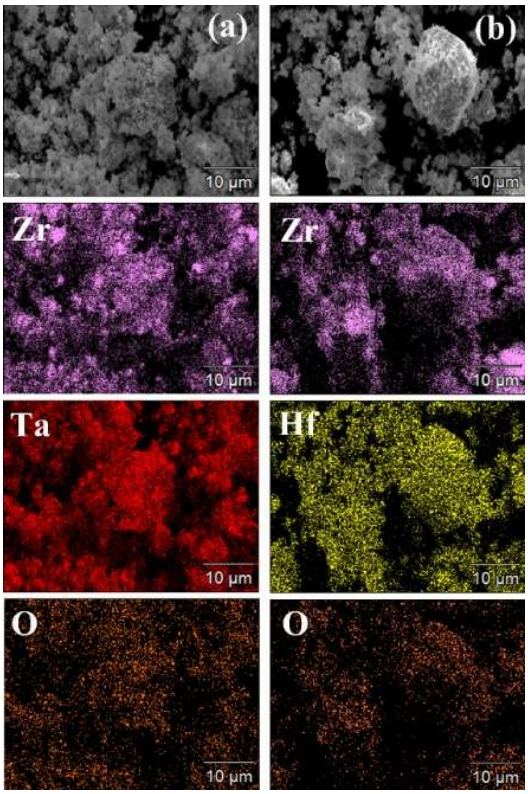

Figure 3.10 - SEM micrographs and corresponding EDX elemental maps of (a) $(Zr,Ta)B_2$, and (b) $(Zr,Hf)B_2$ powders synthesized by SHS.

Indeed, only traces of ZrC (0.6 wt.%) and residual graphite (0.7 wt.%) were detected in the sintered product, other than the limited oxide impurities. The abatement of the residual porosity after SPS is confirmed by the related cross-sectional SEM image reported in **Figure 3.11b**. In addition, the pores' size is significantly reduced, to about 1 µm. It can be observed how a very homogeneous Zr and Hf distribution is achieved, as demonstrated by the elemental maps. It is expected that the presence of graphite promotes the reduction of oxide impurities and therefore improves samples' densities directly, and also acting as solid lubricant, as observed in literature **[23]**. Other authors already succeeded, as mentioned above, in the fabrication of bulk ZHB, with no additional secondary diborides **[53,80,149,150]**. Nonetheless, except for the investigation conducted by **Belisario et al.**

[53], who make use of Flash Sintering to obtain about 95% dense ceramics, more severe temperature levels were required to achieve adequate consolidation levels compared to the optimal (1850 °C) considered in the present study. In particular, **McClane et al. [80]** employed a maximum temperature of 2150 °C for the obtainment of 99.5 % dense ZHB. On the other hand, the very mild conditions tested by **Sitler et al. [149,150]** (1700 °C) led to scarcely densified samples (76.2%). The recognized high sintering ability of SHS powders **[157,158]**, the utilization of the efficient SPS technology for processing highly refractory ceramics **[78]**, and the beneficial use of graphite as carbothermal reductant and solid lubricant agent **[23]**, are the main factors responsible for such outcome.

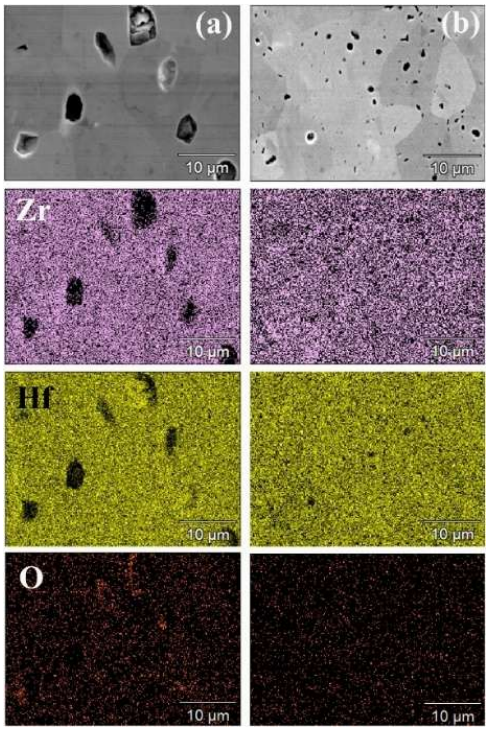

Figure 3.11 - Cross sectional SEM micrographs and corresponding EDX elemental maps of ZHB samples obtained by SPS at (a) T_D=1950 °C with no graphite, and at (b) T_D=1850 °C in presence of 1 wt.% graphite.

As observed in literature for the corresponding ZrB_2 and TaB_2 constituents **[16]**, the synthesis reaction for the formation of ZTB displayed an SHS behaviour. Also in this case, the reactants were not fully converted into the desired binary phase, as shown in **Figure 3.12** and **Table A5a**, with the resulting product consisting of the two individual borides and a mixture of binary solid solutions with

different Zr/Ta stoichiometric molar ratios, which were nominally estimated by applying the Vegards' law. A good agreement between experimental and calculated fit was obtained by considering $(Zr_{0.26}Ta_{0.74})B_2$, $(Zr_{0.35}Ta_{0.65})B_2$, and $(Zr_{0.08}Ta_{0.92})B_2$. This suggest that most of the difficulties in obtaining the equimolar solid solutions lay in the diffusion of ZrB_2 into TaB_2, and not the opposite, as postulated by **Vorotilo et al. [151]**. Other secondary phases, in particular metal oxides, are most likely present, even though they were not clearly detectable by this analysis, due to the corresponding XRD pattern complexity. SEM and EDX results of the reacted ZTB powders are shown in **Figure 3.10b**. The SEM image evidence that powders consist of aggregates of very fine grains. The elemental maps show that Ta and Zr are not uniformly distributed in the SHS product, as confirmed by the small spots showing higher concentration of one of the two metallic constituents, in accordance with the XRD analysis results described above. Despite this, the two transition metals borides are quite well mixed across each grain, and this is expected to favour the formation of the equimolar binary diboride phase during the subsequent SPS stage. EDX analysis also evidenced the presence of oxides on the particles surface. The considerations made for the case of ZHB on SHS rapidity hold true also for this system, therefore the reaction competition can be attempted in the subsequent SPS step. Accordingly, prior to their consolidation, the SHS powders were subjected to a ball milling treatment for 1h (d10=0.30 ± 0.08 μm, d50=1.18 ± 0.08 μm, d90=9.26 ± 2.72 μm, and d43=3.09 ± 0.46 μm), with or without 1 wt.% C.

When the additive free powders were processed for 20 min at 1950 °C by SPS, all secondary diboride phases were transformed to $(Zr_{0.5}Ta_{0.5})B_2$, as reported in **Figure 3.12b** and **Table A5b**. However, the sintered samples were rich of oxide contaminants, namely ZrO_2 (tetragonal and monoclinic) and TaO_2 (tetragonal) accounting to 16.0 wt.% in total (**Table A5b**). These oxides are also responsible for the scarce powder densification level, only 87 %, achieved during SPS. Thus, following the positive effects deriving from the addition of small amounts (1 wt.%) of graphite to the SHS powders of the ZHB system, the same procedure was adopted for ZTB. Correspondingly, 97.5% dense products were obtained when operating at the lower dwelling temperature of 1850 °C. The samples composition consisted of $(Zr_{0.5}Ta_{0.5})B_2$ with only small amounts of ZrO_2, about 2.5 wt.% (**Figure 3.12c** and **Table A5c**).

The results above are confirmed by the SEM micrographs and the related elemental EDX maps shown in **Figure 3.13a-b**, where the samples sintered at 1950 °C (0 wt.% C) and at 1850 °C (1 wt.% C) are compared. The ceramic sintered at T_D=1950 °C with no graphite is characterized by a marked

residual porosity and the presence of a significant amount of metal oxides, despite the obtained uniform elements' distribution. On the other hand, the specimen produced at T_D=1850 ◦C with 1 wt.% C is nearly full dense with Zr and Ta homogeneously distributed, with a marked reduction of O-contaminants.

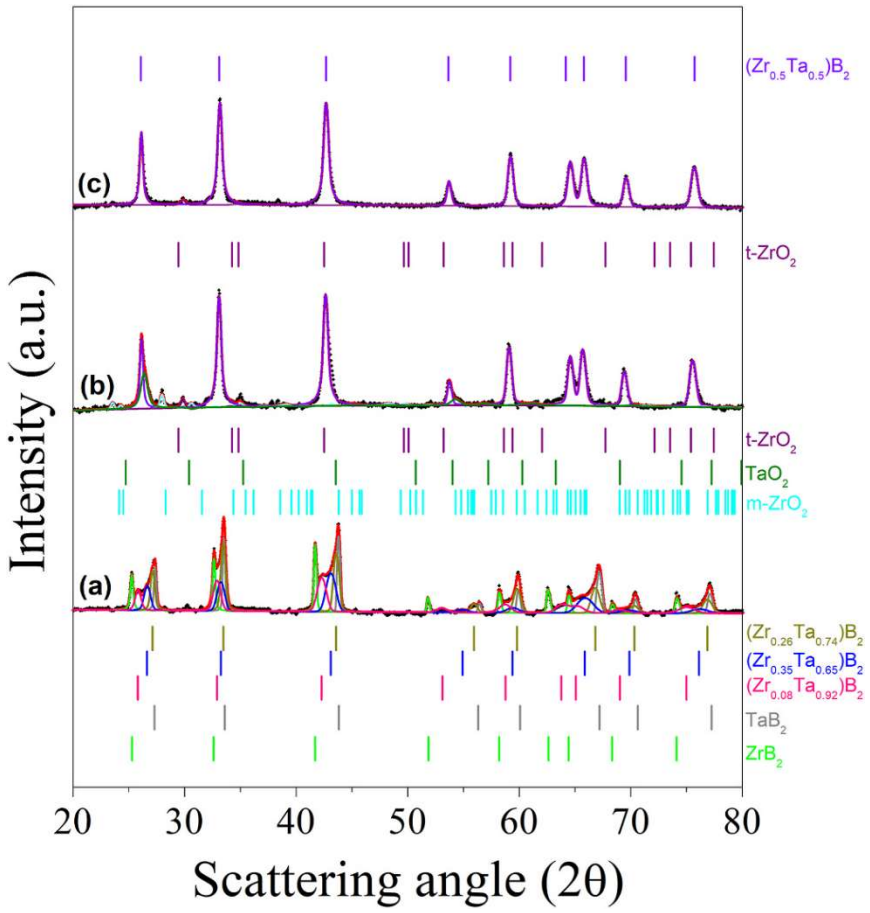

Figure 3.12 - XRD patterns of ZTB products: SHS powders (a), and SPS bulk samples obtained with no additive at T_D = 1950 °C (b) and in presence of 1 wt.% graphite at T_D = 1850 °C (c). Red dots are experimental data, the continuous lines are the calculated best fit.

It should be emphasized that, based on the state of the art, the ZTB equimolar solid solution was obtained for the first time in the present work (i.e. as of 2023) as a single boride phase. This goal, supported by the predictions of **Vorotilo et al. [151]**, disproves another theoretical criterion based on combinatorial methods developed by **Wen et al. [159]**. Therefore, it is clear how more detailed

theoretical studies would be needed to clearly establish a-priori the formation of this type of binary solutions.

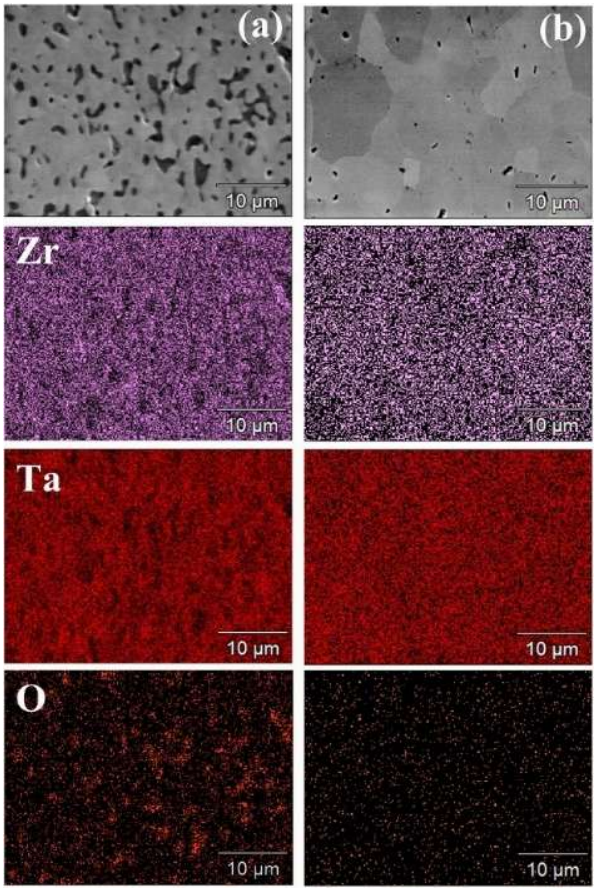

Figure 3.13 - Cross sectional SEM micrographs and related EDX elemental maps of ZTB samples obtained by SPS at (a) T_D = 1950 °C with no graphite, and at (b) T_D = 1850 °C in presence of 1 wt.% graphite.

3.2.3.2 Mechanical properties of ZHB and ZTB systems

Vickers hardness, Young's modulus, and fracture toughness properties measured on the ZHB and ZTB samples obtained under different processing conditions are reported in **Table 3.2**, along with the corresponding density values. The improved densification level (from 90 to 98% and from 87 to 97.5%, for ZHB and ZTB respectively) obtained at a lower temperature (1850 instead of 1950 °C), is also accompanied by a marked increase of both hardness (from 15.56±0.49 to 18.40±0.60 GPa for

ZHB and from 11.37±0.94 to 22.08±0.77 GPa for ZTB) and Young's modulus (from 428.9 ± 32.1 to 528.2 ± 35.6 GPa for ZHB and from 222.2 ± 9.3 to 636.9 ± 32.9 GPa for ZTB). **Table 3.2** also indicates that a modest effect was observed when considering K_{IC} values of the ZTB system, while it was not possible to draw comparison for the case of ZHB. Indeed, the 0 wt.% C sample cracked without the formation of the four cracks at the indent tips, therefore no reliable K_{IC} values could be estimated. This can be probably ascribed to the residual porosity and local defectiveness of this sample.

Regarding ZHB, the measured HV value of the ceramic produced at 1850 °C/1 wt.%C is superior to that of ZrB_2 sample (11.0±0.4 GPa) obtained by the same SHS-SPS route at 1900 °C **[16]**, while it is very close to that of monophasic HfB_2 (18.1±0.4 GPa) prepared by reactive SPS **[154]**.

The ZTB system was specifically chosen to be studied to improve the mechanical properties of ZrB_2, and the obtained results are quite in line with trends reported in literature for its individual constituents, also produced by SHS-SPS by **Licheri et al. [16]**. The combination of ZrB_2 (11.0±0.4 GPa) with the harder TaB_2 made the hardness of the corresponding binary metal diboride product (22.08±0.77 GPa) superior. The fact that the TaB_2 sample displayed a lower HV value (17.5±0.4 GPa) compared to that of ZTB can be ascribed to the modest densification level (93.9 %) achieved for the former system **[16]**. This result is also in agreement with **Vorotilo et al. [151]**, where $(Zr,Ta)B_2$ presented hardness superior to both constituents. As a difference, no super-hardening effect was observed in our study. Such differences could be ascribed to the fact that the measurements in **Vorotilo et al. [151]** were performed with the nano-indentation technique on multiple-boride phase samples rather than with single-phase boride solid solutions, In the latter study, as in our investigation, the fracture toughness of the binary system (2.46 MPa $m^{1/2}$) was also in between to those of ZrB_2 (2.1 MPa $m^{1/2}$) and TaB_2 (3.2 MPa $m^{1/2}$) measured by **Licheri et al. [16]**, for samples produced via SHS-SPS.

Based on the outcomes above, lower mechanical properties are displayed by the ZHB system compared to ZTB. This finding also agrees with the results obtained with HEBs fabricated following the same SHS-SPS processing route. Accordingly, even if the presence of Ta made the fabrication of fully dense quinary metal borides more difficult, the corresponding ceramics showed superior mechanical properties **[24]**.

Table 3.2 - Mechanical properties of bulk ZHB and ZTB samples produced by SHS-SPS in this work in presence and with no graphite addition. The corresponding processing conditions and density values are also reported. EC: Evans and Charles; LF: Lawn and Fuller; EW: Evans and Wilshaw; L: Lankford. n. d.: not determined.

System	Processing Conditions (T_D, %graphite)	ρ (%)	HV (GPa)	Young's modulus (GPa)	K_{IC} (MPa $m^{1/2}$) Method
ZHB	1950°C, 0%C	90	15.56±0.49	428.9±32.1	n.d. (*)
	1850°C, 1%C	98	18.40±0.60	528.2±35.6	1.73 (EC), 1.08 (LF), 1.48 (EW), 2.51 (L)
ZTB	1950°C, 0%C	87	11.37±0.94	222.2±9.3	2.46 (EC), 1.54 (LF), 6.64 (EW), 1.34 (L)
	1850°C, 1%C	97.5	22.08±0.77	636.9±32.9	2.46 (EC), 1.53 (LF), 2.33 (EW), 2.28 (L)

(*) Several cracks formed on the sample during indentation test.

3.2.3.3 Oxidation resistance of ZHB and ZTB systems

The oxidation behaviour of the two ZHB and ZTB products was preliminarily determined by dynamic TGA experiments conducted in air flow up to 1450 °C. The obtained results are reported in **Figure 3.14a-b** in terms of weight gain as a function of temperature. Literature data relative to the corresponding individual diborides prepared either by the SHS-SPS (ZrB_2, and TaB_2) **[16]**, or reactive SPS (HfB_2) **[154]** routes are also reported, for the sake of comparison. Up to 1200–1300 °C, the oxidation curves of both binary diborides are very close to those of the related diboride constituents. **Figure 3.14a** shows that, up to about 1000°C, the normalized weight changes of ZHB, ZrB_2, and HfB_2 samples are quite modest, i.e. within ±1 mg/cm^2. Above this temperature level, an acceleration of the mass gain rate was recorded during the test, especially for ZrB_2 around 1150-1200°C. This change in the slope of the mass gain curve is most probably related to the beforementioned m→t phase transition occurring in ZrO_2 at about 1120°C **[141]**, and the consequent drop in the protection provided by the formed oxide layer. At the same time, ZHB oxidation occurred at a slower and faster rates compared to ZrB_2 and HfB_2, respectively. Therefore, the oxidation curve of the binary system

laid between the ones corresponding to the individual constituents up to 1450°C. The TGA behaviour displayed by the ZHB sample produced in this work is in line with the results from similar tests in flowing air conducted on the 95 % dense sample fabricated by **Belisario et al. [53]**. As a main difference, a weight loss of about 0.5 % was observed by **Belisario et al. [53]** in the temperature range 800–1000 °C, ascribed by the authors to the evaporation of some amorphous phases formed during the synthesis step.

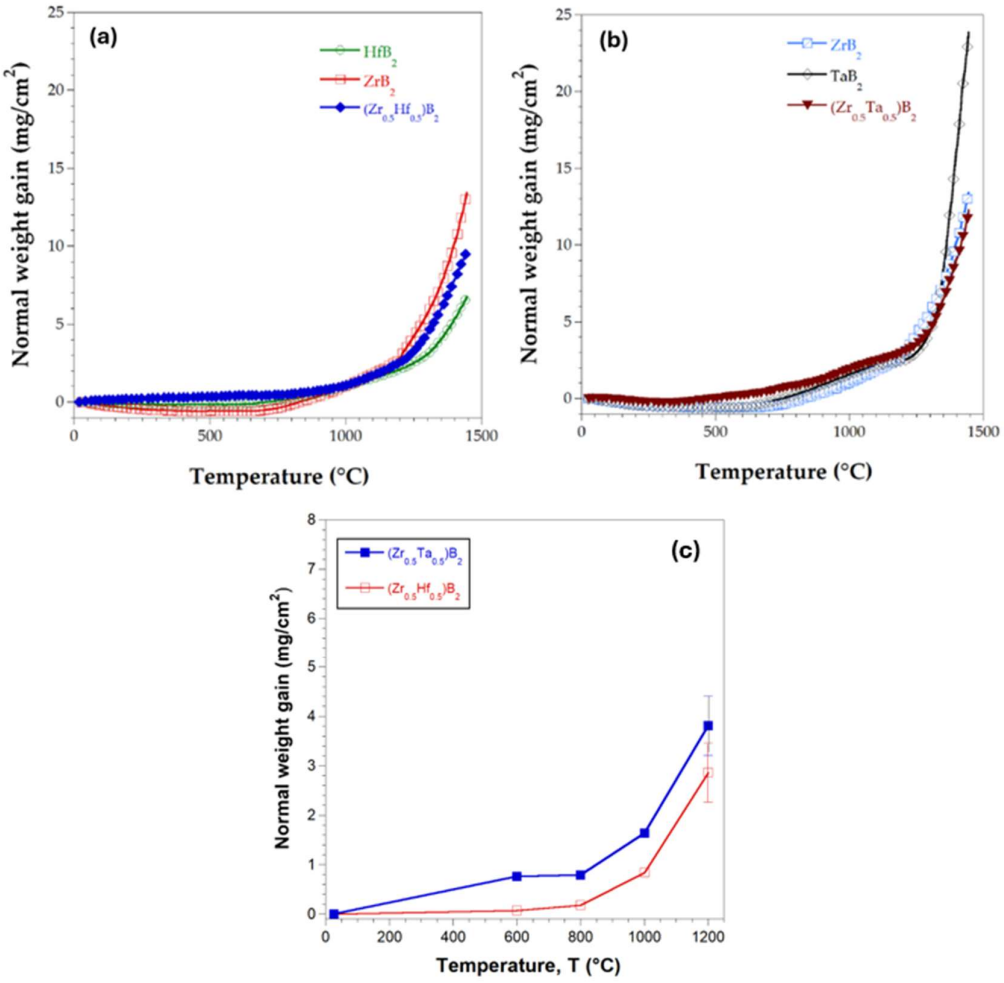

Figure 3.14 - Specific weight changes during (a) TGA oxidation test in air of ZHB samples, (b) TGA oxidation test in air of ZTB samples and (c) oxidation tests in air furnace for both ZTB and ZHB samples produced in this work by SPS (T_D=1850 °C, 1 wt.% C) as a function of temperature. Literature data of TGA results of individual diborides, i.e. HfB_2 (ρ=98.8 %) **[154]**, ZrB_2 (ρ=98.5%) **[16]**, and TaB_2 (ρ=93.9%) **[16]** are also reported for comparison in graph (a) and (b).

For instance, similar results are attained when oxidising ZHB samples for 1 h in stagnant air at different temperatures (**Figure 3.14c**). The mass gain observed at the 1200°C-1h condition (2.86 mg/cm^2 on average) is quite close to what observed during TGA tests (2.60 mg/cm^2). **Figure 3.15** shows the XRD data collected on these samples' surfaces. It is possible to observe that the incipient oxidation occurred at 600°C, and from 800°C onwards, a monoclinic oxide phase became the dominant one (**Figure 3.15a**). This phase can be most probably ascribable to (Zr,Hf)O_2 due to the high mutual solubility of ZrO_2 and HfO_2 (see the HfO_2-ZrO_2 phase diagram, **Figure B1** in **Appendix B [148]**). This fact is supported by SEM micrographies and EDX maps shown in **Figure 3.16**, where the cross section of the specimens oxidised at 1200°C are reported. Indeed, the presence of a very uniform distribution of Zr and Hf metal cations confirms the obtainment of a (Zr,Hf)O_2 solid solution. The formation of this mixed oxide phase could be associated to the better oxidation resistance observed for the ZHB system, likely due to the higher stability of such oxidation product, if compared to pure ZrO_2.

As for the oxidation resistance of the ZTB system, **Figure 3.14b** reports the normalized weight gain along with those of ZrB_2, and TaB_2 for comparison. Mass changes lower than ±1 mg/cm^2 were measured up to about 700 °C, above which the three diborides start to gain weight at rates in the range of 4.8–6.0·10^{-3} mg/(cm^2 °C), about constant up to 1200 °C. As the test proceeded, these ceramics oxidized at higher rates, with the TGA curves of ZTB, and ZrB_2 almost overlapped. On the other hand, individual TaB_2 was much more sensitive to the oxidizing environment if compared to the two Zr-containing systems. In the latter regard, it should be pointed out that the lower relative density (higher porosity) of TaB_2 sample (93.9%), compared to those of ZrB_2 (98.5%) and ZTB (97.5%), is expected to negatively affect its oxidation resistance. The oxidation behaviour of ZTB samples heat treated in stagnant air and reported in **Figure 3.14c**, is similar to that observed during TGA (**Figure 3.14b**). For instance, a mass gain of 3.8 mg/cm^2 was observed at 1200°C, which is consistent with the value of about 3.0 mg/cm^2 obtained during TGA tests. XRD patterns of ZTB samples oxidised in air are shown in **Figure 3.15b**. Also in this case, the evidence of incipient oxidation is observed at 600°C, while from 800°C onwards, Zr- and Ta- oxides become the dominant phases. The detected tetragonal zirconia in the ZTB oxidised samples could explain the overlapping of ZrB_2 and ZTB mass gain curves observed in TGA. Indeed, this weight behaviour suggests that the role of ZrO_2 is similar in the two systems, both being probably subject to the m→t transformation at temperatures lower

than 1200°C. Orthorhombic Ta_2O_5 was also detected. Even if XRD analysis evidenced the presence of individuals oxides only, the formation of a stabilizing mixed (Zr,Ta)-oxide in the ZTB samples cannot be excluded. Indeed, when observing in **Figure 3.17** the elemental maps of the cross section of the sample oxidised at 1200°C, Ta and Zr are finely distributed across the oxide scale. In this regard, ZrO_2-Ta_2O_5 phase diagram (**Figure B2** in **Appendix B [160]**) suggest that the $Ta_2Zr_6O_{17}$ mixed oxide phase could be formed at these temperatures. This is an orthorhombic phase with the main peaks close to those of t-ZrO_2. It is therefore difficult to distinguish the two phases via XRD, so that more detailed analysis might be needed to prove the formation of a mixed oxide. Based on the information above, the scarce densification of the TaB_2 sample and the possible incorporation of Zr- and Ta-oxides to form stable $Ta_2Zr_6O_{17}$ could justify the superior oxidation resistance of the ZTB system with respect to the average performances of the individual constituents.

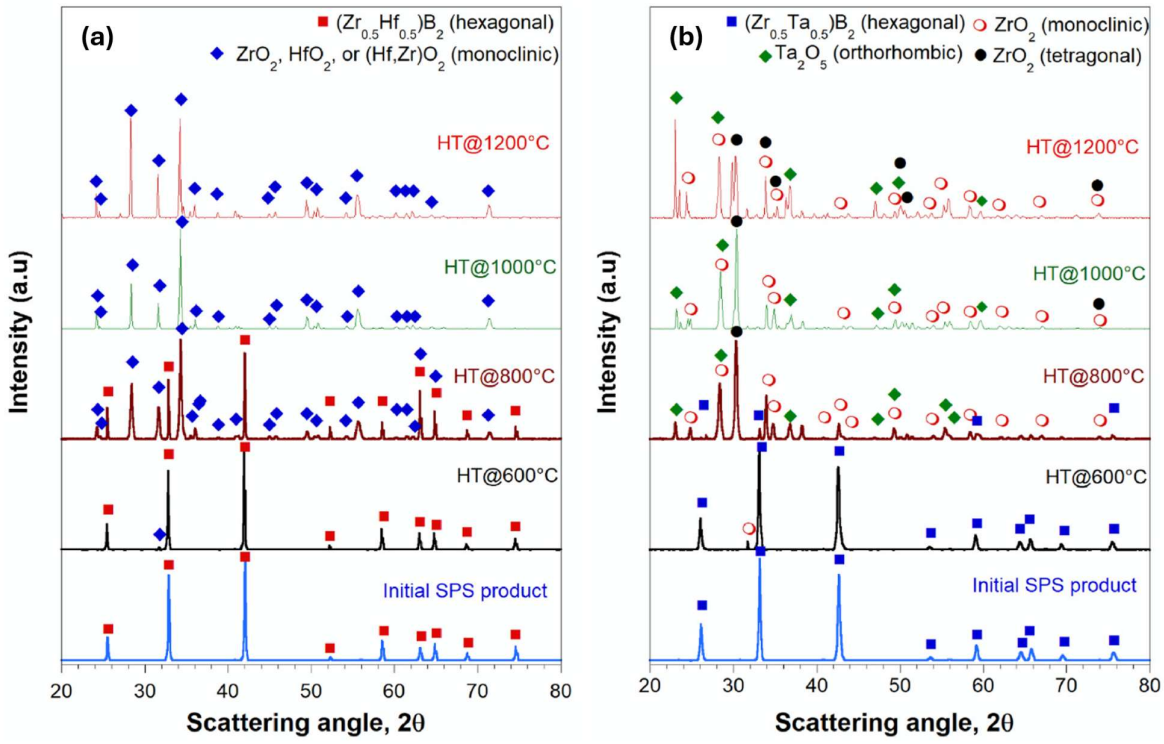

Figure 3.15 - XRD patterns of (a) ZHB, and (b) ZTB samples' surface after being heat treated in air furnace at different temperatures.

Comparing the two binary systems, a clear superior oxidation resistance is displayed by ZHB, with respect to ZTB (**Figure 3.14c**). Such hierarchical order can be considered representative of the oxidative behaviour of the two solid solutions, as the relative densities of the related samples exposed to oxidation environments were nearly the same, about 98 and 97.5%. Another element that confirms the lower oxidation resistivity of ZTB is that XRD peaks of the diboride phase can be barely detected at 800°C in the corresponding pattern (**Figure 3.15b**). Conversely, the XRD analysis performed on the ZHB product indicates that the original boride phase is still significantly present at 800 °C (**Figure 3.15a**). Comparing the SEM micrographies of the oxidised ZHB (**Figure 3.16**) and ZTB (**Figure 3.17**) samples, it is possible to observe that the formed oxide layers are both characterized by a thickness in the range 40–50 µm, albeit ZHB layer was observed to be more compact and regular with respect to the ZTB one.

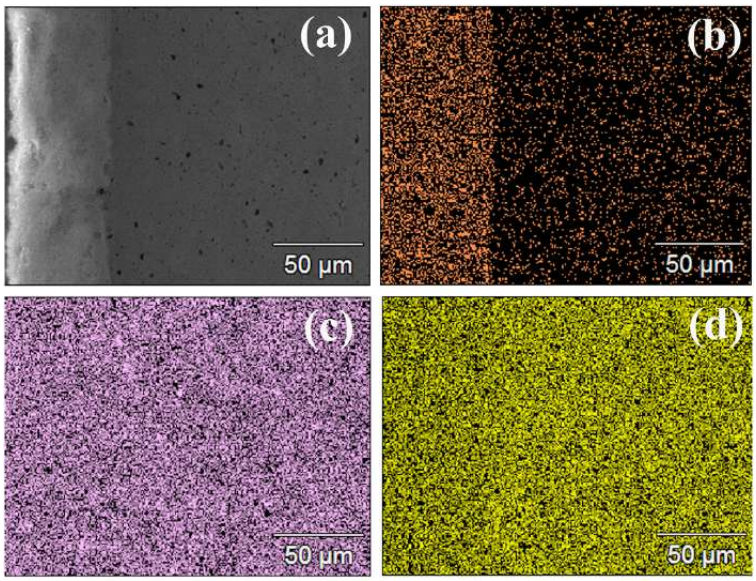

Figure 3.16 - ZHB sample after heat treatment in air furnace at 1200 °C: (a) cross sectional SEM micrograph, (b) O, (c) Zr, (d) Hf elemental maps.

To further validate the conclusions drawn in this work on the promising oxidation behaviour manifested by these two binary systems, especially that shown by ZHB (clearly superior to ZrB_2), higher temperature tests, closer to the ones experienced in the proposed aerospace applications, would be needed. This requires the use of more performant facilities, such as tube furnaces

operating at higher temperatures or ablation devices. These two approaches are the object of two ongoing works, in collaboration with the German Aerospace Centre (DLR, Germany) (high temperature experiments), and the University of Perugia (Italy) (ablation tests on ZHB system). To further improve the oxidation resistance of these systems, especially for ZTB, which revealed interesting mechanical properties, the use of Nb-coating can be tested. Indeed, this strategy was able to improve the stability of the produced oxide scale in the case of pure ZrB_2 **[161]**. Its application to these two binary systems is also among the scopes of the ongoing collaboration with DLR.

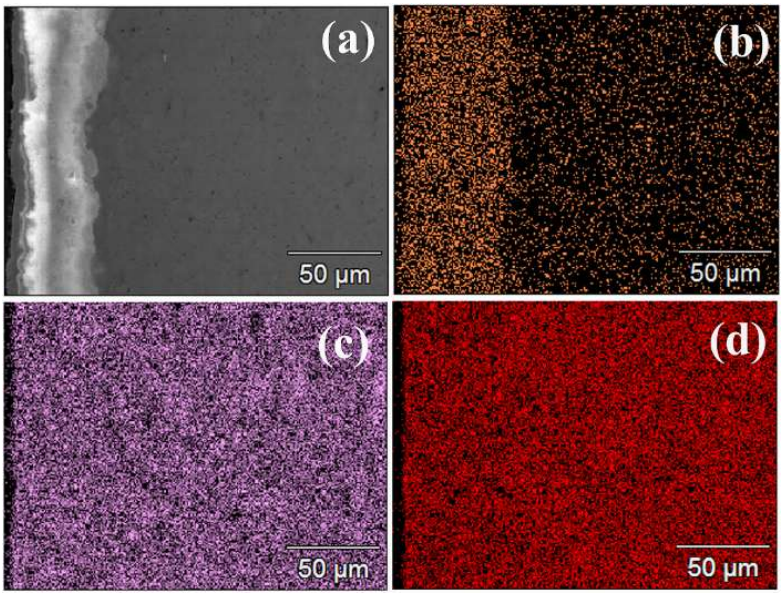

Figure 3.17 - ZTB sample after heat treatment in air furnace at 1200 °C: (a) cross sectional SEM micrograph, (b) O, (c) Zr, (d) Ta elemental maps.

The results described in this Section have been published in Barbarossa, S., **Casu, M.**, Orrù, R., Locci, A. M., Cao, G., Garroni, S., Bellucci, D., & Cannillo, V. (2024). Synthesis, sintering, mechanical properties, and oxidation behavior of $(Zr_{0.5}Me_{0.5})B_2$ (Me = Ta, Hf) solid solutions. *Ceramics International*, *50*(7), 12158–12166. https://doi.org/10.1016/J.CERAMINT.2024.01.119

3.3 Niobium-based binary borides

3.3.1 Introduction

Niobium and Zirconium are 5th period transition metals, have very similar atomic weight, i.e. 92.906 and 91.224 respectively **[58]**. This is also reflected on the densities of the corresponding diborides, 6.97 g/cm^3 (NbB_2) and 6.09 g/cm^3 (ZrB_2) **[47]**, and makes NbB_2 a possible alternative candidate to develop lightweight binary solid solutions, as for ZrB_2-based ones described in **Section 3.2**. However, being the two transition metals of different groups, some different properties are expected for instance in the oxidation products, due to the peculiar tendence of V group metal oxides to melt at a rather low temperature or form eutectics when mixed to IV group TM oxides **[27]**. As a member of IV group borides, ZrB_2 is certainly more investigated than NbB_2 **[5,136].** However, studies have been also addressed to the fabrication and characterization of NbB_2 **[81,162-165]**. The latter system is also one of the base constituents often involved in the various HEBs investigated so far **[21-26,72-74,117-124]**. In particular, the effect of the Nb content on the densification behavior, composition, microstructure and mechanical properties of (Hf,Zr,Ti,Ta,Nb)B_2 ceramics was investigated by **Feng et al. [73]**. Only a fraction of the Nb added was observed to dissolve into the main HEB phase, while a Nb-rich secondary phase was formed in all the compositions investigated. The presence of the latter phase was considered responsible for the reduction of grain size (from 13.9±5.5 to 5.2±2.0 μm, as the Nb content increased from 0 to 20 at.%), and for the corresponding increase of Vickers hardness and Young's modulus properties. The extensive use of such metal on complex HEB formulations further justifies the study of binary solid solutions involving it, to better understand its role in the complex mechanisms that drive HEBs properties.

As anticipated in the previous Section, another application of Nb was found in the framework of UHTCs materials. By covering ZrB_2 surface with metallic Nb-coatings by means of magnetron sputtering, the oxidation resistance of this ceramic was markedly improved **[161]**. This outcome was explained by the increased stability of the protective glass at the ceramic surface caused by liquid Nb_2O_5 formed during the oxidation test.

Nb is one of the critical raw materials identified by the European Union, due to its extensive use in steel reinforcement and the concentration of its production outside EU, mostly in Brazil, which accounts for 92% of global extraction **[142]**. Nonetheless, its market price, estimated to be on average, as of 2025, 82.86 $/kg **[166]**, is still by far inferior to that of Hafnium (estimated to be 3.800

$/kg **[143]**), or Tantalum (321-417 $/kg **[167]**). For this reason, its use from individual to HEBs compositions deserves to be thoroughly considered.

Similarly to the methodology applied in **Section 3.2** for Zr-based solid solutions, the attention was focused on binary compositions to effectively track the changes in NbB_2 properties caused by its substitution with 50 mol.% of other transition metal borides. However, despite the potential benefits deriving by the use of Niobium, only a little attention has been paid so far to binary compositions containing this element. For instance, the obtainment of $(Nb_xHf_{1-x})B_2$ has been considered only in two recent studies, where controversial results are reported **[159,168]**. Specifically, the preparation of $(Nb_{0.9}Hf_{0.1})B_2$, $(Nb_{0.5}Hf_{0.5})B_2$, and $(Nb_{0.1}Hf_{0.9})B_2$ powders failed when using the high throughput molten salt synthesis method **[159]**. Such experimental findings agree with theoretical results provided by the formation criterion developed by the same authors. A different outcome arose from **Kurbatkina et al. [168]**, starting from elemental reactants ball milled for 12 h (BPR=6), reacted via SHS and sintered by HP. The authors were able to obtain $(Nb_{0.2}Hf_{0.8})B_2$, $(Nb_{0.4}Hf_{0.6})B_2$, and $(Nb_{0.5}Hf_{0.5})B_2$ in bulk form. XRD analysis revealed that the sintered samples mainly consisted of the desired solid solutions with minor secondary phases (unidentified).

Analogously, only very few studies have been dedicated to the $(Nb_xTi_{1-x})B_2$ system **[159,169,170]**. Specifically, **Demirskyi et al. [169]** investigated the $(Nb_{2/3}Ti_{1/3})B_2$, $(Nb_{0.5}Ti_{0.5})B_2$, and $(Nb_{1/3}Ti_{2/3})B_2$ formulations using TiB_2, and NbB_2 as precursors. A multistep SPS routine was applied and, depending on the processing conditions adopted, either $(Nb,Ti)B_2$ solid solutions or two-phase composites consisting of TiB_2 and NbB_2 were obtained. The high throughput molten salt synthesis method mentioned previously was also employed by **Wen et al. [159]** for the preparation of $(Nb_xTi_{1-x})B_2$ powders with different composition (x=0.1, 0.5, 0.7, 0.8, 0.9). While $(Nb_{0.9}Ti_{0.1})B_2$, and $(Nb_{0.8}Ti_{0.2})B_2$ were synthesized as single-phase products, multiple phases resulted when considering the other three compositions. As for the case of $(Nb,Hf)B_2$, the experimental outcomes obtained with $(Nb,Ti)B_2$ were supported by the formation criterion proposed by the authors. More recently, and in contrast to **Wen et al. [159]**, the synthesis of $(Nb_{0.75}Ti_{0.25})B_2$, $(Nb_{0.5}Ti_{0.5})B_2$, and $(Nb_{0.25}Ti_{0.75})B_2$ was successfully accomplished at 1850°C by SPS from TiB_2 and NbB_2 powders **[170]**. The resulting sintered samples, with relative densities of 95.4 (x=0.25), 97.5 (x=0.5) and 98.6% (x=0.75), consisted of the expected solid solutions.

Based on the studied conducted so far, few and contradictory results are available regarding the possibility of synthesizing $(Nb_xHf_{1-x})B_2$ and $(Nb_xTi_{1-x})B_2$ solid solutions. In addition, the characterization of the produced ceramics was rather incomplete. For instance, the oxidation behavior of (Nb,Hf)B_2 is totally unexplored. As for the (Nb,Ti)B_2 system, oxidation tests have been carried out by **Kaplan Akarsu et al. [170]** only for the $(Nb_{0.25}Ti_{0.75})B_2$ composition, while no results are available for the equimolar and other formulations.

This situation opens the door for investigating these two systems in this work. A more comprehensive study on these ceramics would indeed be able to provide a valuable contribution to fill such processing and characterization gaps. As for their synthesis, benefits could be obtained using the two-step SHS-SPS approach, which was also employed with success for the fabrication of dense and single-phase Zr-based solid solutions (**Section 3.2**). Along this line, bulk $(Nb_{0.5}Hf_{0.5})B_2$ and $(Nb_{0.5}Ti_{0.5})B_2$ solid solutions are prepared in this work by SHS-SPS. In particular, this study focuses on the influence of the SPS holding temperature and dwelling time on the composition and density of the two binary diboride products. In addition, following the beneficial effect observed in previous studies (oxide impurities removal, improved powders reactivity and densification), 1 wt.% graphite is also employed in the present investigation.

Optimal bulk ceramics are exposed to flowing and stagnant air at high temperatures to provide a preliminary indication of their oxidation behavior under such conditions. Hardness, Young's modulus and fracture toughness properties are also measured. To evaluate the effect produced by the substitution of 50 mol.% of NbB_2 with HfB_2 or TiB_2, individual diboride samples are also produced by SHS-SPS and properly characterized, for the sake of comparison

3.3.2 Materials and Methods

Commercially available Nb, Ti, Hf and B powders listed in **Table 2.1** were employed for the synthesis of the different borides prepared in this Section, according to the SHS process described in **Section 2.1.1**. This include the use of a 10 mol.% excess B in reaction (4) (modified to take into account the presence of two metal reactants) to overcome the presence of oxide impurities in the elemental powders:

$$0.5\mathrm{Nb} + 0.5\mathrm{Me} + 2.2\mathrm{B} \rightarrow \mathrm{Nb_{0.5}Me_{0.5}B_2};\ (\mathrm{Me{=}Hf,\ Ti}) \quad (4c)$$

For the sake of brevity, NB, TB, HB, NTB, and NHB abbreviations will indicate samples obtained either by SHS or SPS when considering NbB_2, TiB_2, HfB_2, $(Nb_{0.5}Ti_{0.5})B_2$, and $(Nb_{0.5}Hf_{0.5})B_2$ systems, respectively.

After SHS, particle size of the ball milled powders was measured by laser light scattering analysis (CILAS 1180, France). Proper amounts (from 2.3 to 5.7 g, depending on the system) of these powders were employed in each SPS experiment, carried out according to the procedure described in **Section 2.1.2**. The dwell temperature (T_D) and holding time (t_D) values to produce the bulk samples were varied, depending on the system, in the range 1850-2050 °C and 20-40 min, respectively. It is important to state that higher temperature levels and longer dwelling times were not applicable due to the limitations of the SPS apparatus used in this work. The heating rate and applied pressure were maintained the same, 200 °C/min, and 20 MPa, respectively. For the sake of reproducibility, each experiment was repeated at least twice.

Phases identification and microstructural characteristics of the synthesized powders and sintered products was performed by X-ray diffraction analysis using a SMARTLAB diffractometer with a rotating anode source of copper (λCu Kα = 1.54178 Å) working at 40 kV and 100 mA over a range of scattering angles 2ϑ from 20 to 130, in steps of 0.05° with 15 s acquisition time per angle. Phases amount (wt.%) and related structural parameters were evaluated with the Rietveld method by analyzing the XRD patterns with the MAUD program **[131]**. For the estimation of crystallite size and microstrain, the isotropic model was applied. Regarding the line broadening, a pseudo-Voigt function was employed. The tabular results of this characterization is reported in **Appendix A.c**.

Microstructure and elemental distribution of SHS and SPS products were investigated by high-resolution scanning electron microscopy (HRSEM, mod. S4000, Hitachi, Tokyo, Japan) equipped with a UltraDry EDX detector (Thermo Fisher Scientific, Waltham, MA, USA). Samples density was determined by the Archimedes' method, using distilled water as immersing medium. The theoretical values of 6.97 **[47]**, 4.50 **[171]**, 11.21 g/cm^3 **[47]**, were used for NbB_2, TiB_2, and HfB_2, respectively, to calculate the corresponding relative densities. The values (ρ_c) of 5.77 and 9.11 g/cm^3 for $(Nb_{0.5}Ti_{0.5})B_2$, and $(Nb_{0.5}Hf_{0.5})B_2$, respectively, were estimated according to related lattice parameters from CIF files (COD-1510775 and COD-1510708) by using Equation 1, as described in **Section 3.1.2**.

The micro-indentation technique was used to evaluate the hardness and Young's modulus of the samples. Testing was carried out with the Open Platform system (CSM Instruments, Peseux, Switzerland), utilizing a Vickers indenter tip. A 3 N load was applied, with a loading/unloading rate of 6 N/min, and the maximum load was held for 15 seconds. For each sample, a minimum of 15 measurements were taken, and the load-penetration depth curve was automatically recorded for each indentation. The elastic modulus was then calculated using the Oliver and Pharr method, based on the load-unloading curves **[155]**. Fracture toughness was also assessed by applying a 5 N load to generate crack propagation from the indent tips; the loading/unloading rate was 10 N/min. The toughness was calculated from the crack lengths using well-established equations from the literature **[133-134]**.

The oxidation resistance of optimal sintered products was evaluated in air by thermogravimetric analysis (NETZSCH, STA 409PC Luxx Simultaneous DTA-TGA Instrument, Germany) as well as using a muffle furnace (LT 24/11/B410, Nabertherm, Lilienthal, Germany). Non-isothermal (dynamic) TGA tests were conducted from room temperature to 1450 °C (2 °C/min) and 0.1 L/min air flow. Furnace experiments consisted in heating the specimens in stagnant air at a rate of 4 °C/min from room temperature to a maximum value, in the range of 600-1200 °C, followed by an isothermal step of 1h duration. The resulting samples were examined by XRD (Bruker D8 Advance diffractometer, copper source λCu Kα = 1.54178 Å, working at 40 kV and 40 mA over a range of scattering angles 2ϑ from 20° to 130°, in steps of 0.05° with 5 s acquisition time per angle) and SEM/EDX.

3.3.3 Results and Discussion

3.3.3.1 Synthesis and sintering of individual borides

Given the high enthalpy of formation of the three individual diborides from their elements, i.e -251.040 (NbB_2), -323.800 (TiB_2), -335.975 kJ/mol (HfB_2) **[58]**, the reactant mixtures exhibit, upon ignition, a self-propagating character.

Figures 3.18a-3.20a shows the XRD patterns of the resulting products. It is possible to state how the elemental reactants are almost completely converted during SHS into the expected hexagonal phases. Indeed, while no other phases were detected by XRD analysis on NB powders, only low amounts of $TiBO_3$ (~1.6 wt.%), and HfO_2 (~0.6 wt.%), were found in TB and HB samples, respectively (**Tables A6a-A8a**).

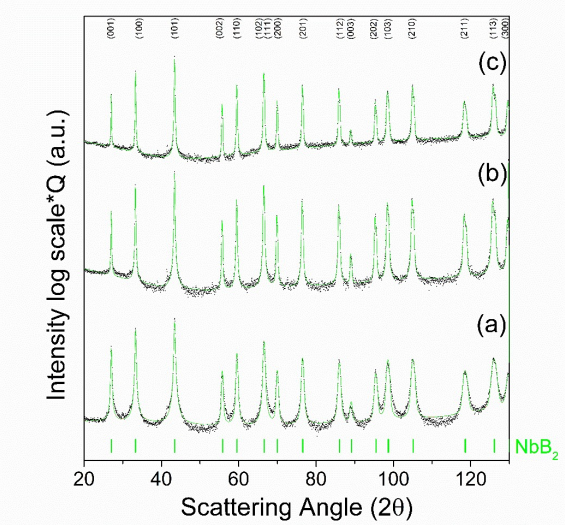

Figure 3.18 - XRD patterns and related Rietveld profiles of NB samples: (a) SHS powders, SPS products obtained at T_D=1950°C with (b) no graphite, and (c) after the addition of 1 wt.% C. Experimental data (black dots) and NbB_2 refined phase (light green solid line) are reported. The light green Bragg's positions for NbB_2 are provided. The related structural parameters are reported in **Table A6a**.

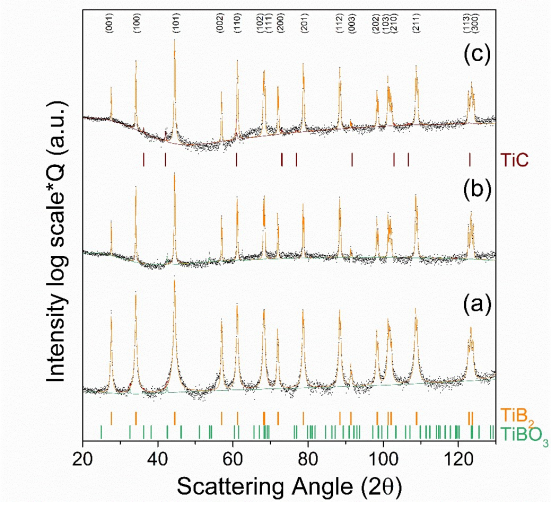

Figure 3.19 - XRD patterns and related Rietveld profiles of TB samples: (a) SHS powders, SPS products obtained at T_D=1950°C with (b) no graphite, and (c) after the addition of 1 wt.% C. Experimental data (black dots), calculated intensity (red line), TiB_2 refined phase (orange solid line), $TiBO_3$ refined phase (green solid line) and TiC refined phase (brown solid line) are reported. Bragg's positions for all the phases are provided. The related structural parameters are reported in **Table A7a**.

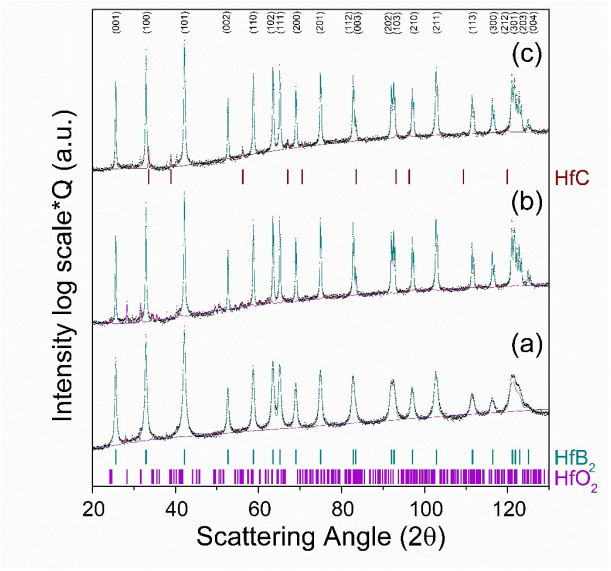

Figure 3.20 - XRD patterns and related Rietveld profiles of HB samples: (a) SHS powders, SPS products obtained at T_D=1950°C with (b) no graphite, and (c) after the addition of 1 wt.% C. Experimental data (black dots), calculated intensity (red line), HfB_2 refined phase (dark cyan solid line), HfO_2 refined phase (purple solid line) and HfC refined phase (brown solid line) are reported. Bragg's positions for all the phases are provided. The related structural parameters are reported in **Table A8a**.

The crystallite size of the diboride products in the ball milled SHS powders, also estimated by the Rietveld analysis, was at the nanoscale, i.e. about 53 (NbB_2), 88 (TiB_2), and 52 nm (HfB_2). The three batches of powders were also examined by SEM and EDX analysis (**Figures 3.21a-3.21c**), which evidenced a uniform metal content, to support the fact that the expected product composition was attained by SHS, except for the minor oxide phases mentioned above.

Particle size parameters for these three sets of powders are reported in **Table 3.3**. Slightly coarser powders (d43 = 7.46μm) are obtained for the case of the HB system, while NB and TB showed more similar particle size, with d43 values of 4.86 and 3.24 μm, respectively. Since the desired individual diboride phases were already obtained by SHS, there is no need to further transform residual reactants or secondary products by SPS. Therefore, the different operating conditions adopted during the sintering step, which are summarized in **Table 3.3**, were aimed at maximizing the densification of the three batches of powders.

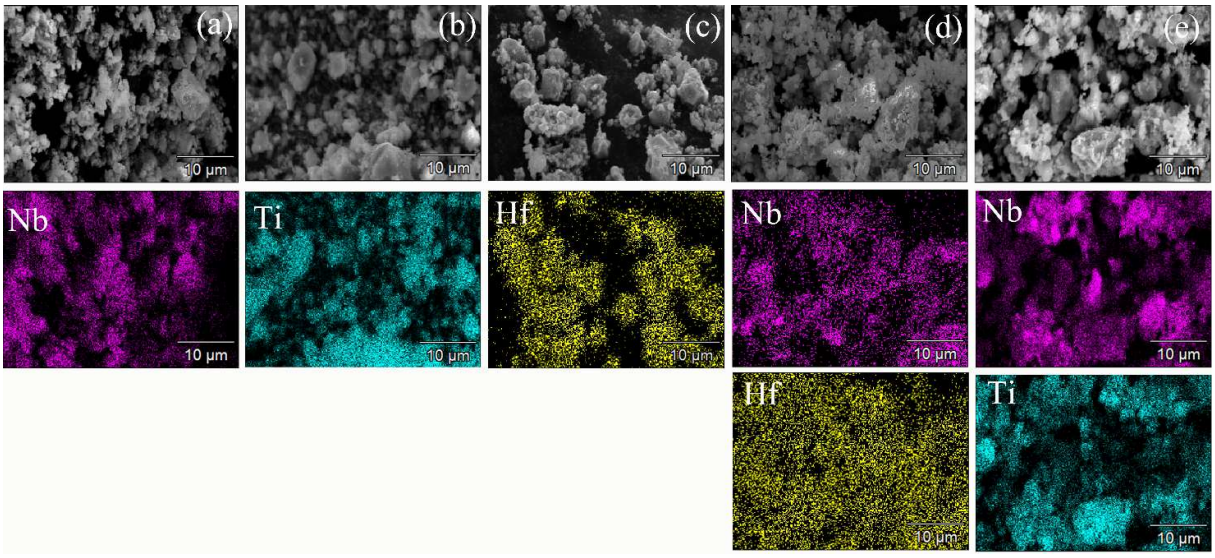

Figure 3.21 - SEM micrographs and associated EDX metal maps of (a) NB, (b) TB, (c) HB, (d) B, and (e) NTB powders prepared by SHS.

Let's consider first the case when no graphite was added to the SHS powders. As reported in **Table 3.3**, only the TB product reached a high densification level (98.2%) after SPS at 1950°C/20min/20MPa. In contrast, under the same conditions, NB and HB samples were scarcely consolidated, with relative densities equal to 90.7 and 88.3%, respectively. The latter value is consistent with **Musa et al. [154],** who achieved densification levels of approximately 90% when using the SHS-SPS method to obtain bulk HfB_2. On the other hand, the fabrication of NbB_2 utilizing this two-step route is investigated for the first time in this work.

As for their composition, no other phases, compared to the corresponding SHS powders, were detected by XRD analysis, whose results are reported in **Figures 3.18b-3.20b** and **Tables A6b-A8b**. The presence of $TiBO_3$ and HfO_2 as secondary phases in TB and HB products, is therefore confirmed. The Rietveld analysis also evidenced the crystallite size of NbB_2, TiB_2, and HfB_2 phases increased from 53, 88, and 52 nm to 120, >200, and 155 nm, respectively, after SPS.

As shown in **Figures 3.22a, 3.22c, and 3.22e**, the outcomes above are consistent with SEM/EDX observations. Indeed, the TB sample is highly consolidated (**Fig. 3.22c**), whereas NB and, above all, HB are not. Nonetheless, metals appear to be uniformly distributed into each ceramic. EDX analysis

performed in pores of the samples sintered without graphite, reveals that even if no oxides were detected by XRD, some O-impurities are present inside pores. In the case of NB, the oxides **(Figure 3.22g)** could be either amorphous or in an amount that is below the detection limit of XRD analysis.

Table 3.3 - Characteristics of SHS powders and related SPS products obtained in this work for the preparation of bulk single-phase NbB_2, TiB_2, HfB_2, NTB, and NHB at different conditions

System	SHS powders composition	SHS particle size parameters (μm)	SPS conditions T_D (°C)/t_D (min)/P (MPa)/xC (wt.%)	Relative density ρ_r (%)
NB	Single phase	d10: 0.32±0.10 d50: 2.29±0.33 d90: 14.27±1.53 d43: 4.86±0.52	1850/20/20/0	88.3±0.6
			1950/20/20/0	90.7±0.6
			1950/20/20/1	92.2±1.0
			2050/20/20/1	92.4±0.7
TB	Single phase	d10: 0.24±0.09 d50: 1.42±0.29 d90: 9.11±0.93 d43: 3.24±0.43	1950/20/20/0	98.2±0.3
			1950/20/20/1	98.9±0.9
HB	Single phase	d10: 0.24±0.04 d50: 1.84±0.45 d90: 26.88±4.88 d43: 7.46±1.58	1950/20/20/0	88.3±0.1
			1950/20/20/1	97.2±1.3
NHB	Multiple phases	d10: 0.40±0.10 d50: 1.99±0.31 d90: 17.36±2.09 d43: 5.52±0.71	2050/40/20/1	97.4±0.2
NTB	Multiple phases	d10: 0.37±0.12 d50: 2.02±0.18 d90: 11.83±0.86 d43: 4.12±0.28	2050/20/20/1	93.6±0.8
			2050/40/20/1	93.5±0.6

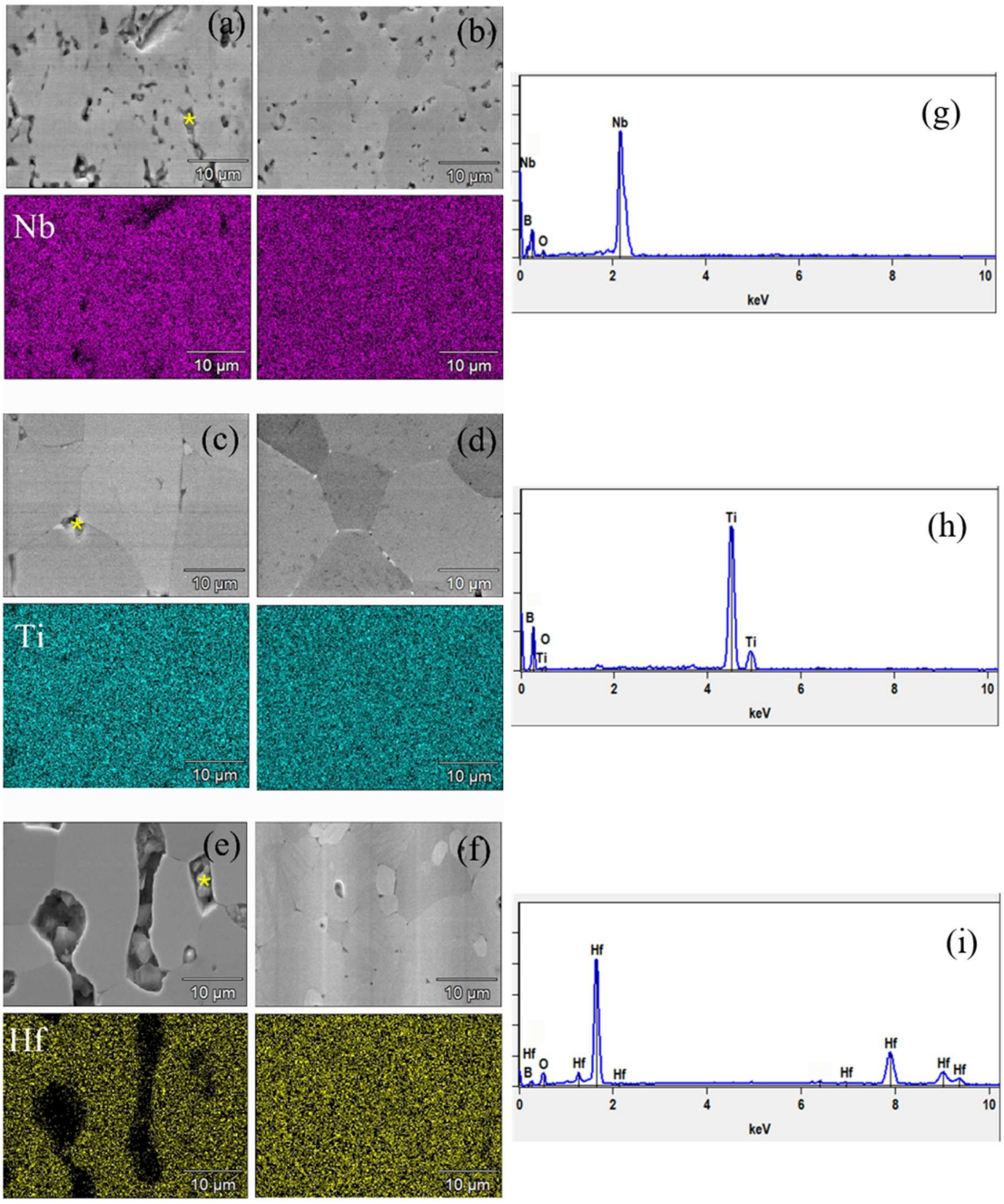

Figure 3.22 - SEM micrographs and associated EDX metal maps of individual diborides produced by SPS: NB obtained at 1950°C/20min/20MPa with no graphite (a) and with 1 wt.% C (b); TB prepared at 1950°C/20min/20MPa with no graphite (c) and with 1 wt.% C (d); HB produced at 1950°C/20min/20MPa with no graphite (e) and with 1 wt.% C (f). EDX analysis spectra performed on the pores (marked with a yellow asterisk) of the NB (g), TB (h) and HB (i) samples obtained by SPS at 1950°C/20min with no graphite addition.

The low O-signals in pore regions revealed by EDX for the case of TB **(Figure 3.22h)**, could be ascribed to the small amount of $TiBO_3$ identified by XRD analysis. Finally, no doubts regarding the presence of HfO_2 inside pores of HB specimens, as evidenced by EDX analysis results shown in **Figure 3.22i**.

The oxides found on sintered samples, particularly for the case of HB, are thought to be the main responsible for the low densification level achieved during SPS. To remove them, graphite was added (1wt.%) to SHS powders prior to SPS, according to the beneficial effect observed when investigating other metal diboride systems on the base of the same strategy. However, as reported in **Table 3.3**, the relative density of the NB sample was only slightly improved, from 90.7±0.6 to 92.2±1.0%, with the use of graphite. This outcome is also testified by the SEM micrograph shown in **Figure 3.22b**. No detectable compositional differences were correspondingly evidenced by XRD analysis (**Figure 3.18c**). Moreover, the attempt made to further reduce residual porosity by increasing the sintering temperature to 2050°C only provided minor changes of NB sample density (92.4±0.7%).

Table 3.3 and Figure 3.22d show that the already high densification achieved in the TB sample at 1950°C with no additive (98.2±0.3%) was almost unaffected by the introduction of graphite (98.9±0.9%). Nonetheless, titanium borate was not detected anymore in the product, while a small amount of TiC (1.3 wt.%) is correspondingly formed (**Figure 3.19c and Table A7c**). $TiBO_3$ was also found as an intermediate product formed during the carbothermal synthesis of TiB_2 assisted by high-energy milling **[172]**. The transformation of $TiBO_3$ to TiB_2 was postulated to occur in the two following steps:

$$TiBO_3 + 3C \rightarrow TiB + 3CO(g) \quad (5)$$

$$2TiB + B_2O_3 + 3C \rightarrow 2TiB_2 + 3CO(g) \quad (6)$$

which are likely to take place also in our study with the addition of graphite and the possible presence of B_2O_3 (in glassy form).

The major effect produced by graphite was observed when processing HB powders. **Table 3.3 and Figure 3.22f** evidence the significant improvement obtained in sample density (from 88.3±0.1 to 97.2±1.3%). Furthermore, XRD analysis (**Figure 3.20c and Table A8c**) shows that HfO_2 was fully reduced by graphite and that HfC (3.1 wt.%) was formed. The small quantities of TiC and HfC detected in TB and HB products, respectively, affect only marginally the calculated values of relative densities, which remain roughly the same (TB) or slightly decrease, from 97.2 to 97.1% (HB), if these

carbides are also considered in the estimation of the theoretical density. In addition, their presence is in line with similar results reported in the literature **[173]**, where secondary carbide phases were formed when graphitic carbon was used to remove O-contaminants in metal diborides. As explained in **Barbarossa et al. [23]**, the following reactions can be considered responsible for the carbothermal reduction of TiO_2 and HfO_2, as well as for the corresponding formation of TiC and HfC, respectively:

$$MO_2 + 2C \rightarrow M + 2CO \quad (7)$$

$$MO_2 + 3C \rightarrow MC + 2CO \quad (8)$$

where M=Ti or Hf.

Based on the results reported above, it is possible to state that the synthesis of the three individual diborides can be successfully obtained by SHS but only the resulting TiB_2 powders were highly densified by SPS at 1950°C/20min/20MPa. The consolidation of the HB system was strongly promoted with the addition of 1 wt.% of graphite, which was able to remove oxides contaminant originally present in SHS products. On the other hand, the introduction of such an additive determined only a modest improvement of the relative density of the NB ceramic. As evidenced by XRD analysis (**Figure 3.18** and **Table A6**) and SEM/EDX results (**Figure 3.22**), the latter system contained relatively lower amounts of oxide impurities, so that the major role played by graphite is to act as a solid lubricant rather than as a reducing agent **[23,24]**, which apparently was not sufficient to achieve high consolidation levels. In any case, the obtained relative densities were adequate to provide samples for evaluating the oxidation and mechanical properties to be compared with those of the corresponding NHB and NTB ceramics.

3.3.3.2 Synthesis and sintering of Nb-based solid solutions

As for the cases of individual diborides, also the reaction fronts generated during the combustion synthesis of NTB and NHB from their elemental precursors were able to self-propagate across the related pellets. However, differently from individual borides, the SHS process was unable to lead to the desired phases. For instance, when the NHB system was investigated, a multiphase product was obtained after SHS, with significant amounts of HfB_2 (27.6 wt.%), and NbB_2 (18.7 wt.%) also formed, along with the dominant $(Nb_{0.5}Hf_{0.5})B_2$ phase (53.1 wt.%) (**Figure 3.23** and **Table A9a**). Traces of HfO_2 (0.6 wt.%) were also detected. SEM/EDX observations further proved that Nb and Hf were not

homogeneously distributed into the SHS powders (**Figure 3.21d**). **Table 3.3** shows that particles' size after 1h BM treatment (d_{43} = 5.52 μm) was in between to the values obtained for their individual counterparts.

Likewise, the SHS process did not succeed in fully converting initial precursors into $(Nb_{0.5}Ti_{0.5})B_2$. More specifically, according to the XRD analysis (**Figure 3.23** and **Table A10a**), the resulting product contained, other than the equimolar phase (62.9 wt.%), also NbB_2 (23.6 wt.%), and TiB_2 (13.5 wt.%). The obtainment of a multiphase product reflects the inhomogeneous Nb and Ti distribution observed by SEM/EDX in SHS powders (**Figure 3.21e)**. As for particle size (**Table 3.3**), slightly finer particles, compared to the NHB ones, were produced for the Ti-containing system (d43 = 4.12 μm), which is consistent with data obtained for the individual diborides.

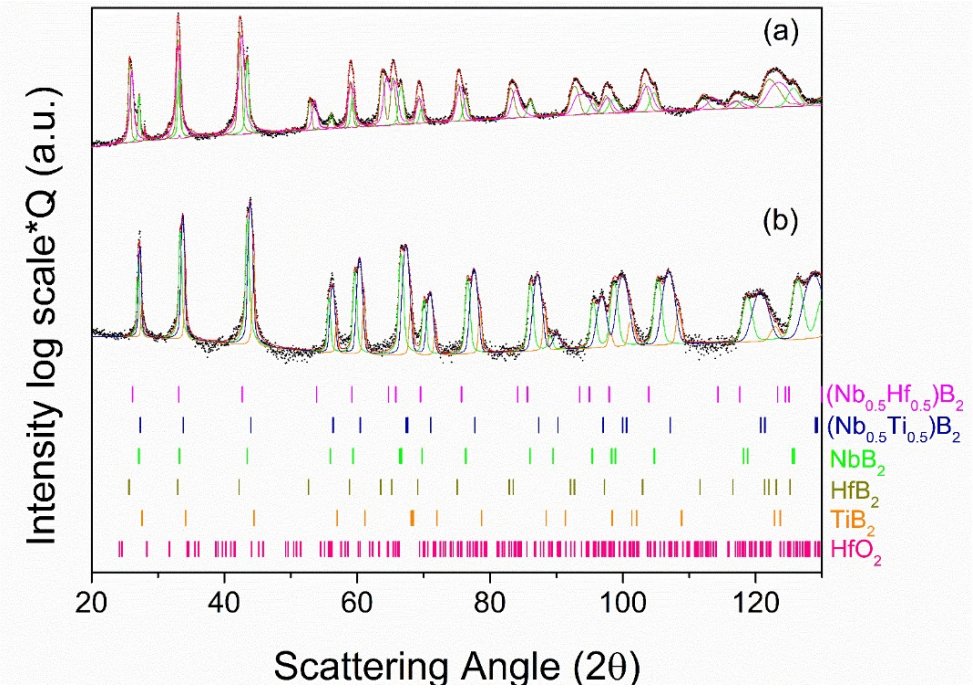

Figure 3.23 - XRD patterns and related Rietveld profiles of NHB (a) and NTB (b) powders produced by SHS. Experimental data (black dots), calculated intensity (red solid line), $(Nb_{0.5}Hf_{0.5})B_2$ (magenta solid line), $(Nb_{0.5}Ti_{0.5})B_2$ (blue solid line), NbB_2 (light green solid line), HfB_2 (dark yellow solid line), TiB_2 (orange solid line) and HfO_2 (pink solid line) refined phases are reported. Bragg's positions for each phase are provided.

Therefore, differently from the individual systems examined in the previous Section, the role of the SPS stage for the fabrication of NHB and NTB ceramics must be considered twofold, i.e. not only aimed at consolidating SHS powders but also to transform secondary boride phases into the expected equimolar solid solutions. With the aim of identifying the milder sintering temperature and holding time conditions for achieving the latter goal, the effect produced when varying these two parameters on the resulting SPS products composition was systematically investigated. The XRD patterns of samples obtained when processing NHB powders under different SPS conditions and in presence of graphite are shown in **Figure 3.24**. The amount of each phase and the corresponding microstructural parameters evaluated by the Rietveld analysis are summarized in **Table A9**.

These data evidence that an increase of either the sintering temperature from 1850°C to 2050°C (t_D=40 minutes) or the holding time from 20 to 40 minutes (T_D=2050°C) determined a progressive improvement in the composition of the NHB product. On the other hand, secondary Nb-rich and Hf-rich (Nb,Hf)B_2 phases are detected in samples produced at T_D values lower than 2050°C. This holds also true when operating at the latter temperature level but with t_D values shorter than 40 minutes. Therefore, the desired $(Nb_{0.5}Hf_{0.5})B_2$ phase with no secondary borides was achieved under the temperature/time conditions of 2050°C/40min. As reported in **Table 3.3**, the resulting ceramic was 97.4±0.2% dense and also contained a low amount of $(Nb_{0.5}Hf_{0.5})C$ (2 wt.%).

The influence of the dwell temperature and the holding time on product composition was also examined for the case of the NTB system. **Figure 3.25** shows the XRD patterns of the sintered samples obtained with 1 wt.%C when the dwell temperature increased from 1950 to 2050°C (t_D=40 min) and the holding time was extended from 10 to 40 min (T_D=40 min). The corresponding phases content and microstructural parameters are listed in **Table A10**. The composition of the NTB product obtained after 40 min by SPS at 1950°C with 1wt.%C was highly improved compared to that of SHS powders, but a relevant amount of a Nb-rich phase (8.7 wt.%) was still found. **Figure 3.25** and **Table A10** also reveal that the expected single-phase product was obtained as the dwell temperature increased to 2050°C. Moreover, the study of the effect of the holding time at T_D=2050°C showed that an extension of this parameter from 10 to 20 minutes was sufficient to lead to the $(Nb_{0.5}Ti_{0.5})B_2$ solid solution with no secondary boride phases (**Figure 25** and **Table A10**).

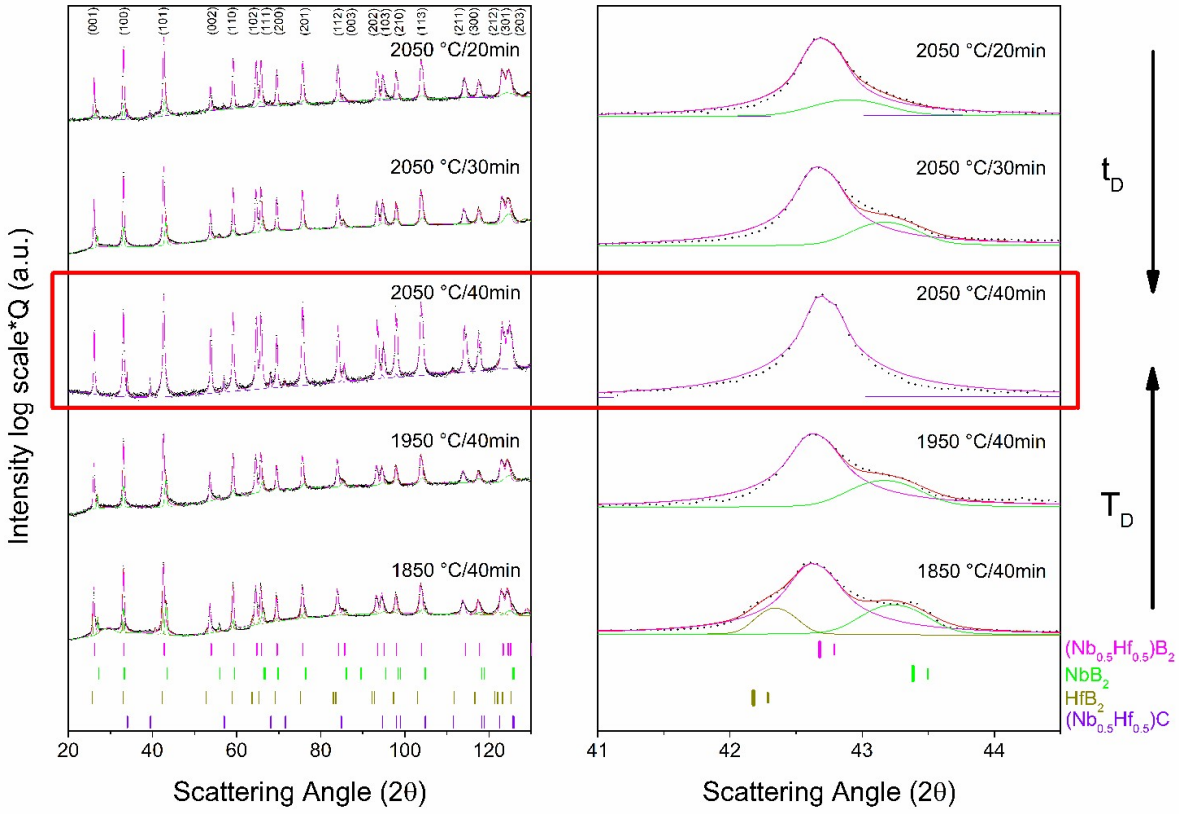

Figure 3.24 - XRD patterns and related Rietveld profiles of NHB samples produced by SPS, in presence of 1wt.% graphite, at different sintering temperatures and dwelling times. Experimental data (black dots), calculated intensity (red solid line), Hf-rich (Nb,Hf)B_2 refined phase which evolves into ($Nb_{0.5}Hf_{0.5}$)B_2 in pattern 2050°C/40min (magenta solid line), Nb-rich (Nb,Hf)B_2 refined phase (light green solid line), HfB_2 refined phase (dark yellow solid line) and ($Nb_{0.5}Hf_{0.5}$)C refined phase (purple solid line) are reported. Bragg's positions for ($Nb_{0.5}Hf_{0.5}$)B_2, NbB_2, HfB_2 and ($Nb_{0.5}Hf_{0.5}$)C phases are provided. Details on (101) reflections of metal diborides phases are reported on the right side. The related structural parameters are reported in **Table A9**. The red frame includes the XRD pattern (general and detailed views) of the optimal NHB sample.

The beneficial role played by graphite to promote the formation of the equimolar solid solutions in NHB and NTB systems is unequivocal. Indeed, when the additive-free SHS powders were directly exposed to the SPS conditions (2050°C/40min and 2050°C/20min for the NHB and NTB systems, respectively) that guarantee, with graphite, that the latter goal was achieved, a multiphase ceramic was produced (**Figure 3.26** and related **Tables A9f and A10f**). In particular, for the case of the NHB

system, a Nb-rich phase (~20 wt.%) was present in the 89.7% dense ceramic produced by SPS at 2050°C/40min. SEM micrographs and related EDX maps shown in **Figures 3.27a-3.27b** evidence that pores and Nb-richer zones (with no, or poorer in Hf) were nearly eliminated with the introduction of the reducing agent.

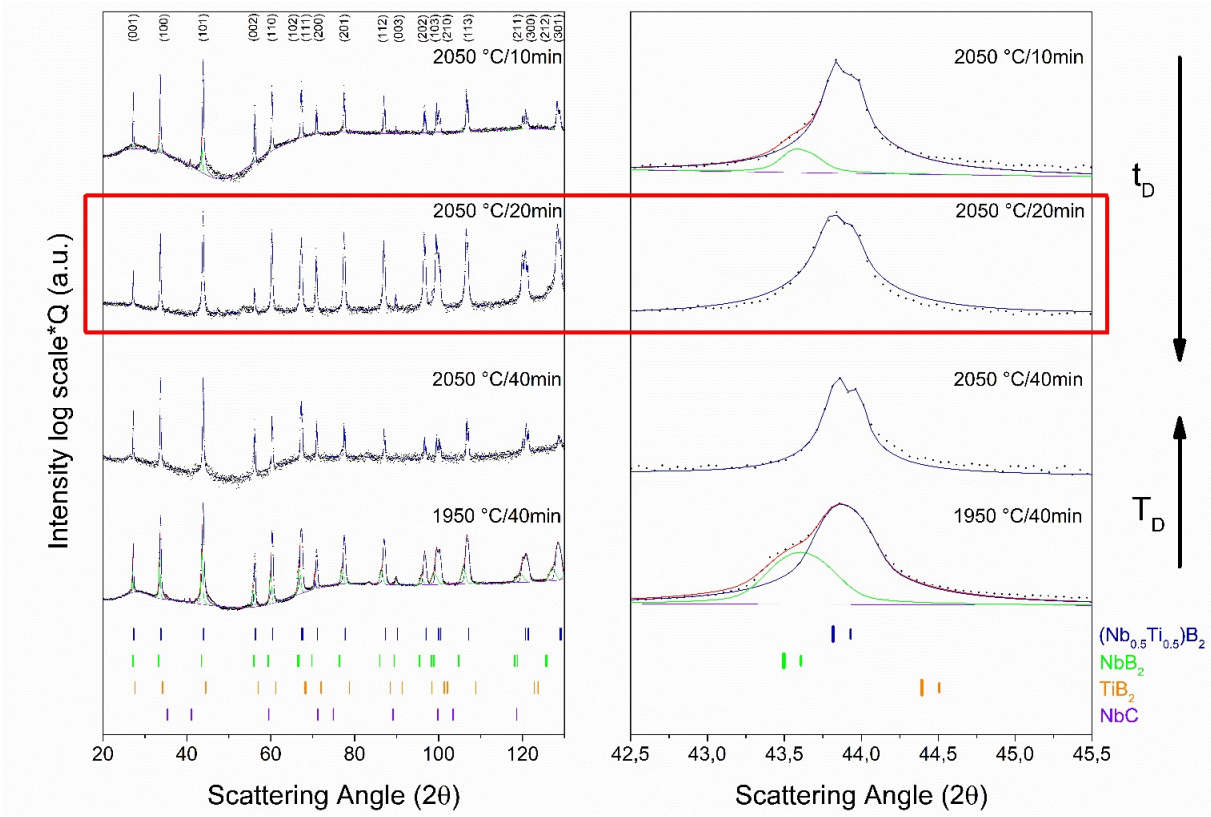

Figure 3.25 - XRD patterns and related Rietveld profiles of NTB samples produced by SPS, in presence of 1wt.% graphite, at different sintering temperatures and dwelling times. Experimental data (black dots), calculated intensity (red solid line), Ti-rich (Nb,Ti)B_2 refined phase which evolves into ($Nb_{0.5}Ti_{0.5}$)B_2 in pattern 2050°C/20min and 2050°C/40min (blue solid line), Nb-rich (Nb,Hf)B_2 refined phase (light green solid line) and NbC refined phase (purple solid line) are reported. Bragg's positions for ($Nb_{0.5}Ti_{0.5}$)B_2, NbB_2, TiB_2 and NbC phases are provided. Details on (101) reflections of metal diborides phases are reported on the right side. The related structural parameters are reported in **Table A10**. The red frame includes the XRD pattern (general and detailed views) of the optimal NTB sample.

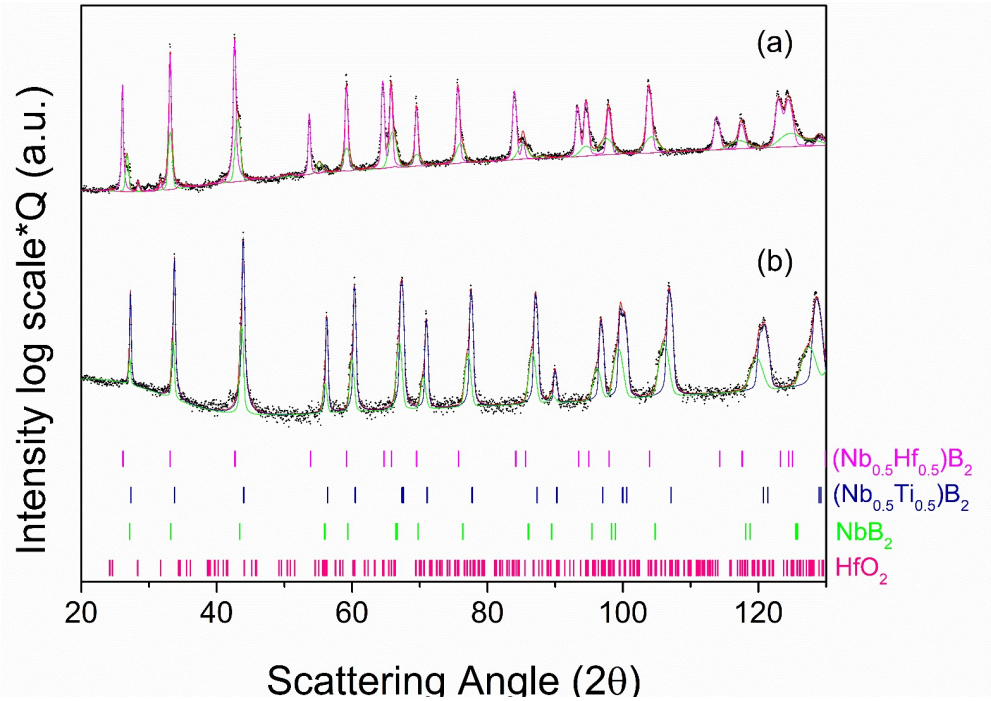

Figure 3.26 - XRD patterns and related Rietveld profiles of NHB (2050°C/40min) (a) and NTB (2050°C/20min) (b) samples produced by SPS with no graphite. Experimental data (black dots), calculated intensity (red solid line), $(Nb_{0.5}Hf_{0.5})B_2$ (magenta solid line), $(Nb_{0.5}Ti_{0.5})B_2$ (blue solid line), Nb-rich $(Nb,M)B_2$ (M=Hf,Ti) (light green solid line) and HfO_2 (pink solid line) refined phases are reported. Bragg's positions for $(Nb_{0.5}Hf_{0.5})B_2$, $(Nb_{0.5}Ti_{0.5})B_2$, NbB_2 and HfO_2 are provided.

A Nb-rich phase (7.3wt.%) was also still found in the bulk NTB product obtained by SPS at 2050°C/20min with no graphite (**Figure 3.28a** and **Table A10f**). Similarly to the case of the individual NB system, the use of such an additive provided only moderate benefits in terms of product consolidation, with an increase of the sample density from 92.8±0.4% (2050°C, 0wt.% C) to 93.6±0.8% (2050°C, 1wt.% C). As seen in **Figures 3.28a-3.28b**, the results above, particularly product homogeneity, are confirmed by SEM/EDX outcomes. The SEM micrograph also shows that some large surface pores, and various cracks are present on the sample. This feature is expected to negatively affect mechanical properties.

It is worth mentioning that, when the fabrication by SHS-SPS of Nb-containing HEBs was carried out without using graphite as an additive **[25]**, Niobium was one of the most difficult elements to solubilize into the ceramic matrix. Nb-rich zones were also observed by other authors in HEB

ceramics fabricated using alternative processing methods **[22,73,174]**. Their presence was ascribed to the slow diffusion of Nb during the formation of the solid solution **[73]**. Thus, to promote the dissolution of this element, more severe sintering conditions were needed, which is also the case of binary diborides investigated in the present work. However, as discussed above, the use of graphite played also a favorable role in achieving this goal in the present study.

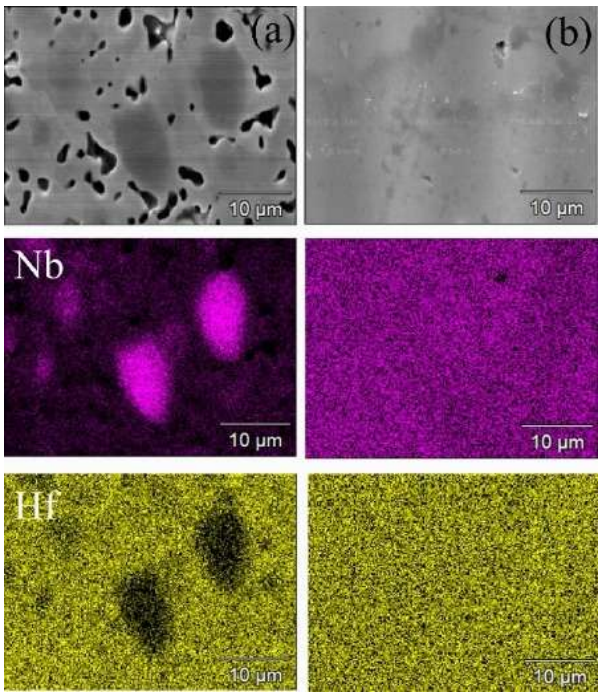

Figure 3.27 - SEM micrographs and associated EDX metal maps of NHB products obtained by SPS at 2050°C/40min/20MPa: with no graphite (a) and with 1 wt.%C (b).

Grain size of diboride phases in NHB and NTB products varied from 5 to 30 µm, similarly to the individual boride samples, and in line with the values reported by **Kurbatkina et al. [168]** for the (Nb,Hb)B_2 solutions obtained in their work, in the range of 2-30 µm.

Finally, equimolar (Nb,Ti)B_2 and (Nb,Hf)B_2 solid solutions are successfully produced in this work by the SHS-SPS method starting from elemental powders and using graphite as additive. Single phase binary diborides are obtained after processing the two SHS powders by SPS at 2050°C/20MPa, while a longer holding time was requested by NHB (40 min) as compared to NTB (20 min). Graphite played

a crucial role to promote, during SPS, the conversion of secondary phases found in SHS powders into the desired equimolar diborides. NHB powders consolidation was also highly facilitated by the introduction of such an additive, with an increase of the relative density from 89.7 to 97.4%. On the other hand, a modest effect (relative density from 92.8 to 93.6%) was observed when considering the NTB sample. This fact was consistent with the behaviour displayed by individual diborides and it could be ascribed to the major beneficial effect produced by graphite to reduce oxide contaminants in Hf containing systems.

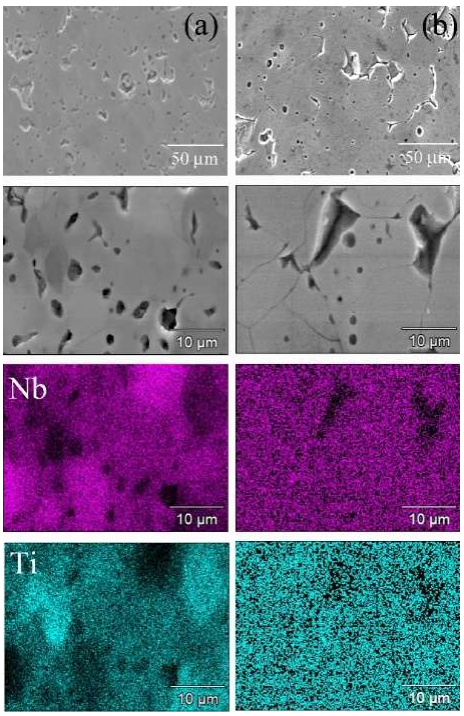

Figure 3.28 - SEM micrographs at different magnitudes and associated EDS metal maps of NTB products obtained by SPS at 2050°C/20min/20MPa: with no graphite (a) and with 1 wt.%C (b).

3.3.3.3 Mechanical properties

The measured Vickers hardness, Young's modulus and fracture toughness values of samples fabricated in this work under the SPS conditions which guaranteed the obtainment of the relatively denser and single-phase products are reported in **Table 3.4**.

Table 3.4 - Mechanical properties of bulk NB (ρ=92.2±1.0%), TB (ρ=98.9±0.9 %), HB (ρ=97.2±1.3%), NTB (ρ=93.6±0.8%), and NHB (ρ=97.4±0.2%) samples produced by SPS in this work. EC: Evans and Charles; LF: Lawn and Fuller; EW: Evans and Wilshaw; L: Lankford; n.d.: not determined.

System	Hardness (GPa)	Young's Modulus (GPa)	K_{IC} (MPa $m^{1/2}$) Method
NB	15.47 ± 0.99	361 ± 21	4.01 ± 0.81 (EC), 2.51 ± 0.5 (LF), 3.71 ± 0.6 (EW), 6.8 ± 1.42 (L)
TB	24.52 ± 1.99	548 ± 38	3.28 ± 1.16 (EC), 2.05 ± 0.73 (LF), 3.01 ± 1.1 (EW), 4.49 ± 1.66 (L)
HB	17.38 ± 0.72	581 ± 29	3.87 ± 0.99 (EC), 2.42 ± 0.62 (LF), 3.58 ± 0.74 (EW), 7.09 ± 1.88 (L)
NTB	10.21 ± 2.01	324 ± 34	n.d.(*)
NHB	18.47 ± 0.60	586 ± 68	2.71 ± 1.06 (EC), 1.69 ± 0.67 (LF), 2.42 ± 1.12 (EW), 4.85 ± 1.98 (L)

(*) Multiple cracks formed on the samples' surface during indentation test.

Among the individual diborides, the TB sample displayed superior hardness (24.52 ± 1.99 GPa), while the HB sample exhibited the highest and Young's modulus (581±29 GPa). In contrast, the low densification level (92.2±1.0%) of the NB ceramic was detrimental for the corresponding mechanical properties. This is consistent with **Maity et al. [164]** findings, who measured Vickers hardness of 3.3 GPa for the 82.8% dense NbB_2 sample they produced. On the other hand, values equal or above 20 GPa could be obtained for this system when reaching relative densities equal or exceeding 97% **[73,109,136].** The measured K_{IC} values of NB samples, for instance 4.01±0.81 MPa $m^{1/2}$ when using

the Evans and Charles formula (**Table 3.4**)**,** are in line with literature data reported for the same system, in the range of 3.76-4 MPa $m^{1/2}$ **[73,109,136]**. TB and HB showed rather high elastic moduli, i.e. 548±38 and 581±29 GPa, respectively, which are similar to or even exceed the values obtained in previous investigations for such ceramics, in the range of 500-565 **[136,171]** and 445-480 GPa, respectively **[12,14,136].** Nonetheless, higher hardness values were measured in the latter studies, up to 35 (TB) and 28 GPa (HB), respectively **[136],** whereas the K_{IC} values measured in the present work fall within the ranges of data reported in the literature for TiB_2 and HfB_2 **[20,136,154]**.

Regarding the mechanical properties of binary diborides, the 97.4% dense NHB ceramic exhibited Vickers hardness and Young's modulus equal 18.47±0.60 GPa and 586±68 GPa, respectively (**Table 3.4**). The latter values are very close, even slightly better, than those ones measured for the HB sample obtained in this work, 17.38±0.72 GPa and 581±29 GPa, respectively. A relatively lower elastic modulus (510 GPa) and a nanohardness (Berkovich tip) of 34.2 GPa were reported very recently by **Kurbatkina et al. [168]** for a 94% dense $(Nb_{0.5}Hf_{0.5})B_2$ sample. No further studies are available in the literature on mechanical properties of $(Nb_{0.5}Hf_{0.5})B_2$.

Similarly to the case of NB, the modest powder consolidation (ρ=93.6±0.8%) achieved when processing NTB powders by SPS (2050°C, 20 min, 20 MPa) can be considered responsible for the low values of Vickers hardness (10.21±2.01 GPa) and Young's modulus (324±34 GPa) correspondingly measured (**Table 3.4**). Moreover, for this sample, multiple cracks were generated on the samples' surface during indentation test, so that no reliable K_{IC} data could be obtained.

Comparing the mechanical characterization results for the Nb-based solid solutions (**Table 3.4**) with those for Zr-based ones (**Table 3.2**), it is possible to state that while ZTB presents superior mechanical properties, NHB is better than ZHB in Vickers' Hardness, Young's modulus and K_{IC}. On the other hand, NTB samples, most probably due to their low relative density, displayed the lowest mechanical properties.

3.3.3.4 Oxidation resistance

Sintered NTB (2050°C, 20min, 1% C) and NHB (2050°C, 40 min, 1% C) samples were exposed at high temperatures to flowing or stagnant air and their behavior was compared to those of the corresponding individual constituents also produced by SHS-SPS. Weight gain, compositional and

structural changes occurring during oxidation tests, including the thickness of the formed oxide layer as well as its stability, were examined.

From the TGA curves reported in **Figure 3.29a**, it is seen that the NTB sample (blue line) started to gain weight at about 800°C, i.e. at a higher temperature compared to NB (green line, about 600°C) and TB (orange line, about 700°C) specimens. The relatively lower mass change of the binary specimen was kept up to about 1300°C, above which the curve grew in an exponential manner.

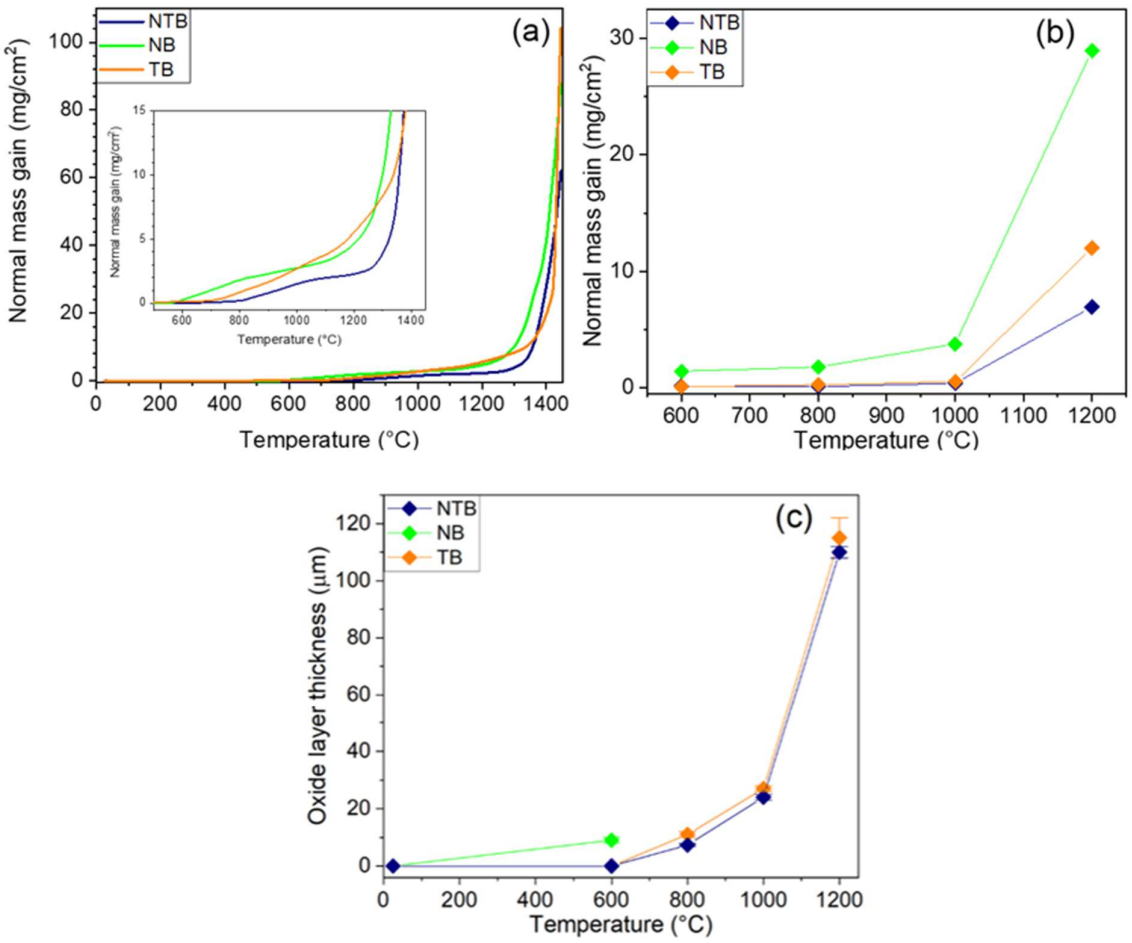

Figure 3.29 - Specific weight changes during (a) TGA oxidation test in air and (b) after 1h in air furnace at 600, 800, 1000 and 1200 °C for the NTB, NB, TB samples produced in this work via SHS-SPS. (c) Oxide layer thickness of samples subjected to oxidation tests at different temperatures in air furnace. NB (green line and dots), TB (orange line and dots) and NTB (blue line and dots)

Figure 3.30a shows a different behavior for the NHB sample (magenta line), which began to gain mass at temperature slightly higher (approximately 650°C) than that observed with the NB constituent (green line), whereas a very little weight change took place in the HB ceramic (ochre line) for temperature below 1000°C. Such performance was kept for the entire temperature range investigated, with the TGA curve of the binary system which follows, albeit staying slightly underneath, that of NB. In contrast, HB displayed much higher thermal stability, with a gradual and slower mass increase up to 1450°C.

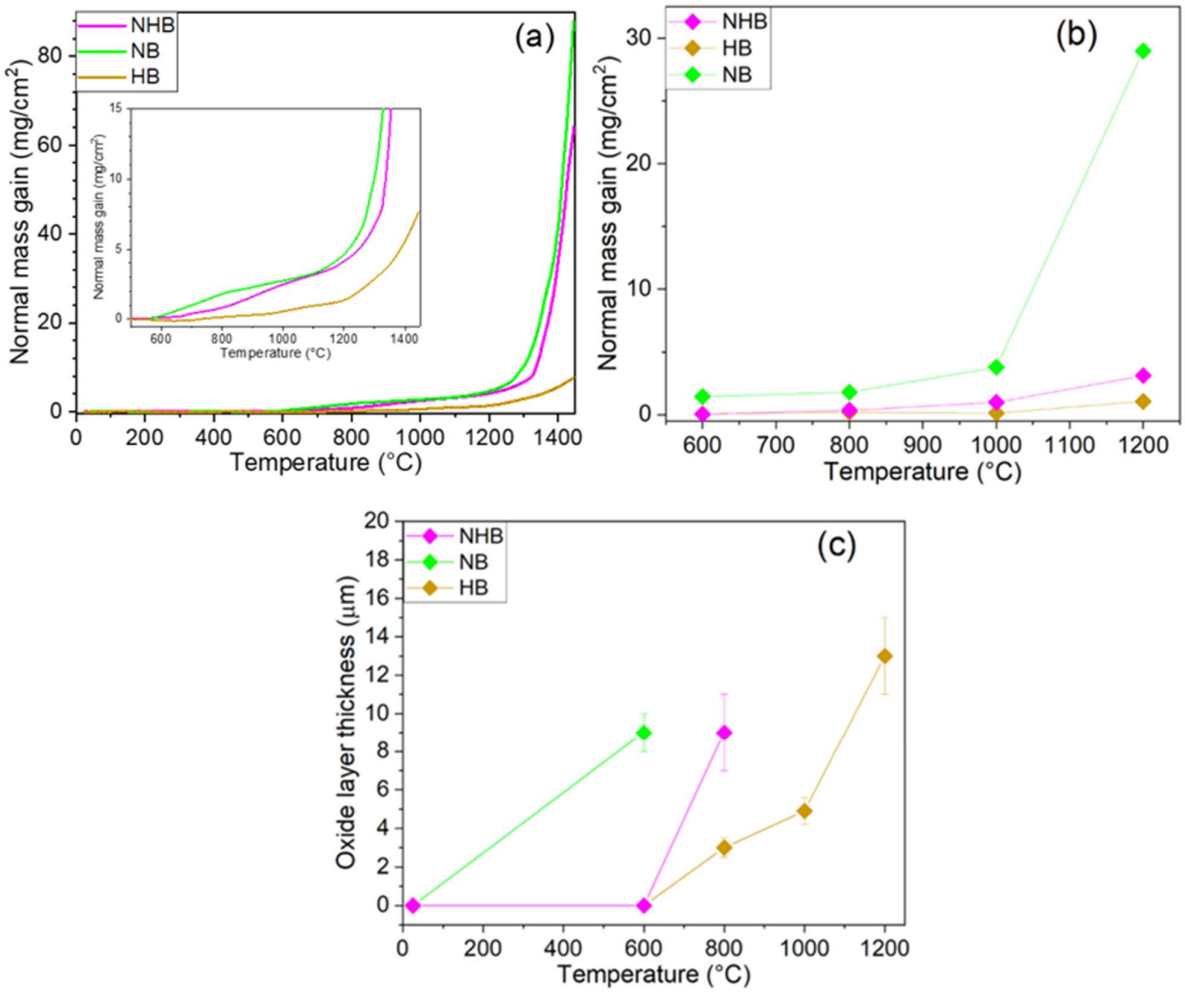

Figure 3.30 - Specific weight changes during (a) TGA oxidation test in air and (b) after 1h in air furnace at 600, 800, 1000 and 1200 °C for the NHB, NB, HB samples produced in this work via SHS-SPS. (c) Oxide layer thickness of samples subjected to oxidation tests at different temperatures in air furnace. NB (green line and dots), HB (ochre line and dots) and NHB (magenta line and dots)

Outcomes deriving from oxidation experiments in air furnace were consistent with TGA tests. Changes in samples appearance after the test conducted at different temperatures can be observed from the related optical images shown in **Figures 3.31a-3.31b**.

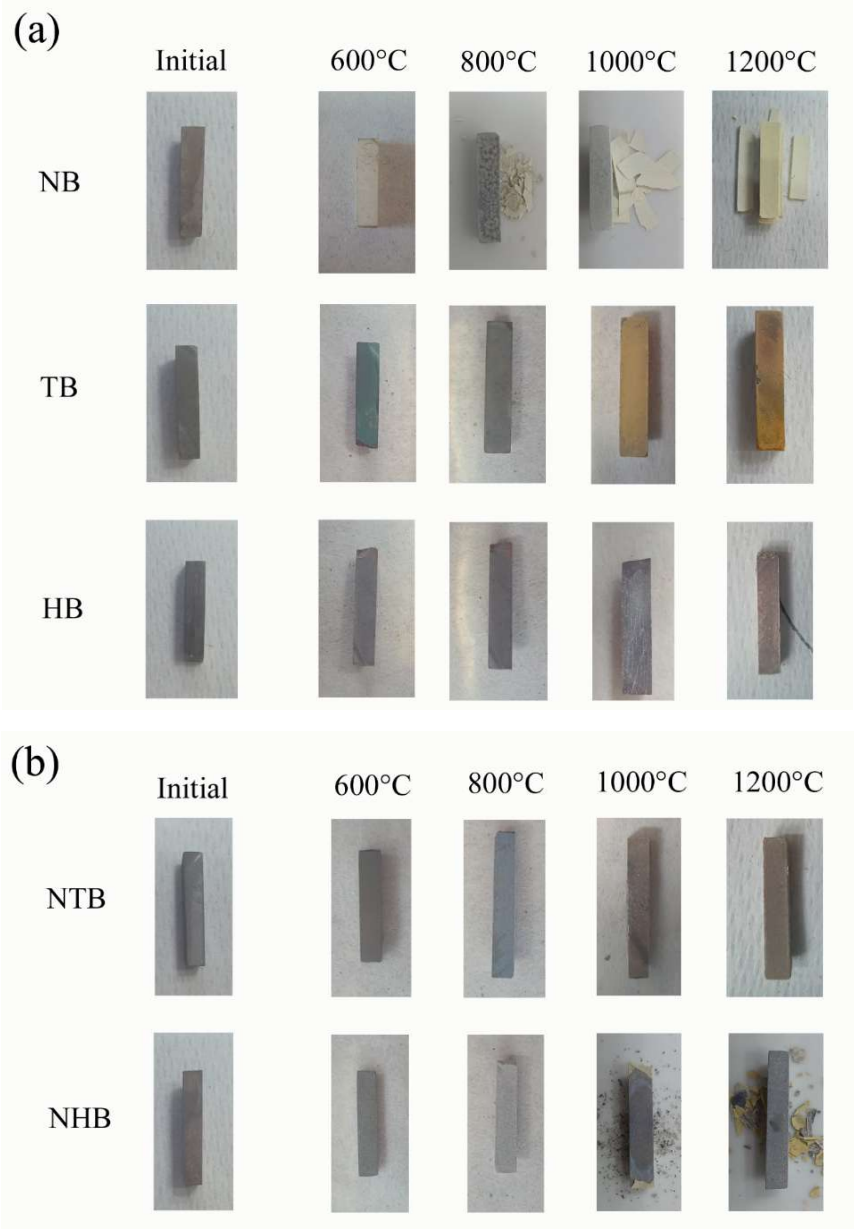

Figure 3.31 - Optical images showing the changes of (a) individual, and (b) binary diboride samples fabricated in this work after oxidation experiments in air furnace at different temperatures.

As for the individual systems, the oxide layer (white-yellow colored) formed on the NB ceramic processed at 800°C separated from the sample, and this negative feature became progressively more relevant when more severe temperature conditions were applied. In contrast, no oxide scale exfoliation took place when heat treating TB samples, while their original gray-brown color turned to yellow-orange at 1000°C, due to compositional transformations occurring on their surface, as discussed afterwards. Finally, HB samples were much less altered by the received treatment in air furnace.

Interestingly, the solid solution formed from the equimolar combination of NbB_2 and TiB_2 behaved like the latter diboride rather than the former one, with no detachment of the oxide layer (**Figure 3.31b**). In contrast, the presence of Niobium apparently played a prominent, negative, influence on the oxidation behavior of the NHB system, as demonstrated by the separation of the oxide scale from the bulk in samples exposed to 1000°C or higher temperatures. In this regard, it should be considered that the NHB sample had a higher relative density compared to that of the NTB specimen, i.e. 97.4 and 93.6%, respectively. Therefore, the oxidation behavior cannot be attributed to differences in samples' porosity since the less resistant sample also possessed higher relative density.

As shown in **Figure 3.29b**, during tests in air furnace, NB samples increased their weight progressively up to 1000°C, above which a significant mass gain is generated. The value of 28.9 mg/cm^2 measured at 1200°C in the present work is reasonably in line with results obtained by **Akin et al. [165],** who reported, for the same temperature, an increase of mass gain from about 28 to approximately 50 mg/cm^2, as the exposure time was raised from 90 to 360 min, respectively. The marked rise in the NB weight as the temperature increased can be readily ascribed to the separation of the oxide layer (**Figure 3.31a**). Indeed, the latter cannot offer a protective barrier for the diffusion of oxygen, which can then reach more easily the sample bulk. On the other hand, lower changes were observed in TB and NTB products, the latter being apparently less affected by the oxidative environment, in accordance with the images depicted in **Figures 3.31a-3.31b**.

As reported in **Figure 3.30b**, a peculiar situation is encountered with the NHB system, which manifested, for temperatures exceeding 1000°C, a lower rate in mass gain increase compared to that provided by TGA. Such discrepancies can be likely ascribed to the active role played by air flow during

the latter test to enhance oxidation phenomena with respect to the case of furnace experiments conducted in stagnant air.

In what follows, the results above will be correlated with outcomes provided by XRD analysis performed on the surface of the annealed samples and SEM/EDX observations of the corresponding cross sections. **Figure 3.32(a)** shows that Nb_2O_5 (orthorhombic) represents the major phase present on the surface of NB samples heat treated at 600°C, with the original diboride phase still detected.

This fact agrees with **Ma et al. [175]** who observed the onset of the oxidation of NbB_2 powders occurring at about 500°C. The transformation of niobium pentoxide from the orthorhombic to monoclinic configuration occurred when the annealing temperature increased to 800°C. This is consistent with **Nico et al. [176]**, who reported that any Nb_2O_5 polymorph is transformed to m-Nb_2O_5 after a heat treatment in air. The only difference is that, in the present study, such a transformation was observed to occur at a lower temperature (800°C) rather than for temperature exceeding 1000°C **[176]**. Such discrepancy might be due to the systems undergoing oxidation being different, i.e. NbB_2 instead of elemental Niobium, respectively. In any case, the phase transition of NbO_2 from the orthorhombic to the monoclinic structure is accompanied by a marked cell volume expansion, from 706 to 1358 $(Å)^3$ **[176]**. This feature could be then considered the main responsible for the separation of the oxide layer from the bulk occurred correspondingly (see **Figure 3.31a)**.

A niobium borate phase, ascribed to Nb_3BO_9 ($3Nb_2O_5 \cdot B_2O_3$), was also formed at 800°C during the oxidation of NB sample in our investigation. Its presence was also observed by **Akin et al. [165]** who postulated the occurrence of the following reaction:

$$3Nb_2O_5\,(s)+B_2O_3\,(l) \rightarrow 2Nb_3BO_9\,(s) \qquad (9)$$

According to XRD analysis, the relative content of niobium borate progressively increases as the temperature was raised up to 1200°C.

The heat treatment at 600°C of the TB sample resulted in the incipient formation of TiO_2 (**Figure 3.32b**), which is congruent with the fact that the beginning of TiB_2 oxidation in air occurs in the range 400-500°C **[20]**. XRD peaks intensity of the latter phase becomes notably higher in samples exposed at 800°C, with lower amounts of TiB_2 still found. Finally, when the test was conducted at higher temperatures (1000 or 1200°C), TiO_2 was the only phase evidenced by this analysis.

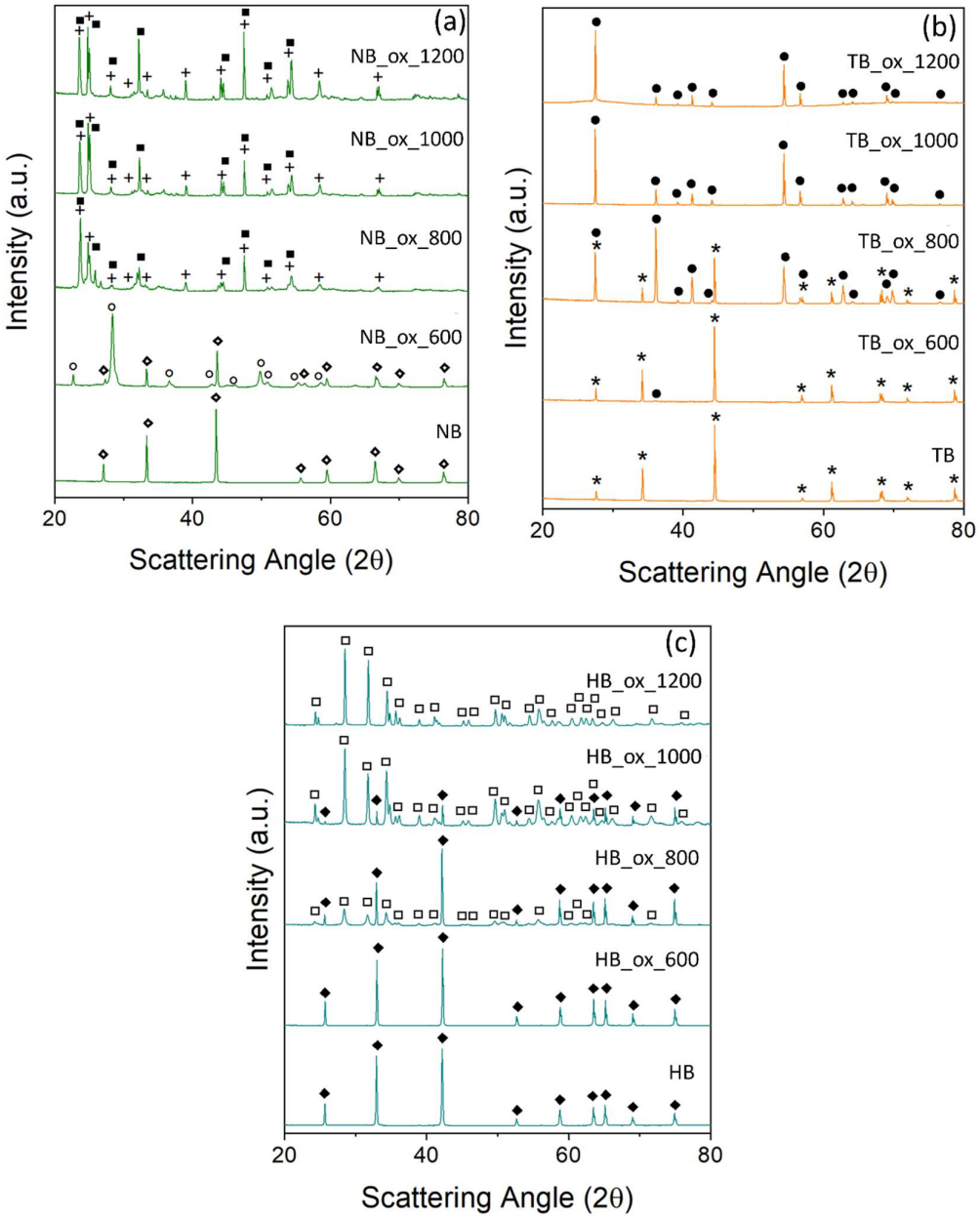

Figure 3.32 - XRD patterns relative to the surface of individual diborides samples after being heat treated in air furnace at different temperatures: NB (a), TB (b), HB (c). Patterns of NB_ox_800, NB_ox_1000, and NB_ox_1200 systems are related to the oxide layers separated during the test from the corresponding samples (see **Figure 3.31a**). ◇ NbB_2 hexagonal (COD-1510778), ○ Nb_2O_5 orthorhombic (PDF 30-10873), ✚ Nb_2O_5 monoclinic (P 1 2/m 1) (COD 2107337 or PDF 27-1311), ■ $Nb_3BO_9/3Nb_2O_5{\cdot}B_2O_3$ (PDF 19-0867), ✶ TiB_2 hexagonal (COD-2002800), ● TiO_2 (rutile) tetragonal (PDF-21-1276), ◆ HfB_2 hexagonal (COD-1510711), □ HfO_2 monoclinic (COD-9013470).

XRD patterns shown in **Figure 3.32c** indicate that no oxidation occurred on HB samples annealed at 600°C. In addition, while HfO_2 was detected on samples processed at 800°C, HfB_2 still represented the dominant phase. As the temperature was further increased, the latter one was progressively replaced by HfO_2, which was the only phase found in samples heat treated at 1200°C.

The substitution of 50 at.% Nb with Ti apparently provided a delay in the oxidation of the diboride phase. Indeed, in contrast with the NB system, no oxides were detected by XRD analysis on the surface of the NTB sample at 600°C (**Figure 3.33a**). However, a mixed oxide and a B-poor titanium borate, associated to $TiNb_2O_7$ and $TiB_{0.024}O_2$, respectively, were found at 800°C, along with the original $(Nb_{0.5}Ti_{0.5})B_2$ phase. The latter one completely disappeared at temperatures equal to or exceeding 1000°C.

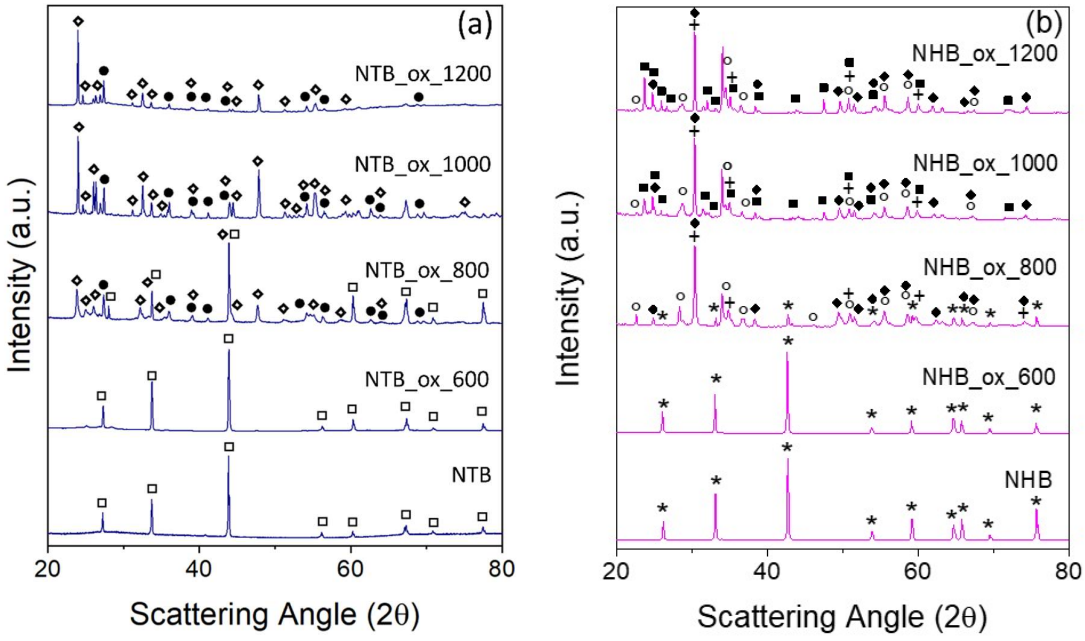

Figure 3.33 - XRD patterns relative to the surface of binary diborides samples after being heat treated in air furnace at different temperatures: NTB (a), and NHB (b). Patterns of NHB_ox_1000, and NHB_ox_1200 systems are related to the oxide layers separated during the test from the corresponding samples (see **Figure 3.31b**). □ $(Nb_{0.5}Ti_{0.5})B_2$ hexagonal (COD-1510775), ● $TiB_{0.024}O_2$ tetragonal (PDF-87-0921), ◇ $TiNb_2O_7$ monoclinic (PDF-39-1407), ✶ $(Hf_{0.5}Nb_{0.5})B_2$ hexagonal (COD-1510708), ○ Nb_2O_5 monoclinic (Pearson 1232958), + HfO_2 cubic (PDF-53-0560), ◆ $Nb_{16.8}O_{42}$ orthorhombic (COD 2106534), ■ $Nb_{12}O_{29}$ orthorhombic (COD-1541318).

Based on XRD analysis (**Figure 3.33a**), and in agreement with literature and the TiO_2-Nb_2O_5 phase diagram (**Figure B3** in **Appendix B**) **[177,178]**, $TiNb_2O_7$, once formed, did not undergo any structural transformation as temperature was raised to 1200°C. Moreover, no Nb_2O_5 was detected, differently from the case of individual NB sample, where volume changes associated to its orthorhombic to monoclinic phase transition were considered responsible for the observed detrimental oxidation behaviour. Consequently, the formation of the more stable mixed oxide made the oxide layer generated on NTB ceramics relatively less stressed, i.e. less prone to exfoliate, differently from that formed on the NB sample, where the o- to m-Nb_2O_5 phase transition took place (**Figure 3.31**).

Consistently with the higher thermal stability of HfB_2 in air (**Figure 3.32c**), the replacement of 50 at.% Nb with Hf also produced beneficial effects, at least at low temperatures, as testified by the absence of oxides in the XRD pattern of NHB sample annealed at 600°C (**Figure 3.33b**). Nonetheless, an increase of the temperature to 800°C was accompanied by remarkable compositional changes, with the ceramic surface mainly consisting of two niobium oxides, i.e. Nb_2O_5 (monoclinic) and $Nb_{16.8}O_{42}$ (orthorhombic), along with HfO_2. A residual amount of $(Hf_{0.5}Nb_{0.5})B_2$ was also found. As the temperature in the furnace was raised to 1000°C, the original diboride was not detected on the sample surface, and the formed oxide layer separated (**Figure 3.31b**), whereas a new niobium oxide, associated to $Nb_{12}O_{29}$ (orthorhombic), was detected together with Nb_2O_5, $Nb_{16.8}O_{42}$, and HfO_2. No further compositional changes were observed at 1200°C. The cell volume of o-$Nb_{12}O_{29}$ (303 $(Å)^3$) formed at 1000°C is significantly smaller than those of m-Nb_2O_5 (1358 $(Å)^3$) and o-$Nb_{16.8}O_{42}$ (708 $(Å)^3$) **[176]**, already present at 800°C. Therefore, as for the case of the NB system described previously, the oxide detachment in the NHB sample at 1000°C observed in **Figure 3.31b** can be attributed to the corresponding volume changes accompanying such phase transformation. Although the formation of mixed oxides in the Nb-Hf-O system is possible **[179]**, their presence was not detected in our experiments, differently to the case of the NTB sample, where the stable $TiNb_2O_7$ phase was produced.

SEM/EDX investigations (**Figure 3.34**) evidenced the formation of an oxide layer on the surface of each diboride ceramic. As reported in **Figures 3.29c and 3.30c**, the thickness of such layers monotonically increased as the oxidation temperature was augmented. In particular, the oxide covering the NB ceramic heat treated at 600°C, above which it separated from the rest of the sample

(**Figure 3.31a**), was 9 ±1 μm thick whereas, consistently with XRD findings, SEM/EDX observations confirm TB and NTB samples were not, or only barely, affected by the oxidizing environment at 600°C. At 800°C or higher values, an oxide layer with a growing and comparable thickness was formed on the latter two ceramics. For instance, the layers produced at 1200°C on TB and NTB samples were 115 ±7 and 110 ±2 μm thick, respectively. Based on the outcomes described above, the less resistant system during oxidation experiments was undoubtedly NB followed by TB, while their equimolar combination produced a solid solution with relatively higher stability compared to its constituents.

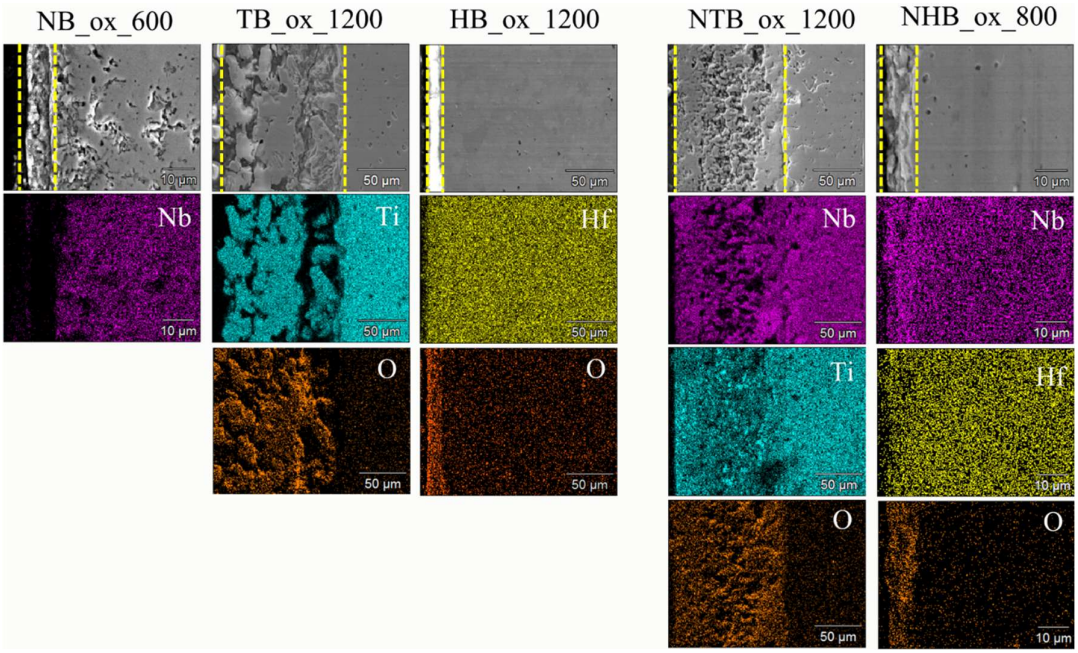

Figure 3.34 - Cross sectional SEM micrographs and corresponding EDS elemental maps of samples after receiving 1h heat treatment in air furnace under the highest temperature condition where no separation of the formed oxide layer was observed: NB (600°C), TB (1200°C), HB (1200°C), NTB (1200°C), and NHB (800°C).

Figure 3.30c shows that the thickness of the oxide layer formed on the Hf-containing binary sample (magenta line and dots) is in between to those of its individual constituents (green and ochre lines-dots for NB and HB, respectively). Due to the separation of the oxide formed on NB and NHB samples

for temperatures equal to or above 800 and 1000°C, a complete comparison of these data is not possible in the whole temperature range. Nonetheless, these data and the corresponding mass gain measured after the same test (**Figure 3.30b**) allow us to state that the three systems exhibited higher sensitivity to the oxidizing environment in the following order: NB>NHB>HB.

The cross sections of oxidized samples relative to highest temperature conditions (i.e. 1200°C-1h or that above which the separation of the oxide layers occurred) were examined in detail by SEM/EDX, as shown in **Figure 3.34**. It is seen that the exposition of the NB ceramic to air at 600°C determined a significant sample degradation. In particular, the generated oxide layer was very porous and friable, so that it was significantly removed during polishing. This is the reason why EDX signals on this layer are very weak and the O-map irrelevant (not reported in **Figure 3.34**). **Figure 3.34** also evidences that the 115 ±7 μm thick oxide product formed at 1200°C on the TB sample is apparently well attached to the bulk, but it is also very irregular and porous. In contrast, under the same annealing condition, a very thin (13 ±2 μm) and compact layer of HfO_2 is produced on the surface of the HB ceramic. This finding confirms the superior oxidation resistance of HfB_2, as a consequence of the fact that the volume contraction accompanying phase transition of the formed HfO_2 from the monoclinic to tetragonal structure, and the consequent formation of cracks and other defects, takes place at high temperatures, near to 1800°C **[141]**, i.e. well above of the conditions adopted in this work.

Let's consider now the behavior of the two-components ceramics. The oxide layer formed at 1200°C on the NTB sample displays an irregular microstructure while it is more compacted compared to that generated at the same condition on the TB ceramics. This finding is coherent with the relatively lower mass gain exhibited at 1200°C by the first system with respect to the second one, as shown in **Figure 3.29b**. It is then confirmed that the solid solution resulting when coupling Nb and Ti diborides in equimolar proportion is thermally more resistant compared to the individual constituents. As for the NHB product heat treated at 800°C, a beneficial effect was provided by the replacement of 50 at.% Nb with Hf, which allowed the oxide layer to resist at higher temperatures (200°C above) with respect to that formed on the NbB_2 sample. Nonetheless, such benefit ceased as the temperature was raised to 1000°C, under which the oxide layer separation occurred (**Figure 3.31b**). As discussed previously, the latter event corresponded to the phase transformations involving niobium oxides formed in both NB and NHB samples as the oxidation temperature was progressively raised. These compositional changes are accompanied by volume expansion/contraction phenomena and, consequently, thermomechanical stresses are generated in the oxide scales, which make them less

stable and prone to detach from the sample, as experimentally observed. The latter statement is supported by the fact that such an event was not observed when heat treating TB, HB, and NTB ceramics (**Figures 3.31a-b**), since the related oxides did not undergo any phase transition as the temperature increased from 600 to 1200°C (**Figures 3.32b, 3.32c, 3.33a**).

The oxidation behaviour of $(Nb_{0.5}Hf_{0.5})B_2$, which can be considered in between of those manifested by its individual constituents, is heavily influenced by the behaviour of Nb-oxides correspondingly formed. Moreover, as observed in **Figure 3.31**, NB and NHB appeared to be the most sensitive systems to the oxidation environment, with the formed oxide layers which separate from the bulk when the two samples were exposed to 600 and 800°C, respectively. In particular, during oxidation of NbB_2, the phase transition from o- to m-Nb_2O_5 took place at 800°C. A similar outcome is obtained at 1000°C with the NHB system , with the partial transformation of m-Nb_2O_5 and $Nb_{16.8}O_{42}$ to o-$Nb_{12}O_{29}$. Such chemical transformations are accompanied by significant volume contraction/expansions, and the resulting thermomechanical stresses in the oxide layers are likely responsible for their separation from the samples at the abovementioned temperatures.

Conversely, more stable oxide scales were generated on the surface of TB, HB, and NTB ceramics, where the types of oxide products did not change in the whole temperature range investigated (600-1200°C). In particular, the formation of a mixed oxide ($TiNb_2O_7$), which did not undergo any phase transition during the oxidation of the NTB sample, was highly beneficial to generate a more stable oxide scale. Based on the observation above, it is possible to state that the formation of stable binary oxides has the ability to mitigate the problematic cracking phenomena due to phase transitions, as for the case of Nb oxides.

The activity and obtained results described in this Section have been reported in Cappai, L., **Casu, M.**, Locci, A. M., Cao, G., Garroni, S., Cannillo, V., Bellucci, D., & Orrù, R. (2025). From individual to equimolar binary transition metal diborides: The case of $(Nb_{0.5}M_{0.5})B_2$, M=Ti, Hf. *Journal of the European Ceramic Society*, *45*(8), 117277. https://doi.org/10.1016/J.JEURCERAMSOC.2025.117277

3.4 Optimization of the SHS technique for the synthesis of metal boride ceramics

3.4.1 Introduction

As described in **Section 1.2.1**, transition metal borides can be synthesized by different solid-state pathways, including the borothermal (1) and direct (4) reactions:

$$\mathrm{MeO_2} + \frac{10}{3}\mathrm{B} \rightarrow \mathrm{MeB_2} + \frac{2}{3}\mathrm{B_2O_3} \quad (1)$$

$$\mathrm{Me} + 2\mathrm{B} \rightarrow \mathrm{MeB_2} \quad (4)$$

Reaction (4) is strongly exothermic, while reaction (1) is generally endothermic or, for few diboride systems, slightly exothermic (see **Figure 1.4** for the case of ZrB_2). Comparing these two synthesis pathways, the main advantage of BR reaction is the relatively low cost of transition metal oxides compared to elemental precursors, whereas its drawback is the high energy consumption of the synthesis process, caused by its typical endothermicity. This causes the need to perform such process in furnaces for several hours and at high temperatures (typically >1300 K) **[47,48,180]**. On the contrary, taking advantage of the strong exothermicity of reaction (4), the advantage of the DR reaction performed via SHS is the lack of need of external energy supply and the rapidity of the process (~seconds). However, the use of expensive elemental reactants makes it less convenient.

The two processes present specular advantages and disadvantages in terms of precursor costs and energy consumption. Indeed, the combination of these two synthesis pathways, using both reduced metals and metal oxides as staring reactants, but keeping the SHS self-propagation advantages, lays in the framework of process integration between exothermic and endothermic processes, successfully applied in other case studies **[181]**. The aim of this approach is then to maximise the use of metal oxides, while keeping the short processing times and energy saving advantages of the SHS technique. In this regard, the thermodynamic requirement to be generally satisfied by a reacting system to be self-sustaining is to possess an adiabatic temperature (T_a) equal or exceeding ~1800 K **[63]**. The T_a of IV group metal borides reacting systems (TiB_2, ZrB_2 and HfB_2) is far higher than the latter criterion (for example 3190 K for TiB_2, see **Table 1.1**), opening the door for the use of the excess generated energy to sustain endothermic processes, such as parallel TiB_2 synthesis via the cheaper borothermal reaction. Reactions (2) and (3):

$$MeO_2 + \frac{1}{2}B_4C + \frac{3}{2}C \rightarrow MeB_2 + 2CO \quad (2)$$

$$MeO_2 + B_2O_3 + 5C \rightarrow MeB_2 + 5CO \quad (3)$$

were not considered for this scope, because of their stronger endothermicity compared to that of reaction (1), as seen in **Figure 1.4** for the case of ZrB_2. In the present study, a thermodynamic analysis was developed to assess the T_a values resulting from the variation of the relative contribution of integrated BR and DR reactions to synthesize TiB_2, ZrB_2 and HfB_2 compounds. An experimental SHS campaign was also conducted to validate the reliability of the theoretical analysis, and to test the resulting optimal conditions.

3.4.2 Materials and Methods

3.4.2.1 Thermodynamic analysis

Defining Z as the molar fraction of the desired product obtained according to reaction (4) and $(1 - Z)$ as the molar fraction obtained by reaction (1), the enthalpy balance for the adiabatic SHS process is:

$$0 = \Delta h_r + \upsilon_{MeB_2} q_{MeB_2} + (1 - Z)\upsilon_{B_2O_3} q_{B_2O_3} \quad (3)$$

where the heat generated by the combined reactions can be described as:

$$\Delta h_r = \upsilon_{MeB_2} \Delta h_{f,MeB_2} + (1 - Z)\upsilon_{B_2O_3} \Delta h_{f,B_2O_3} - (1 - Z)\upsilon_{MeO_2} \Delta h_{f,MeO_2} \quad (4)$$

The expression of the adsorbed heat by the two products $q_{Me\ _2}$ and $q_{B_2O_3}$ variates according to the physical state of the latter ones. Specifically, it depends upon the value of the adiabatic temperature compared to the phase transition temperatures of the product:

$$q_{Me\ _2} = \begin{cases} \int_{T_0}^{T_a} C_{P,MeB_2,s}\, dT & T_a < T_{m,MeB_2} \\ \int_{T_0}^{T_a} C_{P,MeB_2,s}\, dT + \Delta h_{s\rightarrow l,MeB_2} & T_a = T_{m,MeB_2} \end{cases} \quad (5)$$

$$q_{B_2O_3} = \begin{cases} \int_{T_0}^{T_a} C_{P,B_2O_3,s}\,dT & T_a < T_{m,B_2O_3} \\ \int_{T_0}^{T_a} C_{P,B_2O_3,s}\,dT + \Delta h_{s\to l,B_2O_3} & T_a = T_{m,B_2O_3} \\ \int_{T_0}^{T_{m,B_2O_3}} C_{P,B_2O_3,s}\,dT + \Delta h_{s\to l,B_2O_3} + \int_{T_{m,B_2O_3}}^{T_a} C_{P,B_2O_3,l}\,dT & T_{m,B_2O_3} < T_a < T_{b,B_2O_3} \\ \int_{T_0}^{T_{m,B_2O_3}} C_{P,B_2O_3,s}\,dT + \Delta h_{s\to l,B_2O_3} + \int_{T_{m,B_2O_3}}^{T_a} C_{P,B_2O_3,l}\,dT + \Delta h_{l\to g,B_2O_3} & T_a = T_{b,B_2O_3} \\ \int_{T_0}^{T_{m,B_2O_3}} C_{P,B_2O_3,s}\,dT + \Delta h_{s\to l,B_2O_3} + \int_{T_{m,B_2O_3}}^{T_{b,B_2O_3}} C_{P,B_2O_3,l}\,dT + \Delta h_{l\to g,B_2O_3} + \int_{T_{b,B_2O_3}}^{T_a} C_{P,B_2O_3,g}\,dT & T_a > T_{b,B_2O_3} \end{cases} \quad (6)$$

where:

$$C_{P,i,j}(T) = A_{i,j} + B_{i,j}T + C_{i,j}T^2 + D_{i,j}T^3 + E_{i,j}T^{-2}; i = MeB_2, B_2O_3; j = s, l, g \quad (7)$$

Terms related to the gas or liquid state have been not considered for MeB_2, given the fact that the melting point of all three diboride systems investigated in this study corresponds to the maximum adiabatic temperature achievable in the limit case of Z=1. The Δh_r and molar latent heats were taken from Ref. **[58]**. HfB_2 heat of fusion was not available, so it was assumed to be of the same order of magnitude as the ones of the two other diborides. i.e. $1 \cdot 10^5$J/mol.

C_P coefficients (**Table 3.5**) were regressed from heat capacity data reported in Ref. **[58]**.

Regarding the phase transition temperatures, it is well known that the effect of pressure on melting temperatures is generally considered negligible. On the contrary, pressure can affect the boiling temperature of B_2O_3. Accordingly, the corresponding boiling temperature can be obtained by solving the following liquid-vapor equilibrium condition:

$$g_{B_2O_3,g}(T_{b,B_2O_3}, P) = g_{B_2O_3,l}(T_{b,B_2O_3}) \quad (8)$$

where the liquid phase has been assumed incompressible. The results obtained by solving Eq. (8) were correlated through the following Antoine-like relation, adapted from Ref. **[182]**:

$$T_{b,B_2O_3} = \frac{\beta}{\alpha - \ln P} - \gamma \quad (9)$$

and the fitted parameters are also reported in **Table 3.5**. The set of non-linear algebraic equations was solved employing MATLAB® software.

Table 3.5 - Fitted parameters for the thermodynamic analysis (n.d.: not determined)

Parameter	B_2O_3	TiB_2	ZrB_2	HfB_2
$\mathbf{A_{i,s}}$	3.67877	56.38012	64.21351	65.14057
$\mathbf{B_{i,s}}$	0.28055	0.02586	0.00942	0.01842
$\mathbf{C_{i,s}}$	$-2.65712\cdot10^{-4}$	$-3.3469\cdot10^{-6}$	$1.36824\cdot10^{-9}$	$-9.23555\cdot10^{-9}$
$\mathbf{D_{i,s}}$	$1.05139\cdot10^{-7}$	$-4.80596\cdot10^{-14}$	$-2.18756\cdot10^{-13}$	$2.4396\cdot10^{-12}$
$\mathbf{E_{i,s}}$	$-3.46430\cdot10^{5}$	$-1.74644\cdot10^{6}$	$-1.65824\cdot10^{6}$	$-1.88264\cdot10^{6}$
$\mathbf{A_{i,l}}$	129.704	n.d.	n.d.	n.d.
$\mathbf{B_{i,l}}$, $\mathbf{C_{i,l}}$, $\mathbf{D_{i,l}}$, $\mathbf{E_{i,l}}$	0	n.d.	n.d.	n.d.
$\mathbf{A_{i,g}}$	72.20376	n.d.	n.d.	n.d.
$\mathbf{B_{i,g}}$	0.03472	n.d.	n.d.	n.d.
$\mathbf{C_{i,g}}$	$-1.18376\cdot10^{-5}$	n.d.	n.d.	n.d.
$\mathbf{D_{i,g}}$	$1.34692\cdot10^{-9}$	n.d.	n.d.	n.d.
$\mathbf{E_{i,g}}$	$-1.34685\cdot10^{6}$	n.d.	n.d.	n.d.
$\boldsymbol{\alpha}$	17.40323	n.d.	n.d.	n.d.
$\boldsymbol{\beta}$	$3.80644\cdot10^{4}$	n.d.	n.d.	n.d.
$\boldsymbol{\gamma}$	-146.60608	n.d.	n.d.	n.d.

3.4.2.2 Experimental validation

To properly validate the proposed model, SHS experiments were performed starting from the powders in **Table 2.1**. Differently from what was reported in **Section 2.1.1**, reactant powders were either mixed for 20 min (ball-to-powder weight ratio, BPR=0.2), using plastic vials, and agata balls with a BML-2 roller bank (Witeg, Germany) or ball milled for 1h (BPR=1) by means of a SPEX 8000 (SPEX CertiPrep, USA) device with stainless steel vials and balls. All the other details on the SHS equipment reflect what was reported in **Section 2.1.1**.

The composition of SHS products was determined by X-Ray Powder Diffraction (XRD) analysis using a D8 (Brucker, Germany) diffractometer (Bragg-Brentano geometry) equipped with a copper anode (Cu Kα radiation λ=1.5418 nm) working at 40kV and 40mA. The analysis was performed in the 20°-80° 2θ range, with a step-size of 0.015° and 0.2 seconds for each step.

The high temperatures encountered during SHS should lead to the evaporation of B_2O_3, but its presence in the synthesis product cannot be excluded. It should be noted that boria, B_2O_3 (solubility in water=2.2 g/100g **[182]**) easily reacts with air humidity to form crystalline boric acid, H_3BO_3 (solubility in water=5.04 g/100g **[182]**) according to reaction (10):

$$B_2O_3 + 3H_2O \rightarrow 2H_3BO_3 \quad (10)$$

Thus, to assess the presence of residual byproducts, the reacted powders were analyzed via XRD after being in contact with air for 1 and 28 days after synthesis. As literature suggests **[180]**, given the high solubilities of boria and boric acid in H_2O, their removal was performed by treating the powders with distilled water at room temperature, followed by a filtering step.

3.4.3 Results and Discussion

The B_2O_3 phase diagram, calculated according to Eq. (8), is reported in **Figure 3.35**, **Figure 3.36** shows the effect of Z on the adiabatic temperature of the reacting systems investigated in this work. It can be clearly seen that T_a increases as the fraction of the direct exothermic reaction augments. It is worth mentioning that the predicted adiabatic temperatures for the case of Z =1 (or Z =100%) agree with the literature data **[62,63]**.

The influence of B_2O_3 evaporation on T_a is clearly reported in **Figure 3.36**. Horizontal segments indicate Z ranges where $T_a = T_{b,B_2O_3}$. It can be seen that, as P increases, the effect of B_2O_3 boiling on T_a shifts to higher temperature and Z values. The minimum values of Z (Z_{min}) that fulfill the adiabatic temperature constrain of $T_a \geq$ 1800 K are indicated by the circles in **Figure 3.36** and correspond to 6.78% for TiB_2 (**Figure 3.36a**), 43.73% for ZrB_2 (**Figure 3.36b**), and 50.26% for HfB_2 (**Figure 3.36c**). For each Z_{min} value, the minimum pressure (P_{min}) required to retain B_2O_3 in the liquid state during the process can be also calculated according to Eq. (7). The resulting P_{min} corresponds to the vapor pressure of B_2O_3 at 1800 K (0.0036 bar). The condition P > 0.0036 bar makes the heat generated by the direct reaction completely available to sustain the borothermal reaction, instead of being partially consumed by B_2O_3 boiling. Thus, the thermodynamic analysis provides the minimum Z value requested to guarantee the SHS regime as well as the minimum pressure level needed to maintain B_2O_3 in the liquid state.

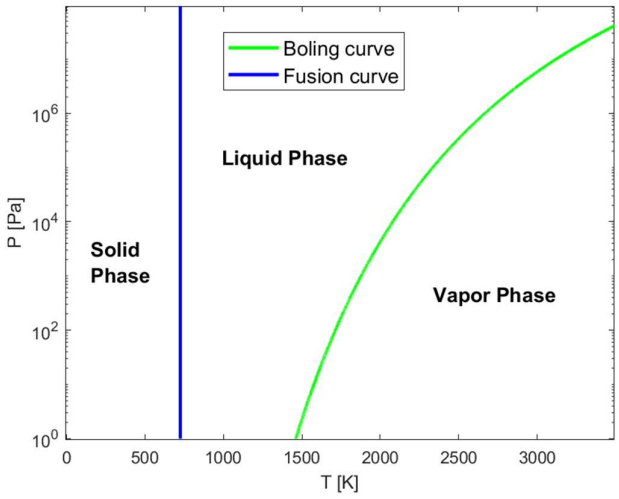

Figure 3.35 – B_2O_3 phase diagram calculated according to Eq. (8).

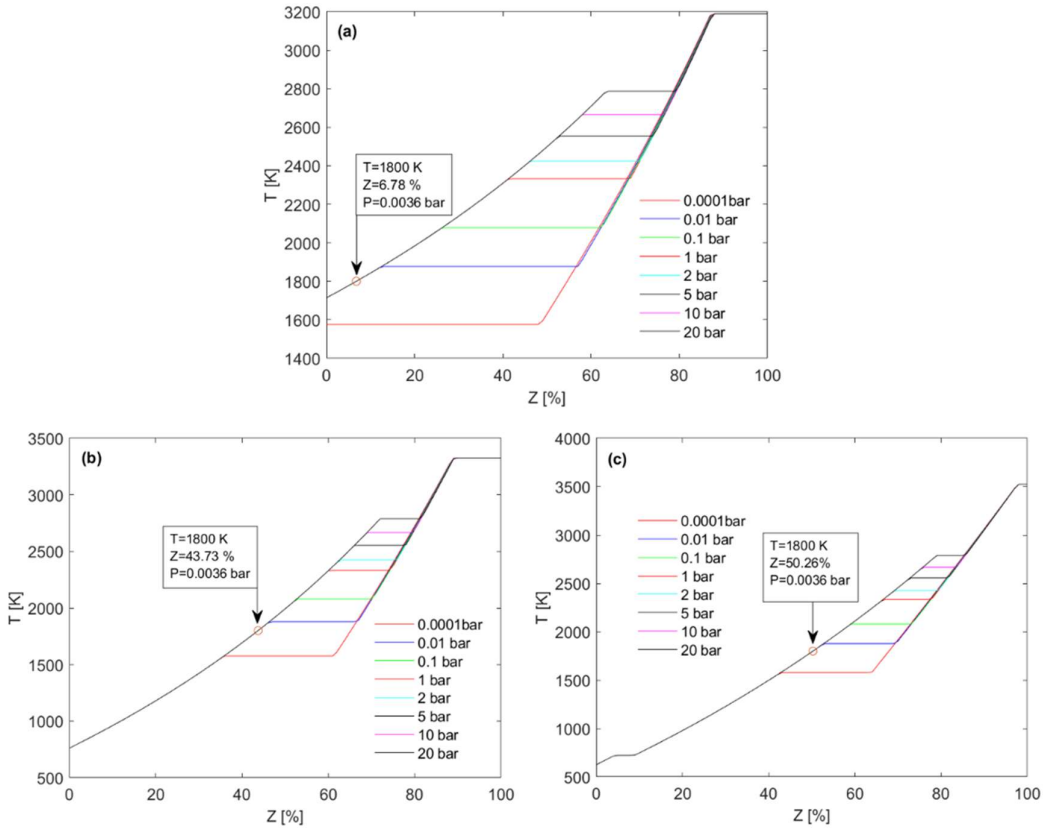

Figure 3.36 – Calculated adiabatic temperatures as a function of Z and pressure for TiB_2 (a), ZrB_2 (b), and HfB_2 (c).

The theoretical predictions were experimentally tested under P = 2 bar. This value allows to minimize oxygen contamination inside the chamber while limiting technical complexity. A dedicated study was performed to verify the self-sustaining character of the process. The results obtained for the case of TiB_2 are reported in **Figure 3.37**, where the measured reaction front propagation velocities are also shown as a function of Z.

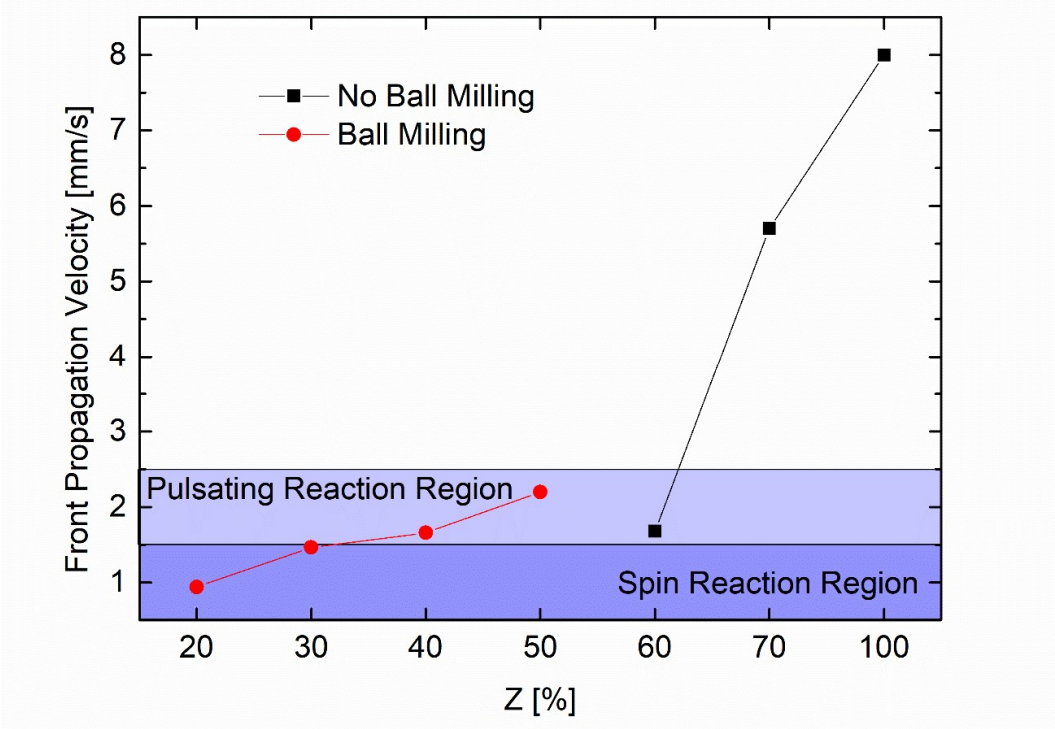

Figure 3.37 – Front propagation velocity measured as a function of Z for the case of TiB_2.

It can be observed that, when no BM treatment was carried out on powder reactants, the front velocity rapidly decreases as Z is progressively reduced. In particular, a pulsating behavior was manifested by the reaction front when Z = 60 %. On the other hand, for lower values of Z, the reaction stops to propagate shortly after ignition. The starting mixture was alternatively preliminarily processed by BM, as described in **Section 3.4.2.2**. In the latter case, the combined synthesis reaction self-propagated for values of Z down to 20%, albeit the related front displayed a pulsating or spinning behavior. The corresponding front propagation velocities were in the ranges 1.5-2.5 and 0.5-1.5 mm/s, respectively. The threshold limit of Z equal to or below which the reaction did not self-

propagate was found to be 10%. The extended SHS regime can be likely ascribed to the improved interfaces formation among the starting reactants provided by the BM treatment. The latter one also facilitates the removal of the superficial oxide impurities that typically cover metallic powders. Both these aspects then reduce kinetic limitations apparently present in the synthesis process.

ZrB_2 and HfB_2 systems show a similar qualitative behavior to that displayed by TiB_2. In particular, with no BM, the reaction was capable to self-propagate down to Z = 70%. In contrast, after the preliminary milling treatment, the SHS character was guaranteed down to Z = 60%. The synthesis reaction did not self-sustain for Z values equal or lower than 50 %, regardless of the BM step. In the latter regard, it should be noted that the theoretical predictions foresee values of $\mathrm{Z_{min}}$ of 10-15% lower than those observed experimentally. Such discrepancies could be likely associated to some remaining kinetic limitations, most of which are reduced by the BM treatment.

After being pulverized, SHS samples were characterized by XRD, and the obtained results are reported in **Figure 3.38**. Specifically, **Figure 3.38a** shows that with the process integration of the DR and BR synthesis routes, the desired TiB_2 phase can be produced either after simply mixing initial precursors (Z = 60 %) or taking advantage of a BM treatment (Z = 20%-BM). Only slight amounts of oxide impurities (associated to TiO and Ti_2O_3) were detected by XRD, along with the main diboride phase, using the combined DR-BR route, Likewise, **Figures 3.38b** and **3.38c** show that the integrated process is able to produce the desired ZrB_2 and HfB_2 phases with minor impurities. As far as B_2O_3 is concerned, whose presence is expected in the synthesized powders as byproduct according to reaction (1), no boiling likely occurs during SHS under the investigated conditions. The fact that boria was not detected by XRD analyses is explained by its amorphous nature. However, the presence of such an impurity can be evidenced leaving the synthesized powders for 28 days in air, since boria is converted into crystalline boric acid (H_3BO_3), as demonstrated by **Figure 3.39a**. However, 28 days after a leaching step with distilled water, no trace of H_3BO_3 was found (**Figure 3.39b**).

On the basis of these results, the process integration of the borothermal and direct synthesis reactions for the obtainment of transition metals diborides succeeded in the obtainment of the desired materials, with considerable expected savings. To this aim, a thermodynamic analysis was first performed to predict the optimal conditions for maximising the use of cheaper metal oxides as initial precursors, while guaranteeing a self-sustaining behaviour of the synthesis reaction. With this approach, the heat generated in excess by the strongly exothermic direct reaction can be exploited

to sustain the endothermic/low exothermic borothermal one, thus reducing the costs associated to metal reactants and energy consumption.

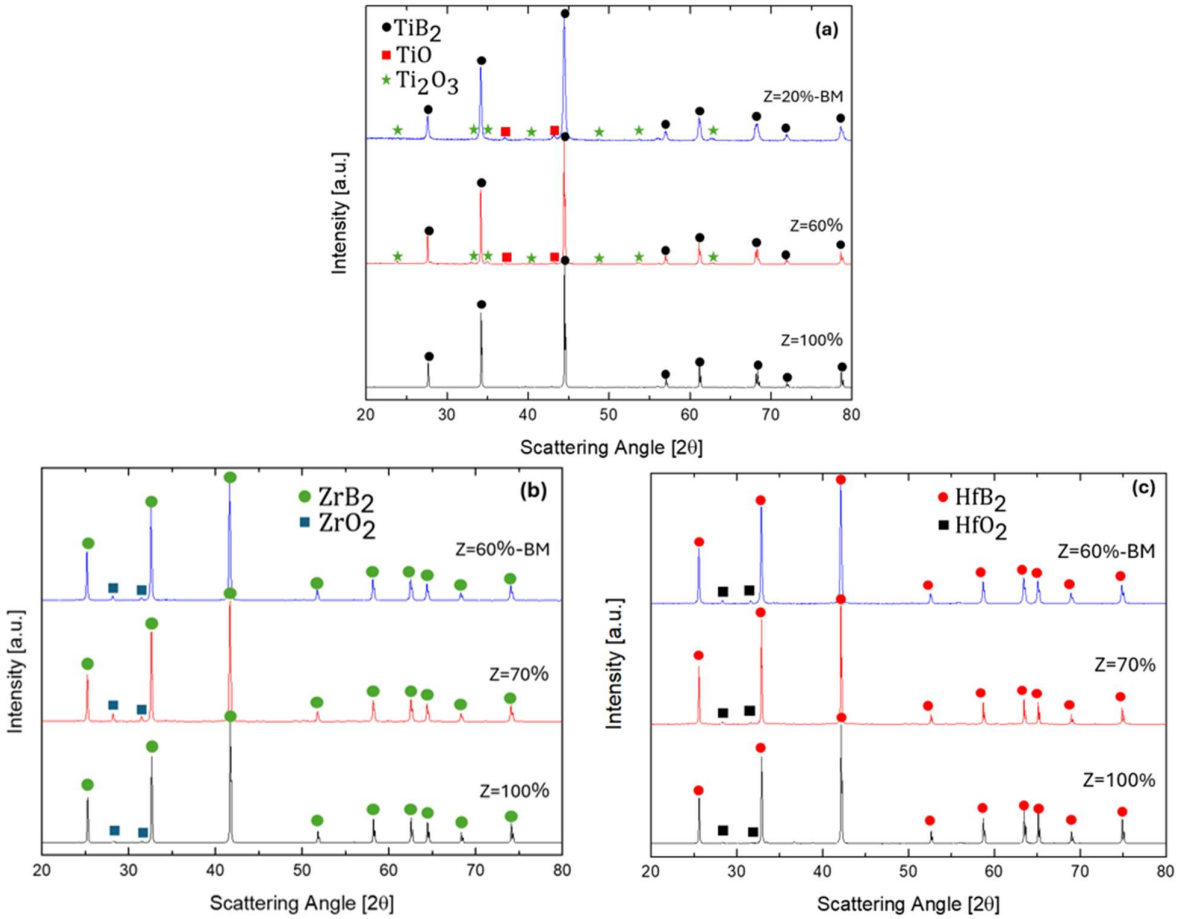

Figure 3.38 - XRD patterns of TiB_2 (a), ZrB_2 (b), HfB_2 (c) systems for the complete direct synthesis, and the last combination for which the reaction self-propagated with and without prior BM.

The obtained powders mainly consist of desired diboride phases, alongside with B_2O_3 byproduct, whose presence was removed by leaching it with distilled water. In the future, additional efforts can be made to further reduce the impurities detected after the integrated SHS process considered in this work. Finally, the considerable economic advantages achievable with this approach could be extended also to multicomponent borides, thus contributing to expand the applications field of such performant Ultra-High Temperature Ceramics.

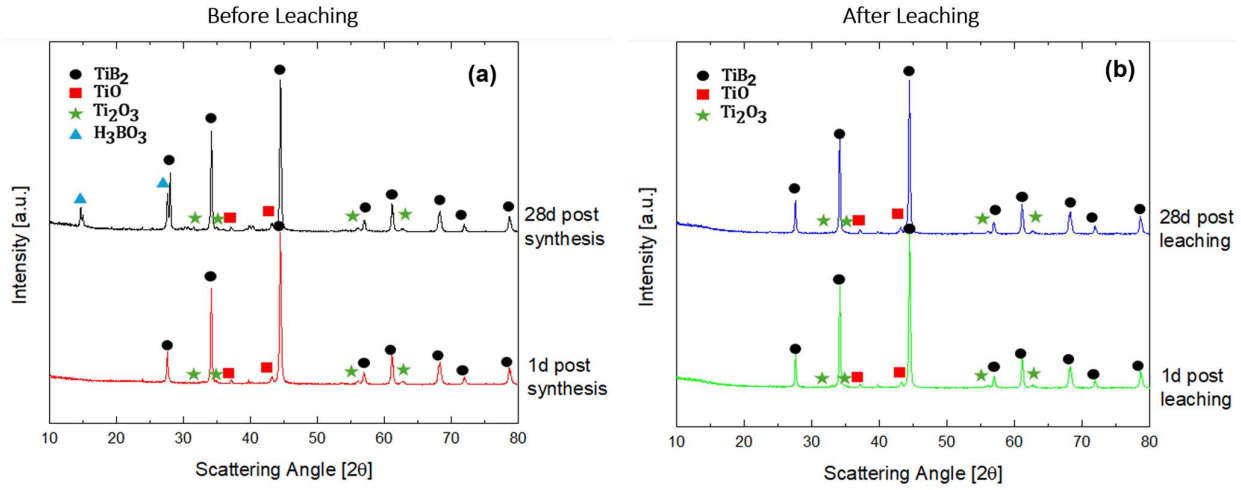

Figure 3.39 - XRD patterns of TiB_2 obtained by SHS analyzed 1 day and 28 days after synthesis (a), and 1 day and 28 days after the leaching process (b).

3.4.4 Notation

A – heat capacity coefficient, J/(mol K)

B – heat capacity coefficient, J/(mol K^2)

C – heat capacity coefficient, J/(mol K^3)

C_P – heat capacity at constant pressure, J/(mol K)

D – heat capacity coefficient, J/(mol K^4)

E – heat capacity coefficient, (J K)/mol

g – molar Gibbs free energy, J/mol

q – molar adsorbed heat, J/mol

P – pressure, bar

T – temperature, K

Z – molar fraction, -

Greek letters:

α – Antoine law parameter, ln(bar)

β – Antoine law parameter, K ln(bar)

γ – Antoine law parameter, K

Subscripts:

0 – standard reference state

a – adiabatic

b – B_2O_3 boiling

B_2O_3 – referred to boria

g – gas state

i – referred to a generic product

j – referred to a generic phase

l – liquid state

m – melting

MeB_2 – referred to the transition metal diboride

MeO_2 – referred to the transition metal oxide

s – solid state

min – minimum value

max – maximum value

Δh_f - molar formation enthalpy, J/mol

$\Delta h_{l \to g}$ – liquid to gas molar latent heat, J/mol

Δh_r – molar reaction enthalpy, J/mol

$\Delta h_{s \to l}$ - solid to liquid molar latent heat, J/mol

υ – stoichiometric coefficient, -

The activity and related results presented in this Section have been reported in **Casu, M.**, Locci, A. M., Traversari, G., Cao, G., & Orrù, R. (2025). Process Integration Approach for the Efficient Synthesis of Metal Boride Ceramics. *Chemical Engineering Transactions*, *115*, 997–1002. https://doi.org/10.3303/CET25117167.

3.5 Constitutive modeling of Spark Plasma Sintering applied to transition metal diborides

3.5.1 Introduction

The optimization of the SPS process conditions for the consolidation of individual and multicomponent TMBs was explored from the experimental point of view in **Sections 3.1-3.3**. A modeling study aimed at describing the densification mechanism of these materials under pressure-assisted conditions will be then considered in this one. In this regard, several attempts have been developed in literature to describe the kinetics of pressure-assisted sintering. Pioneering continuum-scale models, notably those by **Olevsky and co-workers [183,184]**, treat SPS as a thermomechanical process, incorporating aspects of temperature distribution, pressure, and macroscopic densification. Based on this approach, further refinements have been proposed to improve the mathematical description of the densification process occurring during SPS **[185-188]**. While these valuable models have contributed significantly to the simulation of SPS for oxide and metallic systems, they generally do not address the densification behavior of TMBs, nor account for the microstructural mechanisms unique to such ceramics, especially early-stage particle rearrangement underload, which plays a critical role in densification kinetics but is often neglected.

Additionally, most models of pressure-assisted techniques adopt a power-law creep description, or the densification rate is related to applied stress and temperature through semi-empirical or phenomenological expressions **[189,190]**. Although this approach can describe the main features of viscous deformation for some materials, it lacks the flexibility to represent transitions between distinct consolidation mechanisms and imposes assumptions regarding the rheological behavior that may not hold true across materials or processing windows. Moreover, few studies explicitly incorporate particle rearrangement as a separate mechanism, an omission that becomes critical for high-hardness materials like TMBs, where this phenomenon precedes or takes place simultaneously with the viscous deformation.

In this Section, a generalized rheological model that describes the dual-mechanism nature of SPS densification in TMBs is proposed. The model conceptualizes the consolidation process as the serial coupling of two rate-controlling elements: a slider representing the rate-independent particle rearrangement at lower temperatures, and a slider and dashpot in parallel ensemble that describes

the nonlinear viscous flow at elevated temperatures. This framework allows the model to naturally simulate the transition between the two mechanisms as a function of temperature, porosity, and strain rate. Therefore, unlike traditional creep-based models, the proposed approach avoids *a priori* assumption about the densifying powder behavior. The strain-rate sensitivity is indeed an output of the fitting process, thus enabling the model to flexibly represent both linear (Newtonian) and nonlinear (shear-thinning) regimes depending on the intrinsic properties of the material and the applied conditions. Furthermore, the proposed model is shown to be thermodynamically consistent. Indeed, the stress–strain rate relationship of the viscous component is derived from a dissipation potential, and it is demonstrated that the adopted yield function of the sliders can be rigorously derived from the dual viscoplastic potential. In this way, the present work provides a thermodynamically consistent framework capable of unifying different densification mechanisms within a single formulation, thus offering a novel tool for reliably simulating the pressure-assisted consolidation of transition metal diborides.

Rheological parameters, including viscosities, pre-exponential factors, activation energies, and strain-rate sensitivities, are obtained through least-squares fitting of porosity–time curves from SPS experiments on HfB_2, NbB_2, and TiB_2, already investigated in **Section 3.3**, referring to samples prepared in absence of additives. These ceramics, in addition to being among the individual metal diborides mostly investigated from the experimental viewpoint, are also frequently involved as constituents of high-entropy borides, which have recently attracted significant interest. It is also shown that accounting for early-stage particle rearrangement is essential for correctly identifying viscosity parameters; neglecting this mechanism systematically leads to underestimated values of, for instance, activation energies. Model results are validated against density data from the literature and used to identify the influence of operating conditions for achieving full densification in each material. This work introduces a physically grounded, generalizable modeling framework for pressure-assisted sintering of ultra-high-temperature ceramics with direct implications for designing advanced aerospace components based on TMBs.

3.5.2 Mathematical model

Spark plasma sintering of transition metal diborides is modelled in this work by assuming that powder compaction is given by the superimposition of two different phenomena: 1) particle

rearrangement of an ensemble of rigid (non-deformable) particles and 2) deformation of a porous continuous matrix (**Figure 3.40**). Both phenomena are caused by the application of the uniaxial load and are supposed to depend upon temperature, porosity, and strain rate levels. From a rheological perspective, particle rearrangement can be represented as an instantaneous plastic deformation of the Body (1) provided that the effective applied stress exceeds the yield strength $\sigma_{Y,1}$ that characterizes this particle ensemble. Creep (viscous sintering) is instead considered responsible for the time-dependent deformation of the continuous Body (2) whose rate depends on its apparent viscosity μ. This quantity is taken temperature, porosity, and shear rate dependent. As for the case of Body (2), it is assumed that viscous consolidation occurs if the effective applied stress is higher than the corresponding yield strength $\sigma_{Y,2}$.

It is worth noting that the present model assumes ideal boride powders, free from oxides, secondary phases, or other surface impurities that are commonly present in real ones. Moreover, other properties of the starting powder (for instance particle size and aspect ratio), which are also expected to affect its densification behavior, are not considered in this work. This simplification is adopted to isolate and characterize the intrinsic densification behavior of the boride phase. While such impurities can influence surface diffusion, particle rearrangement, and effective viscosity, their effects are beyond the scope of the current study and will be considered in future extensions of the model. Moreover, since the present work is focused on the rheological behavior of the powder, temperature was treated as an input rather than a coupled variable and it is assumed to be uniform within the sample, along with a negligible effect of the contact resistances. These features, which are known to play an important role in the SPS technology, have been already addressed in a previous work **[191]**.

The model description can be translated to the rheological schematization shown in **Figure 3.40b-c**, where two elements in series are involved. Element 1 is given by a slider that represents the powder compaction as an effect of the re-packing of rigid particles and their mutual friction and wear. Element 2 is given by a dashpot and a slider in parallel and describes the viscoplastic densification of the porous Body (2) whose rheological equivalent is a Bingham fluid. This representation has also been named as *supple body* **[192]**.

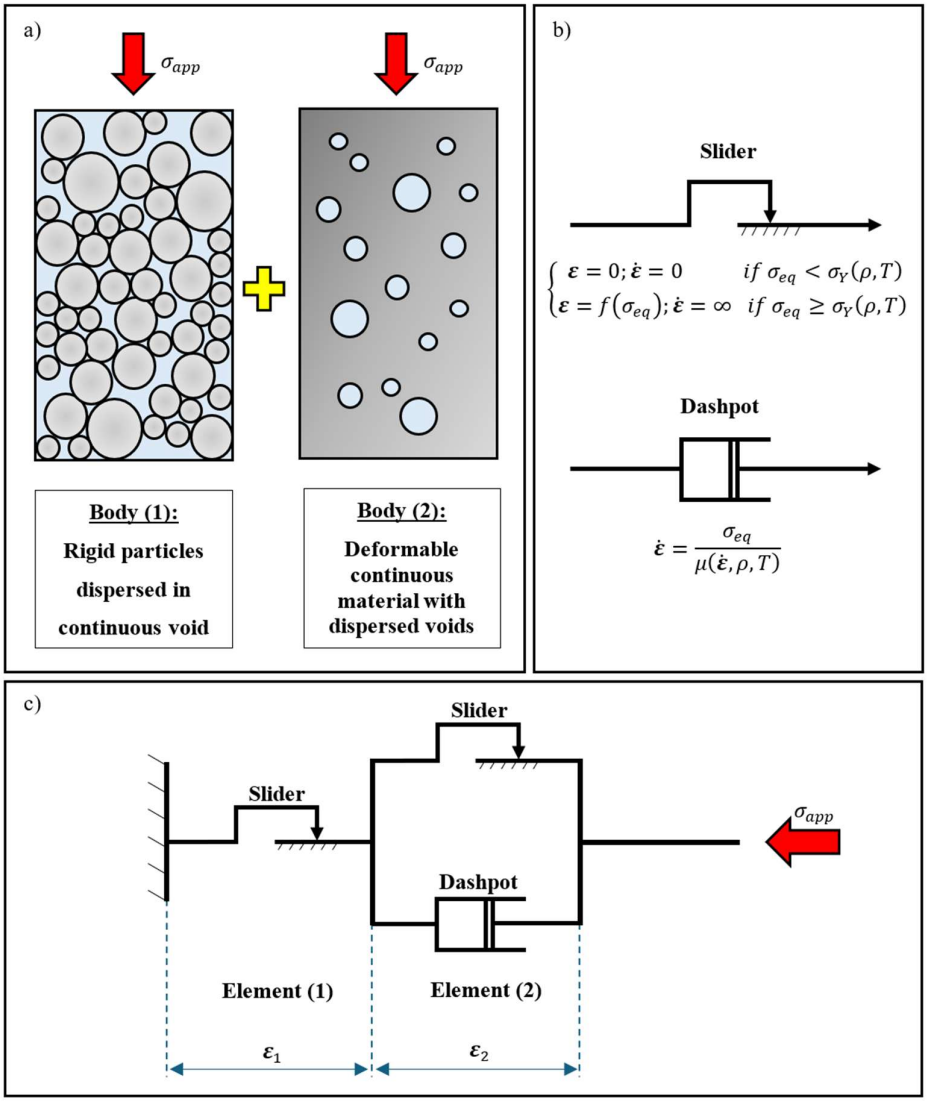

Figure 3.40 - Schematic representation of the two-stage viscoplastic model of densification. a) Conceptual decomposition of the powder compact into two idealized bodies: Body (1) represents the initial stage with rigid particles dispersed in a continuous void network, while Body (2) models the subsequent deformable porous medium consisting of a continuous solid matrix with voids. b) Rheological elements governing densification: the slider simulates particle rearrangement via a stress-dependent ideal plastic threshold (activated when the equivalent stress σ_{eq} exceeds the yield strength σ_Y), while the dashpot describes viscous deformation, governed by an apparent viscosity $\mu(\dot{\varepsilon}, \rho, T)$ dependent on strain rate, porosity, and temperature. c) Mechanical analog of the full model: Element (1) accounts for particle rearrangement while Element (2) reproduces the densification of the continuous porous matrix through viscous flow. The two elements act in series and are subjected to the same applied uniaxial stress σ_{app}.

According to the description reported above, $\boldsymbol{\varepsilon}_1^P$ is the plastic (rate independent) strain of Element 1 and $\boldsymbol{\varepsilon}_2^{VP}$ represents the viscoplastic strain (rate dependent) of Element 2. The total strain of the sample is thus defined as follows:

$$\boldsymbol{\varepsilon} = \boldsymbol{\varepsilon}_1^P + \boldsymbol{\varepsilon}_2^{VP} \tag{10}$$

Where:

$$\boldsymbol{\varepsilon}_1^P = \begin{cases} 0 \; if \; \sigma_{eq} < \sigma_{Y,1} \\ \neq 0 \; if \; \sigma_{eq} \geq \sigma_{Y,1} \end{cases} \tag{11a}$$

$$\boldsymbol{\varepsilon}_2^{VP} = \begin{cases} 0 \; if \; \sigma_{eq} < \sigma_{Y,2} \\ \neq 0 \; if \; \sigma_{eq} \geq \sigma_{Y,2} \end{cases} \tag{11b}$$

The total strain tensor $\boldsymbol{\varepsilon}$ determines the sample consolidation whose dynamics can be described in terms of the relative density field $\rho(\vec{x}, t)$, that is given by the total mass balance (continuity) equation:

$$\frac{\partial \rho}{\partial t} + \nabla \cdot (\rho \vec{v}) = 0 \tag{12}$$

The velocity field $\vec{v}(\vec{x}, t)$ appearing in Eq. (12) can be obtained by solving the linear momentum balance equation:

$$\frac{\partial}{\partial t}(\rho \vec{v}) + \nabla \cdot \mathbf{T} - \rho \vec{g} = 0 \tag{13}$$

Tensor $\mathbf{T}$ can be interpreted as the linear momentum flux and it can be split into two parts:

$$\mathbf{T} = \rho \vec{v} \vec{v} + \boldsymbol{\sigma} \tag{14}$$

The first term on the r.h.s. of Eq. (14) represents the convective part of the flux. Second term is the Cauchy stress tensor, which completely described the state of stress of the compacting sample. Expression of the latter tensor depends upon the mechanical properties of the materials the system

is composed of. Neglecting inertial and gravitational effects, the momentum balance equation (13) assumes the well-known pseudo-stationary form:

$$\nabla \cdot \boldsymbol{\sigma} = 0 \tag{15}$$

By considering a disk-shaped sample pressed in a cylindrical die, Eqs. (12) and (15) can be written down in cylindrical coordinates:

$$\frac{\partial \rho}{\partial t} + \frac{1}{r}\frac{\partial}{\partial r}(\rho r v_r) + \frac{1}{r}\frac{\partial}{\partial \vartheta}(\rho v_\vartheta) + \frac{\partial}{\partial z}(\rho v_z) = 0 \tag{16}$$

$$\frac{1}{r}\frac{\partial}{\partial r}(r\sigma_{rr}) + \frac{1}{r}\frac{\partial \sigma_{r\vartheta}}{\partial \vartheta} + \frac{\partial \sigma_{rz}}{\partial z} - \frac{\sigma_{\vartheta\vartheta}}{r} = 0 \tag{17a}$$

$$\frac{1}{r^2}\frac{\partial}{\partial r}(r^2\sigma_{r\vartheta}) + \frac{1}{r}\frac{\partial \sigma_{\vartheta\vartheta}}{\partial \vartheta} + \frac{\partial \sigma_{\vartheta z}}{\partial z} = 0 \tag{17b}$$

$$\frac{1}{r}\frac{\partial}{\partial r}(r\sigma_{rz}) + \frac{1}{r}\frac{\partial \sigma_{\vartheta z}}{\partial \vartheta} + \frac{\partial \sigma_{zz}}{\partial z} = 0 \tag{17c}$$

By taking advantage of the usual axial symmetry assumption and neglecting friction between the consolidating powders and the (rigid) die internal wall (leading to negligible shear stresses), Eqs. (16) and (17) simplify as follows:

$$\frac{\partial \rho}{\partial t} + \frac{\partial}{\partial z}(\rho v_z) = 0 \tag{18}$$

$$\frac{1}{r}\frac{\partial}{\partial r}(r\sigma_{rr}) - \frac{\sigma_{\vartheta\vartheta}}{r} = 0 \tag{19a}$$

$$\frac{\partial \sigma_{zz}}{\partial z} = 0 \tag{19b}$$

By assuming a spatially uniform distribution of the density and neglecting radial gradients, the following system governing equations holds:

$$\frac{\partial \rho}{\partial t} + \rho\frac{\partial v_z}{\partial z} = 0 \tag{20}$$

$$\sigma_{rr} = \sigma_{\vartheta\vartheta} \tag{21a}$$

$$\frac{\partial \sigma_{zz}}{\partial z} = 0 \tag{21b}$$

The connection between the strain tensor and the velocity field is given by the strain rate tensor defined as follows:

$$\dot{\boldsymbol{\varepsilon}} = \frac{d\boldsymbol{\varepsilon}}{dt} = \frac{1}{2}(\nabla\vec{v} + \nabla\vec{v}^{T}) \tag{22}$$

Under the simplifying conditions mentioned above, Eq. (22) reduces to

$$\dot{\varepsilon}_{zz} = \frac{d\varepsilon_{zz}}{dt} = \frac{\partial v_z}{\partial z} \tag{23}$$

and, after substituting Eq. (13) into Eq. (20) and expressing Eq. (10) in terms of strain rate, the following governing equation of the sample density is obtained:

$$\frac{d\rho}{dt} = -\rho\left(\frac{d\varepsilon^{P}_{zz,1}}{dt} + \frac{d\varepsilon^{VP}_{zz,2}}{dt}\right) \tag{24}$$

Eq. (24) restates that the sample density evolution is given by the sum of the plastic deformation of Element 1 and the viscoplastic consolidation of Element 2. Note that the partial derivative has been replaced by the ordinary one since density is assumed spatially uniform (only time dependent). In what follows the constitutive relations for bodies (1) and (2) are described.

The reader is referred to the **Section 3.5.4** for the definition of all mathematical symbols used in the text and in **Appendix C**, where a detailed mathematical description of the model can be found.

The proposed mathematical model involves eight parameters to be determined. To reduce the number of adjustable ones and the risk of overfitting, a three-steps strategy was applied, leveraging physical insights (**Figure C1**), as well as taking advantage of the available experimental data and adopted operating conditions. First step involves the calculation of $\sigma^{0}_{Y,1}$ and A_T by analyzing specific points of the experimental porosity time-profile. Only the first part of the latter is then used to fit the parameters $\sigma^{\infty}_{Y,1}$ and B_T, thus completing the determination of the slider parameter set. Finally, the remaining four parameters (i.e., those ones related to the dashpot) are fitted by using the entire porosity time-profile. Each step is described in detail in what follows.

At the end of the powder pre-compaction step, the sample is still at room temperature, and its porosity θ^{0} depends solely on the externally applied load. Under these low-temperature conditions,

particle rearrangement is the only active consolidation mechanism. As such, the material behaves as a perfectly plastic solid, and the equivalent stress within the compact must equal its yield strength: $\sigma_{eq}(\theta = \theta^0) = \sigma_{Y,1}(T = T^0)$, or stated differently and limited to the used experimental data, $\sigma_{eq}^0 \approx \sigma_{Y,1}^0$. Given that σ_{eq}^0 can be analytically calculated from the initial porosity, using the relations reported in **Appendix C** and **Table C1**, the value of $\sigma_{Y,1}^0$ is obtained. **Table 3.6** reports the corresponding values used for each material in this initial calibration step. This procedure allows to indirectly estimate one of the yield parameters, thus reducing the number of parameters to be determined to seven.

Table 3.6 - Initial values of some model variables.

Variable	$\mathbf{HfB_2}$	$\mathbf{NbB_2}$	$\mathbf{TiB_2}$
$\theta^0[-]$	0.42574	0.43722	0.42001
$\sigma_{eq}^0[\mathrm{MPa}]$	39.648	41.507	38.755

Additional reduction on the latter comes from the analysis of the experimental porosity time evolution (shown in the next section). Since, under the adopted experimental conditions, during the first period of consolidation, particle rearrangement is directly linked to the evolution of $\sigma_{Y,1}$, the first inflection point in the porosity curve is assumed to correspond to the inflection point in the $\sigma_{Y,1} - T$ curve (**Figure C1**). Given the known heating profile and the experimentally determined time instant corresponding to the porosity profile inflection point, the parameter A_T can be estimated prior to the fitting process, thus further reducing the number of unknown parameters to six.

Moreover, since it is assumed that during the early stage of consolidation particle rearrangement is the only mechanism active for all the investigated materials (NbB_2, HfB_2, TiB_2), the corresponding data segment was used to fit the remaining two yield strength parameters, $\sigma_{Y,1}^{\infty}$ and B_T. The remaining model parameters, including viscosity-related ones, were estimated by fitting the full porosity-time profile over the entire sintering cycle. A summary of all calculated and fitted model parameters is provided in **Table 3.7**, where they are explicitly labeled as either *calculated* (calc.) or *adjusted* (adj.) for clarity.

Table 3.7 - Summary of model parameters.

Material		$\mathbf{HfB_2}$		$\mathbf{NbB_2}$		$\mathbf{TiB_2}$	
Parameter	**Type**	**Without Slider**	**Complete**	**Without Slider**	**Complete**	**Without Slider**	**Complete**
$A_T[\mathrm{K}]$	Calc.	-	1074.6	-	1020.0	-	1045.7
$\sigma_{Y,1}^{\infty}[\mathrm{MPa}]$	Adj.	-	34.855	-	36.508	-	33.354
$B_T[\mathrm{K}]$	Adj.	-	62.607	-	33.487	-	35.786
$\sigma_{Y,1}^{0}[\mathrm{MPa}]$	Calc.	-	39.648	-	41.507	-	38.755
$a^0\ [\mathrm{Pa}\cdot\mathrm{s}]$	Adj.	$1.1812\ 10^5$	$1.1456\ 10^5$	$6.6416\ 10^6$	$3.5161\ 10^6$	$5.6744\ 10^4$	$4.1093\ 10^4$
$Q_\eta\left[\frac{\mathrm{kJ}}{\mathrm{mol}}\right]$	Adj.	272.87	287.44	188.75	224.50	442.75	669.83
$\lambda^0\left[\frac{\mathrm{s}}{\mathrm{K}^{\left(\frac{\mathrm{m}}{\mathrm{m}-1}\right)}}\right]$	Adj.	0.09534	0.11897	14.295	12.425	0.26040	0.27156
$m\ [-]$	Adj.	0.11469	0.12284	0.18970	0.19759	0.10817	0.07976
R^2		0.99890	0.99993	0.99841	0.99985	0.99710	0.99946

Finally, preliminary simulations revealed that, under the experimental conditions investigated in this study, the equivalent stress remains above the possible yield strength $\sigma_{Y,2}$ of the porous continuous matrix (Body (2)) throughout the densification cycle. As a result, the slider of Element 2 in the rheological model (**Figure C1**) remains inactive, and densification due to viscous deformation is never hindered. Therefore, since the exact values of $\sigma_{Y,2}$ are not needed in the simulated scenarios, $\sigma_{Y,2}$ was set to zero in the numerical implementation to reduce the number of fitting parameters. Nevertheless, the general formulation of the model, which includes both the slider and the dashpot in parallel for Element 2, has been retained to make it applicable to other systems or operating conditions where the yield strength of the porous continuous matrix may play a more prominent role.

3.5.3 Results and Discussion

3.5.3.1 Model fitting and mechanistic insights into densification behavior

Figures 3.41a–3.41c present the experimental and modeled porosity–time curves related to the spark plasma sintering of SHS-synthetized HfB_2, NbB_2, and TiB_2 powders, respectively, all processed under identical conditions (as reported in **Section 3.3**): an applied pressure, σ_{app}, of 20 MPa, a heating time, t_H, from room to the desired temperature, of 10 min, a dwell temperature, T_D, of 1950 °C, and a dwell time, t_D, of 20 min, no sintering additive. Across all three materials, the porosity–time curve exhibits a characteristic multi-stage behavior. In the early part of the heating stage (up to ~300 s), a gradual decrease in porosity is observed despite the relatively low temperature. According to the proposed approach, this initial densification is attributed to particle rearrangement driven by the applied uniaxial pressure, a mechanism well modelled by the plastic slider component of the rheological model (**Figure 3.40**).

Following this initial rearrangement stage, a plateau appears in the curve of porosity, indicating a temporary halt in sample densification. This corresponds to an intermediate temperature range where neither particle rearrangement nor significant viscous flow is active. As the temperature continues to rise and exceeds a threshold at 300-400 s, viscous deformation starts to occur and becomes progressively dominant. This transition marks the onset of the dashpot-controlled regime. As the temperature increases further, viscous deformation results in a faster porosity decrease until the densification process smoothly enters into the dwell stage where the temperature is held constant.

Despite these shared characteristics, material-specific differences emerge in the shape and slope of the densification curves. HfB_2 (**Figure 3.41a**) and NbB_2 (**Figure 3.41b**) exhibit similar porosity evolution, with comparable timing and consolidation degree in both the rearrangement and viscous regimes. In contrast, TiB_2 (**Figure 3.41c**) shows a steeper and more abrupt transition from the rearrangement stage to the viscous regime. The dwell phase begins at a lower porosity, and the overall densification is more pronounced than in the case of other materials.

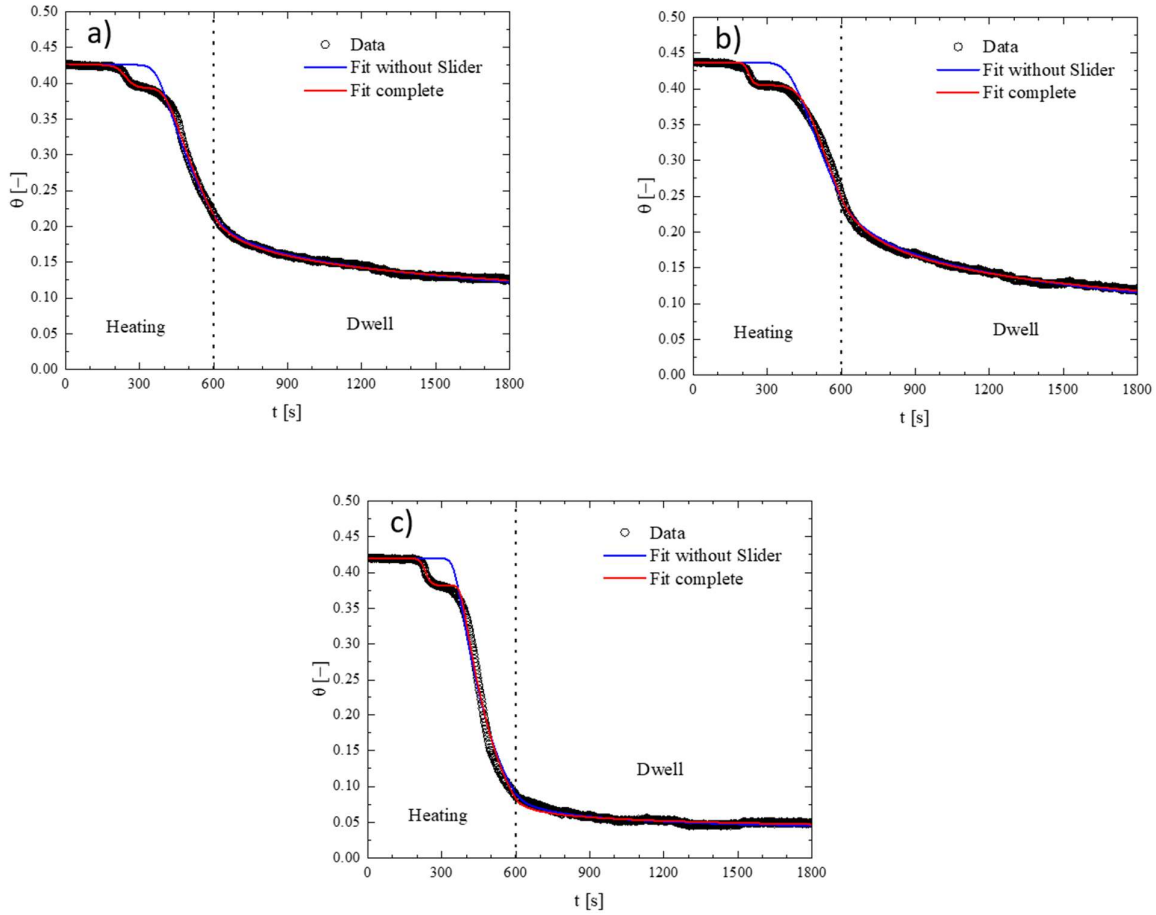

Figure 3.41 - Comparison between experimental and simulated porosity time profiles for a) HfB_2, b) NbB_2, and c) TiB_2 samples during SPS. Experimental data (black open circles) are fitted using two different modelling approaches: a complete model that includes both the slider and dashpot elements (red line), and a reduced model without the slider contribution (blue line). The temperature cycle consists of a heating stage up to 1950 °C in 10 minutes followed by a 20-minute isothermal dwell. The vertical dashed line indicates the transition between the non-isothermal heating and isothermal dwelling stages. The improved agreement achieved by the complete model highlights the importance of accounting for particle rearrangement to accurately simulate the densification behaviour during the initial stages of sintering.

Experimental data are compared in **Figure 3.41** with two model predictions: the complete rheological model (red line), which includes both particle rearrangement and viscous flow, and a reduced model (blue line) that considers only viscous deformation. The complete model accurately simulates both the early-stage rearrangement and the later viscous driven consolidation, closely matching the entire experimental curve. In contrast, the reduced model underestimates densification during the non-isothermal heating and fails to capture the initial drop in porosity. This demonstrates the necessity of including a distinct particle rearrangement mechanism to correctly describe the full sintering behavior of the investigated borides.

The comparison shown in **Figure 3.41** highlights the proposed model ability to accurately reproduce the experimental porosity evolution for all three TMBs under the selected SPS conditions. The improvement provided by the introduction of the slider element, particularly during the non-isothermal heating stage, underscores the need to account for a yield stress threshold governing particle rearrangement. To better understand the basis of this agreement, it is essential to examine the values of the material parameters used in the simulations.

Table 3.7 reports the full set of model parameters used to simulate the densification behavior of HfB_2, NbB_2, and TiB_2, for both the complete rheological model (with both slider and dashpot) and the simplified one (dashpot only). The high regression coefficients (R^2 > 0.999) for the complete model in all cases confirm the excellent agreement between simulations and experimental data. For all three diborides, the complete model includes a temperature-dependent yield strength σ_Y defined by four parameters: A_T, transition temperature (≈ 1020–1075 K); B_T transition width (≈ 33–63 K); σ_Y^0, low-temperature asymptotic yield stress (≈ 39–42 MPa); σ_Y^∞, high-temperature asymptotic yield stress (≈ 33–36 MPa).

As shown in **Figure C1**, this sigmoidal behavior controls the activation and deactivation of the particle rearrangement mechanism. It is worth pointing out that the yield strength values reported in **Table 3.7** should not be interpreted as an intrinsic mechanical property of the fully dense materials. Rather, they are indicators of the effective resistance to particle rearrangement within the porous compact during the early stages of sintering. As already mentioned, particle rearrangement is assumed to occur between rigid, undeformable particles, and the slider captures the onset of sliding or micro-slipping between them.

The temperature dependence of the yield strength does not intrinsically reflect bulk material softening but how a temperature increase facilitates abrasion, wearing, interparticle bonding disruption, oxide layer breaking and weakening, and, in general, all those phenomena which make rearrangement easier. This explains why the slider parameter values are similar across all three materials. In fact, they are governed primarily by powder characteristics, such as particle size distribution, surface condition, or packing heterogeneity, rather than intrinsic differences in the crystalline boride phases. Consequently, these parameters are best viewed as compact-level properties, instead of material constants. In this regard, it is worth mentioning that the boride powders were all produced according to the same technique and processed under identical conditions before undergoing SPS.

The viscous component of the model is characterized by the pre-exponential viscosity factor a^0, the activation energy for viscous flow Q_η, the coefficient λ^0 and the strain rate sensitivity m. **Table 3.7** shows that activation energies vary significantly between materials: TiB_2 shows the highest value (≈ 670 kJ/mol), suggesting its greater thermal resistance to flow, while NbB_2 has the lowest one (≈ 225 kJ/mol). Analysis of the coefficient m reinforces earlier observations: TiB_2 has the lowest value (≈ 0.08), indicating pronounced nonlinearity and plastic-like flow under stress, while HfB_2 and NbB_2 exhibit higher m values (≈ 0.12–0.20), reflecting a more viscous-dominated response.

Importantly, the comparison between models (with vs. without slider) shows that omitting particle rearrangement leads to significantly different values for key parameters, particularly for a^0 and Q_η in the case of NbB_2 and TiB_2 (**Table 3.7**). These discrepancies demonstrate how neglecting early-stage plasticity causes the model to compensate by inflating viscosity-related parameters, resulting in distorted material characterization. Moreover, the complete model yields slightly better fits in all cases, with R^2 values higher than its simplified version.

The simulated evolution of mechanical stresses during SPS of hafnium diboride, niobium diboride, and titanium diboride is shown in **Figures 3.42a–3.42c**, respectively. All simulations were performed under the same SPS conditions mentioned above. The plots display the time evolution of the equivalent stress σ_{eq} (red), the yield strength $\sigma_{Y,1}$ associated with particle rearrangement (blue), the applied axial stress σ_{app} (magenta), and the radial and hoop stresses p generated by the lateral constraint (green). For all three materials, simulations confirm the sequence of the consolidating mechanisms already identified in **Figure 3.41**. It is apparent that an initial plastic regime, where

$\sigma_{eq} = \sigma_{Y,1}$, indicating that particle rearrangement is active, is followed by a transition phase during which σ_{eq} drops below $\sigma_{Y,1}$. This marks the cessation of plastic yielding, and the beginning of a viscous-dominated regime.

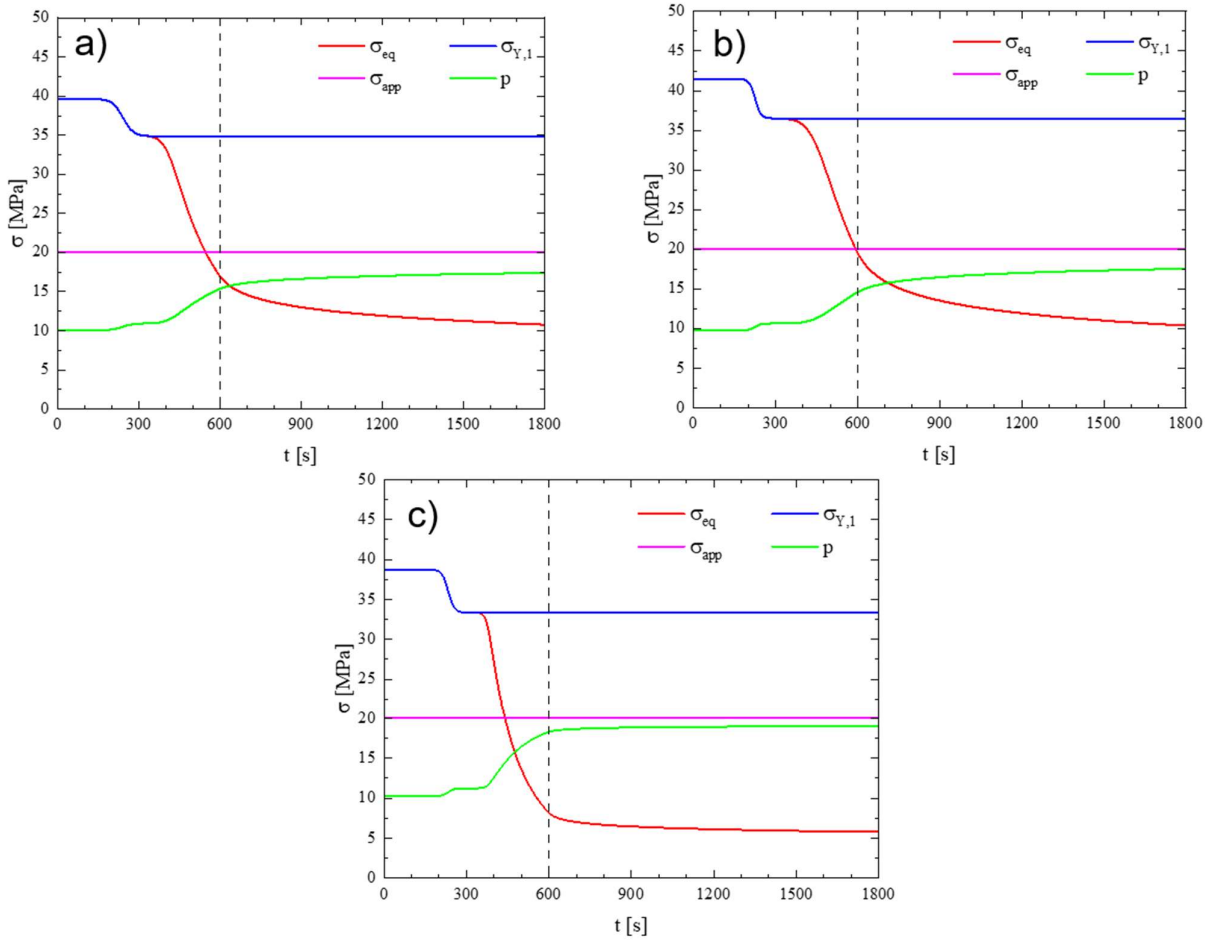

Figure 3.42 - Evolution of stress-related quantities during SPS at σ_{app} = 20 MPa, t_H = 600 s, t_D = 1200 s, and T_D = 1950 °C for: a) HfB_2, b) NbB_2, and c) TiB_2. Each panel shows the evolution of the equivalent stress (σ_{eq}, red), applied stress (σ_{app}, magenta), radial and hoop stresses (p, green), and yield stress ($\sigma_{Y,1}$, blue) as functions of time. The vertical dashed line marks the end of the heating stage (t = 600 s). In all cases, σ_{eq} drops below $\sigma_{Y,1}$ indicating that particle rearrangement ceases and only viscous deformation remains active. The evolution of p, which increases during densification, reflects the contribution to the consolidation behavior of each material due to the rigid die walls.

For HfB_2 (**Figure 3.42a**) and NbB_2 (**Figure 3.42b**), the profiles are nearly identical. Both materials sustain plastic deformation until approximately 300 s, after which the equivalent stress decreases steadily as temperature increases, and viscous flow dominates. The yield strength of Element 1 (**Figure 3.40**) remains constant throughout, while the radial stress p gradually rises due to enhanced resistance to lateral flow as densification proceeds. These results reflect the similar rheological responses of these two borides, as well as their sintering kinetics observed in the corresponding porosity–time curves shown in **Figures 3.41a–3.41b**. While following the same general pattern, TiB_2 (**Figure 3.42c**) displays clear distinctions. Although the transition from plastic to viscous behavior occurs at about the same time of the other borides, σ_{eq} decreases more sharply afterward. Additionally, the radial stress p increases more rapidly and reaches a higher final value, approaching the level of the applied uniaxial pressure closer than the other two borides. This behavior is consistent with the greater sensitivity to strain rate of the viscous deformation exhibited by TiB_2, as attested by its lower Bird–Carreau exponent m, confirming a more plastic-like behavior under elevated temperatures of this boride (**Table 3.7**).

Overall, simulation results shown in **Figures 3.41** and **3.42** emphasize the importance of properly describing the interplay between stress state and deformation mechanism during SPS. The agreement between predicted stress evolution and densification trends validates the physical structure of the rheological model and suggests that early-stage plasticity followed by viscous flow governs the densification of transition metal diborides.

The stress profiles presented in **Figure 3.42** reveal when and how the plastic rearrangement mechanism becomes active or ceases during sintering, depending on the material and process conditions. To gain deeper insight into how this stress evolution translates into actual deformation behavior, **Figure 3.41** analyzes the associated strain rate profiles and the interplay between particle rearrangement and viscous flow across different pressures, materials, and activation energies. **Figure 3.43a** shows the time evolution of the densification strain rate $\dot{\varepsilon}$ for HfB_2 (red), NbB_2 (green), and TiB_2 (blue) during SPS under identical processing conditions (20 MPa, 10-minute heating, 1950 °C dwell). The profiles are derived from the complete rheological model and reflect the interplay between particle rearrangement and viscous deformation across the sintering cycle. All three materials exhibit a non-monotonic strain rate evolution with two distinct peaks. The first peak,

occurring early during heating (before ~300 s), corresponds to the particle rearrangement, driven by the applied pressure. A second, sharper peak in the 300-600 s time interval marks the transition into viscous-dominated deformation as the temperature approaches the dwell point. Among the three, TiB_2 shows the most pronounced and deepest minimum in strain rate, indicating a more abrupt and intense densification during the non-isothermal heating period. This behavior is consistent with its lower sensitivity exponent m, which results in a sharper switch between deformation regimes. In contrast, HfB_2 and NbB_2 show smoother strain rate transitions, with HfB_2 exhibiting slightly earlier and more gradual strain rate evolution than NbB_2. These results evidence the different rheological characteristics extracted from the model fits and provide insight into the time-dependent consolidation kinetics of each diboride system under identical external loading.

Figure 3.43b shows the strain rate profiles of the two rheological components, slider ($\dot{\varepsilon}_1$) and dashpot ($\dot{\varepsilon}_2$), as functions of time during SPS of HfB_2, under two applied pressures: 20 MPa (solid and dotted red lines) and 80 MPa (solid and dotted magenta lines). The simulation isolates the deformation contributions of each mechanism, providing insight into their relative timing of activation and interaction. At 20 MPa, the strain rate profile clearly shows a sequential activation of the involved mechanisms. The slider (solid red line) dominates the early densification occurring during the first period of heating (~150–300 s), corresponding to particle rearrangement under applied load. Once this mechanism is no longer operating and stress declines below the yield threshold, the dashpot (dotted red line) activates, driving densification through viscous deformation during the later heating period and dwell stage. This time separation confirms that, at lower pressure, particle rearrangement and viscous deformation occur primarily in series. In contrast, at 80 MPa, both slider and dashpot are active simultaneously during heating. The higher stress magnitude accelerates viscous deformation and reduces the temporal dominance of the slider. As a result, the characteristic peak in rearrangement strain rate is largely masked by the concurrent viscous response, which begins earlier and rises more sharply. This overlap of mechanisms demonstrates that, at higher applied pressures, the two deformation modes act in parallel, rather than sequentially. This analysis highlights that the apparent dominance and sequence of deformation mechanisms during SPS are not solely due to intrinsic material properties, but also strongly depend on the applied pressure. The model ability to resolve these contributions offers a powerful tool for optimizing processing conditions to favor desired densification pathways.

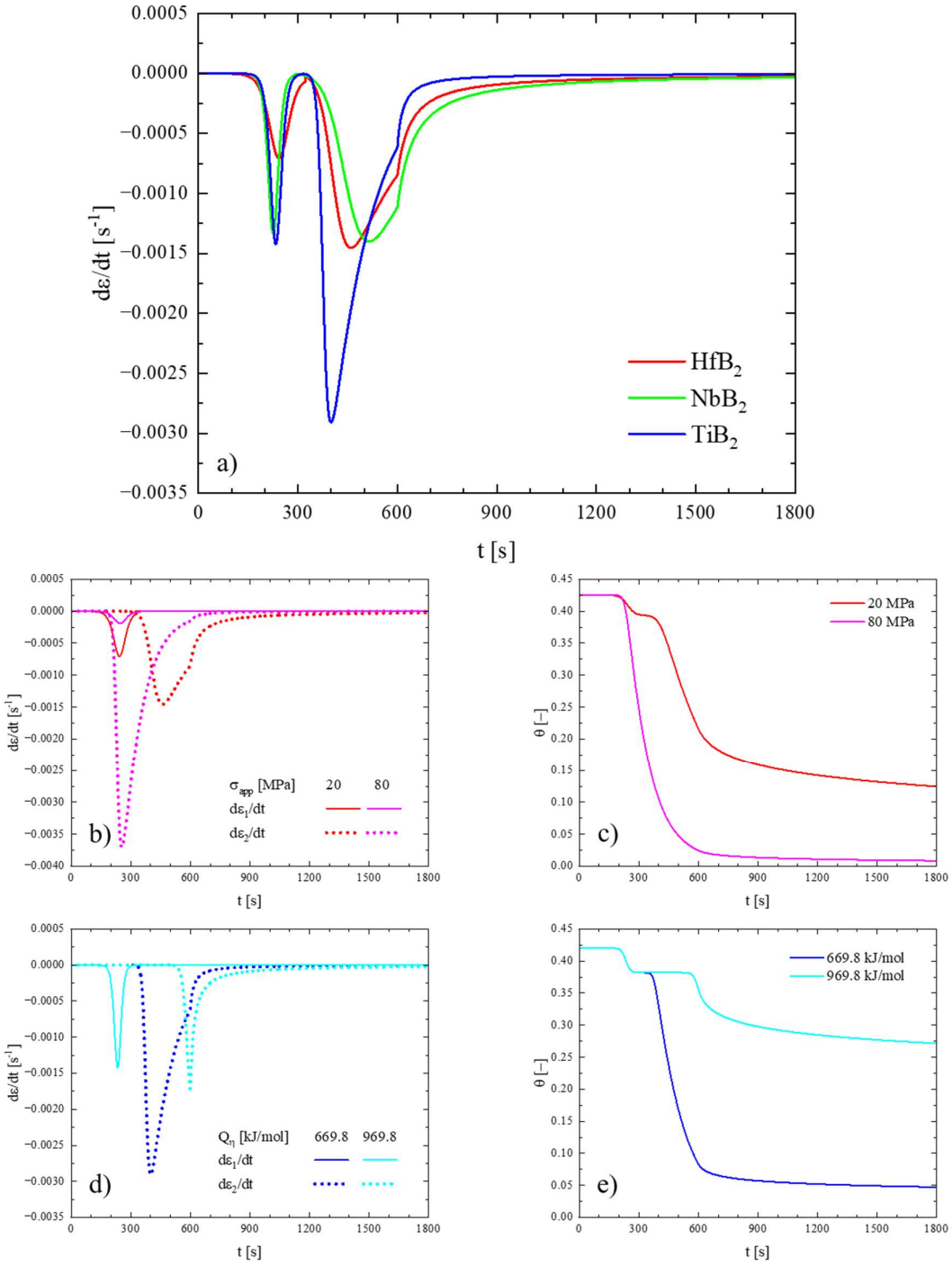

Figure 3.43 - a) Simulated strain rate during densification by SPS of transition metal diborides (σ_{app} = 20 MPa; t_H = 600 s; T_D = 1950 °C); b) effect of applied pressure on strain rates time evolution for HfB_2; c) effect of applied pressure on porosity time evolution for HfB_2; d) effect of shear viscosity activation energy on strain rates time evolution for TiB_2; e) effect of shear viscosity activation energy on porosity time evolution for TiB_2.

In **Figure 3.43c**, the time evolutions of porosity θ corresponding to the same simulations reported in **Figure 3.43b** are presented. It is clearly shown the effect of pressure on the kinetics and extent of consolidation. At 80 MPa, porosity decreases rapidly, and the sample nearly reaches full density ($\theta \sim 0.01$) within the first 600 s, even before the isothermal dwell stage begins. In contrast, at 20 MPa, the densification process is slower and remains incomplete, with porosity leveling off above 10%. An important result from **Figure 3.43c** is that at high applied pressure, the contribution of particle rearrangement can be entirely masked within the densification curve. The apparent smooth, rapid densification may lead to the incorrect assumption that viscous sintering alone is responsible for the observed behavior. However, as shown in **Figure 3.43b**, particle rearrangement is still active, but its strain signature becomes indistinguishable from the viscous contribution in the macroscopic porosity profile (see **Figure 3.43c**). This illustrates a critical limitation in interpreting densification data using porosity-time curves alone. Without a mechanistic model that separates the deformation modes, the risk is to overestimate the role of viscous deformation and neglect early-stage rearrangement, leading to significant errors in the derivation of rheological parameters such as activation energy and viscosity pre-exponential factors (see **Table 3.7**).

While **Figure 3.43c** highlights how the applied pressure influences the visibility and sequencing of the two densification mechanisms, the effect of material properties, specifically the activation energy for viscous flow, is shown in **Figure 3.43d**. The latter presents the strain rate profiles of the slider ($\dot{\varepsilon}_1$) and dashpot ($\dot{\varepsilon}_2$) during SPS of TiB_2, simulated using two different values of activation energy for viscous flow, i.e., the reference value Q_η = 669.8 kJ/mol (dark blue curves) and an artificially increased value Q_η = 969.8 kJ/mol (cyan curves). This analysis isolates the effect of thermal activation on the relative timing of the two deformation mechanisms. For the reference Q_η, the transition from particle rearrangement (slider activity) to viscous deformation (dashpot activity) is nearly continuous. As the slider strain rate decays after ~300 s, the dashpot is already becoming active, creating an overlap between the mechanisms, similar to the low-pressure case for HfB_2 shown in **Figure 3.43b**.

However, when the activation energy is increased to 969.8 kJ/mol, viscous flow is strongly suppressed during heating, and dashpot activation is significantly delayed, only emerging well after the completion of particle rearrangement. This introduces a temporal gap between mechanisms, in which neither slider nor dashpot are substantially active. The strain rate briefly falls toward zero before recovering during the dwell phase. This behavior contrasts with previous cases and

demonstrates the possibility of a third mechanistic regime, where viscous deformation is delayed (**Figure 3.43d**), in addition to the sequential, immediate transition (**Figure 3.43b**, 20 MPa) and the simultaneous overlap (**Figure 3.43b**, 80 MPa). These results emphasize that the relative timing of particle rearrangement and viscous deformation is not fixed but depends on a complex interplay between material parameters (e.g., viscosity) and operating conditions (e.g., pressure, heating rate). The proposed mechanistic model may help to reveal such distinctions, which are invisible in experimental porosity data alone.

For the sake of completeness, **Figure 3.43e** shows the evolution of porosity θ corresponding to the simulation reported in **Figure 3.43d**. For the reference value of Q_η, densification proceeds rapidly after the completion of particle rearrangement, reaching high density level during the early dwell period (dark blue curve). In contrast, with the increased activation energy, the delayed onset of viscous flow results in a slower porosity reduction and an incomplete densification even after 30 min. This finding implies that relatively high values of Q_η suppress viscous flow at intermediate temperatures, widening the temporal gap between the early-stage plastic response and the later-stage viscous consolidation.

The results presented in **Figure 3.43** collectively highlight the versatility and physical fidelity of the proposed rheological model. By explicitly capturing the time-dependent interaction between particle rearrangement and viscous deformation, the model reveals how densification mechanisms are influenced not only by material properties (e.g., activation energy, viscosity exponent) but also by external conditions such as applied pressure. Depending on these factors, deformation mechanisms may occur sequentially, overlap in time, or be separated by periods of mechanical inactivity. These insights, unresolvable from porosity curves alone, demonstrate the necessity of mechanistic modeling to guide accurate parameter identification and optimize sintering protocols for high-performance ceramics.

A potential concern with the proposed model could stem from the relatively high number of adjustable parameters (six), which might, in turn, raise the question of overfitting. In particular, one might argue that assuming a material linear behavior (i.e., $m = 1$) would reduce the parameter to four (see **Appendix C** and **Table 3.7**) and still allow for accurate reproduction of the experimental porosity profiles. However, attempts to optimize the model with $m = 1$ (not shown) did not satisfactorily succeed, indicating that the linear assumption fails to capture the densification

behavior of all the investigated borides. To support this point, the isothermal stage (1950 °C), during which the slider is inactive since $\sigma_{eq} < \sigma_Y$ (see **Figure 3.42**), is analyzed. The intrinsic material viscosity is calculated as the ratio between applied stress, σ_{app}, and equivalent strain rate, W, where the latter, which includes the effect of the varying porosity, has been evaluated from the (smoothed) experimental data reported in the inset of **Figure 3.44**. As shown in this figure, the viscosity increases significantly with time, despite the constant temperature. This trend highlights the inherent strain-rate sensitivity of the viscous flow. Hence, a strain rate independent-viscosity model (i.e., $m = 1$) is inconsistent with experimental evidence in the case of TMBs densification, further justifying the inclusion of a non-Newtonian behavior in the model.

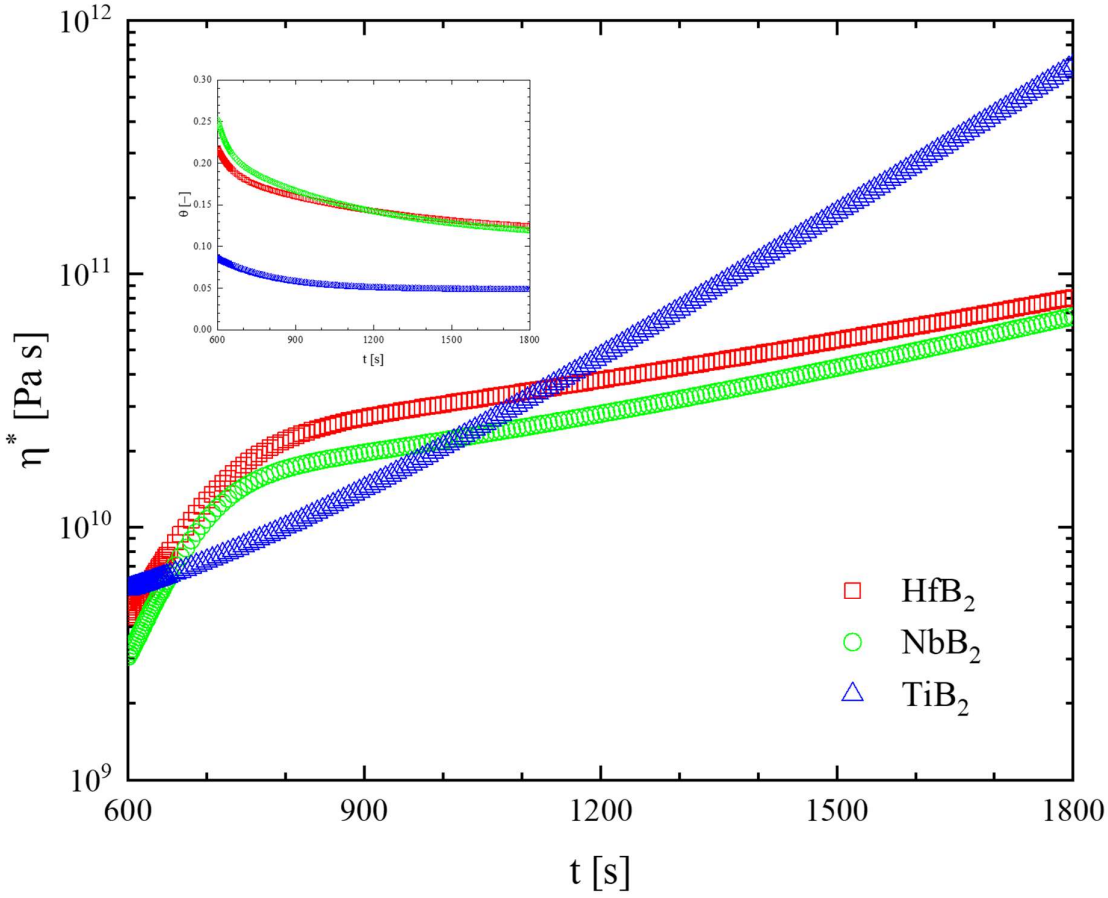

Figure 3.44 - Estimation of (porosity independent) shear viscosity η^* based on the experimental (smoothed) porosity time profiles during the isothermal period of densification reported in the inset.

While the results discussed above clearly demonstrate that the linear case cannot reproduce the densification behavior of transition metal diborides under the investigated conditions, it is preferred to retain a generalized constitutive formulation capable of describing both Newtonian ($m = 1$) and non-Newtonian ($m \neq 1$) viscous behavior. This decision stems from the need for a flexible and broadly applicable framework. For different materials, temperatures, or other sintering regimes (e.g., viscous glass-forming ceramics), linear behavior may be a valid approximation. Hence, the model was developed with sufficient generality to allow such cases to emerge naturally from the parameter identification procedure, rather than imposing *a priori* any assumption. This approach ensures that the model can be extended or applied to a wider class of materials or different consolidation methods without substantial modifications.

3.5.3.2 Apparent and intrinsic viscosity behavior

This section investigates the rheological properties of HfB_2, NbB_2, and TiB_2 as modelled by means of the proposed approach, with a particular emphasis on the evolution of apparent and intrinsic viscosities, the role of strain-rate sensitivity, and the physical interpretation of fitted parameters such as the activation energy and the coefficient m. This analysis combines simulated and experimentally derived values to clarify how material response varies with temperature, strain rate, and porosity.

Figure 3.45 displays the time evolution of the apparent viscosity μ during SPS of HfB_2 (red), NbB_2 (green), and TiB_2 (blue). A striking feature is the drastic initial decrease in viscosity, spanning more than 80 orders of magnitude within the first few hundred seconds. This sharp decrease is primarily governed by the rapid temperature rise during heating, which reduces both the shear viscosity, η, and bulk viscosity, κ. Closer inspection of the inset (300–600 s) reveals the presence of a viscosity minimum occurring before the end of the non-isothermal heating stage. Such a behavior reveals competing effects: On one hand, the continued increase in temperature tends to lower viscosity; on the other hand, the progressive loss of porosity (i.e., improved densification) increases mechanical resistance and tends to raise the viscosity. The presence of a minimum value thus reflects a crossover point where thermal softening is momentarily balanced by microstructural stiffening. After this point, the apparent viscosity increases slightly before stabilizing during the isothermal dwell stage.

Material-specific trends are also evident. TiB_2 exhibits the highest viscosity in the early stage, consistent with its greater stiffness and slower initial densification. However, due to its higher strain-

rate sensitivity (lower m), TiB_2 undergoes a sharper drop in viscosity and rapidly transitions toward a more plastic-like response as shear rate increases. By the start of the dwell period, all three materials converge to similar viscosity levels, corresponding to fully activated viscoplastic flow at steady temperature and low strain rates. It is worth noting that the observed viscosity minimum, and the interplay between thermal softening and densification-induced stiffening, can only be observable through mechanistic modeling that resolves time-dependent porosity and strain rate contributions.

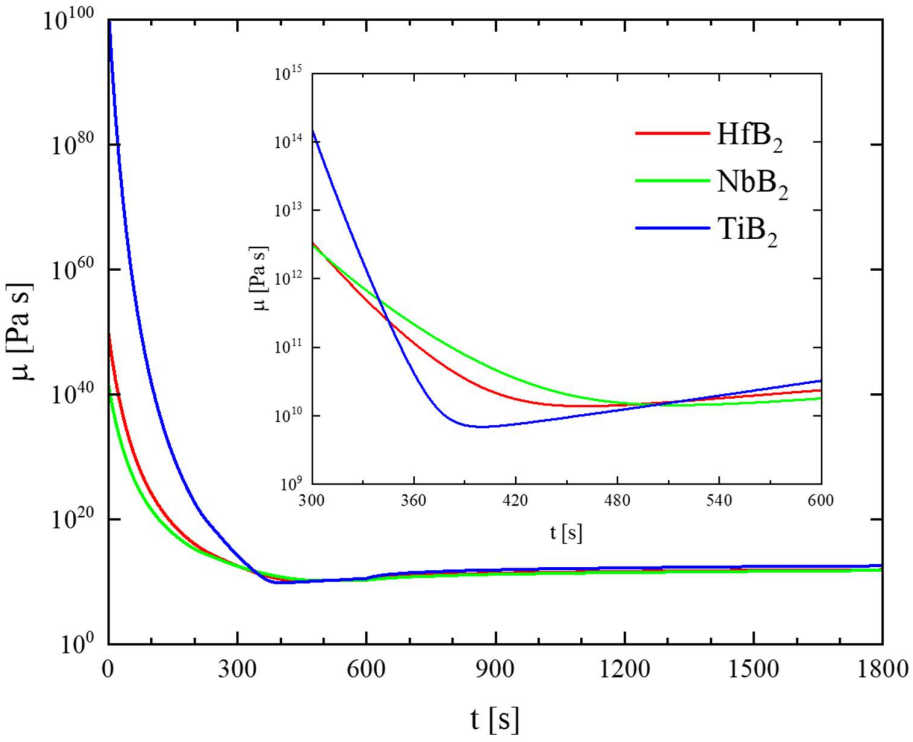

Figure 3.45 - Simulated apparent viscosity μ during densification of transition metal diborides (σ_{app} = 20 MPa; t_H = 600 s; T_D = 1950 °C).

Figure 3.46 shows the calculated zero-rate shear viscosity η^0 of dense HfB_2 (red), NbB_2 (green), and TiB_2 (blue) as a function of temperature. This property, which represents the intrinsic shear viscosity of each material (i.e., independent of porosity and strain rate), is obtained from the fitted parameters. All three borides exhibit the expected thermo-activated viscous response, with η^0 decreasing exponentially with increasing temperature, consistent with an Arrhenius-like trend.

However, clear material-specific differences are evident. Specifically, TiB_2 shows the highest intrinsic viscosity across the temperature range, reflecting an inherently stronger resistance to thermally activated shear deformation. NbB_2 displays the lowest viscosity, indicating higher atomic mobility at lower temperatures, while HfB_2 lies between the two. It can be also seen that, at the process-relevant sintering temperatures (T > 1500 K), viscosity differences narrow but remain significant. For example, even at 2000 K, TiB_2 still exhibits a zero-shear viscosity several orders of magnitude higher than that of NbB_2.

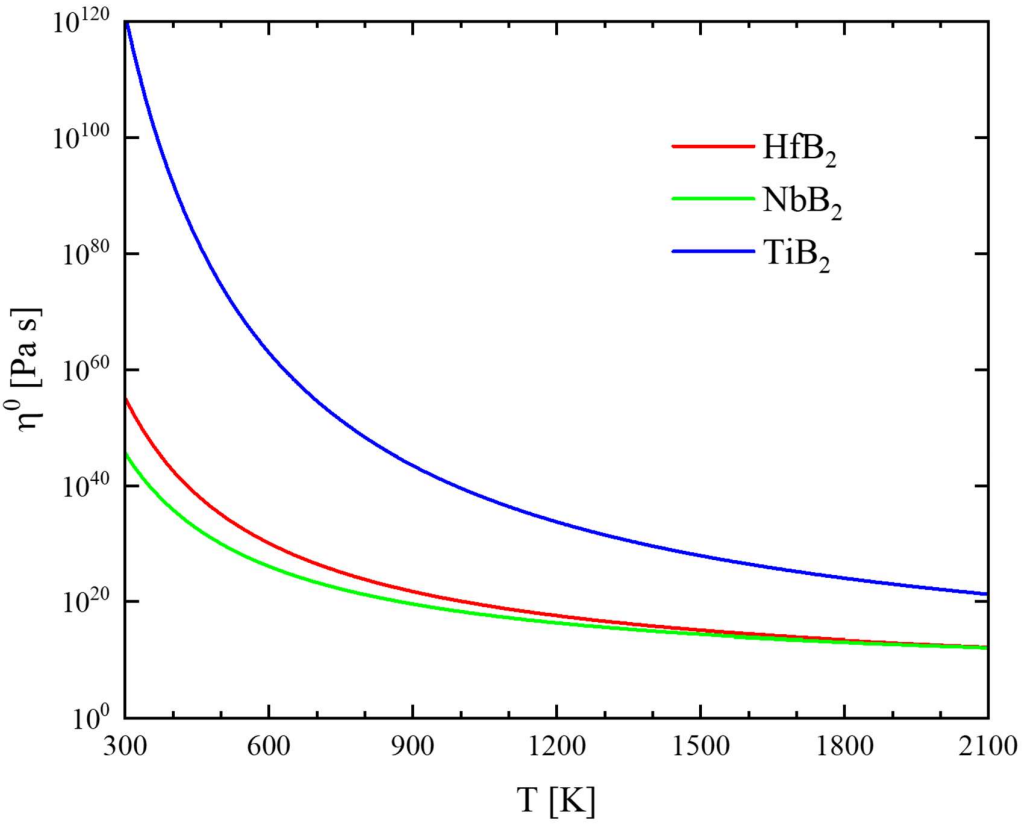

Figure 3.46 - Calculated zero-rate shear viscosity η^0 (porosity and strain-rate independent) of transition metal diborides as a function of temperature.

This figure provides a useful benchmark for material comparison, offering insights into the intrinsic flow resistance that must be overcome during pressure-assisted densification. Importantly, these values cannot be extracted from porosity or strain data alone, because they are accessible only

through the parameterized rheological modeling framework developed in this work. By isolating the viscosity temperature dependence from the porosity and strain rate ones, this analysis bridges the gap between experimental process response and fundamental material properties, thus providing a guide material selection and process tuning for applications requiring high-temperature formability or low flow resistance.

Although the model predicts extremely high apparent and zero-shear viscosity values at low temperatures (see **Figures 3.45** and **3.46**), particularly below the active sintering range, this behavior is both expected and physically consistent with the adopted rheological framework. In fact, these values emerge from extrapolation to low temperatures of the viscosity description, which provides a mechanically consistent transition from the rigid solid-like behavior at low temperature and shear rate to the viscoplastic (fluid-like) flow under high temperature and shear rate. Importantly, although deformations corresponding to these high viscosities are hardly observable or experimentally measured, the proposed viscosity description is qualitatively validated by the negligible densification experimentally observed during the early heating stage (see **Figure 3.41**).

Moreover, although the estimated viscosities at low temperatures may appear extremely high, such values are not only physically reasonable but have been known and accepted for decades within the ceramics and glass communities **[193-195]**. These high values reflect the inherent resistance of these materials to flow, particularly in the early stages of densification when deformation is strongly constrained by particle contacts and limited diffusion pathways. Overall, it should be emphasized that, beyond their exact numerical values, very high viscosity at low temperature serves primarily to limit deformation outside the range of operating conditions where densification is experimentally observed. In other words, they are essential for ensuring that the model simulates the transition from the rigid (undeformable)-body behavior to the fluid-like (densifying) one when temperature and applied pressure levels are increased.

Figure 3.47 shows the simulated shear viscosity η^* of HfB_2 (red), NbB_2 (green), and TiB_2 (blue) as a function of the equivalent strain rate W at the constant temperature of 1950 °C. The curves correspond to model predictions based on the fitted parameters, while the discrete markers represent viscosity values indirectly estimated from the experimental porosity evolution during the isothermal dwell stage (see **Figure 3.44**). All three materials exhibit clear non-Newtonian shear-thinning behavior, consistent with the adopted Bird–Carreau model. At very low strain rates, TiB_2

retains an extremely high viscosity plateau (as seen in **Figures 3.45** and **3.46**), indicating a much more solid-like response in the low-deformation regime. In contrast, NbB_2 and HfB_2 transit into the shear-thinning region and reach comparable viscosities with TiB_2 at higher strain rates.

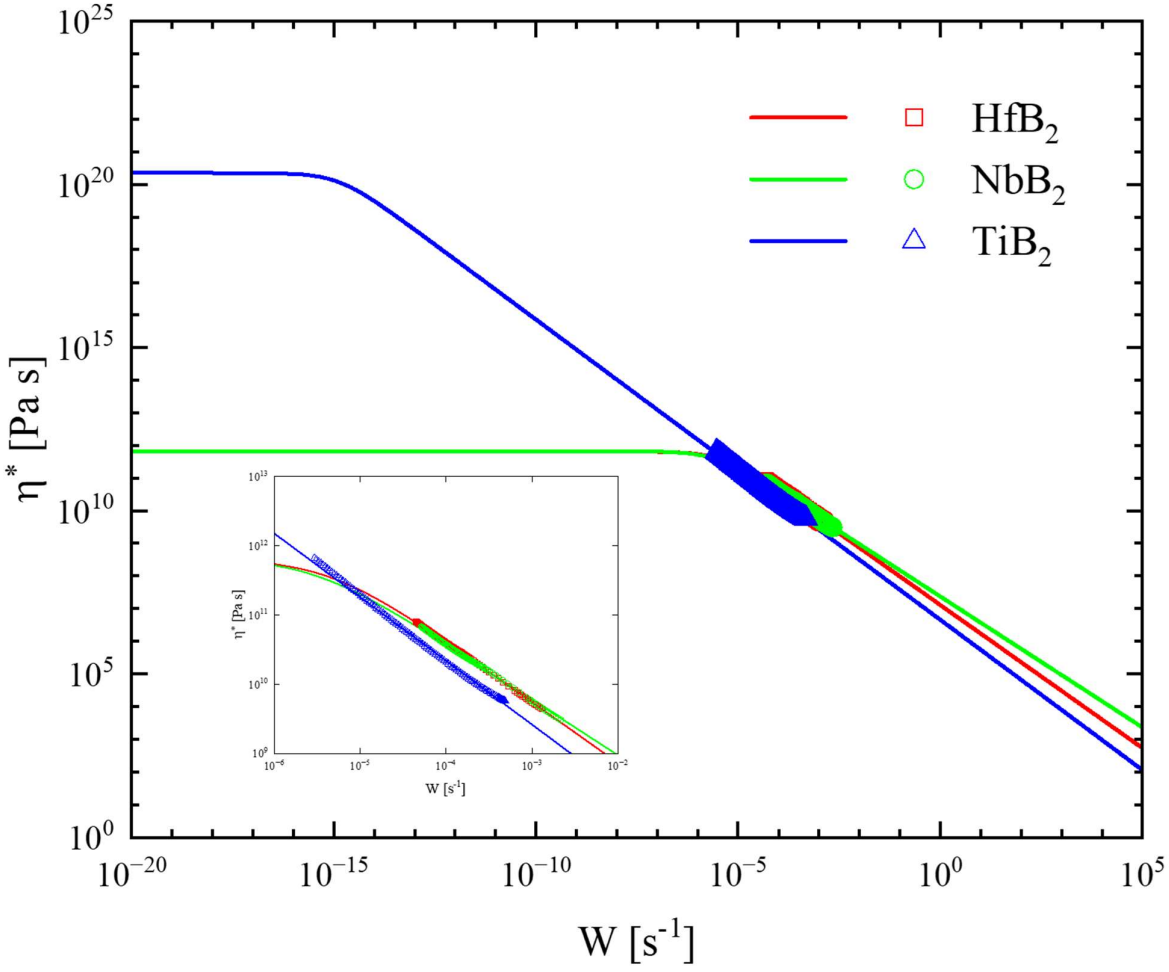

Figure 3.47 - Simulated (lines) of shear viscosity η^* of dense (pore less) transition metal diborides at 1950 °C as a function of the equivalent strain rate. Points represent the shear viscosity η^* at the same temperature as the estimate based on (smoothed) experimental data related to the isothermal period (see **Figure 3.44**).

The experimental viscosity estimates (symbols) align closely with the predicted curves in the strain rate range covered by the SPS data, confirming the validity of the proposed model. The inset highlights this match on a magnified scale, further validating both the fitting methodology and the

extracted rheological parameters. Together with **Figures 3.45** and **3.46**, this analysis confirms that apparent viscosity during sintering results from the interaction of material intrinsic (bulk) viscosity, the evolving porosity, and the imposed shear rate. The zero-rate viscosity η^0 (**Figure 3.46**) serves then as the upper limit of η^* as $W \to 0$.

While the sintering process under standard SPS conditions typically operates in the shear-thinning (non-Newtonian) regime due to elevated shear rates, realistic linear-viscous behavior is expected under specific conditions. Innately, at low external stresses (e.g., $\ll$ 20 MPa), the strain rate induced during SPS is significantly low. If the material is also partially consolidated, the reduced driving force for densification can lead to near-zero effective strain rates, especially during the latter part of the dwell period. Under such conditions, the Bird–Carreau model naturally approaches its Newtonian plateau ($\eta^* \to \eta^0$). Furthermore, in interrupted or slow-ramp sintering experiments, especially those designed to examine early-stage sintering or stress relaxation, densification proceeds very slowly **[196,197]**. These conditions are commonly used to study sintering kinetics or microstructure evolution at low driving forces and would naturally fall into the linear regime. In some alternative applications of the SPS process, sintering is carried out pressure-less, or the applied load is removed after an initial consolidation stage, while the temperature level is held, to retain the desired porosity **[198,199]**. In these cases, the still porous samples could then experience low strain rates so that sintering could occur in the Newtonian (linear-viscous) regime.

These examples demonstrate that the linear-viscous plateau predicted by the Bird–Carreau model is not only a formal extrapolation but corresponds to realistic thermomechanical conditions. Therefore, the use of a rheological model that allows for both linear and non-linear regimes, rather than enforcing a power-law creep formulation with $m < 1$, enhances the versatility of the proposed approach and expands upon classical sintering descriptions, such as those based on the conventional creep models. Finally, it should be pointed out that the use of the Bird–Carreau constitutive law offers another significant advantage over classical power-law (Norton-type) formulations. As shown above, the Bird–Carreau model allows for the identification of the zero-shear viscosity η^0 which characterizes the intrinsic material resistance to deform in the limit of low strain rates. This information is inaccessible in traditional approaches, which inherently assume non-Newtonian behavior across all strain rates and do not represent a Newtonian plateau. As such, the Bird–Carreau formulation provides a more flexible and physically meaningful framework for capturing the full range of material rheology relevant to sintering.

3.5.3.3 Model validation

Figure 3.48 presents a validation of the rheological sintering model through a direct comparison with experimental data from the literature for HfB_2, NbB_2, and TiB_2 **[163,165,169,200-202]**. Each panel explores the model ability to capture the densification response under varying processing conditions and for the different materials. In **Figure 3.48a**, the model successfully reproduces the trend of increasing final density of HfB_2 with dwell temperature, as reported by **Venugopal et al. [200]** and **Dubey et al. [201]**, using a constant heating rate (*HR*) of 100 °C/min, a dwell time of 10 min, and an applied pressure of 50 MPa. The deviations between predicted and measured densities remain within ±3.8% (except for just a single datum), highlighting the accuracy of the proposed model across a broad temperature range. Model-predicted and experimentally measured final densities for NbB_2 are compared in **Figure 3.48b**, drawing from several sources with significantly different SPS parameters. Despite the variability in heating rates (ranging from 2 to 185 °C/min), dwell temperatures (1750–1950 °C), pressures (20–80 MPa), and dwell times (5–20 min), the model maintains good agreement, with differences below ±2.1%. In **Figure 3.48c**, the predicted evolution of TiB_2 density as a function of dwell time at 1500 °C and 50 MPa (*HR* = 50 °C/min) closely matches the experimental results from **Balcı et al. [202]**. The model captures the weak sensitivity of final density to extended dwell times in this material, which is consistent with the relatively high viscosity and low strain rate observed for TiB_2 after a significantly high degree of densification is already achieved. Finally, **Figure 3.48d** shows the dependence of TiB_2 final density on applied pressure at fixed thermal conditions (T_D = 1500 °C, t_D = 15 min). The model predicts a clear increase in densification with increasing pressure, consistent with experimental observations. The maximum deviation remains below 1%, confirming that the model robustly predicts the influence of pressure on the densification kinetics.

Collectively, these validation results demonstrate that the proposed rheological model, calibrated solely on experimental porosity-time data under a single set of SPS conditions, can be effectively extrapolated to a wide range of thermal and mechanical scenarios. This generalization capability is crucial for the predictive use of the model in process optimization and materials design. Overall, the consistency between predictions and literature data, despite differences in sintering setup, powder batches, and possible microstructural variability, validates the transferability and predictive strength of the rheological model when fitted using only a limited set of porosity-time data.

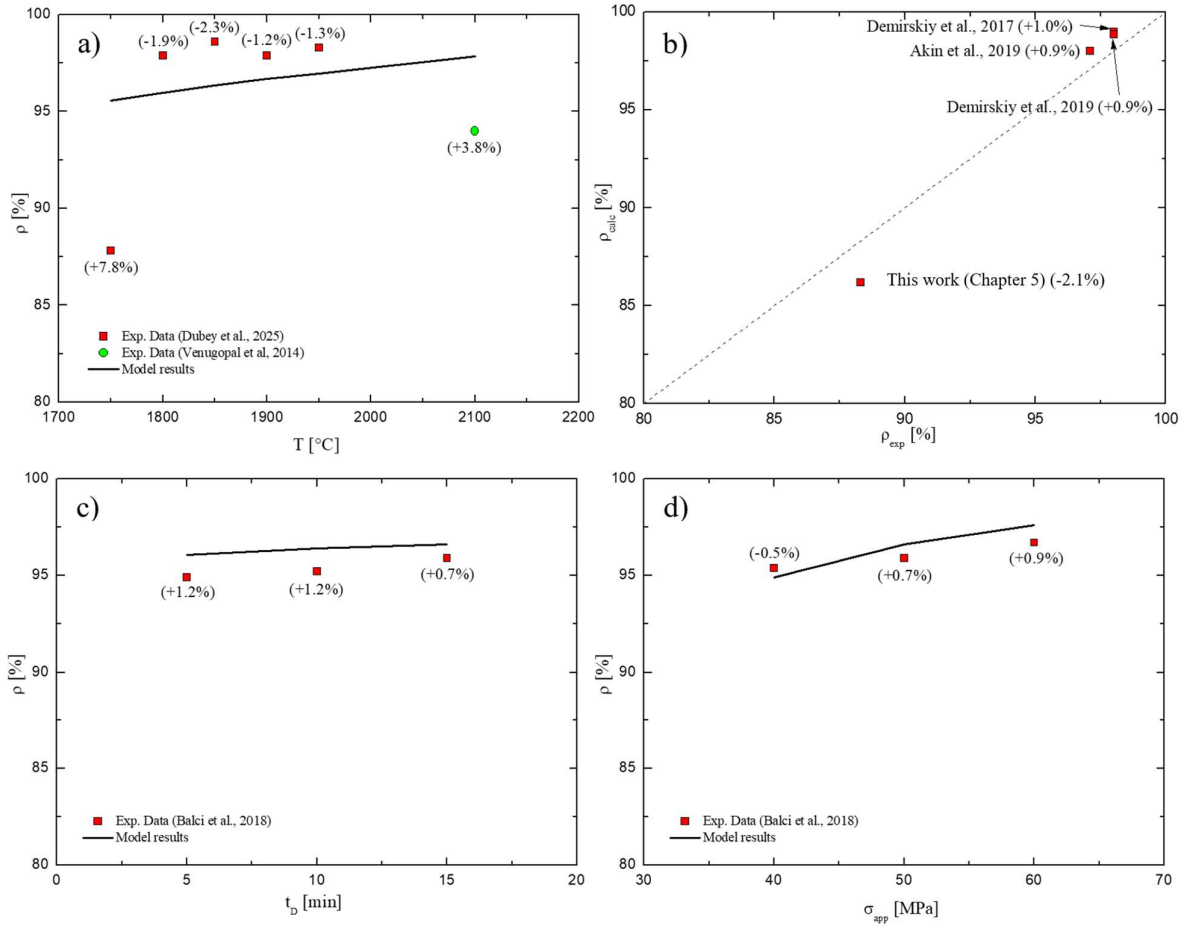

Figure 3.48 - Comparison between experimental data taken from the literature and model outcomes: a) final relative density of HfB_2 samples as a function of the dwell temperature, T_D (HR = 100 °C/min; t_D = 10 min; σ_{app} = 50 MPa) – data from **Venugopal et al. [200]** and **Dubey et al. [201]**; b) final calculated relative density of NbB_2 samples versus the experimental one. Operating conditions are as follows: **Akin et al. [165]**: HR = 2 °C/min; T_D = 1750 °C, t_D = 5 min, σ_{app} = 50 MPa; This work (slightly modified conditions with respect to those in **Section 3.3**): HR = 185 °C/min; T_D = 1850 °C, t_D = 20 min, σ_{app} = 20 MPa; **Demirskyi et al., 2017 [163]**: HR = 110 °C/min; T_D = 1950 °C, t_D = 10 min, σ_{app} = 80 MPa; **Demirskyi et al., 2019 [169]**: HR = 110 °C/min; T_D = 1900 °C, t_D = 10 min, σ_{app} = 80 MPa; c) final relative density of TiB_2 samples as a function of the dwell time, t_D (HR = 50 °C/min; T_D = 1500 °C; σ_{app} = 50 MPa) – data from **Balcı et al. [202]**; d) final relative density of TiB_2 samples as a function of the applied pressure, σ_{app} (HR = 50 °C/min; T_D = 1500 °C; t_D = 15 min) – data from **Balcı et al. [202]**. Numbers in brackets indicate the difference (percentage) between the calculated and the experimental relative densities.

Along this line, **Figure 3.49** explores the densification response of transition metal diborides (HfB_2, NbB_2, TiB_2) under a range of SPS conditions, highlighting the model predictive capabilities and, crucially, revealing the relative effectiveness of different process variables in promoting full densification. Specifically, **Figure 3.49a** presents the porosity evolution simulated over an extended processing time to 12 hours at constant temperature (1950 °C) and low applied pressure (20 MPa). Despite the prolonged holding time, none of the materials attain full density (defined here as relative density >99%). This clearly indicates that under moderate pressure, densification eventually stalls due to insufficient driving force for viscous deformation and pore closure. Notably, TiB_2 densifies faster than HfB_2 and NbB_2, due to its higher strain rate sensitivity and despite its higher intrinsic viscosity (see **Table 3.6** and **Figure 3.46**), but still fails to cross the full density threshold within practical sintering times.

Figure 3.49b directly confirms the conclusion that applied pressure is the most influential variable for achieving full density. At a fixed temperature and sintering time, increasing the pressure from 30 to 70 MPa significantly accelerates densification of HfB_2, with higher pressure yielding a denser final microstructure. The predicted final relative density as a function of the dwell temperature at constant pressure (20 MPa) and total sintering time (30 min) is illustrated in **Figure 3.49c** for the three borides investigated in this work. While relative density increases with temperature, the thermal levels required to achieve >99% dense samples should exceed 2700 °C for all the investigated diborides. These temperature levels are experimentally challenging or nearly impractical for all conventional pressure-assisted sintering techniques, due to intrinsic limitations in equipment and risk of failures at such extreme temperatures.

Taken together, **Figures 3.49a–3.49c** indicate that while temperature and time are important, pressure seems to be the most effective and experimentally accessible variable for ensuring full densification of these ultra-high temperature borides. This conclusion is qualitatively supported by literature reports: for example, **Sani et al. [203]** demonstrated that TiB_2 samples with high relative density required applied pressures of 60 MPa. Conversely, in **Section 3.3** it was shown that, when lower pressures are used, the addition of sintering aids (e.g., graphite) becomes necessary to promote densification. The proposed model thus offers not only quantitative insight into densification kinetics, but also clear guidance for process optimization under practical constraints.

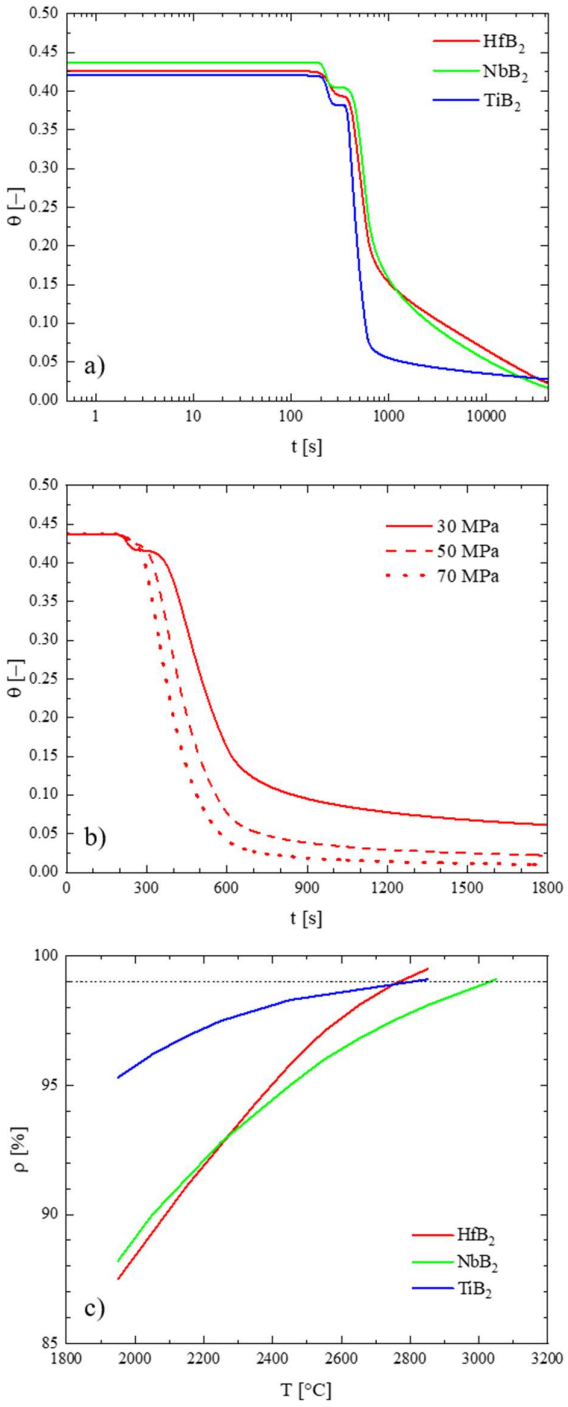

Figure 3.49 - Simulated effect of operating conditions on densification of transition metal diborides: a) porosity time profile up to 12 h (σ_{app} = 20 MPa; t_H = 600 s; T_D = 1950 °C); b) HfB_2 porosity time profile for different values of the applied pressure, σ_{app}; c) final relative density as function of the dwell temperature (σ_{app} = 20 MPa; t_H = 600 s; t_D = 1200 s). Dashed line in Figure c) gives the 99% relative density.

Finally, it is possible to state that the model successfully captures the distinct densification behaviors of the three diborides, particularly the enhanced plasticity of TiB_2 at elevated temperatures and the similar response of HfB_2 and NbB_2. Simulated stresses and strain-rates time evolutions were analyzed in detail, revealing the synergic effects of particle rearrangement and viscous deformation, and highlighting the transition from sequential to simultaneous operation of these mechanisms, depending on processing conditions. The calculated material viscosities are consistent with values reported in the literature for high-temperature ceramics and glasses, and the strain-rate dependence is experimentally confirmed from isothermal-stage data.

Importantly, the model shows strong predictive capability beyond the fitting variable ranges. It accurately reproduces final densities reported in independent SPS studies and provides insight into the influence of process variables. Simulation outcomes indicate that applied pressure is the most effective parameter for achieving near-full density, whereas extended dwell time or elevated temperature alone may not be sufficient or practical. Beyond fitting, the model provides mechanistic insight and predictive power, enabling informed design of processing strategies for ultra-high-temperature ceramics. Its general structure is adaptable to other material systems and sintering methods where linear or nonlinear viscous flow and early-stage plasticity coexist.

3.5.4 Notation

Latin letters

A empirical coefficient depending on ρ, [-]

A_T midpoint inflection temperature for σ_Y, [K]

a^0 pre-exponential factor, [Pa s]

B empirical coefficient depending on ρ, [-]

B_T steepness of the sigmoidal function for σ_Y, [K]

F yield function, [Pa]

$f(\theta)$ porosity dependence function for equivalent strain rate, [s^{-1}]

$\vec{g}$ gravity field, [m s^{-2}]

HR heating rate, [K s^{-1}, °C s^{-1}]

I_1 the first invariant of the Cauchy stress tensor, [Pa^2]

J_2 second invariant of the deviatoric Cauchy stress tensor, [Pa^2]

m strain-rate sensitivity coefficient, [-]

p contact pressure exerted by the sample to the die internal wall, [Pa]

Q_η activation energy, [J mol^{-1}]

r radial coordinate, [m]

$\mathbf{T}$ total stress tensor, [Pa]

T temperature, [K, °C]

T_D dwell temperature, [K, °C]

t time, [s]

t_D dwell period length, [s]

t_H heating period length, [s]

$tr\ (\ )$ trace of a tensor, [-]

$\vec{v}$ velocity field, [m s^{-1}]

W equivalent strain rate, [s^{-1}]

$\vec{x}$ spatial coordinates vector, [m]

Greek letters

$\dot{\gamma}$ second invariant of the strain rate tensor deviator $\boldsymbol{\varepsilon}'$, [-]

δ_{ij} Kronecker delta dunction, [-]

$\boldsymbol{\varepsilon}$ strain tensor, [-]

$\dot{\boldsymbol{\varepsilon}}$	strain rate tensor, [s^{-1}]
$\dot{\varepsilon}_{ij}$	strain rate tensor component, [s^{-1}]
$\dot{\boldsymbol{\varepsilon}}'$	strain rate deviator tensor, [s^{-1}]
$\dot{\varepsilon}'_{ij}$	strain rate tensor deviatoric component, [s^{-1}]
η	shear viscosity, [Pa s]
η^*	shear viscosity of the dense (pore-free) material, [Pa s]
η^0	zero-shear rate viscosity of dense (pore-free) material, [Pa s]
ϑ	hoop coordinate, [rad]
θ	porosity, [-]
Λ	plastic multiplier, [-]
κ	bulk viscosity, [Pa s]
κ^*	shear viscosity of the dense (pore-free) material, [Pa s]
λ	material-specific relaxation time, [s]
λ^0	pre-exponential factor, [s $\mathrm{K}^{\left(\frac{m-1}{m}\right)}$]
μ	apparent viscosity, [Pa s]
ρ	relative density, [-]
$\boldsymbol{\Sigma}$	Σ tensor defined for shorter notation, [Pa]
Σ_{ij}	component of the Σ tensor, [Pa]
$\boldsymbol{\sigma}$	Cauchy stress tensor, [Pa]
σ_{app}	applied stress, due to mechanical load, [Pa]
σ_{eq}	equivalent stress, [Pa]
σ_{ij}	Cauchy stress tensor component, [Pa]
σ'_{ij}	Cauchy stress tensor deviatoric component, [Pa]

σ_Y yield strength, [Pa]

σ_Y^0 low temperature asymptotic value for σ_Y, [Pa]

σ_Y^∞ high temperature asymptotic value for σ_Y, [Pa]

Φ dissipation potential, [Pa s]

φ function of sample porosity for shear viscosity, [-]

Ψ viscoplastic potential, [Pa]

Ψ^P plastic potential, [Pa]

ψ function of sample porosity for bulk viscosity, [-]

Superscripts

^{P} referred to plastic deformation

^{VP} referred to visco-plastic deformation

^{0} referred to t = 0

The modelling activity and related results described in this Section have been reported in the following paper: Traversari, G., **Casu M.**, Cappai, L., Carta, G., Brun, M., Cincotti, A., Orrù, R., Cao, G., & Locci, A. M. (2026), Constitutive Modeling of Pressure-Assisted Powder Consolidation by Spark Plasma Sintering: The Case of Transition Metal Diborides. *Journal of the European Ceramic Society, 46 (3) ,117860*, https://doi.org/10.1016/j.jeurceramsoc.2025.117860

---

4. Processes and Materials for the Space Colonization: *In-Situ* Resource Utilization of Martian Regoliths

This Chapter focuses on ISRU technologies aimed to densify Martian regoliths to obtain materials for solar energy harvesting (**Section 4.1**), construction materials with high mechanical properties (**Section 4.3**) and complex parts via additive manufacturing (**Section 4.3**).

4.1 Processing of Martian regoliths for their application as solar energy absorbers on Mars

4.1.1 Introduction

Among the ISRU technologies to be developed in the near future, *in-situ* surface power generation and storage is one of the key capabilities identified by NASA, along with the utilization of *in-situ* available resources for a broad range of scopes **[40]**. As anticipated in **Chapter 1**, the most abundant and ubiquitous material available on the Martian surface is certainly represented by regolith **[37]**. In this framework, JSC-Mars-1A and Mojave Mars Simulant (MMS) are two of the most investigated Martian regolith simulants, among those ones developed so far (see **Section 2.2.1**). As for their possible exploitation, several works assessed the feasibility of the use of untreated or sintered Lunar regolith as solar energy absorbers **[108]** and thermal energy storage (TES) materials **[97,204-206]**, to the best of our knowledge, no similar studies are available in the literature involving Martian regolith. Generally, sintered regolith is considered the best option for TES, given the enhanced thermal conductivity and mechanical properties of bulk materials if compared to loose dust **[97,98]**.

Accordingly, different consolidation methods, previously applied to terrestrial processes, have been then considered to convert loose Martian regolith into sintered bodies (see **Section 2.2.2**). They include pressureless sintering **[99,100]**, combustion synthesis-based processes **[101-103]**, impact compaction **[104]**, high-pressure consolidation **[104]**, solar sintering **[105]**, additive manufacturing **[99,106]**, and cold sintering **[107]**. Recently, the SPS technology has been successfully applied to process lunar regolith simulants **[108-111]** and Martian ones **[112,113]**. The limited energy request associated with SPS technique is expected to be highly beneficial for its applicability in contexts such

as the proposed Martian outposts. Moreover, the operating conditions typical of the SPS setup, which requires high vacuum during experimental runs, simulate, more closely, the actual Martian atmosphere compared to air sintering. Furthermore, this technique also allows for the obtainment of adequate densification levels without employing additional binders, which may not be available *in-situ*.

In the present work, the JSC-Mars-1A and MMS simulants are first characterized in terms of mineralogy, thermal stability, and density. This is because, even if they have been already extensively used in previous studies, no comprehensive information is available in the literature. In particular, their theoretical densities and several other data, useful for this and future applications, are still missing **[37]**. Subsequently, simulants are Spark Plasma sintered at different temperatures and applied mechanical loads to produce bulk samples. The corresponding compositional, density, porosity and superficial roughness changes are determined. Finally, spectral absorptance/emittance, the integrated solar absorptance and the integrated thermal emittance are studied at the temperature range of 100-600 K, representative of possible conditions in which these materials should be applied within an ISRU context.

4.1.2 Materials and Methods

The regolith simulants used in this section consisted in the Johnson Space Center JSC-Mars-1A **[92]** and the MMS simulant, provided by the Jet Propulsion Laboratory (Pasadena, USA) **[90]**. The chemical compositions (oxide constituents, wt.%) of the two simulants are reported in **Table 2.2** in **Section 2.2.1**.

To evaluate the thermal stability of the two regolith simulants, Thermo-gravimetric analyses were performed on pristine JSC-Mars-1A and MMS using a simultaneous DTA-TGA Instrument (NETZSCH STA 409PC Luxx, Germany). The tests were designed with a heating rate of 2 K/min from room temperature to 800 °C. Given the results of TGA, prior to SPS experiments, JSC-Mars-1A powders were first heat treated in air at 700 °C for 2 h using a muffle furnace (LT 24/11/B410, Nabertherm, Lilienthal, Germany), and then stabilized in air environment at room temperature. Bulk densities of the two materials were determined by a gas displacement pycnometer (AccuPyC 1340, Micromeritics, USA) using helium as adsorbate gas.

Also prior to SPS densification, pristine JSC Mars-1A simulant received a 60 min ball milling treatment (balls to powder weight ratio equal to 2) using a planetary mill (Tecnotest, Italy) to reduce the original powders size (<1 mm) to less than 150 μm. Such treatment was not needed in the case of MMS, which already satisfied the latter condition. Particle size distribution of both powder batches was evaluated by a laser light scattering analyzer (CILAS 1180, France).

Regolith powders were consolidated by the SPS apparatus described in **Section 2.2.2**. Approximately 2.15 g of either pristine (MMS) or heat treated (JSC-Mars-1A) simulants were located inside the graphite dies, while a 3 min dwelling time was selected. The influence of the temperature on samples density was investigated in the ranges 800-1000°C and 950-1050°C for the cases of JSC-Mars-1A and MMS systems, respectively, while t_D was kept constant at 3 min. The effect produced by an increase of the applied mechanical pressure (P) from 15 to 30 MPa was also explored.

While the displacement output recorded in real time provides an indication of the evolution of the sample densification during SPS, the thermal expansion of graphite tools, electrodes and the sample is also responsible for the measured value. The latter contribution, but that of the sample, was evaluated separately under the same SPS conditions. The so-called sample shrinkage (δ), a more reliable index of the densification degree, was then determined.

The obtained bulk samples (about 20 mm diameter and 1.8 to 3 mm height) were properly polished using abrasive paper, to remove possible residual impurities from the graphite tools. Each experimental condition was replicated at least twice. Samples density was measured by the Archimedes' method using acetone as soaking medium (as suggested by the work of **Sizemore and Mellon [207]**) and an Ohaus Explorer Pro (Ohaus Corporation, NJ, USA) analytical balance (± 0.0005 g precision). Relative densities were then evaluated by considering, as reference values, the bulk densities of original JSC-Mars-1A and MMS simulants, as described previously.

X-Ray Powder Diffraction of the simulants, (pristine, heat treated and sintered) were carried out in a Rigaku SmartLab (Bragg-Brentano geometry) equipped with a rotating copper anode (Cu Kα radiation λ=1.5418 nm) working at 40kV and 100mA. The analysis was performed, in the 5°-130° theta/2theta range, with a step-size of 0.05° and for 30 seconds for each step. The attribution of the mineralogical phases was performed with QualX software **[208]**, with a Search and Match approach, using the COD (Crystallography Open Database) as a reference database **[209]**. Crystallographic studies in terms of relative abundance, crystallite size, crystal disorder and cell parameters were

estimated by the Rietveld method, using MAUD (Material Analysis Using Diffraction) program **[131]**. The CIF files used for the Rietveld refinement were provided by the COD Database **[209]**. Rietveld refinement results are reported in detail in **Appendix A.d.**

The microstructural characteristics of the samples surface were examined by SEM (Zeiss Evo LS 15). Surface roughness of the polished samples selected for optical measurements was determined using a contact profilometer (Mitutoyo SJ-201). In particular, the following roughness parameters were considered: Ra, defined as the arithmetic mean of the absolute ordinate Z(x) referring to the length of the measurement profile; Rq defined as the root mean square error for the absolute ordinate Z(x); and Rz, influenced by the surface defects, representing the sum of the maximum height of a peak and the maximum depth of a valley (maximum height of the profile along z). To estimate surface porosity of the sintered samples, SEM micrographs were analyzed using the open-source software GNU Image manipulation Program GIMP (version 2.10). In particular, SEM images were further processed, i.e. brightness and contrast correction, to better evidence pores.

Optical properties of both sintered samples and pristine powders were investigated in collaboration with the Italian National Institute of Optics (Istituto Nazionale di Ottica, CNR-INO) in order to evaluate their behavior when subjected to electromagnetic radiation of different nature. Spectral hemispherical optical reflectance was measured in the range 0.19-16.00 μm wavelength using two instruments: a double-beam spectrophotometer (Perkin Elmer Lambda900) with a 150-mm diameter Spectralon®-coated integrating sphere for the spectral range 0.19-2.50 μm, and a Fourier Transform spectrophotometer (Thermo Fisher iS50) with a gold-coated integrating sphere and a liquid N_2-cooled detector for the wavelength region from 2.5 to 16.0 μm. All the data have been taken for quasi-normal light incidence angle. For opaque materials, as we verified to be the case of these Martian regolith simulants, the normal spectral absorptance α(λ) can be obtained from the experimentally acquired normal hemispherical reflectance ρ'∩(λ) according to the following relation:

$$\alpha(\lambda) = 1 - \rho' \cap (\lambda) \tag{25}$$

which, according to Kirchoff's law, is equal to the normal spectral emittance ε(λ):

$$\alpha(\lambda) = \varepsilon(\lambda) \tag{26}$$

Then, the total solar absorptance can be obtained by spectral integration as:

$$\alpha = \frac{\int_{\lambda min}^{\lambda MAX} \alpha(\lambda) \cdot I_{Sun}(\lambda) \cdot d\lambda}{\int_{\lambda min}^{\lambda MAX} I_{Sun}(\lambda) \cdot d\lambda} \quad (27)$$

And, similarly, the total thermal emittance at temperature T as:

$$\varepsilon(T) = \frac{\int_{\lambda min}^{\lambda MAX} \varepsilon(\lambda) \cdot I_{BB,T}(\lambda) \cdot d\lambda}{\int_{\lambda min}^{\lambda MAX} I_{BB,T}(\lambda) \cdot d\lambda} \quad (28)$$

where the integration boundaries λ_{min}= 0.19 µm, λ_{MAX}= 16 µm, correspond to the boundaries of the spectral range experimentally accessible in our case, $I_{Sun}(\lambda)$ is the solar irradiance as described below, and $I_{BB,T}(\lambda)$ is the blackbody irradiance at the temperature T. As discussed elsewhere **[67]**, the values of α and ε(T) obtained from room-temperature spectra, which are widely used in the literature in the field of solar energy materials, should be considered as approximate values. They are, however, very useful for a first comparison among a set of samples, as well as with literature values. For this reason, this work will consider two significant decimal digits for α and ε(T), despite the actual experimental uncertainty on the reflectance measurements is lower

Unlike the Lunar case, where the absence of any atmosphere allows to consider the extraterrestrial solar irradiance **[210]** as representative of the solar irradiance on the surface of the celestial body **[108],** the actual solar irradiance on the surface must be considered for Mars. It is site- and season-dependent, due to the characteristics of Mars atmosphere and orbit.

4.1.3 Results and Discussion

4.1.3.1 Initial characterization of the Martian regolith simulants

The TGA curves reported in **Figure 4.1a** evidence the different behavior manifested by the two pristine simulants when they are exposed to progressively higher temperatures, up to 800°C. JSC-Mars-1A clearly shows a superior weight loss (about 28%) compared to MMS (about 8%). These results are fairly consistent with **Chow et al. [104]** and **Corrias et al. [102]** findings relative to JSC-Mars-1A (about 30%) and MMS (about 5%), respectively. As also reported by **Karl et al. [37]**, some

plant roots are found in the original JSC-Mars-1A material. This provides direct evidence of the presence of an organic source. This is also confirmed by the significant carbon content, in the range 3.01-3.16 wt.%, **[104,211]** as well as by the traces of ammonium nitrates **[211]** previously detected on this simulant. Even if the presence of organics (in traces) on Mars cannot be excluded **[212]**, the large amount found in JSC-Mars-1A needs to be significantly reduced to closely mimic the actual Martian soil characteristics.

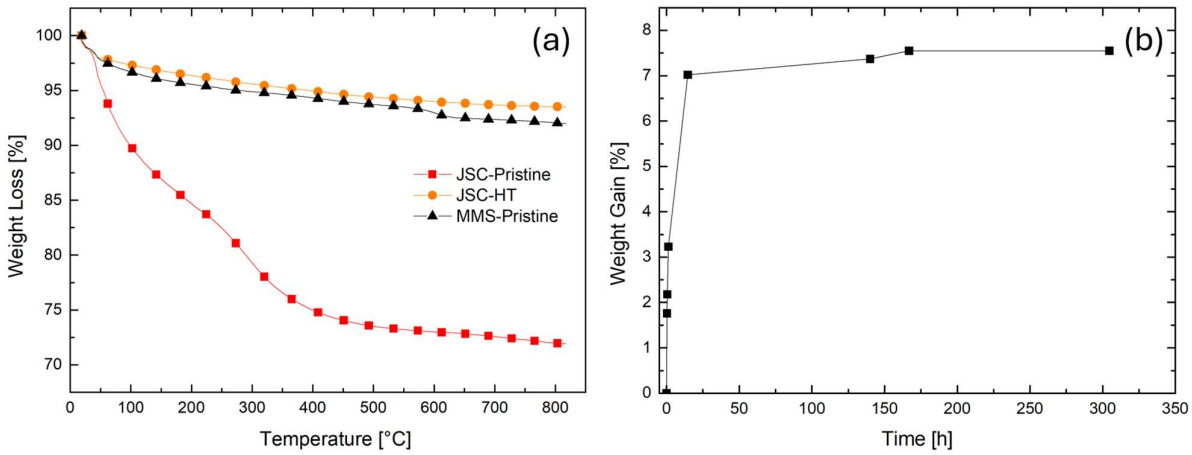

Figure 4.1 - (a) Weight change (%) of JSC-Mars-1A (before and after being heat treated for 2h at 700°C) and MMS simulants during TGA experiment under dynamic conditions. (b) Weight change (%) at room temperature in air of heat treated (700°C, 2h) JSC-Mars-1A simulant.

Nonetheless, the marked mass loss observed during TGA test of JSC-Mars-1A should be mostly attributed to the presence of water. Based on measurements of the Curiosity rover in the Gale crater **[213]** the observed water release is far greater than what expected on Martian soil **[37,208]**. To remove excess water and organic species, JSC-Mars-1A was, before being further processed, heat treated for 2h at 700°C, above which the related TGA curve does not indicate further weight changes (**Figure 4.1a**). As shown in **Figure 4.1b**, heat treated powders regain some weight when exposed to air environment. This phenomenon, ascribed to the high hygroscopicity of JSC-Mars-1A **[214]**, can be considered roughly completed within 3 days (**Figure 4.1b**).

Figure 4.1a also evidenced that the TGA curve associated with the latter material is nearly close to that of untreated MMS, with a measured mass loss of the first simulant equal to about 7 wt.%. The characteristics of both pristine MMS and treated JSC-Mars-1A appear now to be more coherent with Martian mission's findings regarding the limited water content in regolith.

To homogenize the coarser JSC-Mars-1A simulant (< 1mm particle size), the related powders were mildly ball-milled to obtain particles smaller than 150 μm. In contrast, pristine MMS did not need any milling step. Particle size parameters of the two simulants are reported in **Table 4.1**.

Table 4.1 - Particle size parameters of Martian regolith simulants used to obtain bulk samples by SPS

	JSC-Mars-1A	**MMS**
d10 [μm]	2.04±0.33	2.52±0.09
d50 [μm]	23.85±1.06	23.38±0.95
d90 [μm]	57.39±4.03	65.92±2.69
d[4,3] [μm]	27.18±1.55	29.40±1.22

Density of the pristine (MMS) and heat treated (JSC-Mars-1A) simulants measured by pycnometer are about 2.77 and 2.84 g/cm^3, respectively.

Mineralogic composition of as received simulants and heat treated JSC-Mars-1A was deduced by XRD analysis. The related patterns are reported in **Figure 4.2**. After the identification of the mineral components, their relative content (wt.%) was evaluated, together with crystallographic parameters, with the Rietveld method. The obtained results are shown in **Table 4.2**. Each of the simulants presents a relevant texture effect due to the oriented crystal growth typically observed in natural minerals. The corresponding crystallite size, microstrain, and lattice parameters, also estimated with the Rietveld method, are reported in **Tables A11-A14**.

XRD of pristine MMS (**Figure 4.2** and **Table 4.2**) evidence the presence of a major content in plagioclase, mainly attributed to andesine, and 14 wt.% pyroxene, equally distributed between the detected augite and pigeonite phases. Orthoclase, olivine, montmorillonite, and a small amount (3 wt.%) of an amorphous phase were also detected, along with a phase with the Fd-3m special group,

attributed to cobalt iron oxide. The montmorillonite phase presents a stacking fold layer disposition, that was fitted using the Ufer Model.

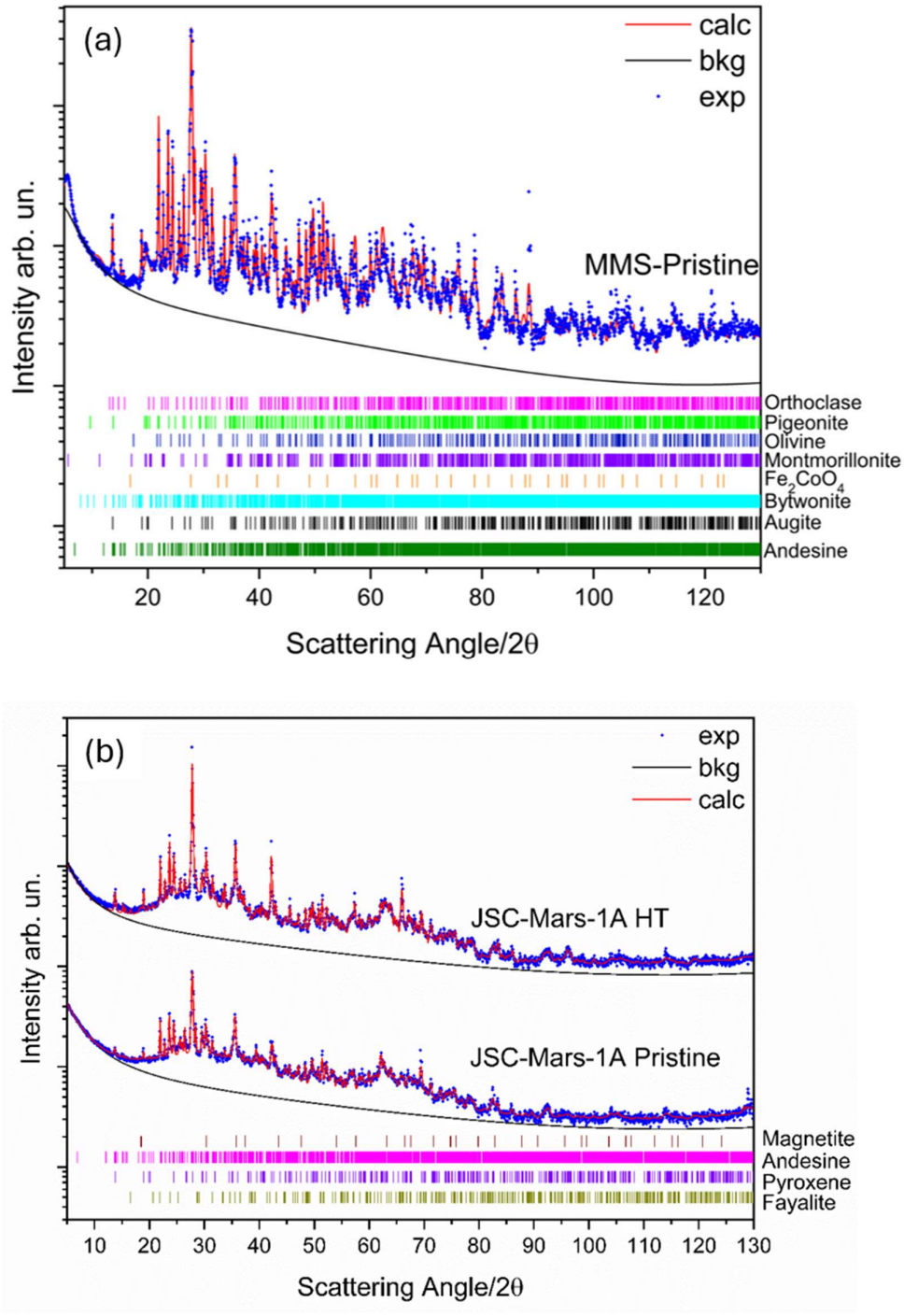

Figure 4.2 - XRD patterns of (a) pristine MMS and (b) JSC-Mars-1A (pristine and heat treated) simulants.

Results obtained in the present study on the composition of MMS simulant generally agree with previous literature findings, with some differences. Indeed, **Peters et al. [90]** also identified plagioclase and pyroxene phases, as well as magnetite and olivine, even though they did not estimate their quantity. More recently, **Clark et al. [214]** performed the quantitative phase analyses of the MMS simulant. The resulting amount of the plagioclase phase was relatively lower (60.7 wt.%) and that of pyroxene (20.7 wt.%) slightly higher compared to the results obtained in this work (**Table 4.2**). Additionally, **Clark et al. [214]** identified the presence of calcite (1 wt.%) as well as a high phyllosilicates content (15.6 wt.%) in the MMS simulant. Both phases were not indicated by the developers of this regolith simulant **[90]**. Accordingly, in this work no calcite was detected while a significantly lower quantity of phyllosilicates (3 wt.%) was found (**Table 4.2**).

Table 4.2 - Phase composition of pristine MMS and JSC-MARS-1A simulants obtained by Rietveld refinement (n.d.: not detected).

Phase	MMS-Pristine (wt. %)	JSC-Pristine (wt. %)	JSC-HT (wt. %)
Amorphous content	3	53	47
Phyllosilicates	3 (**Montmorillonite**)	n.d.	n.d.
Plagioclase	70 (**Andesine**) --- <1 (**Bytownite**)	25 (**Andesine**)	37 (**Andesine**)
Olivine	4	3 (**Fayalite**)	3 (**Fayalite**)
Pyroxene	8 (**Augite**) --- 8 (**Pigeonite**)	18	12
Magnetite	n.d.	1	1
K-feldspar	2 (**Orthoclase**)	n.d.	n.d.
Fe_2CoO_4	1	n.d.	n.d.

Moreover, **Clark et al. [214]** did not report the presence of olivine (4 wt.% in the current case). As stated by the same authors **[214]**, the analysed MMS batch was possibly sourced from a chemically altered area of the Saddleback basalt, and this feature provides a plausible justification for such discrepancies.

As for the pristine JSC-Mars-1A, **Figure 4.2b** and **Table 4.2** evidence the presence of a dominant fraction (53 wt%) of an amorphous phase. In addition, large quantities of plagioclase (25 wt.%) and pyroxene (18 wt.%) were also detected, along with olivine (3 wt.%) and magnetite (1 wt.%). These results match, from the qualitatively viewpoint (no quantitative analysis was provided), with the mineralogic phases indicated by the vendor **[92]**. More recently, **Shindler et al. [91]** provided a semi-quantitative analysis of crystalline phases, whereas the relevant amorphous counterpart (**Table 4.2**) was completely neglected. Nonetheless, the crystalline phases identified by **Shindler et al. [91]** are consistent with the findings of this work. Given the absence of quantification of the amorphous part, and the higher accuracy provided by the Rietveld refinement compared to semi-quantitative analyses, it can be stated that, compared to **Shindler et al. [91]**, the data reported in this work more closely mimic the actual phase composition of the simulant.

Table 4.2 also evidences the fact that the amorphous fraction in the JSC-Mars-1A system is reduced from 53 to 47 wt.% because of the heat treatment received. Correspondingly, the content of crystalline phases, in particular Plagioclase, increased from 25 to 37 wt.%.

4.1.3.2 Spark Plasma Sintering of the regolith simulants

The sintering behavior of MMS (pristine) and JSC-Mars-1A (preliminarily heat treated at 700°C) simulants can be deduced from the corresponding SPS outputs, namely sample shrinkage, and gas pressure inside the chamber, reported in **Figure 4.3** for experiments performed at T_D=1000°C and P=15 MPa.

It is apparent that the two simulants behave quite differently during the SPS test conducted under the same conditions. First, the final value of sample shrinkage (δ) for the JSC-Mars-1A system resulted to be about three times higher than that recorded for MMS. Such discrepancy is consistent with the relative densities of the resulting sintered samples, equal to 99.3 and 76.5% for JSC-Mars-1A and MMS, respectively. In addition, the densification of the latter one is observed to occur very

gradually, at a low rate, until the T_D value is achieved. In contrast, sample shrinkage increased very rapidly, particularly in the temperature range of 200-900°C, when the JSC-Mars-1A simulant was processed. Given the broader sintering window and lower temperatures required for the consolidation of JSC-Mars-1A, the effect of the dwell temperature on sample density was investigated in the range of 800-1000 °C for this system. On the other hand, this study was conducted in the range of 950-1050 °C when considering the MMS counterpart. The observed differences in sintering behavior could be primarily imputable to the diverse composition of the two simulants. In particular, as reported in **Figure 4.2 and Table 4.2**, JSC-Mars-1A is dominated by the amorphous fraction, which highly promotes sample densification, while MMS basically consists of crystalline phases such as andesine and pyroxenes.

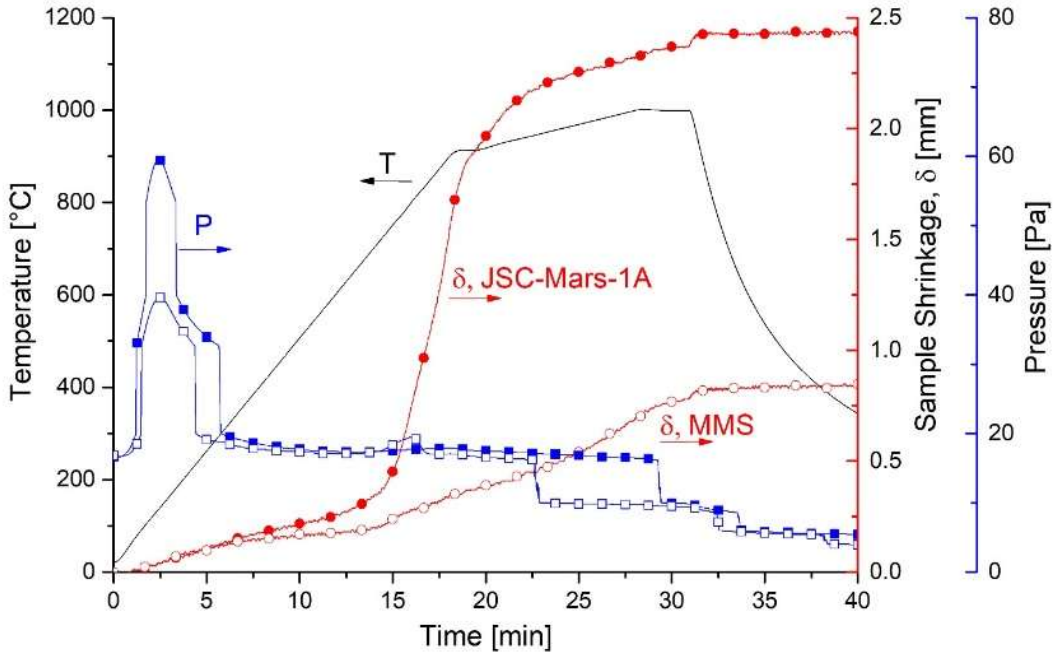

Figure 4.3 - SPS outputs (sample shrinkage, gas pressure inside the sintering chamber) and the corresponding temperature time profile recorded during the consolidation of JSC-Mars-1A (preliminarily heat treated) and pristine MMS regolith powders for the case of T_D=1000°C, P=15 MPa. Filled and empty symbols refer to JSC-Mars-1A and MMS, respectively.

The internal chamber pressure curves reported in **Figure 4.3** indicate that the gases release starting to occur inside the SPS chamber at about 100°C is more evident with JSC-Mars-1A. Such phenomenon can be likely attributable to the evaporation of the adsorbed water in both systems.

The effect of the dwell temperature and the applied pressure on product densification was investigated. **Figures 4.4a-4.4b** underline the positive effect of both parameters on the final specimen densities for the cases of JSC-Mars-1A and MMS, respectively.

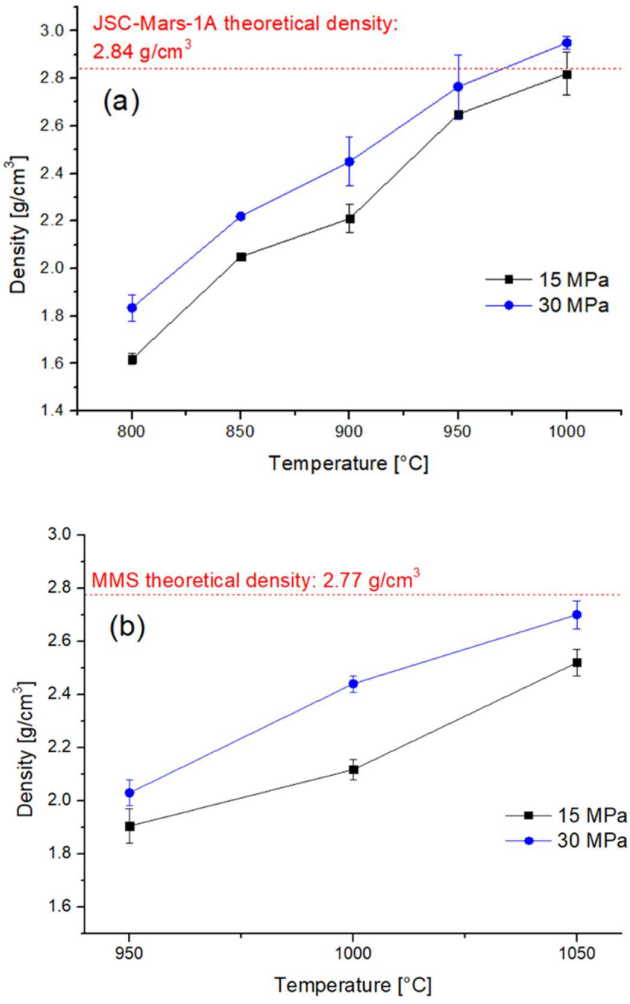

Figure 4.4 - Effect of the dwell temperature, at different mechanical pressure levels, on the density of bulk samples obtained by SPS from (a) JSC-Mars-1A (preliminarily heat treated) and (b) pristine MMS regolith simulants.

As for the JSC-Mars-1A, fully dense samples are obtained at 1000°C/30 MPa. In this regard, it should be noted that the measured density of certain samples obtained under such SPS conditions exceeded the theoretical value. This can be ascribed to the fact that the latter one refers to the starting simulant. However, as discussed afterwards, the JSC-Mars-1A sample is subjected to crystallization phenomena during SPS, which determine compositional/structural modifications, so that the theoretical density of the material is expected to change.

4.1.3.3 Compositional, microstructural and morphological characterization

Compositional and structural changes occurring when JSC-Mars-1A regolith was processed by SPS under different conditions can be deduced from the related XRD patterns shown in **Figure 4.5.** The amount of each phase estimated by Rietveld refinement are plotted in **Figure 4.6** and summarized in **Table 4.3**, while crystallite size, microstrain, and lattice parameters are reported in **Tables A11, A12 and A13**, respectively. **Figure 4.5** and **4.6** show that, during SPS, the amorphous fraction in the simulant progressively decreased down to 16 wt.% as the dwell temperature was augmented up to 1000°C. Correspondingly, the content of both andesine and, at a lower degree, pyroxene increases up to 57 and 23 wt.%, respectively. On the other hand, the relative amount of Fayalite and Magnetite remained nearly the same. As reported in **Table A11**, crystallite size of the different phases tends to increase as the SPS condition became progressively more severe.

In contrast with the behaviour displayed by JSC-Mars-1A regolith, the significantly lower content of the amorphous phase makes the MMS counterpart much more thermally stable. This is testified by the minor changes, with respect to the pristine simulant, in the XRD patterns of the samples produced at different SPS conditions (**Figure 4.7**). This feature is even clearer when observing the corresponding phases' amounts plotted in **Figure 4.8** (see also **Table 4.3** for a summary). The most considerable, but still limited, phase transition phenomenon is the disappearance of the montmorillonite phase, originally present in the pristine material, in the sample sintered at 950°C. In conclusion, it is possible to state that, apart from other minor oscillations, phases originally present in the MMS simulant preserve their quantitative distribution along the entire SPS experimental campaign.

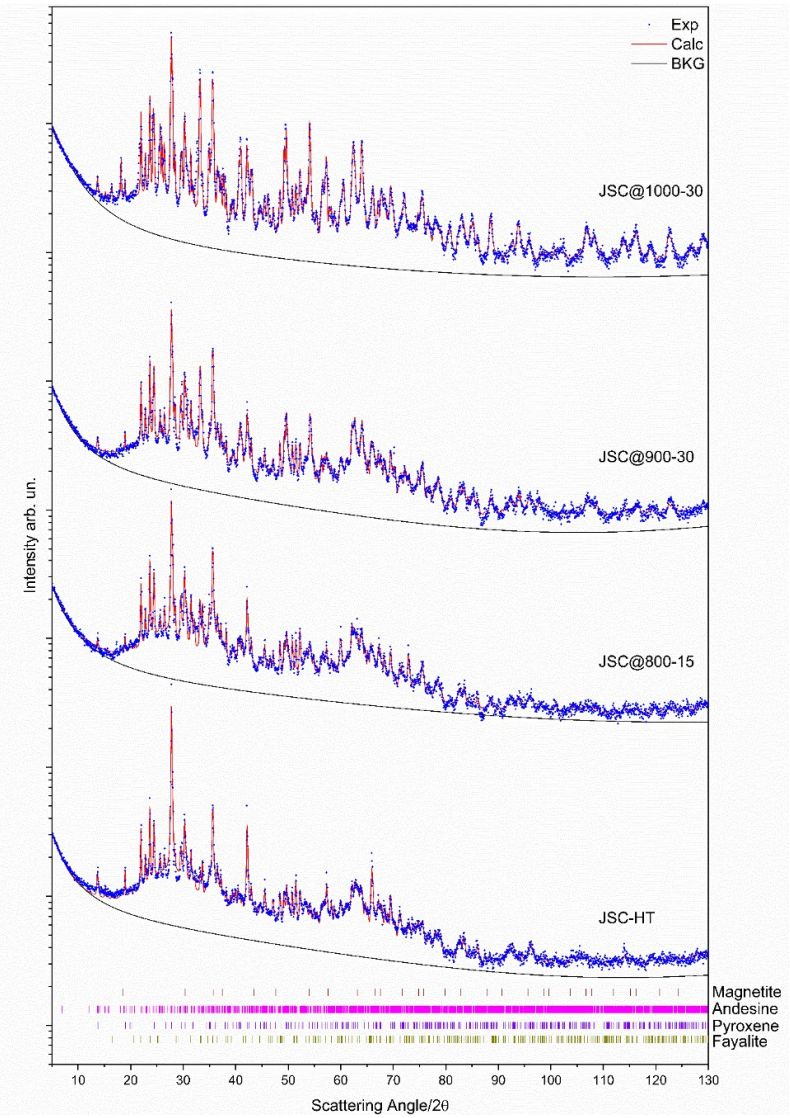

Figure 4.5 - XRD patterns of JSC-Mars-1A bulk samples obtained by SPS at T_D= 800, 900, and 1000°C. The XRD pattern of initial (heat-treated) simulant is also shown, for comparison.

Based on the results obtained, three SPS conditions have been selected for each simulant to produce the SPS samples to be subjected to optical measurements. Specifically, the JSC-Mars-1A specimens obtained at 800°C/15MPa (JSC@800-15), 900°C/30MPa (JSC@900-30), and 1000°C/30MPa (JSC@1000-30) were considered to cover a quite wide relative density range, i.e. from 57 to >99.9%. For the same reason, the MMS samples obtained at 950°C/30MPa (MMS@950-30), 1000°C/30MPa (MMS@1000-30), and 1050°C/30 MPa (MMS@1050-30) were selected.

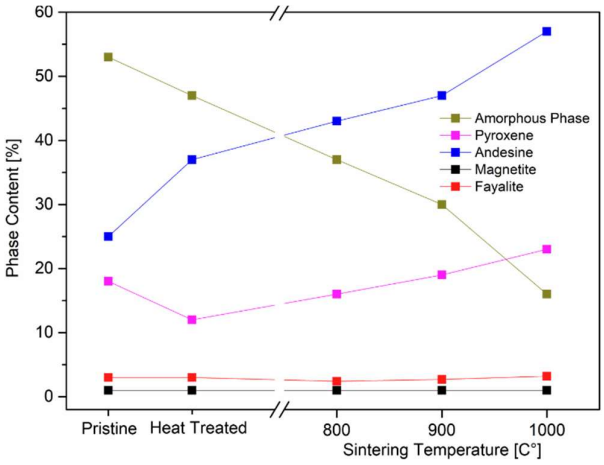

Figure 4.6 - Phase content changes, as determined by Rietveld analysis from XRD patterns (**Figure 4.5**), of JSC-Mars-1A regolith samples after heat treatment at 700°C and during SPS at T_D= 800, 900, and 1000°C with respect to the pristine simulant.

Table 4.3 - Phase composition of sintered JSC-Mars-1A and MMS simulants estimated by Rietveld refinement (n.d.: not detected).

Sample ID	Amorphous content (wt.%)	Plagioclase (wt.%)	Pyroxene (wt.%)	Olivine (wt.%)	Orthoclase (wt.%)	Magnetite (wt.%)	Other (wt.%)
JSC@800-15	37	43(Andesine)	16	2.4 (Fayalite)	n.d.	1	n.d.
JSC@900-30	30	47(Andesine)	19	2.7 (Fayalite)	n.d.	1	n.d.
JSC@1000-30	16	57(Andesine)	23	3.2 (Fayalite)	n.d.	1	n.d.
MMS@950-30	3	71(Andesine) + 1(Bytownite)	8(Augite) + 10(Pigeonite)	2	2	n.d.	3 (Fe_2CoO_4)
MMS@1000-30	2	74(Andesine) + 1(Bytownite)	5(Augite) + 10(Pigeonite)	1	3	n.d.	4 (Fe_2CoO_4)
MMS@1050-30	2	76(Andesine) + 1(Bytownite)	8(Augite) + 7(Pigeonite)	1	1	n.d.	4 (Fe_2CoO_4)

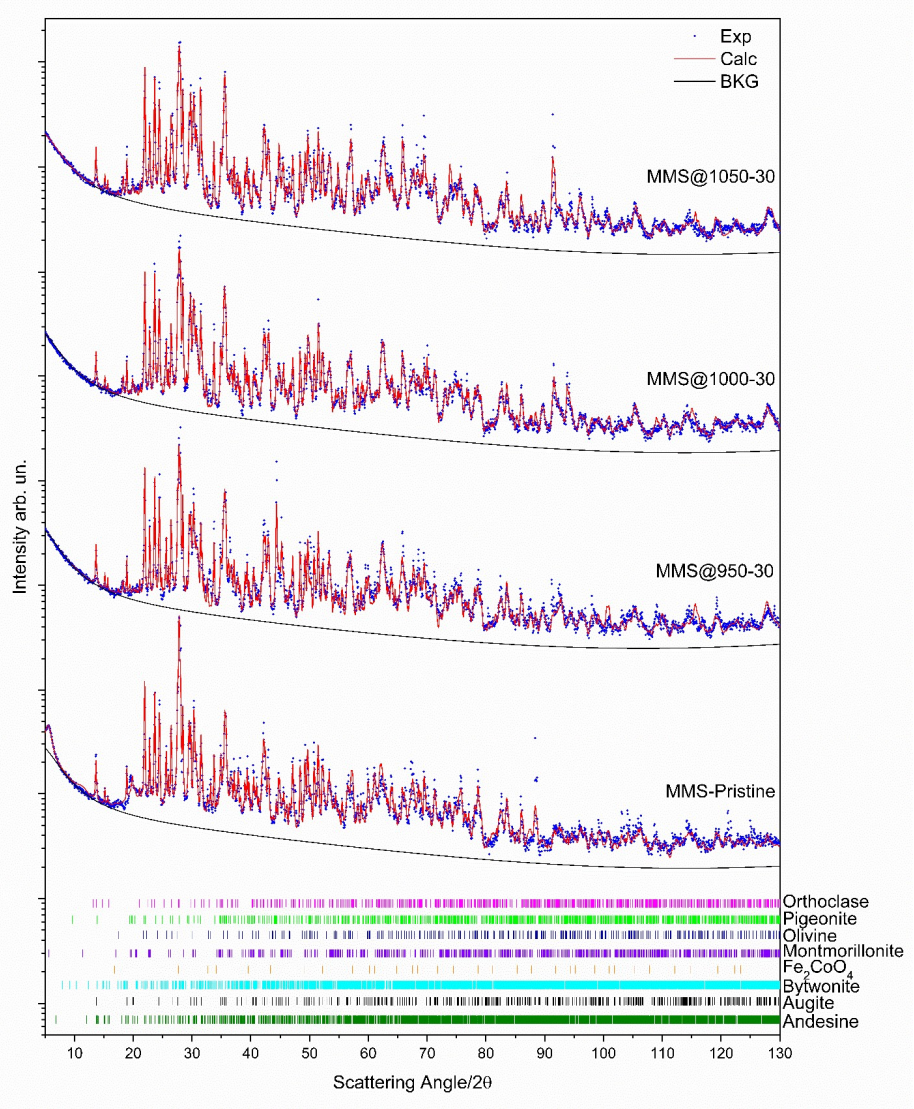

Figure 4.7 - XRD patterns of MMS regolith samples: pristine simulant, and corresponding bulk samples obtained by SPS at T_D= 950, 1000, and 1050°C.

SEM images reported in **Figure 4.9** show the morphological differences on the surface of JSC-Mars-1A and MMS samples sintered at different conditions which will be further characterized from the optical viewpoint. In particular, the JSC@800-15 sample (57% dense) appears to be poorly consolidated, suggesting that the sintering process is in its early stage. On the other hand, JSC@900-

30 (86.3% dense) and, especially, JSC@1000-30 (>99.9% dense) products are highly densified. As for the MMS simulant, **Figure 4.9** shows a different scenario.

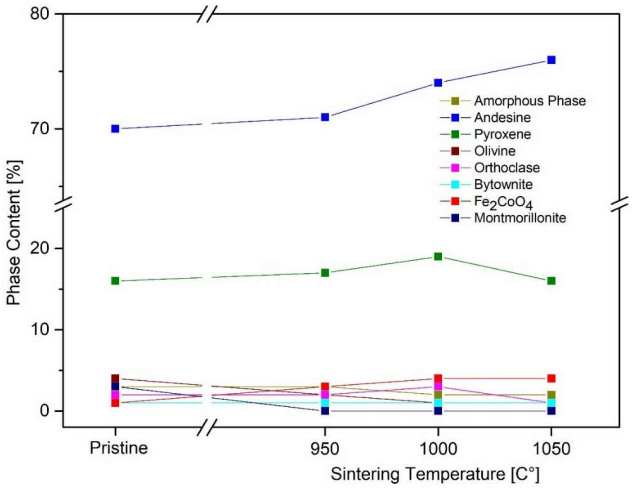

Figure 4.8 - Phase content changes, as determined by Rietveld analysis from XRD patterns (**Figure 4.7**), of MMS regolith samples during SPS at T_D= 950, 1000, and 1050°C with respect to the pristine simulant.

Indeed, even if a progressive densification improvement is achieved as sintering temperature was augmented, bulk MMS samples appear to be less compacted, compared to the JSC-Mars-1A ones, even at the most severe conditions adopted for this system (1050°C/30MPa). Thus, consistently with density data reported in **Figures 4.9(a)-4.9(b)** the MMS system clearly exhibits a more refractory nature with respect to the other simulant.

Since surface porosity and roughness characteristics are expected to affect the optical properties of the bulk samples, these properties have been measured. The obtained results are reported in **Table 4.4**, and **Table 4.5**, respectively. The obtained values confirmed the trend showed by the SEM images (**Figure 4.9**). In particular, the MMS@1050-30 sample resulted to be rougher and more porous than the JSC@1000-30 one. It should be noted that some surface pores observed in bulk samples of both systems (**Figures 4.9a-4.9b**) are due to grain pulling-out generated during the polishing procedure. Therefore, the surface porosity seen in **Figures 4.9a-4.9b** is not representative of the actual densification levels achieved during the SPS process, which are significantly higher.

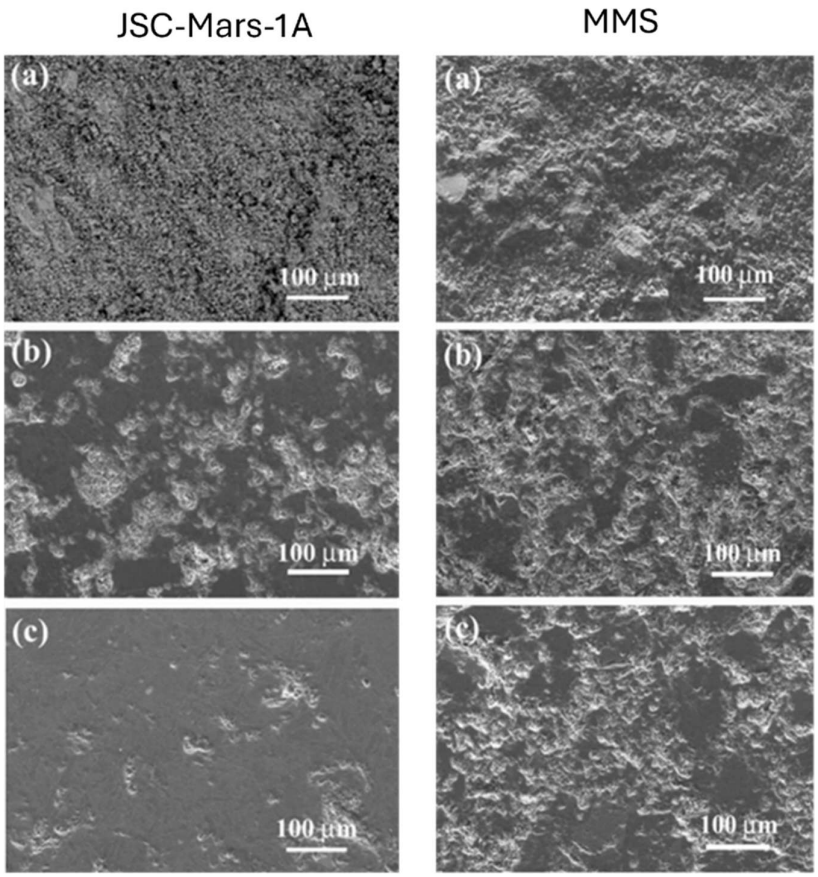

Figure 4.9 - SEM micrograph of SPS samples obtained from the two regolith simulants. JSC-Mars-1A: (a) JSC@800-15, (b) JSC@900-30, and (c) JSC@1000-30; MMS: (a) MMS@950-30, (b) MMS@1000-30, and (c) MMS@1050-30.

Table 4.4 - Average values and standard deviation of surface porosity measured by image analysis on the bulk JSC-Mars-1A and MMS samples obtained by SPS at different conditions.

Simulant	Sample ID	T_D (°C), P (MPa)	Porosity (vol. %)
JSC-Mars-1A	JSC@800-15	800°C, 15 MPa	38.15 ±5.76
	JSC@900-30	900°C, 30 MPa	24.19 ±9.17
	JSC@1000-30	1000°C, 30 MPa	5.47 ±1.59
MMS	MMS@950-30	950°C, 30 MPa	39.86 ±7.10
	MMS@1000-30	1000°C, 30 MPa	34.47 ±10.48
	MMS@1050-30	1050°C, 30 MPa	12.69 ±4.23

Table 4.5 - Average values and standard deviation of roughness parameters measured on the bulk JSC-Mars-1A and MMS samples obtained at different SPS conditions.

Simulant	Sample ID	Ra [μm]	Rz [μm]	Rq [μm]
JSC-Mars-1A	JSC@800-15	10.05±1.03	86.26±9.24	12.86±1.35
	JSC@900-30	1.19±0.08	17.85±3.19	1.78±0.20
	JSC@1000-30	0.48±0.07	12.70±3.33	0.90±0.18
MMS	MMS@950-30	10.49±2.47	84.16±27.66	13.71±3.51
	MMS@1000-30	2.01±0.13	20.45±2.74	2.66±0.19
	MMS@1050-30	1.21±0.09	14.27±2.21	1.73±0.13

4.1.3.4 Optical properties characterization

Preliminarily, optical properties were assessed for the powdered simulants, whose hemispherical reflectance spectra are shown in **Figure 4.10**. The spectrum of untreated JSC-Mars-1A fairly agrees with the available literature data in the range 0.4-2.2 μm wavelength for the similar JSC-Mars-1 simulant **[215]**. As for MMS, the measured reflectance also agrees with available spectra of MMS-2 in the UV-visible-Near-IR **[216]**.

The thermally treated JSC powder shows a considerably increased reflectance with respect to the untreated one. In agreement with published data **[90]**, MMS powders are characterized by a higher reflectance than pristine JSC-Mars-1A in the visible-NIR, even if it is still lower than that of the heat-treated simulant. The highest reflectance for wavelengths longer than 3 μm is shown by MMS. Both pristine simulants and both JSC-Mars-1A samples' curves are characterized by a relatively featureless ferric absorption edge through the visible, an indication of a ferric absorption band around 0.8-0.9 μm (more pronounced in MMS), and relatively flat absorption in the near-IR, except for the bands around 1.4 and 1.9 μm (less intense in MMS), which can be ascribed to OH and H_2O which are not expected in real Mars regoliths **[90]** due to the much drier planetary environment.

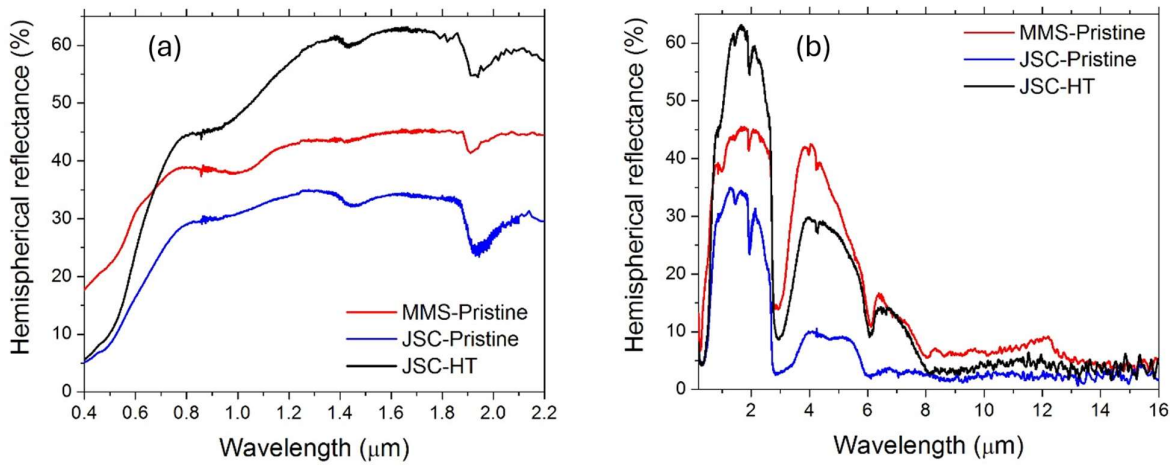

Figure 4.10 - Reflectance spectra of the simulants in powder form. (a) Spectral range 0.4-2.2 μm, to allow the comparison with **Allen et al. [215]** and **Peters et al. [90]**; (b) Full range 0.19-16.0 μm investigated in this work.

Before further describing and discussing the optical properties of such simulants, it should be briefly noted that, as for optical properties, the simulants here investigated are considered as a valid approximation for specific planet locations. For instance, JSC-Mars-1 (of which JSC-Mars-1A is the second produced batch) is recognized to simulate well the bright regions on the surface **[216]**, as well as to reproduce the chemical composition of regoliths analyzed in the course of the Viking lander, Mars and Spirit Rover missions **[99]**. As for the MMS simulant, a similar version named MMS-2 is recognized to offer a good match with the observations of the NOMAD instrument on the ExoMars 2016 Trace Gas Orbiter taken at the Elysium Planitia in clear sky conditions and available in the 400–600 nm wavelength range **[216]**.

Figure 4.11 shows the reflectance spectra of the ceramics sintered at various temperatures, and those of the corresponding powders. Despite the different absolute values in the spectral region below 8 μm between JSC-Mars-1A and MMS-based samples, the two groups show a qualitatively similar behavior: as the sintering temperature is increased, the reflectance decreases for wavelengths lower than 8 μm, while it increases for longer wavelengths. Sintered samples have a generally lower reflectance than the starting powders in the spectral range below 8 μm, whereas this value become higher above this wavelength. If the spectra of sintered pellets are concerned, it should be observed that optical properties of ceramic bulks depend on several parameters: chemical

composition, phases occurring and their relative amounts, total porosity, pore size, grain size, grain crystallographic orientation, and surface roughness. However, among them, the primary parameters affecting optical properties of ceramics for solar applications on Earth have been identified to be the chemical and phase composition **[52,217]**. This seems to provide a reasonable explanation for the differences shown in the spectral shapes of curves in **Figure 4.11**, also considering the opposite trends shown by the curves for wavelengths below and above 8 μm as a function of the sample density. However, surface features like roughness and porosity, here given in Table 4.4 and 4.5 as informative data, will be useful degrees of freedom to further optimize optical properties **[218]**, once the most promising composition/processing technique has been identified.

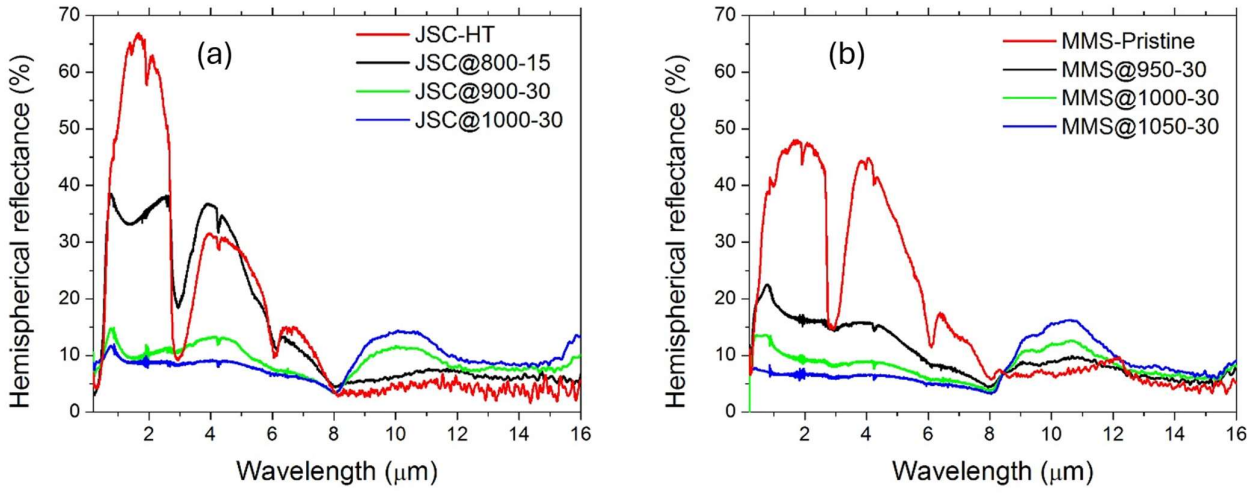

Figure 4.11 - Reflectance spectra of the sintered ceramics obtained from (a) the JSC-Mars-1 simulant and (b) the MMS simulant. The spectrum of the corresponding powders (the annealed one, in case of JSC-Mars-1 simulant) is also indicated for comparison.

4.1.3.5 Optical properties discussion

Before evaluating the potential of a technological application, it is important to define the framework where it should operate. Mars has both similarities and important differences with respect to Earth **[219]**, as summarized in what follows:

1) the duration of the day/night cycle is similar to the terrestrial one;

2) it has an atmosphere, albeit thinner than that of Earth, mainly consisting of CO_2, N_2 and Ar and typically containing a significant amount of suspended dust, which scatters the incoming sunlight;
3) ice is present on the poles which eventually can be used as a source of CO_2 and water;
4) it has a tilted axis, which causes seasons that last longer than terrestrial ones, since the Martian year is about twice longer (669.6 sols i.e. Martian days, equivalent to 687 Earth days). Moreover, while terrestrial seasons are evenly spread over the year, on Mars they vary in length because of the more elliptical orbit: spring in the northern hemisphere (autumn in the southern) is the longest season at 194 sols. Autumn in the northern hemisphere (spring in the southern) is the shortest at 142 sols. Northern winter/southern summer is 154 sols, and northern summer/southern winter is 178 sols. Further differences are concerned with the lower solar irradiance on Mars, being farther from the Sun, and the lower surface temperatures ranging from 130 to 300K **[220]**;
5) finally, dust storms due to winds happen occasionally with a site-dependent occurrence. These phenomena can be local or global, with the latter that can last for weeks and even months. Storms strongly attenuate atmospheric transmission, decreasing the direct solar irradiance on the planet surface and increasing the diffuse component. An extensive database has been built for the optical depth of Mars atmosphere from the data collected from the rovers during several missions (Viking **[213]**, Pathfinder **[32]**, Spirit, Opportunity **[222]**, Curiosity **[223]**, Perseverance **[224].** These data allow to identify the latitudes and seasons where dust storms preferentially occur and, on the other hand, those with the lowest probability. In addition to intensity and light propagation direction, the atmospheric dust modifies the sunlight spectral distribution as well, which, at the planet surface results therefore blue- deficient and enriched in red and IR with respect to the AM0 spectrum. These spectral modifications depend on the dust thickness: the smallest thickness is at high sun angles (mid-day, low latitudes), and for low atmospheric dust content (northern hemisphere summer), while the largest thickness is at low sun angles (early and late in the day) and for high dust content (northern hemisphere winter).

Therefore, due to such a complex scenario, to preliminarily assess the potential of sintered regoliths for solar energy harvest and storage, it was considered, as a case-study, the solar irradiance spectra reported in **Vicente-Retortillo et al. [225]**, corresponding to specific conditions (latitude=0°, winter

solstice at the northern hemisphere, local noon) and with two values of atmosphere optical depth τ: clear-sky (τ=0.3) and dusty (τ=1). It was then calculated the solar absorptance of the materials from Eqs. (25) and (27) considering both the total solar radiation reaching the surface and the direct-only component (i.e. the part of radiation which has not been scattered by the atmosphere). The first case deals with applications where the materials are subjected to non-concentrated solar radiation, like in buildings, to harvest and store heat for habitation or agriculture. The second case deals with applications requiring concentration of solar radiation, i.e. the production of heat at higher temperatures for either thermal use or power production, because the direct component only can be concentrated by optical systems.

Table 4.6 lists the calculated values of solar absorptance. All the sintered simulants always show a higher solar absorptance than the corresponding powders, with values increasing with the sample density. At the lowest and highest sample densities, the absorptance of MMS-based bulks is superior to that of JSC-based ones, while the reverse is true for the samples with the intermediate density level. The absorptance values of each MMS sintered sample and those of the highest-density JSC are very stable and do not change neither for different conditions of dust in the atmosphere nor if we consider direct or total radiation.

Table 4.6 - Solar absorptance values calculated from Eqs. (25), (27).

Sample	**α (total radiation)**	**α (direct radiation)**	**α (total radiation)**	**α (direct radiation)**
	Clear Sky		Dusty	
MMS-Pristine	0.70	0.70	0.69	0.70
MMS@950-30	0.80	0.80	0.80	0. 80
MMS@1000-30	0.87	0.87	0.87	0.87
MMS@1050-30	0.93	0.93	0.93	0.93
JSC-HT	0.72	0.73	0.72	0.74
JSC@800-15	0.75	0.75	0.74	0.75
JSC@900-30	0.88	0.89	0.88	0.89
JSC@1000-30	0.90	0.90	0.90	0.90

Conversely, for the lowest and mid density JSC-Mars-1A -based ceramics, and for both powders as well, some small differences (lower than 1%) in absorptance have been found depending on the dust conditions or the total or direct solar radiation. Overall, both dense samples show a remarkable solar absorptance of 0.90 (JSC-Mars-1A) and 0.93 (MMS), compared with that of powders (0.69-0.70 and 0.72-0.74 only, respectively), showing the potential of using sintered bodies for solar heat production. These remarkable values are maintained for both total radiation and the direct component, proposing them both to be used for absorption of non-concentrated solar radiation, for instance as construction material or residential solar heat collectors (similar to the concept of residential thermal solar panels on Earth), as well as energy-production material in solar-concentrating systems. As a term of comparison, it should be mentioned that optimized solar-selective surfaces for flat-panels solar collectors on Earth (TiNOX® Energy, Almeco) show a solar absorptance of 0.94 **[226]**, fully comparable to the value of our MMS dense bulk, which, however, still has to be optimized.

Figure 4.12 shows samples' thermal emittance estimated using Eqs. (25), (26), (28) in the temperature range 100-600 K. Below 300 K, which is the maximum temperature naturally occurring on the Martian surface **[220]** the higher (JSC-Mars-1A) or a comparable (MMS) emittance with respect to sintered simulants can be found in the powders, which, interestingly, also displayed the lowest solar absorptance. Conversely, the samples with the highest solar absorptance values are also characterized by the lowest emittance. This combination of properties is very promising for converting solar radiation into heat, as the highest efficiency in collection (high α value) is merged to the lowest thermal losses by radiative effects (low ε). Such finding proves the promising approach, for energy applications and within the ISRU perspective, of sintering planetary regolith to produce materials with radically different properties with respect to the pristine ones. At higher temperatures, the emittance of these simulants increases with temperature only about 1% (JSC-Mars-1A) and 2% (MMS) at most, with overall values between 0.90 and 0.95. This makes them promising candidates as radiating materials (e.g. in radiating furnaces or in other applications where the controlled release of heat is required). As for the powders, emittance monotonically drops to 0.84 (JSC-Mars-1A) and 0.80 (MMS), making them more suited as heat storage media. The lowest-density JSC-Mars-1A specimens show an emittance temperature trend similar to that of the starting

powders albeit with a lower emittance, which similarly potentially qualifies them for thermal energy storage applications.

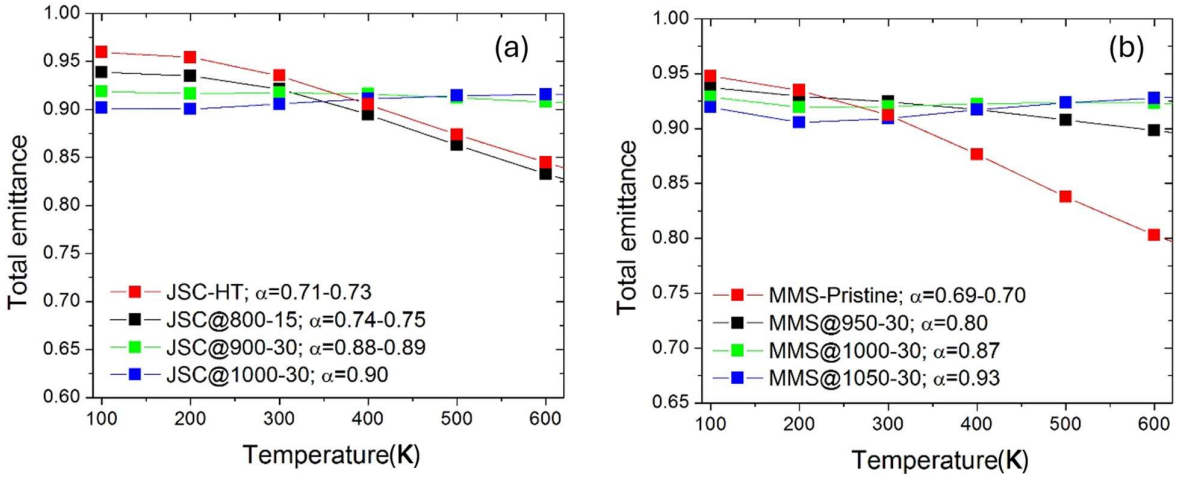

Figure 4.12 - Total emittance calculated from normal hemispherical reflectance spectra for JSC-Mars-1A (a) and MMS (b) samples (Eqs. (25), (26), (28)).

For the mentioned applications, a key parameter is thermal conductivity. **Table 4.7** lists the literature values for some Mars and Lunar regolith simulants, either in powder or bulk forms. It is known that thermal conductivity is affected by several factors besides composition, including particle size (for powders), porosity and atmospheric pressure. Typically, thermal conductivity k of bulk solids is higher than that of powders, this property decreases with sample porosity, and, for porous solids, higher ambient pressures entail higher k. For sintered Lunar regolith simulants, it has been shown a 200-fold increase in thermal conductivity for sintered ceramics with respect to the original powders **[205]**.

From **Table 4.7**, we can see that the considered powdered simulants, which have different compositions, all show a thermal conductivity of the order of magnitude of few 10^{-2} W/mK, reaching values around 10^{-1} W/mK for higher pressures. On the other hand, reported values for thermal conductivities of sintered Mars simulants are in the range 2.8-3.1 W/mK for the dense BH-Mars-S sample (porosity <1%), slightly lower for samples with larger porosity, and about 2.0 W/mK for sintered Lunar simulants. From these results, it is reasonable to expect comparable k values for our

sintered pellets. Therefore, our results on optical properties, associated with literature data on thermal conductivity, confirm the high ISRU potential of regoliths as well as the high level of property manipulation and optimization supplied by the parameters of the sintering process.

Table 4.7 - Literature values of thermal conductivity of some regolith simulants and comparison with terrestrial basalt rocks.

Regolith type	**Sample density (ρ) or porosity (γ)**	**Conditions**	**Thermal conductivity k [W/mK]**	**Reference**
JSC-Mars-1 (powder)	ρ=1.30 g/cm^3	P=0.1÷20 Torr	**k** ~0.01÷~0.1	**[227]**
	ρ=0.91 g/cm^3	P=5 mbar	**k** ~0.07÷~0.12	**[228]**
MMS (powder)	ρ=55÷60% (1.54÷1.66 g/cm^3)	P=600÷2000Pa T=-30÷30 °C	**k**=0.03÷0.07	**[229]**
Actual, data from InSight Mars mission	**γ**=~63%	Real Martian conditions	**k**=0.039±0.002	**[230]**
BH-Mars-S Simulant (sintered solids)	**Sample PSD2-1200°C** **γ**=~10–15%	–100 °C, –60 °C, –20 °C, +20 °C	**Sample PSD2-1200°C** T=-100°C, **k** =2.70 T=+20°C, **k** =2.95	**[231]**
	Sample PSD2-1250°C **γ**=<1%		**Sample PSD2-1250°C** T=-100°C, **k** =2.80 T=+20°C, **k** =3.08	
Lunar regolith simulant (for comparison) - Powder			**k** =0.01	**[205]**
- Sintered solid			**k** ~2.0	
Basalt rock (for comparison) solid			**k** =2.1	**[205]**
			k= 1.5–2.5 W	**[231]**

Notably, such property tunability translates into application flexibility. For instance, when thermal insulation is needed (e.g., in lining habitat walls, or in insulation structures around thermal batteries), regolith should be used as powder or porous solid. In order to supply the needed level of thermal comfort to the interior of habitats, this property should be combined with a high thermal emittance. On the contrary, insulation of thermal batteries requires a low thermal emittance to reduce radiation losses. Still in the field of buildings application, the exterior of habitats should feature a high solar absorptance, which fits with the characteristics of dense sintered regoliths. Similarly, to maximize the thermal solar energy harvest and the efficient transfer to the storage medium, the high solar absorptance and thermal conductivity of dense pellets should be considered. In addition, the storage of sensible heat into a thermal mass would benefit from low thermal emittance combined to high thermal conductivity, to reduce losses and to have an efficient charge/discharge, respectively.

Based on the results above, it is possible to state that the sintering process drastically changed the optical spectra. Very interestingly, the bulk specimens showed a significantly higher solar absorptance than the corresponding powders, with a remarkable value of 0.93 for the highest density MMS sample. As a term of comparison, it is worth to note that this value is approaching that of one of the most advanced thermal solar absorber material available in thermal solar collectors for terrestrial building market to date (TiNOX® Energy, Almeco). At the same time, the thermal emittance of ceramics is lower than that of powders for temperatures below about 300K, and superior for higher temperatures, with values which remain quite stable in the whole investigated temperature range.

Overall, this study proves that sintered and powder regoliths can be synergistically used for different scopes within the ISRU perspective. These include energy production in solar-concentrating systems, storage and release of harvested thermal energy, as well as absorption of non-concentrated solar radiation, while, for example regolith-based compositions employed as construction material.

In this context, mechanical properties play also a prominent role, as an appropriate construction material would need sufficient strength to build permanent bases for future manned missions on Mars. In this regard, the possibility of the construction material to collect solar energy would be of the utmost utility, given the low temperatures recorded on Mars, which can vary from about 130 to 300K according to the day/night and seasonal cycle **[220]**.

The activity and related results discussed in this Section was reported in the following paper: **Casu, M.**, Orrù, R., Licheri, R., Concas, A., Cau, C., Garroni, S., Dell'Oro, A., & Sani E., Processing and Optical properties of Martian Regolith for Solar Energy Applications. Submitted to *Acta Astronautica*.

In this framework, while the processing and microstructural characterization was performed at the University of Cagliari, the evaluation of optical properties and interpretation of the obtained data was carried out at the National Institute of Optics of the Italian National Research Council (CNR-INO).

4.2 Enhanced properties of spark plasma sintered additive-free Martian soil simulants

4.2.1 Introduction

One of the key aspects for the development of a permanent base on Mars is represented by the fabrication of sheltering constructions. The latter ones, other than possessing the necessary structural characteristics, should also withstand to additional threats Mars environment poses, including radiation, dust storms and boulder impacts **[37,44,232]**. Regarding the low temperatures of planet Mars **[220]**, a valuable strategy could be the direct absorption of sunlight, as proposed in **Section 4.1**, accompanied with adequate thermal insulation of the outer base walls.

The materials to be chosen would therefore need to comply with these requirements. Adequate mechanical properties can be achieved after the consolidation of loose Martian regolith. Indeed, several studies have been addressed to regolith consolidation, as reported in **Section 2.2.2**. To this aim, as anticipated in the previous Section, various techniques, including pressureless sintering **[99,100]**, combustion synthesis-based processes **[101-103]**, impact compaction **[104]**, solar sintering **[105]**, additive manufacturing **[99,106],** aggregate bonding **[233,234]**, cold sintering **[107]**, and very recently Spark Plasma Sintering (SPS) **[112,113]** have been proposed. The most representative examples, also involving the evaluation of compressive and flexural strengths, the mechanical properties more typically investigated on Martian regolith derived products, are reported in **Table 4.8**. From this Table, it is possible to observe that, regardless of mechanical testing methods utilized to assess either compressive or flexural strengths, adequate densification levels achieved after sintering usually led to satisfactory properties, comparable or higher than those of concrete used on Earth. A further reduction of sample porosity is expected beneficial to produce even superior mechanical performances, as reported for lunar regoliths or general construction materials **[45,235]**, as well as better radiation shielding capabilities against primary particles, being the stopping power proportional to the material density, according to the Bethe-Bloch formula **[236]**. Another relevant property for the proposed application of Martian regoliths is hardness. In a previous work, the HV value of 710±30 was measured for 59% porous JSC-Mars-1A consolidated via power bed fusion **[232]**.

Table 4.8 - Examples of research studies involving the processing of different Martian regolith simulants and the mechanical characterization of the resulting bulk samples in terms of compressive and flexural strength. When missing, relative densities were calculated from the measured absolute values; n.r.: not reported.

Simulant (additive)	Processing technique	Sample size (mm)	Relative Density (%)	Property (method)	Measured Value (MPa)	Ref.
MGS-1	Cold sintering	Cuboid: 2.5x2.5x2.5	88	Compressive Strength	43	**[25]**
MGS-1	SPS	Cylinder: ***d*** = 20; ***h*** = 20	Up to 85.4	Compressive Strength	Up to 102.7	**[112]**
JEZ-1	SPS	Cylinder: ***d*** = 20; ***h*** = 20	Up to 89.05	Compressive Strength	Up to 136.7	
JSC Mars-1A (Sulphur)	Sulphur concrete	Cuboid: 25.4x25.4x25.4	n.r.	Compressive Strength	63	**[234]**
		Cuboid: 25.4x25.4x127	n.r.	Flexural strength (three-point bending test)	2.3	
MGS-1	SPS	Cylinder: ***d*** = 20; ***h*** = 4	90	Flexural Strength (ball-on-ring test)	24	**[113]**
MGS-1 ($5\%\ Bi_2O_3$)			98		52	
Mixture of MGS-1-MGS-1C (Polymeric binder)	Additive Manufacturing + Pressureless sintering	Cylinder: ***d*** = 16; ***h*** = 2.5	82.7 (Sintering in Air); 83.0 (in Martian atmosphere)	Flexural Strength (ball-on- three balls test)	53.5 (Air); 57.6 (Martian atmosphere)	**[100]**
JSC Mars-1A	Quasi-static compaction / impact compaction	Cuboid: 10x4x3 or 5x2x0.6	n.r.	Flexural Strength (three-point bending test)	50	**[104]**

JSC-Mars-1A (Polyethylene)	Liquid infiltration	Cylinder (Compressive strength): ***d*** = 12.7; ***h*** = 25.4	n.r.	Compressive Strength	41.1	**[233]**
		Cuboid (Flexural strength) of 1:16 thickness to height ratio	n.r.	Flexural strength (three-point bending test)	45	

As observed in **Table 4.8**, SPS is one of the technologies considered for processing Martian regolith, mostly due to its low energy request, compared to conventional hot-pressing **[82]**, which is expected to be highly beneficial in such context. Compared to conventional hot-pressing, which is based on the use of external heating elements, lower energy consumption is requested by SPS, where electric current passes directly through the die and, when electrically conductive, the powder sample, thus generating heat and promoting sintering **[82]**. In addition, the vacuum condition typically adopted during SPS is not so different from the pressure level encountered in Martian atmosphere (about 6 mbar) **[237]**. Furthermore, SPS also permits the obtainment of high densification degree in the sintered regolith, with no need for additional binders, which may not be available *in-situ*. The SPS technology has been also successfully used to process lunar regolith simulants **[108-111,238]**. JSC-Mars-1A and the Mojave Mars Simulant (MMS) were also consolidated by SPS to evaluate their optical properties, as described in **Section 4.1**. To this aim, differently densified samples were produced by empirically varying the dwelling temperature (T_D), and/or the applied pressure (P).

The mechanical characterization of regolith samples produced by SPS was addressed only in two recent studies **[112,113]**. As reported in **Table 4.8**, the maximum compressive strength values measured by **Min et al. [112]** on sintered MGS-1 (up to 85.4% dense) and JEZ-1 (up to 89% dense) simulants were 102.7 MPa (T_D=1100 °C, dwelling time t_D=60 min, P=100MPa) and 136.7 MPa (T_D=1100 °C, t_D=60 min, P=51Pa), respectively. Moreover, flexural strength values reported by **Hoekman [113]** for additive free (90% dense, T_D=1060 °C, t_d=15 min, P=50 MPa) and 5% Bi_2O_3 containing (98% dense, T_D=1050 °C, t_d=15 min, P=50 MPa) MGS-1 samples were 24 and 52 MPa, respectively. Such encouraging preliminary results are expected to be further improved if higher consolidation levels are achieved.

Along this line, an ad-hoc optimization of the SPS process when considering Mars Global (MGS-1) and Jezero Delta Crater (JEZ-1) simulants will be first performed in this work by varying the applied pressure (P), dwelling temperature (T_D), and holding time (t_D). More specifically, a fractional factorial design based on Design of Experiment (DoE) method is chosen, where the influence of the three tunable SPS parameters indicated above is studied according to the so-called Taguchi method **[239]**. This technique, which allows for screening efficiently the effects produced by several process parameters, avoids the need for an excessive number of experimental runs.

The identified optimal SPS conditions will be used to produce highly consolidated bodies, whose compressive strength, flexural strength and Vickers hardness are evaluated. For the sake of comparison, the latter mechanical properties will be also measured on the JSC-Mars-1A and MMS samples obtained via SPS, according to the optimized experimental procedure described in **Section 4.1**.

4.2.2 Materials and Methods

The Martian regolith simulants used in this work are JSC-Mars-1A, MMS, MGS-1, and JEZ-1. Their composition in terms of oxides content (wt.%) is reported in **Table 2.2**, whereas their mineralogical constituents and related contents in **Table 4.9.** Thermogravimetric analyses were performed on pristine and processed MGS-1 and JEZ-1 simulants using a simultaneous DTA-TGA Instrument (NETZSCH STA 409PC Luxx, Germany). The tests were designed with a heating rate of 2 K/min from room temperature to 800 °C, to complete what was already observed for JSC-Mars-1A and MMS in **Section 4.1** (**Figure 4.1**).

These tests were aimed at evidencing if one or more pristine simulants displays significant outgassing phenomena and, in this case, at which temperature they cease to occur. From the obtained results, it is possible to define if, and at which condition, a preliminary heat treatment is needed before consolidation experiments. Indeed, the release of a large amount of gases should be avoided during SPS, where powders are confined into a graphite container, so that a series of negative drawbacks (residual porosity in sintered samples, die/plunger breakage, safety problems, etc.) would correspondingly take place.

Table 4.9 – Summary of phase composition of pristine MMS and JSC-MARS-1A simulants obtained by Rietveld refinement (see **Section 4.1**) and pristine MGS-1 **[93]** and JEZ-1 simulants **[94]**.

Mineral	**JSC-Mars-1A (Section 4.1)**	**MMS (Section 4.1)**	**MGS-1 [93]**	**JEZ-1 [94]**
Amorphous fraction	53	3	-	-
Glass-rich basalt	-	-	22.9	13.5
Plagioclase	25	71	27.1	16.0
K-feldspar	-	2	-	-
Pyroxene	18	16	20.3	12.0
Olivine	3	4	13.7	32.0
Mg-sulfate	-	-	4.0	2.4
Anhydrite	-	-	1.7	1.0
Ferrihydrite	-	-	3.5	2.1
Iron Spinel	1	1	1.9	1.1
Hematite	-	-	0.5	0.3
Mg-carbonate	-	-	-	11.0
Fe-carbonate	-	-	1.4	0.8
Hydrated silica	-	-	3.0	1.8
Phyllosilicates	-	3	-	6.0

According to the obtained results, prior to SPS experiments, JSC-Mars-1A and JEZ-1 powders were heat treated at 700 °C for 2 h in air using a muffle furnace (LT 24/11/B410, Nabertherm, Lilienthal, Germany), and then stabilized in air environment at room temperature. Theoretical densities of the

simulants were determined by a gas displacement pycnometer (AccuPyC 1340, Micromeritics, USA) using helium as adsorbed gas.

Before being processed by SPS, MGS-1 and JEZ-1 regolith simulants were ball milled for 10 min (Spex Mixer Mill 8000M, USA, balls to powder weight ratio equal to 2) to reduce their particles size to less than 150 μm, whereas such condition was already satisfied by the MMS and JSC-Mars-1A powders employed for this study. Particle size distribution was evaluated by a laser light scattering analyzer (CILAS 1180, France).

Bulk samples were obtained by processing regolith powders by the SPS apparatus described in **Section 2.2.2**. Dwelling temperature (T_D), dwelling time (t_D) and, finally, the applied mechanical pressure (P) parameters effects on samples' consolidations were investigated.

Samples density was measured by the Archimedes' method using an Ohaus Explorer Pro (Ohaus Corporation, NJ, USA) analytical balance (± 0.0005 g precision) and acetone as soaking medium (as suggested by the work of **Sizemore et al. [207]**). Relative densities were then evaluated by considering, as reference values, the theoretical densities obtained by pycnometric measurements on either the pristine or heat-treated powders then processed by SPS for obtaining bulk samples.

As mentioned in the Introduction (**Section 4.2.1**), the Taguchi method was adopted in the present work to identify the optimal SPS conditions for processing MGS-1 and JEZ-1 simulants. The selected layout for the screening study was a fractional factorial design performed according to an orthogonal array L9. This array is suitable for a system of 3 control factors with 3 levels. Thus, 9 experimental conditions are required instead of the 27 needed using a full factorial study. The next crucial step of the DoE-aided optimization is the selection of appropriate control levels for the three control factors.

An increase in the values of the chosen processing parameters (T_D, t_D, P) is generally expected to lead to higher samples' density which, in turn, correspond to better mechanical properties. However, temperature should not overcome certain levels, to avoid the occurrence of possible melting or bloating phenomena in the regolith undergoing sintering, that would cause the extrusion of the material out of the die. Moreover, due to the limited bearing capacity of graphite dies used in this work, the applied pressure should not exceed 35 MPa. Additionally, the use of long dwelling times is not convenient, particularly from the energy saving viewpoint.

Based on the considerations above, 35 MPa was selected as the maximum P value, while, according to **Section 4.1**, where t_d was 3 min for all samples, this parameter was investigated in the range 1-5 min. The maximum T_D value ($T_{D,max}$) was established based on preliminary tests to assess the critical temperature condition (T_c) to avoid the occurrence of undesired phenomena (melting, phases decomposition, etc.) in regolith simulants undergoing SPS. As an example, the method used for the evaluation of the T_c value for the case of the MGS-1 simulant is summarized in **Figure 4.13a**, when the SPS experiment was conducted at T_D=1200°C (t_D=5min, P=35MPa). From the related temperature (blue line) and sample displacements (red line) time profiles, it can be observed that after about 22 min from the beginning of the experiment, the slope (black line) of the displacement curve increases suddenly. This event, which took place at about 1100°C (dashed green lines), can be associated with the occurrence of melting phenomena. This is clearly testified by the image of the resulting sample reported in **Figure 4.13b**, which evidences a molten phase was formed and then partially expulsed from the die because of the concurrent application of a mechanical load.

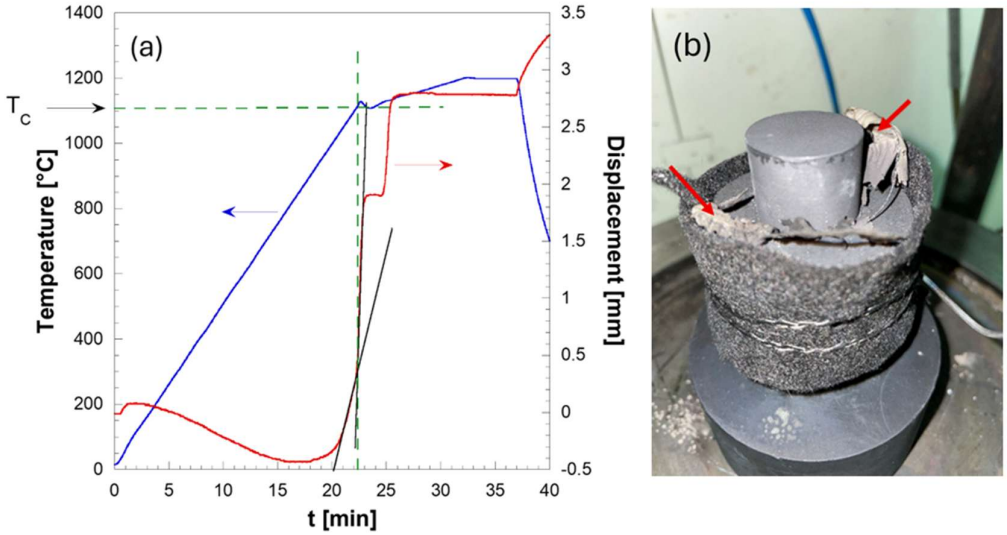

Figure 4.13 - Consolidation of MGS-1 simulant by SPS (T_D=1200°C, t_D=5min, P=35MPa): (a) temperature (blue line) and sample displacement (red line) time profile; (b) evidence of the formation of a molten phase (red arrow) in the resulting sample.

Accordingly, the $T_{D,max}$ value was set 50°C below T_c. The factor levels finally chosen are listed in **Table 4.10a**, while the corresponding conditions to be investigated (treatments) for the optimization of the SPS process based on Taguchi method are reported in **Table 4.10b**.

Table 4.10 - (a) Sintering parameters and their levels selected for screening of MGS-1 and JEZ-1. (b) Sintering optimization treatments prescribed by the Taguchi method

(a)

Level	T_D [°C]	P [MPa]	t_D [min]
1	$T_{D,max}$	35	5
2	$T_{D,max}$ - 50	25	3
3	$T_{D,max}$ – 100	15	1

(b)

Treatment	T_{level}	$t_{d,\ level}$	P_{level}
1	1	1	1
2	1	2	2
3	1	3	3
4	2	1	2
5	2	2	3
6	2	3	1
7	3	1	3
8	3	2	1
9	3	3	2

Density is the primary recorded response selected for the Taguchi method, while the secondary one is the energy consumption during the SPS run, calculated as integral of the applied electrical power with respect to time **[82]**. Using Minitab software **[240]** as a computational tool, the Signal-to-Noise ratios of obtained densities (SN_L) and of consumed energy (SN_S) were calculated for each level of T_D, P and t_D parameters according to the "larger is better" and "smaller is better" approach, respectively, as follows:

$$SN_{\mathrm{L}} = -10\log_{10}\left(\frac{1}{m}\sum_{j=1}^{m}\frac{1}{y_{ij}^2}\right) \tag{29}$$

$$SN_{\mathrm{S}} = -10\log_{10}\left(\frac{1}{m}\sum_{j=1}^{m}y_{ij}^2\right) \tag{30}$$

where m is the number of noise factor levels, y_{ij} is the response value of i-th treatment and j-th noise factor level.

In principle, the aim of the optimization algorithm is to maximize the samples density. In case parameters variation has no effect on the first response, the energy minimal consumption level is selected. This approach allows for the identification of the optimal set of experimental conditions for the two simulants, able to maximize their densification while reducing energetic costs. Once the optimal SPS conditions were identified, samples of different sizes were produced for their characterization.

Pristine, heat treated and sintered simulants were analyzed by X-Ray Powder Diffraction using a D8 (Bruker, Germany) diffractometer (Bragg-Brentano geometry) equipped with a copper anode (Cu Kα radiation λ=1.5418 nm) working at 40kV and 40mA. The analysis was performed in the 10°-130° 2θ range, with a step-size of 0.05° and for 10 seconds for each step. The attribution of the mineralogical phases was performed with EVA software (Bruker, Germany), with a Search and Match approach, using the COD (Crystallography Open Database) as a reference database **[209]**. Mineralogic composition in the differently processed simulants was determined by the Rietveld method, using MAUD program **[131]**, with the CIF files provided by the COD Database **[209].** Microstructure and elemental distribution of sintered samples were investigated by high-resolution scanning electron

microscopy (HRSEM, mod. S4000, Hitachi, Tokyo, Japan) equipped with a UltraDry EDS detector (Thermo Fisher Scientific, Waltham, MA, USA). To estimate the surface porosity of SPS samples, secondary electron SEM micrographs representing different areas of each sample were analysed using the open-source software GNU Image Manipulation Program GIMP (version 2.10), which allowed the calculation of area percentage based on the greyscale intensity values assigned to each pixel.

Compression strength measurement was performed on cylindrical samples of 15 mm diameter and 30 mm height using a servoelectric Instron 5585H testing machine (Instron, USA) equipped with a 250 kN load cell and operating under displacement control at a crosshead rate of 0.25 mm/min. The specimen was loaded via a compression fixture comprising a lower flat platen and an upper spherically seated platen, which ensured uniform loading across the top surface of the specimen. For the evaluation of flexural strength, original SPS samples (25mm diameter and 10 mm in height) were cut to obtain rectangular-section specimens with dimensions of 2x2.5x24 mm. The tests were conducted using a three-point bending fixture designed in accordance with the guidelines provided by the ASTM standard C1161 **[241]**. The loading and support rollers had a radius of 2.5 mm and the span between the axes of the two support rollers was 18 mm. The tests were carried out using a Sun 500 servoelectric testing machine (Galdabini, Italy), equipped with a load cell calibrated for the 0 to 100 N load range. The machine was operated in displacement control at a crosshead rate of 0.25 mm/min. At least five specimens were tested in both compression and flexural strength for each simulant. Vickers hardness was assessed using the micro indentation technique, using a Durascan 20 G5 Lite machine (ZwicKRoell Gmbh, Germany) and employing a diamond indenter in accordance with the ASTM E 384 measurement standard **[242]**, with applied 50 gf and 10 seconds dwell time. The resulting hardness value for each specimen was the average of 27 indentations conducted on three selected areas of the sample, across which nine indentations were conducted moving from the center of the area towards the periphery according to a predetermined path.

4.2.3 Results and Discussion

4.2.3.1 Initial characterization of the Martian regolith simulants

The TGA curves reported in **Figure 4.14** show the different behavior manifested by MGS-1, JEZ-1, JSC-Mars-1A and MMS simulants employed in this work when they are exposed to progressively

higher temperatures, up to 800 °C. Pristine JSC-Mars-1A shows a much higher weight loss (~28%), followed by initial JEZ-1 (~10%), MMS (~8%), and MGS-1 (~4%). These values are fairly in accordance with literature studies, which reported 30% for JSC-Mars-1A **[104]**, 5% for MMS **[102]**, and 4% for MGS-1 **[87]**. As already mentioned in **Section 4.1**, most of the weight loss recorded for JSC-Mars-1A can be attributed to its hygroscopic nature, as well as to some organic content found in the as-received regolith. These two aspects need to be mitigated, to better mimic the actual regolith behavior, prior to proceeding with SPS tests. Accordingly, as done in **Section 4.1**, the latter simulant received a 2h heat treatment at 700°C, above which the related TGA curve does not indicate further weight changes (**Figure 4.15**).

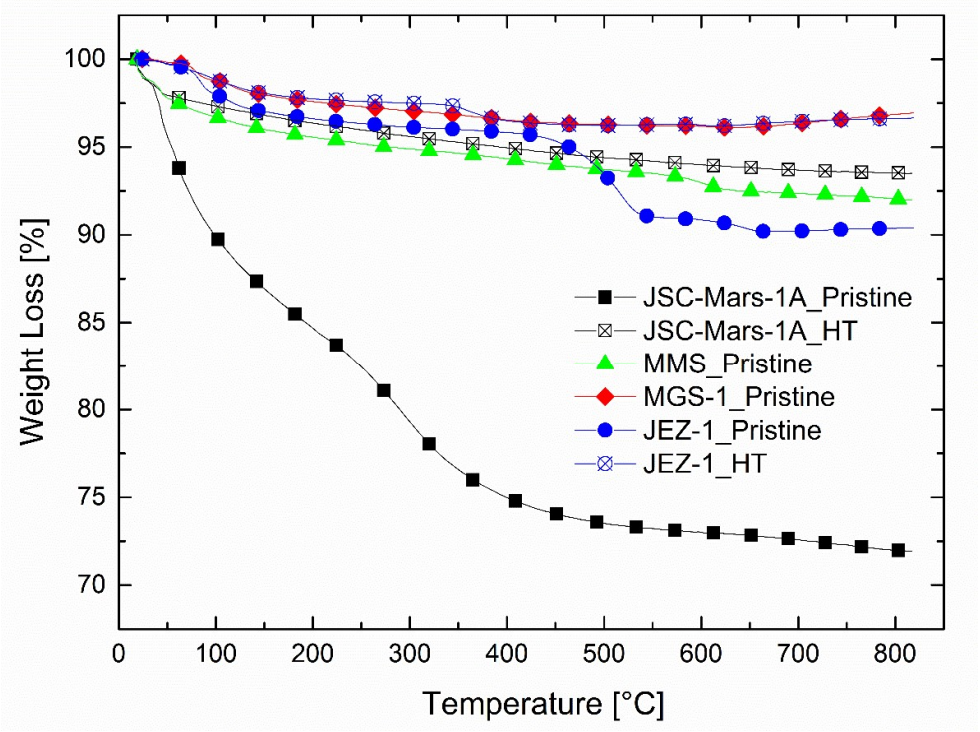

Figure 4.14 - TGA curves reporting weight changes (%) of as received simulants up to 800°C. The behaviour of JSC-Mars-1A and JEZ-1 simulants after being heat treated for 2h at 700°C are also shown.

TGA results shown in **Figure 4.14** also evidenced that JEZ-1 is subjected to an abrupt weight change in the range 450-550°C. This can be likely attributed to the thermal decomposition of Mg-carbonates,

whose content in the initial simulant was about 11% wt. (**Table 4.9**), which is expected to occur at T>450°C **[243]**. Since CO_2 released by carbonate decomposition ($MgCO_3 \rightarrow MgO + CO_2$) is difficult to handle during SPS, as it is not allowed to freely escape from the powder container, also original JEZ-1 simulant was subjected to the same annealing treatment (700°C/2h) received by JSC-Mars-1A. Only minor weight changes are finally displayed, following such heat treatment, by these two simulants (**Figure 4.14**).

As shown in **Figure 4.15**, annealed JSC-Mars-1A and JEZ-1 powders regained some weight when exposed at room temperature to air. This can be ascribed to the high hygroscopicity, albeit at different scales, of these simulants, as reported by **Peters et al. [90]** for the case of JSC-Mars-1A. Based on results shown in **Figure 4.15** all powders were stabilized, after their annealing, for at least 4 days before being further processed.

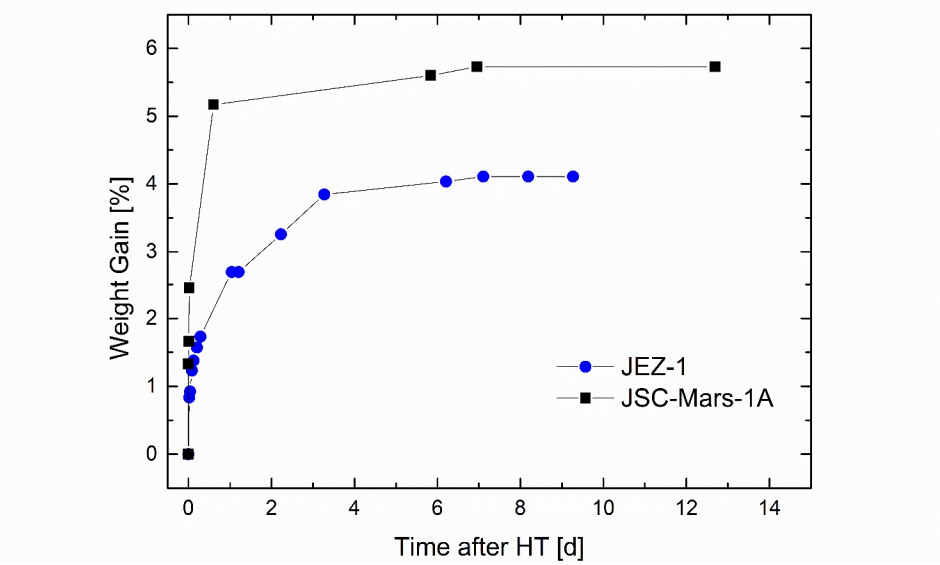

Figure 4.15 - Weight gain (%) of JSC-Mars-1A and JEZ-1 simulants following their heat treatment (700°C, 2h).

Table 4.11 shows the results provided by particle size analysis of the powders used for obtaining bulk specimens by SPS, with the relatively coarser MGS-1 and JEZ-1 simulants preliminarily milled, as described in **Section 4.2.2**. The four batches of powders display similar granulometry, particularly as far as their average size is concerned, with d[4,3] values in the range 22.57-27.83 µm.

The theoretical densities of JSC-Mars-1A, MMS, MGS-1, and JEZ-1 measured by a pycnometer resulted to be 2.84, 2.77, 2.90, and 3.01 g/cm^3, respectively. The slight discrepancies in these values, within 10%, can be attributed to the difference in composition of the simulants shown in **Table 4.9**.

Table 4.11 - Particle size parameters of Martian regolith powders used to obtain bulk samples by SPS.

Particle size parameter [µm]	JSC-Mars-1A	MMS	MGS-1	JEZ-1
d10	2.37±0.34	2.40±0.17	0.94±0.15	1.08±0.24
d50	23.52±1.20	22.12±0.20	13.37±0.91	16.35±1.00
d90	57.37±3.27	62.50±0.32	59.56±5.50	66.89±2.15
d[4,3]	26.82±1.67	27.83±0.19	22.57±1.85	26.15±0.57

4.2.3.2 Optimization of the sintering conditions

The critical temperature values (T_C) that should not be reached during SPS to avoid the occurrence of undesirable phenomena, as described in **Section 4.2.2**, were found to be 1100 °C and 1150, for MGS-1 and JEZ-1, respectively. Therefore, the corresponding $T_{D.max}$ levels (**Table 4.10**) chosen for the two simulants were 1050 °C and 1100 °C, respectively.

Results obtained using the Taguchi method are shown in **Figure 4.16**, where the SN Ratios for the density and energy responses are reported and can be readily ranked. From **Figure 4.16a**, it is observed that dwelling temperature is undoubtedly the most significant parameter, followed by the applied pressure, affecting the densification of MGS-1 simulant. Accordingly, 1050°C and 35 MPa were considered as the optimal T_D and P conditions to be applied for the preparation of dense MGS-1 samples. In contrast, dwelling time does not display a relevant role on samples densification. In contrast, as seen in **Figure 4.16b**, the latter parameter is ranked first in terms of energy consumption in the investigated interval. Given the smaller-the-better approach selected to calculate the energy response SN Ratios, i.e. the higher value in the graph indicates the optimal condition, the shortest dwelling time of 1 min has been therefore selected.

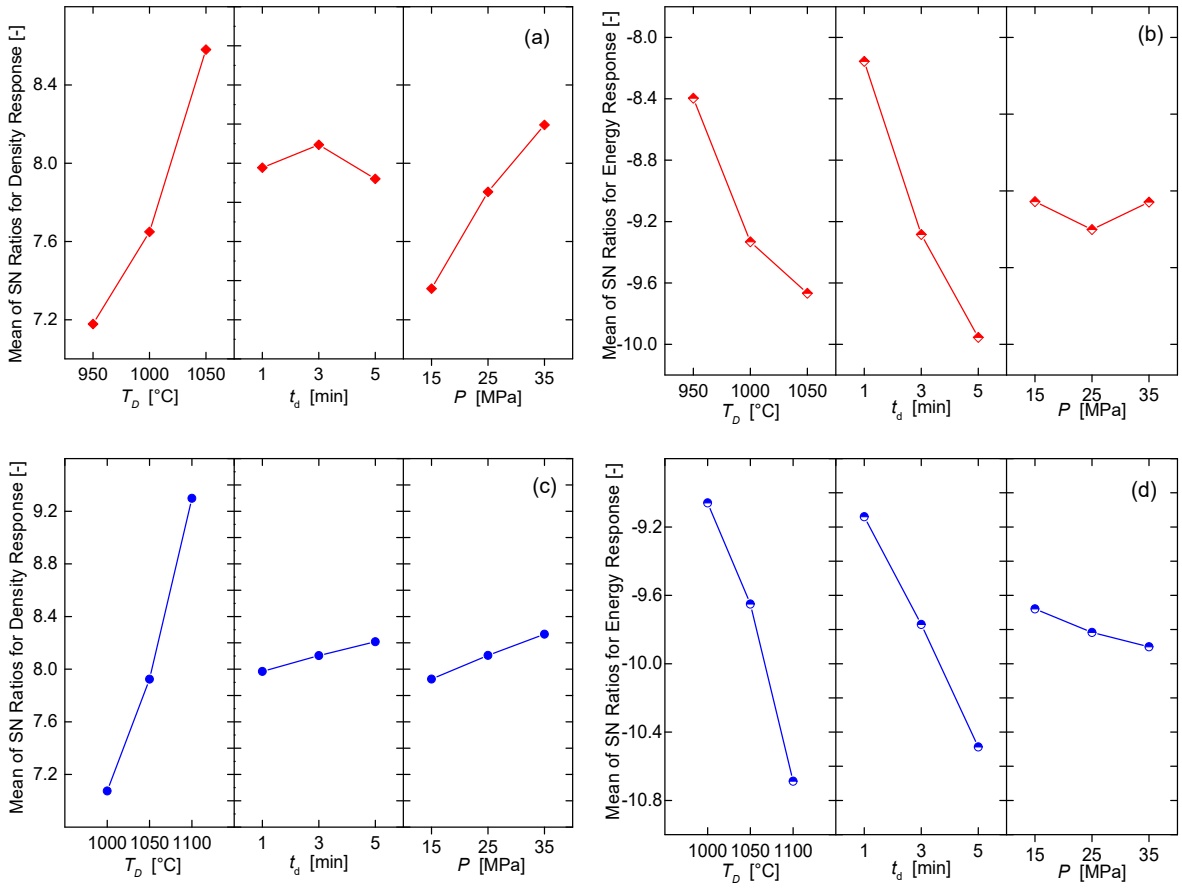

Figure 4.16 - Effect of T_D, t_D, P on the densification and energy consumption during SPS test according to the Taguchi method. Mean of SN Ratios for (a) MGS-1 density, (b) MGS-1 energy consumption, (c) JEZ-1 density, (d) JEZ-1 energy consumption

According to the results shown in **Figure 4.16c**, T_D is the most important factor also affecting the consolidation of JEZ-1 powders. On the other hand, both P and t_D do not seem to play a noteworthy role when the latter simulant was processed by SPS. Therefore, differently from to the case of MGS-1 (**Figure 4.16a**), the applied load only mildly affects JEZ-1 samples densification. This could be ascribed to their compositional differences, as seen in **Table 4.9**. According to results shown in **Figure 4.16d**, the optimal t_D value to be chosen for the sake of energy saving was 1 min, as for MGS-1. In conclusion, the optimal parameters identified for achieving high densification levels when processing by SPS MGS-1 and JEZ-1 simulants were 1050°C/35MPa/1min and 1100°C/15MPa/1min, respectively. Based on the results obtained in **Section 4.1**, 1000°C/30MPa/3min and

1050°C/30MPa/3min were the SPS conditions selected for obtaining highly dense samples using JSC-Mars-1A and MMS simulants, respectively. The applied pressure was further risen to 35 MPa for uniformity with the other two simulants and to address the scaling-up from 3 mm tall samples employed in **Section 4.1** to 15 mm tall ones needed for the compressive strength tests.

Samples for the mechanical testing campaign have been then produced using the processing parameters reported in **Table 4.12**, along with the corresponding relative densities. The latter ones were rather high for the four systems, all exceeding 94% in their average values. The relatively lower consolidation level (94.3%) achieved by the MGS-1 simulant at 1050°C/35MPa/1min denotes its significant refractory nature. On the other hand, as mentioned previously, an increase of the three operating parameters did not produce noteworthy effects (t_D) or should be avoided for the occurrence of undesired melting/bloating phenomena (T_D) or for dies breakage (P).

Table 4.12 - Optimized SPS parameters and corresponding relative density values of samples used for the evaluation of mechanical properties. The theoretical density of initial powders to be processed by SPS (i.e. pristine MMS and MGS-1, and heat-treated JEZ-1 and JSC-Mars-1A) was used for the calculation of relative density of resulting bulk samples.

Simulant	T_D [°C]	P [MPa]	t_D [min]	Relative density [%]
JSC-Mars-1A	1000	35	3	>99.9
MMS	1050	35	3	96.2±4.5
MGS-1	1050	35	1	94.3±3.1
JEZ-1	1100	15	1	97.0±5.8

It is worth mentioning that the extremely high dense samples obtained from JSC-Mars-1A can be ascribed to the dominant amorphous content present in this powder (**Table 4.9**), which could act as a sintering aid to make the consolidation of such simulant strongly facilitated compared to the other three competitors mainly consisting of crystalline phases. In the field of ceramics, the addition of a glassy phase is generally reported to effectively promote sintering phenomena **[244-248].** This is also consistent with **Farries et al. [249]**, who showed that Lunar regolith simulants containing an

amorphous phase sinter at milder temperatures and more uniformly with respect to fully crystalline simulants. Such beneficial effect was ascribed to viscous flow generated by the presence of the glassy phase, which is also likely the motivation for the experimental findings observed in this work.

4.2.3.3 Compositional, microstructural and morphological characterization

Compositional modifications occurring when JSC-Mars-1A, MMS, MGS-1, and JEZ-1 powders are processed by SPS can be deduced from the corresponding XRD patterns shown in **Figures 4.17, 4.18, 4.19** and **4.20**, respectively. The relative content of each phase estimated using the Rietveld method is reported in **Table 4.13**.

Plagioclase, pyroxene and olivine mineral are the main crystalline phases detected, along with a minor content of an iron rich spinel, by XRD analysis in pristine JSC-Mars-1A simulant (**Figure 4.17**). As evidenced by the green line reported in **Figure 4.17**, the original powder is characterized by a dominant amorphous fraction (60.5 wt.%, **Table 4.13**), which only partially crystallizes, mainly into plagioclase, during the heat pretreatment received by this simulant. A more significant drop in the amorphous content (from 43.6 to 6.1 wt%), with a further increase in plagioclase amount (66.3 wt%), occurred during the SPS step, in accordance with what was observed in **Section 4.1** (see **Figure 4.6**). Hematite (11.9 wt%) is also correspondingly formed (**Table 4.13**). Although, as described above, some compositional/structural changes were induced in the JSC-Mars-1A powders by the preliminarily heat treatment at 700°C, the final characteristics of the sintered samples are mostly defined when the simulant was exposed to more severe temperature conditions (1000°C) during the subsequent SPS step. XRD analysis results reported in **Figure 4.18** and **Table 4.13** for the MMS regolith simulant are in good agreement with previous findings **[214]**. Plagioclase (70.4 wt.%) is the main crystalline mineral present in pristine powders, followed by pyroxene (15.4 wt.%) and phyllosilicate (6.4 wt.%). **Figure 4.18** and **Table 4.13** show that only slight compositional changes are produced in the MMS simulant undergoing SPS, to prove its superior thermochemical stability compared to JSC-Mars-1A, similarly to what was observed in **Section 4.1** (see **Figure 4.9**). Nonetheless, it is worth noting that, after SPS, the originally small amorphous content is further reduced from 5.9 to 2.6 wt.%, while the phyllosilicate phase was not detected anymore.

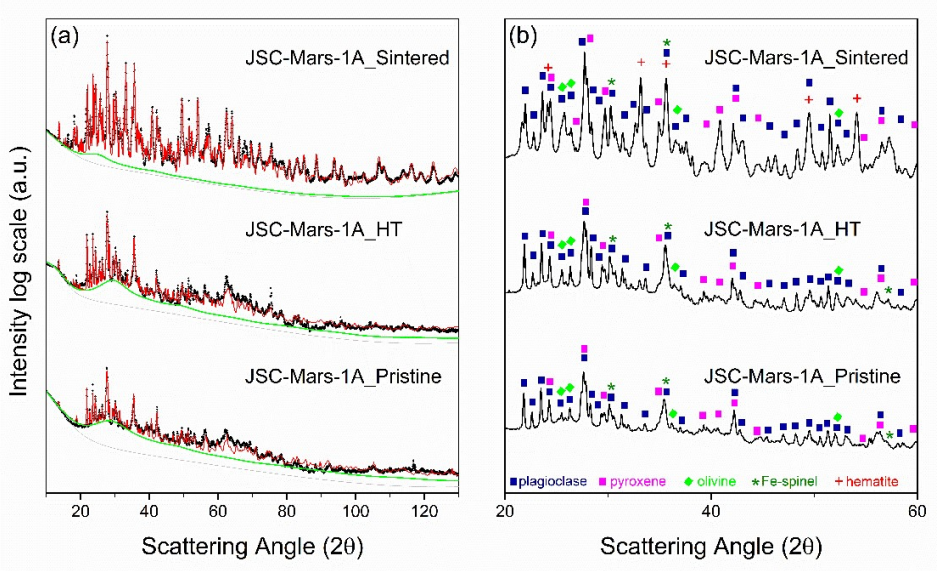

Figure 4.17 - XRD patterns of pristine, heat-treated and sintered JSC-Mars-1A samples (**Table 4.12**). (a) Extensive view with Rietveld refinement: experimental data (black dots), calculated intensity (red solid line) and amorphous content (green solid line). (b) Detailed view indicating crystalline phases detected.

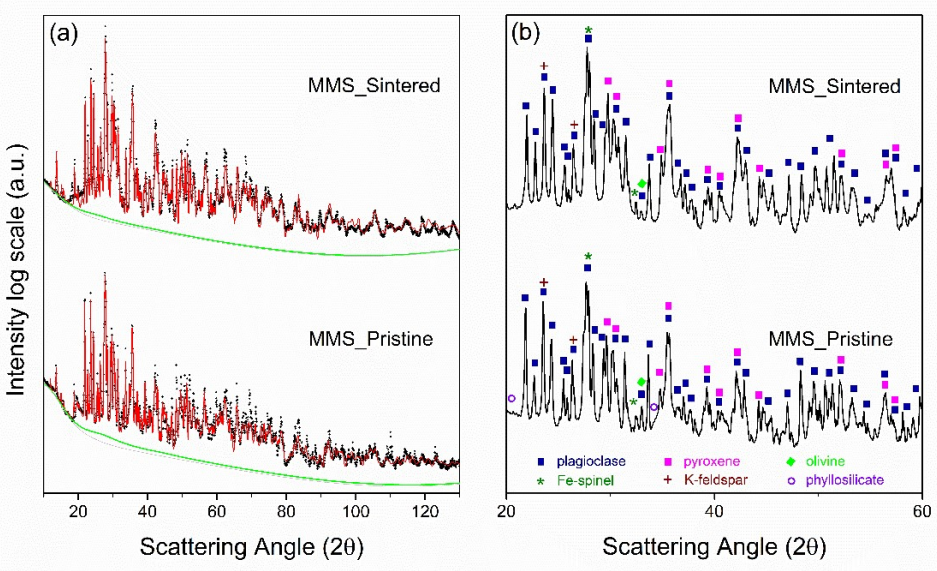

Figure 4.18 - XRD patterns of pristine, and sintered MMS samples (**Table 4.12**). a) Extensive view with Rietveld refinement: experimental data (black dots), calculated intensity (red solid line) and amorphous content (green solid line). (b) Detailed view indicating crystalline phases detected.

As shown in **Figure 4.19** and **Table 4.13**, the main crystalline phases found by XRD in pristine MGS-1 are plagioclase (46.2 wt.%), pyroxene (16.8 wt.%), and olivine (13.7 wt.%). Minor amounts of epsomite (4.7 wt.%), iron spinel (4.2 wt.%), quartz (3.1 wt.%), and gypsum (2.0 wt.%) are also detected, while the amorphous content was estimated to be equal to 9.3 wt.%. Although these outcomes qualitatively agree with the information reported in **Table 4.9**, some differences are found between Rietveld analysis results conducted in the present study and data provided by the producer, who reported a lower amount of plagioclase (27.1 wt.%) and a higher content in the total glass-rich basalt (22.9 wt.%). Such discrepancies can be probably due to the different method utilized to analyse such a complex mineral mixture. The main compositional changes induced by the SPS treatment in the MGS-1 simulant are the disappearance of the hydrated sulphate phases, and the partial crystallization of the amorphous fraction, which decreases down to 3.3 wt.%. Concurrently, the amounts of olivine, iron rich spinel minerals and, albeit at a lower degree, plagioclase, increase.

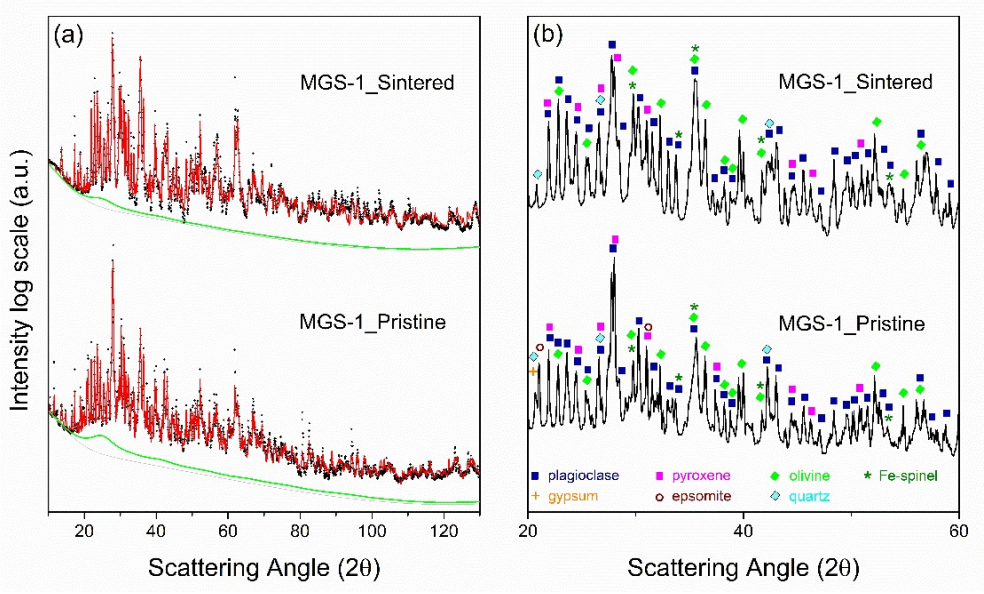

Figure 4.19 - XRD patterns of pristine, and sintered MGS-1 samples (**Table 4.12**). a) Extensive view with Rietveld refinement: experimental data (black dots), calculated intensity (red solid line) and amorphous content (green solid line). (b) Detailed view indicating crystalline phases detected.

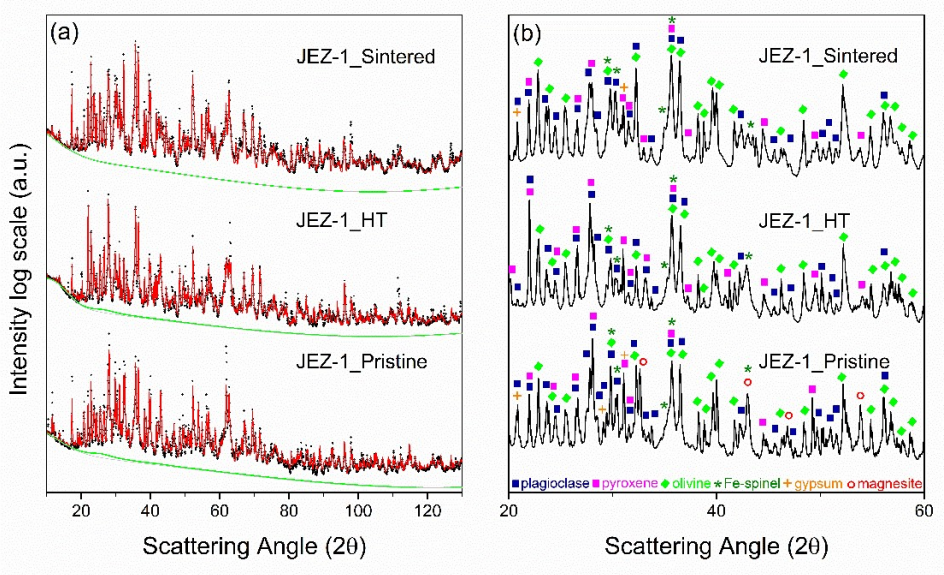

Figure 4.20 - XRD patterns of pristine, heat-treated and sintered JEZ-1 samples (**Table 4.12**). (a) Extensive view with Rietveld refinement: experimental data (black dots), calculated intensity (red solid line) and amorphous content (green solid line). (b) Detailed view indicating crystalline phases detected.

XRD patterns plotted in **Figure 4.20** and the corresponding data reported in **Table 4.13** reveal that olivine (33.4 wt.%), plagioclase (33 wt.%), pyroxene (16.2 wt.%), and magnesite (10.8 wt.%) are the main crystalline constituents of pristine JEZ-1. Rietveld analysis findings fairly agree with information shown **Table 4.9**, as provided by the producer of this simulant. However, as for the case of MGS-1, some differences can be observed, for instance a relatively larger amount of plagioclase and a lower content of the amorphous phase were estimated in the present work. **Figure 4.20** also evidenced that, after the JEZ-1 simulant received the thermal pre-treatment, peaks associated with magnesite disappeared, due to decarbonation phenomena correspondingly taking place. Finally, the main compositional change observed after SPS was the increase in olivine and iron spinel percentages at the expenses of plagioclase.

SEM micrographs of optimal SPS samples produced using the four simulants are shown in **Figure 4.21** along with the related EDX maps of the most representative elemental constituents. From these images, it can be confirmed that a very high degree of densification is reached in all sintered specimens. In addition, residual porosities estimated from SEM micrographs by image analysis, i.e.

0.58±0.34 vol % (JSC-Mars-1A), 3.10±0.89 vol % (MMS), 4.98±0.65 vol % (MGS-1), 2.09±0.62 vol % (JEZ-1), further testify the obtainment of nearly full dense JSC-Mars-1A samples, whereas relatively lower consolidation levels are achieved with MGS-1 powders, consistently with density data reported in **Table 4.12**.

Table 4.13 - Phase composition (wt.%) of regolith simulants determined with Rietveld Refinement from XRD analysis.

	JSC-Mars-1A			MMS		MGS-1		JEZ-1		
	pristine	HT	sintered	pristine	sintered	pristine	sintered	pristine	HT	sintered
Amorphous content	60.5	43.6	6.1	5.9	2.6	9.3	3.3	2.0	1.8	0.1
Plagioclase	24.5	38.0	66.3	70.4	71.0	46.2	50.2	33.0	43.3	29.4
Olivine	3.8	2.6	3.2	0.4	1.7	13.7	18.9	33.4	33.0	49.0
Pyroxene	10.7	11.5	11.5	15.4	21.6	16.8	16.4	16.2	18.1	14.3
Iron Spinel	0.5	4.2	1.0	0.5	0.5	4.2	9.2	2.3	3.8	6.0
Phyllosilicate	-	-	-	6.4	-	-	-	-	-	-
Gypsum	-	-	-	-	-	2.0	-	2.3	-	1.2
K-feldspar	-	-	-	1.0	2.6	-	-	-	-	-
Quartz	-	-	-	-	-	3.1	2.0	-	-	-
Epsomite	-	-	-	-	-	4.7	-	-	-	-
Magnesite	-	-	-	-	-	-	-	10.8	-	-
Hematite	-	-	11.9	-	-	-	-	-	-	-

The heterogeneous character of all sintered samples is evidenced by the EDX maps. Nonetheless, the JSC-Mars-1A-based specimen displays, with respect to the other regolith systems, a more homogeneous microstructure, with the elemental constituents distributed quite uniformly across

the sample. This fact is probably related to the occurrence of the extensive crystallization phenomena occurring during SPS with this simulant, which originally possessed a significantly higher amorphous fraction compared to the other systems. In addition, the use of a relatively lower dwell temperature (1000°C) is also expected to play a role for producing the observed finer microstructure.

In what follows, the EDX analysis results shown in **Figure 4.21** will be correlated to the main phases identified by XRD analysis in the sintered samples obtained from the four simulants (**Table 4.13**).

As for JSC-Mars-1A (**Figure 4.21a**), the main crystalline phase, Plagioclase, appears to be quite homogeneously detected across the sample, as proved by the uniform distribution of its elemental constituents. The small Mg-rich and Al-poor regions indicated by the yellow arrows can be ascribed to either Pyroxene or Olivine. Based on the elemental Fe map, also Hematite, whose content was estimated to be about 12 wt. by the Rietveld analysis (**Table 4.13**), could be considered distributed quite homogeneously in the sintered material. EDX analysis results relative to the MMS specimen (**Figure 4.21b**) evidence the presence of zones (white arrows) locally richer in Mg and Fe while poorer in Ca and Al, which can be likely associated with Ca-poor Pyroxene. Plagioclase phase is more uniformly distributed along the sample. EDX maps of the sintered MGS-1 sample (**Figure 4.21c**) reveal the presence of local regions richer in Mg and deficient in Ca and Al (green arrows) that can be attributed to either Olivine or Ca-poor Pyroxene. This sample presents also Fe-rich and Si-lacking small zones (red arrows), that can unequivocally be attributed to iron spinel, whose content in this simulant is relatively higher compared to the others (**Table 4.13**). Finally, the sintered material generated from the JEZ-1 simulant exhibits a coarser microstructure (**Figure 4.21d**), consisting of several large Mg-rich regions, poorer in Ca and Al (orange arrows) which could be ascribed to Olivine (the main phase) or Ca-poor pyroxene. Plagioclase occupies quite homogeneously the complemental volume of the sample.

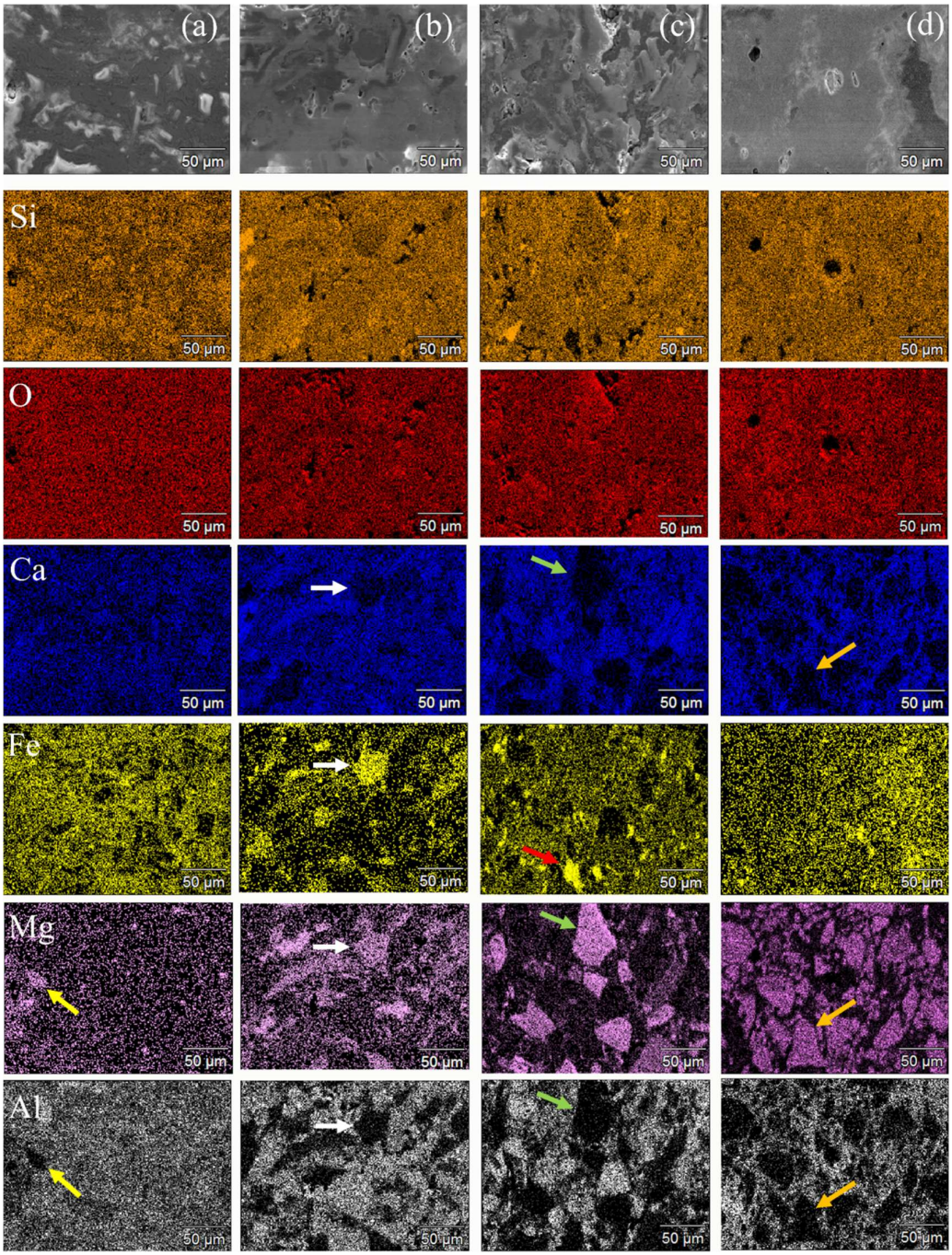

Figure 4.21 - SEM micrographs and corresponding EDX maps of the most representative elemental constituents of bulk samples obtained under the optimized SPS conditions (**Table 4.12**) from Martian regolith simulants: (a) JSC-Mars-1A, (b) MMS, (c) MGS-1, and (d) JEZ-1.

4.2.3.3 Mechanical characterization

The mechanical properties of the bulk samples obtained after processing JSC-Mars-1A, MGS-1, MMS and JEZ-1 simulants under the SPS conditions listed in **Table 4.12** are reported in **Figures 4.22a-4.22c**. As for compressive strength (**Figure 4.22a**), the nearly full dense JSC-Mars-1A sample showed the best performance compared to the other regolith systems here investigated. In addition, the measured value (310 ± 54.37 MPa) was significantly higher than that (63 MPa) reported by **Wan et al. [234]** for the JSC-Mars-1A-based sulphur concrete. Such consideration holds also true when this comparison is extended to other Martian simulants, since the highest compressive strength value reported so far in literature was that obtained by **Min [112]** for the JEZ-1 system, i.e. 136.7 MPa (**Table 4.8**).

The 94.3% dense MGS-1 sample displayed relatively lower compressive strength (160.63 ± 45.17 MPa 151.82 ± 44.62 MPa), which is still superior to the maximum values reported in literature for bulk specimens obtained from the same simulant by cold sintering **[107]** and SPS **[112]**, i.e. 43 and 102 MPa, respectively. This feature can be attributed to the relatively lower samples' density, below 90% in the latter studies (**Table 4.8**). Similar considerations can be made regarding samples deriving from MMS and JEZ-1 simulants, whose compressive strength properties were 178.60 ± 84.11 141.50±16.05, and 201.97 ± 82.77 197.72 ± 60.45 MPa, respectively. While no compressive strength data are available in the literature on MMS-based samples, **Min [112]** reported values of 136.7 MPa, at most, relatively to JEZ-1-based samples prepared by SPS. Also in this case, the superior average compressive strength measured in the present work can be associated to the higher densification level reached (97.0 ± 5.8%) compared to that of samples obtained by **Min [112]** (about 89%). **Figure 4.22b** shows that the JSC-Mars-1A sample also exhibited markedly higher flexural strength (70.58 ± 8.39 MPa) compared to the other Martial simulants tested in this work, i.e. JEZ-1 (39.04 ± 3.44 MPa), MMS (35.54 ± 9.52 MPa), and MGS-1 (24.93 ± 3.14 MPa). As for the JSC-Mars-1A system, the value obtained in this work was better that those reported in the literature using alternative techniques, such as impact compaction (50 MPa) **[104]**, liquid infiltration (45 MPa) **[233]**, and sulphur concrete (2.3 MPa) **[234]**, for processing the same simulant, in some cases in presence of additives. **Hoekman [113]** measured the flexural strength on MGS-1 samples produced by SPS and the resulting value (24 MPa) was nearly close to that obtained in this work (24.93 ± 3.14 MPa). The same authors improved significantly this property (up to 52 MPa) with the introduction of 5%Bi_2O_3. **Karl et al. [100]** reported higher values (53.5 and 57.6 MPa, after sintering in air or Martian atmosphere, respectively) using a

mixture of MGS-1, MGS-1C, and a polymeric binder, first processed by additive manufacturing followed by a pressureless sintering step. Based on the results discussed above, it is possible to state that, among the four regolith-like resources here investigated, the best compressive and flexural performances of the corresponding bulk materials are exhibited in the following hierarchical order: JSC-Mars-1A> JEZ-1> MMS ≈ MGS-1.

Differently from the mechanical properties discussed above, **Figure 4.22c** evidenced that Vickers micro-hardness measurements provided closer values among the sintered samples resulting from the four Martian simulants. The long error bars in graphs shown in **Figure 4.22c**, which indicate that the measured values were rather spread out, are due to the heterogeneous nature of these simulants, as observed in **Figure 4.21**. In any case, it is possible to state that the JEZ-1 sample possessed the highest hardness (1001 ± 93 HV, 1 HV = 0.0098 GPa), followed by JSC-Mars-1A (907 ± 168 HV) and MSG-1 (901 ± 107 HV) products, while MMS-based specimen resulted relatively softer (802± 129 HV). As expected, these values are all superior to that (710±30 HV) measured by **Goulas et. al. [232]** on 59% porous samples prepared by additive manufacturing from JSC-Mars-1A simulant. While the hardness values relative to various extraterrestrial construction materials resulting from Lunar regolith simulants have been reported in the literature **[238]**, no other data, except for **Goulas et. al. [232]**, are available, to the best of our knowledge, for samples produced using Martian simulants. Based on the results discussed above, it is possible to state that, among the four regolith-like resources here investigated, the best mechanical performances of the corresponding bulk materials are exhibited in the following hierarchical order JSC-Mars-1A> JEZ-1> MMS ≈ MGS-1.

The diverse Vickers hardness values of the samples generated from the four simulants can be somehow correlated with their compositional differences. As discussed above, olivine, plagioclase and pyroxene, are the three main mineral families present in these simulants (**Table 4.13**). A Vickers hardness of about 1100 HV was reported for highly dense olivine samples **[250,251]**.

Relatively lower HV values are reported for Plagioclase, in the range of 7-9 GP (equivalent to 712-918 HV), depending on the specific phase belonging to this mineral family **[252,253]**. Finally, Pyroxenes are characterized by generally lower hardness, in the range 4.9-8.5 GPa (equivalent to 500-867 HV) **[254]**.

Therefore, the superior hardness properties possessed by the JEZ-1 sample can be more likely ascribed to the fact that this material is richer in Olivine compared to the other contenders (**Table**

4.13). In contrast, the lower hardness value exhibited by the MMS sample can be attributed, other than its relatively lower densification degree, also to the higher content in the "softer" Pyroxene mineral and the lower fraction of "harder" Olivine. The fact that, despite its higher relative density, JSC-Mars-1A samples show lower HV values compared to JEZ-1 ones, can be explained with their different Olivine content, i.e. 3.2 and 49 wt.%, respectively.

Therefore, the mineralogical differences of the various Martian regolith-like samples obtained in this work by SPS also play an important contribution for defining their mechanical performances which are, in general and regardless of the type of simulant, superior with respect to the state of the art.

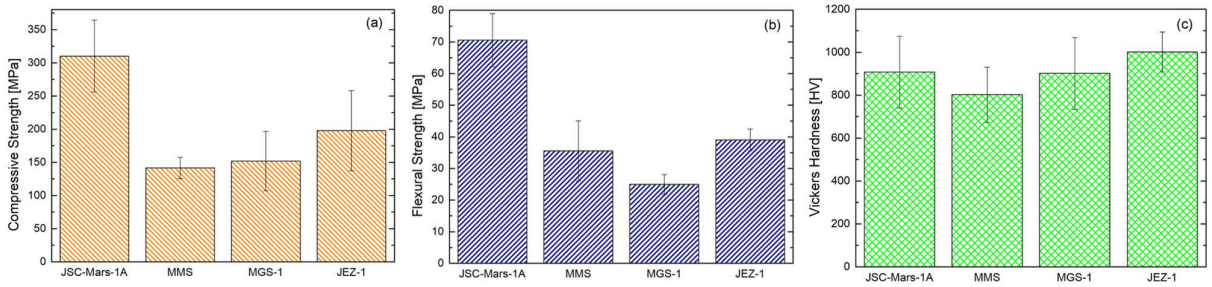

Figure 4.22 - Mechanical properties evaluated for the 4 regolith simulants sintered at their tailored optimal conditions. (a) Compressive strength, (b) Flexural strength, and (c) Vickers Hardness.

In this regard, a beneficial role is certainly played by the use of an electric current assisted sintering technique, like the SPS, that allows for the rapid fabrication of highly performant structural components from Martian simulants. Indeed, the optimization of the SPS process allowed to provide fully dense and fairly uniform microstructures from JSC-Mars-1A powders at relatively milder sintering temperature (1000 °C). This is mainly ascribed to the dominant amorphous fraction present in this simulant, initially equal to about 60 wt% then reduced to approximately 44 wt% after the preliminary annealing treatment carried out to remove water and organics from the raw material. During SPS, the amorphous content markedly decreased down to about 6 wt% and the obtained ceramics exhibited compressive strength, flexural strength, and Vickers hardness values equal to about 310 MPa, 70 MPa, and 1000 HV, respectively. Relatively lower mechanical properties were obtained using the other three simulants, and this feature can be primarily associated to the residual

porosity present in the corresponding sintered samples, particularly for the case of the MGS-1 system (about 5 vol%).

To further reduce the still high thermal budget required with SPS, which might represent a problem for *in-situ* applications, the development of less energy-demanding fabrication technologies capable of producing highly dense Martian-regolith-derived materials, with mechanical properties similar or even better than those obtained in this study, would signify an important advancement in this field. To this aim, the cold sintering technology, widely applied in the ceramic densification framework **[255-258]**, represents a good candidate. Unfortunately, as reported in the introduction (**Section 4.2.1**), the use of cold sintering for Martian regoliths led so far to scarcely densified samples, with consequently poorer mechanical properties **[107]**.

SPS presents some limitations when complex shapes are needed. In this regard, additive manufacturing (AM) is expected to be the most convenient and versatile fabrication method to apply. Unfortunately, so far AM techniques, associated to pressureless sintering, generally led to modest densities (about 80-85%, see **Table 4.8**). Nonetheless, it is expected that such complex-shaped parts, even if less performant than the highly dense ones obtained in this work via SPS, will be complementary to satisfy the needs of future Martian bases. The use of AM methods for processing Mars regolith will be investigated in the subsequent **Section 4.3**.

The research activity and associated results presented in this Section have been reported and discussed in the following publication: of this Section have been published as **Casu, M.**, Licheri, R., Bambas, D., Aymerich, F., Cappai, L., Concas, A., Cao, G., & Orrù, R. (2025). Enhanced properties by spark plasma sintering of additive-free Martian soil simulants for ISRU applications. *Ceramics International*, *51*(24), 42046–42058. https://doi.org/10.1016/j.ceramint.2025.06.423

4.3 Sintering of Mars regolith shaped using additive manufacturing methods

4.3.1 Introduction

As stated in **Section 1.3**, Mars is a differentiated terrestrial planet with a complex geological history. In this framework, mineral deposits present on Mars' surface could be exploited to enrich the ISRU construction materials of particular phases, with the ultimate aim of tailoring the regolith properties and facilitating processability of these materials, without the need of complex separation processes **[100]**. In this regard, numerous clay deposits detected on the surface of Mars are potentially suitable for this purpose **[259]**.

Clay shaping is a universal and versatile technology employed by all human civilizations and has been known since the Neolithic period **[106]**. Given its high versatility, clay shaping is expected to have extraordinary value as an ISRU technique **[106]**. To process clay, water is required. Numerous pieces of evidence of water on planet Mars have been proposed, either as subsurface ice **[260]**, hydrated materials **[261]**, or salt-rich brines **[262-254]**. Among the possible sources of water, the latter two are distributed on the planet's surface, even if usually associated with high concentrations of dissolved salts. Indeed, such salt content could allow the stability or metastability of brines on the surface of Mars, where pure liquid water is not stable **[265]**.

While most previous clay processing studies were based on pure water **[99,100,106]** the direct utilization of salt brines for construction materials would eliminate the need for water purification, reserving pure water to human consumption and enhancing the applicability of the proposed technology especially in the early stages of human presence on Mars.

Given the unavailability of Martian soils and brines for research, which have never been brought to Earth, both regolith and brine simulants are required for Earth-based ISRU studies. In this regard, while several Martian regolith simulants are currently available for researchers **[37]**, limited efforts have been made to simulate Martian saltwater. In a recent NASA document, however, a Martian saltwater recipe is proposed based on the microscopy, electrochemistry, and conductivity analyzer (MECA) instrument on the Phoenix lander on Mars **[266]**. Other saltwater simulants have been proposed in literature, such as "Instant Mars", however, its authors did not report the exact recipe but only the ion concentrations, also in this case based on Phoenix lander findings **[265]**.

A previous study revealed that additive manufacturing (AM) of clay-rich simulants can lead to green bodies with compressive strength similar to general-purpose concrete, albeit with the aid of polymeric binders **[106]**. If further increases in mechanical performance are needed, consolidation techniques such as sintering could be employed **[100]**. Additive manufacturing is expected to play an important role in ISRU technologies, as it would enable flexible remote production. Recently, several AM-based approaches have been proposed in this framework. For example, laser fusion of regolith powder beds led to samples with high porosity (>59%) and Vickers hardness of 710 ± 30 HV **[232]**, material extrusion with phosphoric acid (33 wt.% non-ISRU-compatible) led to compressive strengths of about 20 MPa **[267]**. Robocasting resulted in green bodies with compressive strengths of 7.55 ± 1.33 MPa **[106]** and Layerwise Slurry Deposition (LSD) led to compressive strength of 30.8±2.47MPa, before sintering **[106]** and flexural strength of 57.5/53.3 MPa when sintered in terrestrial/simulated Martian atmosphere **[100]**. Recently, injection molding was tested to simulate the binder jetting process by using a 6.25% NaCl aqueous solution as a binder, achieving a peak compressive strength of 25.46 MPa after sintering at 1200°C for 1 h **[268]**.

Among the traditional technologies employed to process ceramic slurries, slip casting (SC) is able to obtain high powder packing density, up to 60 % of the theoretical density, a low organic content (typically 2 wt%) and is capable of processing a broad range of particle sizes **[269]**. These features, including the possibility of employing limited or no polymeric additives, make this technology particularly interesting in the AM-ISRU scenario. SC has previously been employed on Martian regolith slurries both for the obtainment of unfired green bodies (compressive strength of 3.34 ± 0.22 MPa, 42.2% porosity) **[106]** and sintered parts (flexural strength of 51 MPa, 28.23% porosity) **[100]**.

Recently, the innovative Laser Induced Slip Casting (LIS) technology, falling in the category of additive manufacturing processes, has been proposed as the evolution of conventional SC capable of obtaining voluminous ceramic parts with properties comparable to those of conventionally manufactured ones **[270]**. LIS technology is based on the selective drying of a slurry using a laser (**Figure 4.23**), with many features resembling the well-established stereolithography **[270]**. If compared to conventional SC, LIS allows faster generation of parts with arbitrary geometries without the need for gypsum molds **[271]** and with the automation advancements associated with AM processes **[270]**. In this regard, LIS technology has been successfully employed for the additive manufacturing of ceramic materials such as silicon nitride **[270]**.

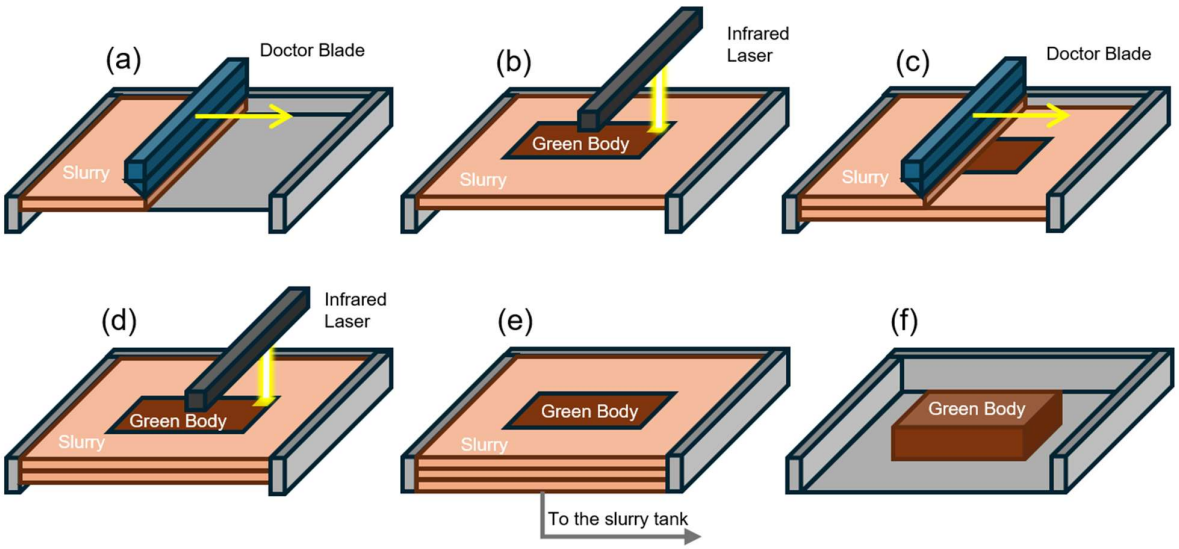

Figure 4.23 - Illustration of the LIS process, inspired by **Lüchtenborg et al. [270].** a) The first layer of slurry is deposited in the build platform by the doctor blade. b) The laser locally dries the slurry, producing the first layer of the green body c) A new layer of slurry is deposited. d) The laser locally dries the second layer of slurry. e) The excess slurry is drained f) The printed green body remains.

In this study, LIS technology, the evolution of traditional SC, is evaluated as a possible ISRU additive manufacturing technology for the obtainment of sintered parts with compressive strength equal to or higher than general-purpose concrete (i.e., 20-40 MPa). Samples obtained with conventional SC have been produced for the sake of comparison. No polymeric dispersant or binder is employed, and to maximize applicability and ISRU compliance of the proposed technology, a Martian Saltwater Simulant **[266]** instead of deionized water used as a dispersant.

The obtained green bodies are characterized by their relative density, linear sintering shrinkage, composition, and compressive strength. Sintering experiments are carried out in terrestrial atmosphere conditions and a simulated Martian atmosphere **[100]**. Sintered parts are characterized by their relative density, water adsorption (as frost-resistant ceramics are expected to have water absorption < 3-5% **[100,272]**, composition, thermal conductivity in the Martian temperature range, and finally compressive strength.

4.3.2 Materials and methods

4.3.2.1 Regolith and Martian saltwater simulants

The third-generation simulants Mars Global Simulant (MGS-1) and (MGS-1C) were employed in this work. Given the fact that a different MGS-1 batch, with respect with the one presented in **Section 2.2.1**, has been used in this work, their detailed chemical and mineralogical compositions will be reported in **Table 4.14** and **Table 4.15**, respectively **[273,274]**.

Table 4.14 - Oxide constituents (wt.%) of MGS-1 and MGS-1C simulants and the MGS-1/16 mixture employed in this work. Producer values as well as values obtained via XRF on the same batches used in this work have been taken from **Karl et al. [106] and references therein**. The calculated MGS-1/16 mixture values refer to the latter.

Oxide	MGS-1 (Producer data)	MGS-1 (measured)	MGS-1C (Producer data)	MGS-1C (Measured)	MGS-1/16 mixture (calculated)
SiO_2	45.57	44.36	53.16	51.15	44.78
Al_2O_3	9.43	12.71	16.89	13.98	12.79
FeO_T	16.85	16.85	8.24	10.86	16.48
MnO	0.1	0.1	0.04	0.05	0.10
MgO	16.5	13.84	12.57	6.84	13.40
CaO	4.03	7.36	2.02	3.48	7.12
Na_2O	3.66	1.65	1.91	2.24	1.69
K_2O	0.43	0.46	0.47	0.54	0.47
TiO_2	0.3	0.39	0.21	0.28	0.38
P_2O_5	0.37	0.11	0.35	0.09	0.11
Cr_2O_3	0.12	0.13	0.02	0.04	0.12
SO_3	2.63	1.73	1.16	1.05	1.69

Table 4.15 - Phase composition (wt.%) of MGS-1 **[273]** and MGS-1C **[274]** simulants and the MGS-1/16 mixture employed in this work (n.r.: not reported).

Mineralogical Phase	MGS-1 [273]	MGS-1C [274]	MGS-1/16 mixture (Calculated)
Glass-rich basalt	22.9	13.7	22.3
Plagioclase	27.1 (Anorthosite)	16.4 (Anorthosite)	26.4 (Anorthosite)
Pyroxene	20.3	12.2	19.8
Olivine	13.7	8.2	13.4
Mg-sulfate	4.0	2.4	3.9
Anhydrite	1.7	1.0	1.7
Ferrihydrite	3.5	2.1	3.4
Spinel	1.9 (Magnetite)	1.1 (Magnetite)	1.9 (Magnetite)
Hematite	0.5	0.3	0.5
Fe-carbonate	1.4	0.8	1.4
Hydrated silica	3.0	1.8	2.9
Phyllosilicates	n.r.	40.0 (Montmorillonite)	2.5 (Montmorillonite)

Clay minerals allow for the wet processing of Martian regolith without the need for any additional binder or plasticizer, as was reported in previous literature findings **[106]**. However, high amounts of clay can be detrimental. In fact, the higher the clay content, the worse the problems associated with shrinkage and cracking during drying and sintering. The scenario usually proposed to mitigate this problem consists of tempering a high clay content terrain, possibly sourced from phyllosilicate deposits on Mars, with a generic soil with a composition close to the Martian average **[106]**. MGS-1C (40% montmorillonite, see **Table 4.15**) and MGS-1 are good candidates to mimic the former and the latter, respectively. Blending the two simulants, it is possible to tailor the processability of the slurry according to the case study. In this work, MGS-1C was added to MGS-1 according to extents, varying from 1:32 to 1:4. The calculated oxide constituents and phase compositions of the 1:16 mixture (MGS-1/16) have been reported in **Table 4.14** and **Table 4.15**, respectively. Given the rather

coarse dimensions of the as-received simulants, a preliminary dry milling step of the two separated simulants was performed. A steel milling vessel in a vibratory disc mill TS250 (Siebtechnik GmbH, Germany) was employed by operating in batches of 200 g, which were milled for 2 min and then rested for 2 min for a total of 4 cycles.

In the framework of maximizing the ISRU potential of the proposed technology, no other ingredient other than water would be needed to wet-process regoliths. With this aim, previous studies assessed the processability of slurries based on just pure water **[106]**. However, water present on Mars could be available as salt-rich brine. The direct use of such saltwater to process regoliths would allow for the cutting of energy costs and technical complexity associated with water purification on Mars. To assess this possibility, a Martian saltwater simulant (MSW) was prepared according to the Mars "dirty" water recipe based on the chemical compounds detected by the Phoenix lander **[266]**, as reported in **Table 4.16**. Double-deionized water (DDW) was used as a solvent. The simulant was stirred on a hot plate (T=80°C) for 12 h to facilitate salt dissolution.

Table 4.16 - Mars saltwater simulant (MSW) composition (1 L solution) **[266]**.

Formula	Compound	Quantity (g)	Supplier	Product Code
H_2O	Double deionized water	1000	-	-
$CaCO_3$	Calcium Carbonate	1.6	Riedel-de Haen AG Seelze-Hannover	12003
$MgCO_3$	Magnesium Carbonate	0.8	Roth	3530.2
$MgSO_4*7H_2O$	Magnesium Sulphate Heptahydrate	1.2	Merck	5886
KCl	Potassium Chloride	0.032	Roth	6781.1
$NaHCO_3$	Sodium Bicarbonate	0.14	Honeywell Fluka	31437
$Ca(ClO_4)_2*4H_2O$	Calcium Perchlorate Tetrahydrate	0.46	ThermoFisher Scientific	39063
$Mg(ClO_4)_2*6H_2O$	Magnesium Perchlorate Hexahydrate	0.332	Aldrich	309303

4.3.2.2 Wet processing

After the milling step, the powders were mixed according to different MGS-1C to MGS-1 ratios to obtain blends with a clay content ranging from 1% to 10%. The milled powders were then passed through a 250 µm sieve to break clay agglomerates and facilitate dispersion. MSW was added to the desired extent. A wet milling step was then performed to guarantee a proper dispersion of the regoliths in the saltwater simulant. 8 mm diameter (30% of slurry weight) and 3 mm diameter (10% of slurry weight) zirconia balls were used as milling media in a 1h treatment performed on a roller bank (ROBO, Alpine, Germany) set at 150 rpm. Prior to printing, the two tunable parameters (clay content in solids and solid loading) were investigated to find an optimum that guaranteed the best slurry processability. To this aim, a rheological characterization was performed. The solid load was varied between 40 to 55 wt.% to meet a viscosity dependence on shear rate close to that of a reference Al_2O_3 slurry provided as standard for LIS printing by the company QEP3D GmbH (Stahnsdorf, Germany). To measure the viscosity of the slurries, a Physica MCR301 rheometer was used (Anton Paar, Austria). The measurement is performed using a two-plate setup with a plate diameter of 25mm and controlling the shear rate with an amplitude sweep. The shear rate was systematically varied using a linear ramp from 5 to 100 1/s over a duration of 145 seconds. Subsequently, it was kept constant at 100 1/s for a duration of 10 seconds before being linearly ramped back down to 5 1/s. Other than viscosity, shear stress was investigated as a function of shear rate. Slurries produced according to different MGS-1C to MGS-1 ratios and 50 wt.% solid loading were then preliminary slip cast with a conical mold and characterized in terms of the extent of cracks formed during printing and subsequent drying. This aspect is crucial both for SC and LIS printing outcomes. Particle size distribution of the solids dispersed in the slurry was characterized using an LS13320 laser diffraction size analyzer (Beckman Coulter, USA). For both rheological and particle size characterization, each measurement was repeated three times.

LIS printing was performed using a CeraMax Vario V900 LIS machine (Lithoz, Austria). The CeraMax Vario V900 is equipped with a 120 W CO_2-Laser that has a focused spot with a diameter of ~0.5 mm. The machine has a build volume of up to 250x250x290 mm^3 and can print complex geometries by stacking several printed layers of individual heights from 200 µm up to 1 mm. The slurry is stored in a reservoir from which it is pumped and spread out by a doctor blade, which deposits it on a build plate that is lowered into the vat for every new layer. In this study, a build platform made from glass

is used. During printing, the infrared CO_2 laser progressively dries the slurry according to customizable parameters (see **Figure 4.23**). After each layer is printed, the excess slurry is fed again to the reservoir. Before printing can begin, the air humidity inside the build area needs to be brought up to 90%. This helps to avoid uncontrolled slurry drying in spots not part of the printed object.

Several printing parameters can be tuned to find an optimal configuration that guarantees effective drying, prevents cracking, and limits water reabsorption from the upper layers and the lateral margins of the printed part. The Laser Speed defines the speed at which the focused laser beam travels along its path. The faster the laser travels, the less it dries the slurry. Common speeds range from 10 m/s to 15 m/s. The wattage defines the laser power. Naturally, the higher the wattage, the more the slurry is dried. The CeraMax Vario V900 is capable of up to 120 W, but the typical employed wattage lies around 20-25 W. It is important to note that the higher the wattage, the more effective the drying process, but also the higher the possibility of developing cracks. The line spacing defines the distance between the lines of the laser's path. As the line spacing decreases, the total length of the path is augmented, thus increasing the total time the slurry is exposed to the laser. The smaller the line spacing, the more the slurry gets dried. A typical value for line spacing is 0.025 mm. One run of the laser completing its path across the geometry is not enough to sufficiently dry one layer of slurry. The number of hatches defines how many drying cycles are performed on each layer. This value greatly varies depending on the slurry. It usually ranges from two to 25 hatches per layer. If the path of the laser is not altered between hatches of a single layer, stress can be induced into the green body and wetting gradients can be amplified. To combat this, the geometry of the path for each Hatch is usually rotated according to the parameter "Rotation Between Hatches". Generally, for symmetric geometries, a value of 90° is used. Another relevant parameter is the Line Scheme. Finally, an appropriate Layer Height needs to be selected.

In this study, two configurations, namely A and B, are tested. With respect to the B one, configuration A is an enhanced drying program which aims to maximize the water removal from each printed layer, thanks to an increased Wattage and Number of Hatches. The investigated parameters for the printing of Martian regolith slurries are reported in **Table 4.16**. To maximize the output of the printing sessions, rather simple blocks of dimensions 80x80x5 mm are printed with the LIS machine, and smaller square-section green bodies with a 2:1 aspect ratio (dimensions about 15x5x6 mm) are cut from them.

Table 4.17 - Investigated parameters for the LIS process. Values reported in italics identify a parameter that was varied and optimized for the obtainment of the LIS printed part.

Parameter	Config. A	Config. B
Laser Speed	7 m/s	7 m/s
Wattage	*30 W*	*22 W*
Line Spacing	0.025 mm	0.025 mm
Number of Hatches	*30*	*22*
Rotation Between Hatches	90°	90°
Line Scheme	Snake	Snake
Layer Height	0.25 mm	0.25 mm
Dimensions of the Printed Part	80x80x5 mm	80x80x5 mm

For the sake of comparison, the same optimized slurry composition employed for LIS printing was used to obtain, via slip casting, cylindrical samples of aspect ratio >2:1 (dimensions about 15 mm height x 6 mm diameter). To do so, polymeric cylindrical molds were employed. The bottom side of the mold was placed in contact with a gypsum plate, while from the top, the slurry was poured in. A mold release spray aided the process, and after 72 hours, the cast detached from the mold due to shrinkage during drying and could therefore be removed. The two sides of the slip-cast cylinders were finally polished with abrasive paper (grit 320).

4.3.2.3 Sintering and characterizations

Thermogravimetric analyses (TGA) were performed to evaluate the degassing behavior in oxidizing and inert atmospheres of LIS-printed green bodies in preparation for the sintering experiments. The experiments were performed with a simultaneous DTA-TGA STA 409PC Instrument (Netzsch, Germany) coupled with an OmniStar mass spectrometer (Pfeiffer Vacuum, Germany). Given the possibility to track the evolved gas during the experiments, differently from **Sections 4.1** and **4.2**,

the weight loss and evolved gas were tracked in the RT-1200°C interval, with a heating rate of 10 K/min. To evaluate the effect of the salts on the thermal stability of the printed part, tests were conducted in an air atmosphere for the MSW green body printed via LIS and a special LIS-printed green body was obtained with DDW. Additionally, inert conditions experiments were conducted in the N_2 atmosphere for MSW LIS printed samples. Each experiment was reproduced at least twice.

Pressureless sintering experiments described in **Section 2.2.2** were conducted both in oxidizing conditions (air) and in simulated Martian conditions (925 Pa CO_2). For the latter, the furnace was evacuated for 10 min with a rotary vane vacuum pump RV8 (Edwards Limited, UK) and flushed with CO_2 three times before reaching the desired pressure value and sealing the oven chamber. Further details on simulated Martian atmosphere sintering can be found elsewhere **[100]**. A minimum of three samples (SC and LIS) were placed inside the sintering area to evaluate experimental deviations. For each atmosphere, an optimal configuration was identified on the basis of relative density maximization, minimization of water adsorption and undesired excessive deformation and/or bloating avoidance.

Sintered samples were then characterized in terms of linear sintering shrinkage and relative density. The latter was evaluated by Archimedes' method using acetone as a soaking medium (as suggested by **Sizemore et al. [207]**) and an MC1 Analytic AC210P (Sartorius, Germany) analytical balance. Relative densities were then evaluated by considering, as reference values, the true densities evaluated on crushed LIS green body by an Ultrapyc1200e helium pycnometer (Quantachrome Instruments, USA). Water adsorption experiments were conducted by submerging the samples in double-deionized water for 10 minutes and recording the weight before and after experiments. Phase transitions occurring after the thermal treatments were evaluated by means of ex-situ X-ray Powder Diffraction (XRD) analysis on pulverized sintered samples. A D8 (Bruker, Germany) diffractometer was used (Bragg-Brentano geometry), equipped with a copper anode (Cu Kα radiation λ=1.5418 nm) working at 40kV and 40mA. The analysis was performed in the range 2θ = 10°- 130°, with a step size of 0.05° and 10 seconds for each step. The attribution of the mineralogical phases was performed with EVA software (Bruker, Germany) with a Search and Match approach, using the COD (Crystallography Open Database) as a reference database **[209]**.

To evaluate compressive strength, 10 LIS samples and 10 SC samples were sintered at the two optimized conditions for oxidizing and reducing atmospheres. The obtained specimens were tested

in a Zwick RetroLine (Zwick/Roell, Germany) machine. Heat conductivity between 100 K and 300 K was measured on selected samples using the Thermal Transport Option on a Physical Properties Measurement System (PPMS, Quantum Design). Copper leads for contacting the sample heater and two thermometers were attached to the sample rods of dimensions ≈ 5×5×15 mm³ using silver epoxy glue.

4.4.3 Results and Discussion

4.3.3.1 Compositional optimization of the slurry

Rheologic experiments reported in **Figure 4.24** show that, as expected, the higher the water content in the slurry (and the lower the solid loading), the lower the viscosity. As also shown in **Figure 4.24**, the viscosity of the reference Al_2O_3 slurry provided by the company QEP3D as standard for LIS printing is almost constant over the shear rate, linearly increasing the shear stress. While the viscosity of the slurry with 45 wt.% water is closest to the reference at a shear rate of about 20 1/s, it gets considerably lower at higher shear rates. Overall, the most comparable slurry is the one with 50 wt.% water. Especially at higher shear rates, the viscosity is very similar to that of the reference slurry. This is important for the LIS process, as the slurry will experience similar shear rates while being pumped through the tubes. Similar results have been obtained for the 50 wt.% saltwater slurry (50 wt.% solid loading), for this reason, all subsequent experiments have been performed with it.

Preliminary slip casting of the 50 wt.% solid load slurry produced starting from MGS-1 and MGS-1C simulants mixtures in the range from 1:32 (1 wt% clay) to 1:4 (25 wt.% clay) confirmed that the higher the clay content, the more extensive the cracks after drying. To keep a good compromise between the processability of the slurry and the cracking phenomenon, the 2.5 wt.% (MGS-1/16) clay composition was selected and used for all subsequent experiments. According to particle size analysis results (d_{10}=0.59 µm, d_{50}=2.74 µm, d_{90}=8.28 µm, d_{span}=2.81 µm)**,** the combined effect of dry and wet milling results in a slurry characterized by small, dispersed particles.

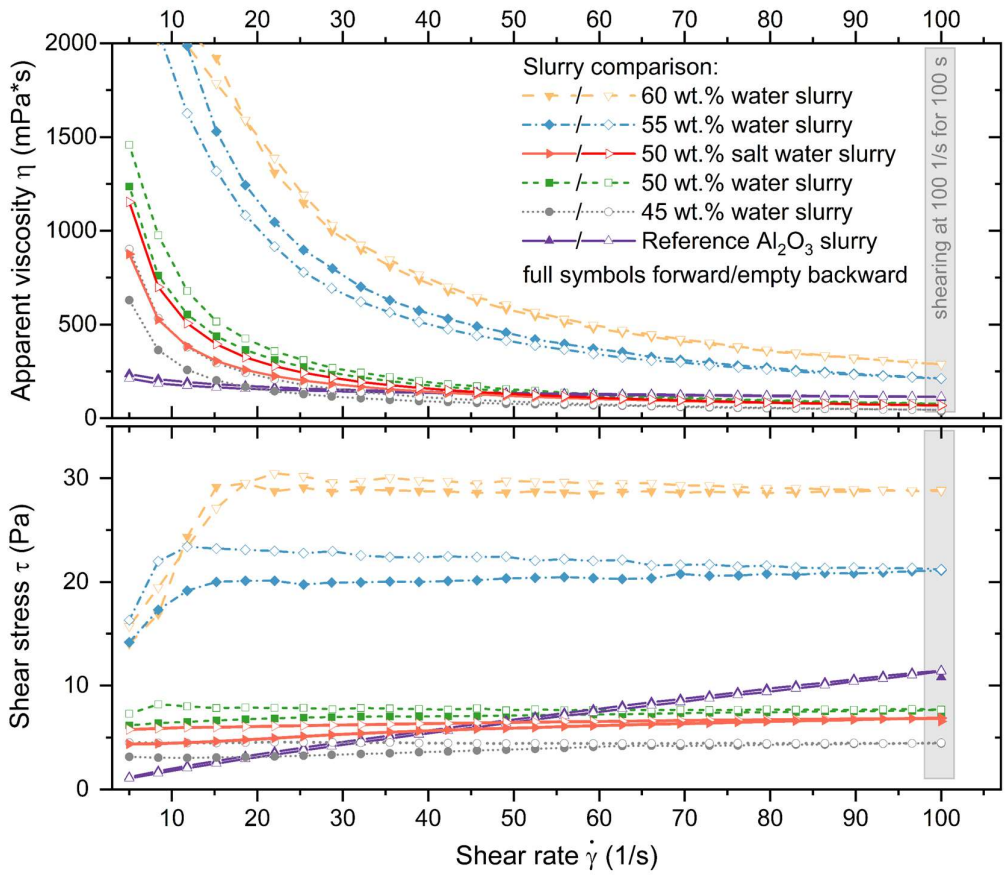

Figure 4.24 - Viscosity and shear rate over shear stress for different slurries: comparison of 60-45 wt.% water, 50 wt.% saltwater content and Al_2O_3 reference slurry.

4.3.3.2 Additive Manufacturing

The saltwater-based slurry prepared according to the optimized solid loading (50 wt.%) and mixture of MGS-1 and MGS-1C simulants (MGS-1/16 powders) was printed according to A and B configurations reported in **Table 4.17.** While B succeeded in printing the 80x80x5 mm block (**Figure 4.25b**), when printing with configuration A, cracks appeared already during the LIS process, as reported in **Figure 4.25a**. This difference is ascribable to the harsher drying in configuration A, where both laser Wattage and Number of Hatches parameters were higher. This resulted in humidity gradients across the printed part, causing cracks and exfoliation, as highlighted in **Figure 4.25a**.

This outcome underlines the importance of the tunability of LIS parameters if compared to traditional slip casting, when it comes to controlled drying. By appropriately tuning two of the machine parameters, it was possible to obtain 80x80x5 mm blocks, which were then cut into smaller

square-section green bodies with a 2:1 aspect ratio (dimensions about 15x5x6 mm) and used for subsequent sintering and characterization. Cylinders of about 15mm in height and 6 mm in diameter were obtained through slip casting, and their sintering and characterization results were used as a comparison for those obtained for the LIS samples.

LIS printed parts showed an average density of 1.63±0.07 g/cm³, while a higher value of 1.83±0.03 g/cm³ was measured for SC samples. If compared to the pycnometric density of 3.03±0.01 g/cm³, measured on the dried starting slurry, the relative densities for the green bodies are about 53.8% and 60.4% for the LIS and SC samples, respectively. The different densities of the LIS and SC green bodies could be ascribable to the different drying that the same slurry encountered. In the LIS process, the new slurry is progressively added on top of each dried layer during printing, causing water reabsorption that could determine a resulting higher water content at the end of the process if compared to SC. This water content is then eliminated through the final drying step in a controlled atmosphere. However, a higher porosity is retained.

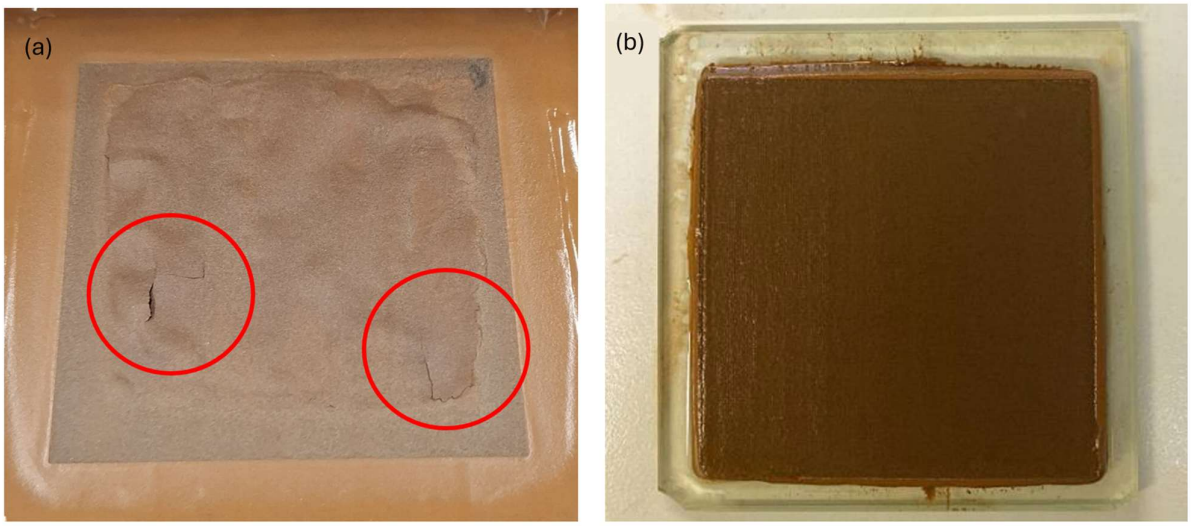

Figure 4.25 - LIS parts (80x80x5 mm) printed according to (a) configuration A and (b) configuration B starting from MSW slurry. The part printed according to configuration A was photographed while still in the build platform, when cracks (highlighted with red circles) started to appear.

4.3.3.3 Thermogravimetric analyses

The obtained LIS green bodies were characterized for their thermal stability in different atmospheres. **Figure 4.26a** shows the thermal stability and developed gas in the air atmosphere of LIS-printed green bodies according to configuration B (see **Table 4.17**) in the case of MSW-based slurry and DDW-based slurry. This comparison aims to highlight possible differences deriving from the salts added during the preparation of the liquid dispersant MSW according to **Table 4.16**.

From **Figure 4.26a** it can be observed how both the MSW and DDW-based green bodies show a rather similar behavior. Both samples showed progressive mass loss when exposed to rising temperatures, with a final loss of about 4.9% at 1200°C. This phenomenon, other than water evaporation, can be attributable to the thermal decomposition of carbonates and sulfates. This is present both in the case of MSW and DDW samples, indicating that its origin lies not only in the added salts (which in the case of MSW-based green bodies account for no more than 0.5 wt.%) but also in the raw powders, particularly rich in $MgSO_4$ and $FeCO_3$ (see **Table 4.15**). Looking in detail at the spectra recorded by the mass spectrometer on the gases developed during the TG analyses, two peaks in the CO_2 signal (blue lines) are recorded at about 400°C and 600 °C for the case of both MSW and DDW-based green bodies. These peaks are attributable to carbonates, whose decomposition is expected to produce CO_2 as detected for natural phases in the 350°C-450°C range for the case of siderite ($FeCO_3$) **[275]**, 450-700 °C for magnesite ($MgCO_3$) **[243]** and 600-800°C for pure calcite ($CaCO_3$) **[276]**, all species either present in the pristine simulants (**Table 4.15**), or added during the preparation of MSW (**Table 4.16**) The slope of the mass loss curve increases in correspondence of the CO_2 peaks, confirming that some species are indeed releasing a volatile gas in that range, and therefore the sample is losing mass.

Looking at the SO_2 spectra (green lines), a significant increase in concentration can be observed for temperatures higher than 800°C, in agreement with the decomposition of magnesium sulfate usually observed in the range 800-1100°C **[277]**. The consequent drop in the weight loss curve can be related to such a phenomenon.

Figure 4.26b shows that a limited impact is generated by undergoing thermal treatment in inert conditions, such as the N_2 atmosphere. A slight (1.4%) decrease in mass loss is observable, with a final value at 1200°C equal to 3.5%. The most significant difference is the onset of the SO_2 degassing (caused by $MgSO_4$ decomposition) at lower temperatures. This outcome could be related to the

occurrence of $MgSO_4$ decomposition at lower temperature levels observed when operating in reducing conditions **[277,278]**, which in this case may be caused by interactions with other reducing species in the tested powders and allowed by the absence of free oxygen in the flowing gas.

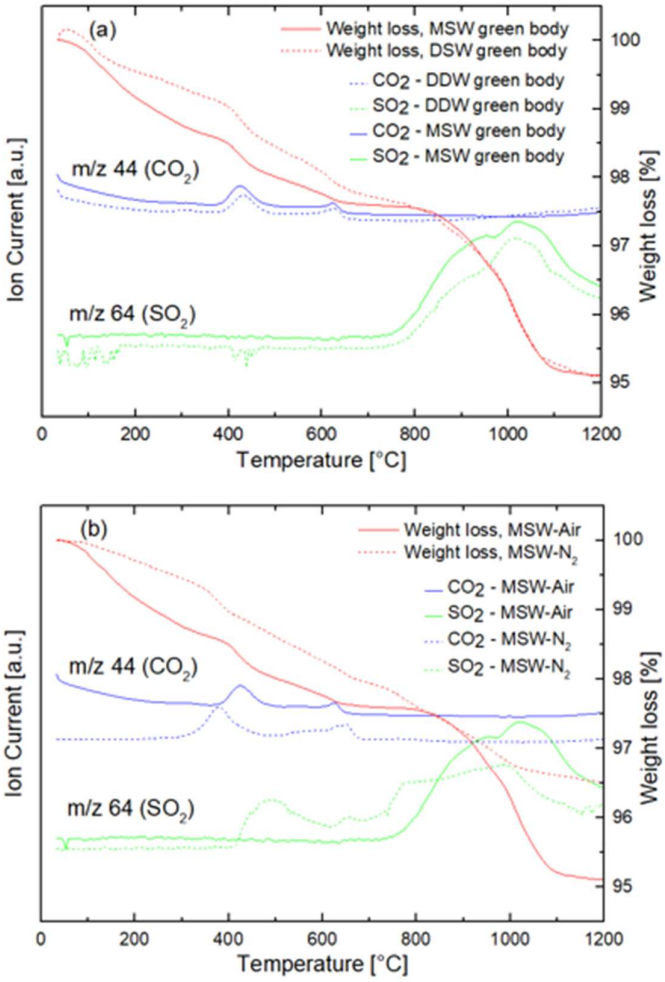

Figure 4.26 - Weight loss and evolved gases during the TG analyses in air. (a) Comparison between LIS-printed green bodies prepared with DDW and MSW. (b) Comparison of TG analyses in air and N_2 for the case of LIS-printed green bodies prepared with MSW.

4.3.3.4 Sintering conditions optimization

Figure 4.27 evidences the recorded results in terms of achieved relative density, water adsorption and linear sintering shrinkage recorded for the LIS and SC printed green bodies under oxidizing

conditions (air atmosphere). Relative density increases when the dwelling temperature of the sintering process is gradually raised (**Figure 4.27a**). It can be noted that the relative density gap observed for LIS and SC green bodies is present for all sintering conditions up to T_D=1190°C, then an asymptotical level of relative density of about 85-86% is achieved for T_D ≥1200°C, for both LIS and SC samples. As reported in **Figure 4.27b**, samples obtained at T_D ≥1200°C also show high linear sintering shrinkages (>9%) and very low water absorption (<1%), suggesting that the sintering phenomenon is causing significant shape changes and reduction of porosity. To calculate the relative densities, the theoretical value of 3.03 g/cm^3, obtained for the crushed LIS green bodies, was used. Further pycnometer analyses on the crushed sintered samples suggest that only marginal variation in theoretical density occurs during sintering, with obtained values ranging from 3.03 to 3.05 g/cm^3.

The samples obtained at T_D≥1200°C (shown in **Figure 4.29**) showed significant deformation and onset bloating, and severe adhesion to the sintering plate. These aspects are not compatible with the acceptable shape retention goal proposed for this study and have, therefore, been considered unsuitable for further characterization.

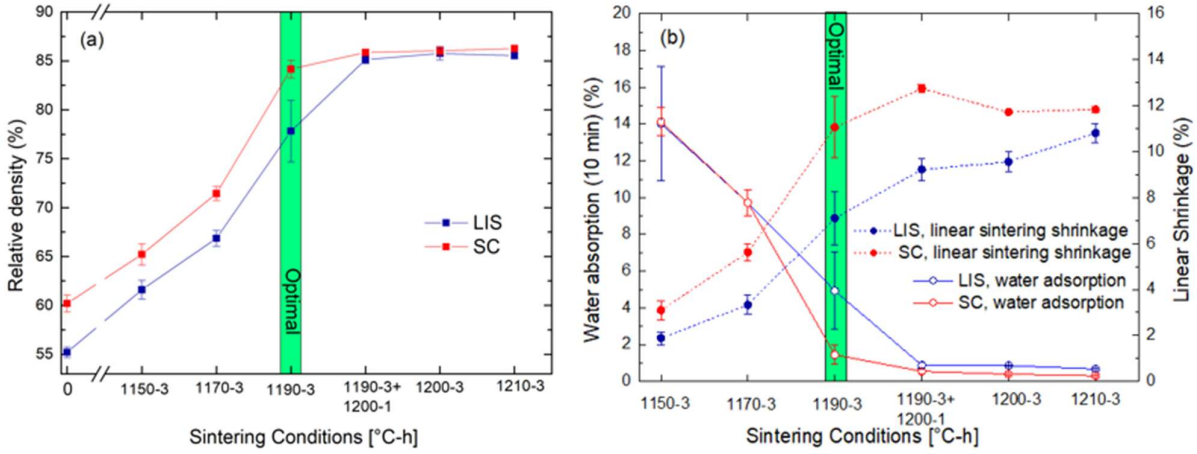

Figure 4.27 - Sintering test results in terms of (a) relative density and (b) 10 minutes of water adsorption and linear sintering shrinkage in an air atmosphere. The green box evidences the optimal condition.

The higher sintering condition that avoids such phenomena while still guaranteeing acceptable densification levels is 1190°C-3h. However, water adsorption is still >3% for the case of LIS samples (4.93±2.09%). In **Karl et al. 2020b [100]**, adding a second sintering step at a 10°C higher temperature after the first 3 h dwelling at the original T_D resulted in lower water absorption and higher linear shrinkage while preventing bloating and excessive deformation due to the limited time at the higher temperature level. In this study, operating with a two-step 1190°C-3h + 1200°C-1h sintering routine succeeded in obtaining samples with low water absorption (0.88±0.16% LIS, 0.54±0.13% SC), but the same problems encountered when operating with one-step sintering at $T_D \geq 1200$°C were also present. This different behaviour, if compared to the results reported in **Karl et al. 2020b [100]**, could be ascribable to the lower clay content in the green bodies (5 vs 2.5 wt.% in this study) and the milder T_D employed in the previous work (1145°C), all aspect capable of allowing a higher processability and finer tunability of the sintering conditions. Given the negative outcome of the two-step test, the 1190°C-3h condition was considered optimal, tested for the achieved compressive strength and further characterized. The relative density achieved in the case of LIS and SC samples are 77.82±3.14% and 84.16±0.89%, respectively.

When operating under simulated Martian conditions (i.e., 925 Pa CO_2), similar trends in relative density, water absorption and linear sintering shrinkage can be observed, as reported in **Figure 4.28**.

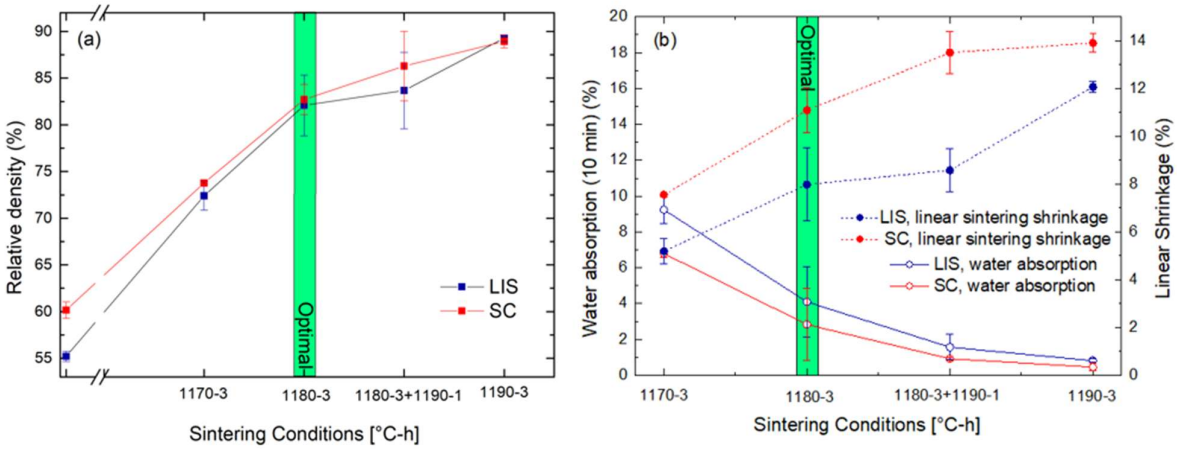

Figure 4.28 - Sintering test results in terms of (a) relative density and (b) 10 minutes of water absorption and linear sintering shrinkage in the simulated Martian atmosphere. The green box evidences the optimal condition.

In this case, and in agreement with previous findings **[100]**, operating under a simulated Martian atmosphere causes a slight shift of the sintering window towards milder conditions. Operating at the optimized condition for air atmosphere (1190°C-3h) under CO_2 atmosphere causes the onset of the bloating phenomenon, significant observed deformation and adhesion to the sintering plate. Working at 1170°C causes an important reduction in terms of relative density, linear shrinkage and an abrupt increase of water absorption while operating at the middle point of 1180°C for 3 h allows to obtain relatively high densification levels both for the case of LIS (relative density of 82.08±3.26%) and SC samples (relative density of 82.71±1.62%). Also, in this case, the two-step sintering schedule 1180°C-3h + 1190°C-1h was tested to further improve the water absorption parameter, which in the case of LIS samples is 4.10±1.97% at 1180°C-3h. This strategy is successful in obtaining the desired water absorption level while also increasing relative density for both LIS and SC specimens. However, as recorded for the air atmosphere sintering tests, it is sufficient to generate pronounced deformation and adhesion to the sintering plate. For this reason, the 1180°C-3h sintering condition was considered optimal, then chosen for compressive strength tests and further characterization.

Observing the difference between the relative densities of LIS and SC samples for the case of CO_2 sintering (**Figure 4.28a**), it is possible to see a lower gap if compared to the air sintering results (**Figure 4.27a**). This difference can be ascribable to the vicinity of the tested conditions in the CO_2 atmosphere to high densification levels. The difference observed in the case of air sintering, which derives from the lower LIS green body density, is already compensated at T_D=1170°C by the ongoing sintering phenomena.

Examining **Figure 4.29**, where photographs of the obtained samples are depicted, it is easy to note how both LIS and SC samples sintered under an air atmosphere exhibit a colour shift which starts with the yellowish-brown of the unsintered sample, moving towards bright red at 1150°C-3h, and fading to darker shades of red up until 1210°C-3h. On the contrary, samples sintered under simulated Martian atmosphere show a darker colour starting from the 1170°C-3h condition. This phenomenon is an indicator of undergoing phase transitions in the sintered pieces, underlying the need for further compositional analysis of the obtained samples.

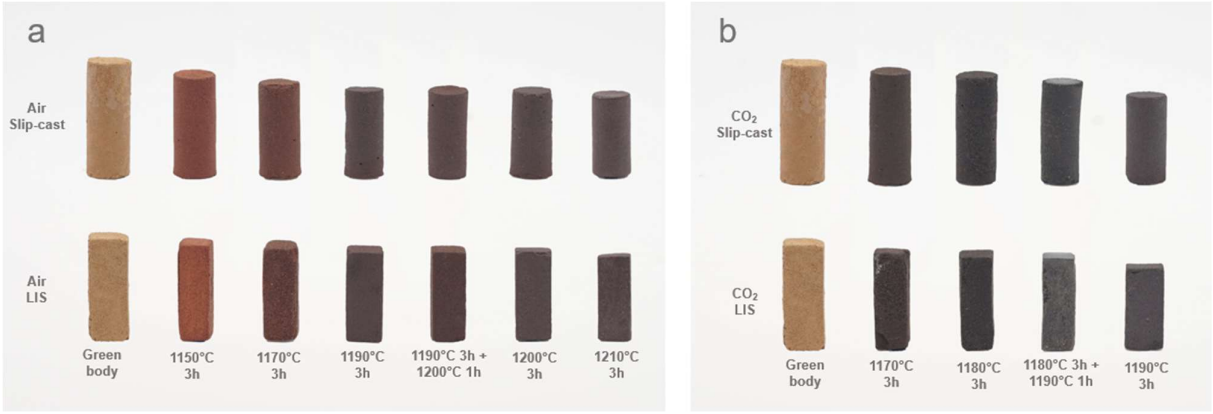

Figure 4.29 - Samples sintered under different conditions in (a) air and (b) simulated Martian atmosphere. The images were produced by combining photos of individual samples (due to different perspectives in these photos and slightly varying green body sizes, the heights were adapted to match the observed linear sintering shrinkages).

4.3.3.5 Compositional characterization, thermal conductivity and mechanical properties

To better understand the origin of the peaks detected in the green body powders and in the sintered parts, a focus on the 2θ range 2θ = 20°- 60° of XRD data collected on pristine MGS-1 and MGS-1C simulants has been reported in **Figure 4.30**, as well as the XRD data collected on the crushed LIS green body. Indeed, the two raw simulants are characterized by two dominant phases ascribable to the plagioclase and pyroxene groups. A minor olivine phase is present, while traces of Siderite ($FeCO_3$) and Epsomite ($MgSO_4$) have been also detected. It is worth noticing that a significant amorphous content characterizes the simulant. Basaltic glass, hydrated silica, and ferrihydrite all contribute to the amorphous fraction reported by **Cannon et al. [87]**, while they have not been detected via XRD due to their nature. It is then possible to state that the detected crystalline phases are in agreement with the compositions reported by the producer (**Table 4.15**). Regarding MGS-1C, Montmorillonite, Quartz and Calcite ($CaCO_3$) have also been detected, while it can be noted that the intensity associated with the Epsomite peak is higher than in the case of MGS-1. In the LIS green body (black line in **Figure 4.30**), the Plagioclase, Pyroxene, Olivine and Siderite phases are present, with relevant intensities associated with the Epsomite and Calcite phases, mostly deriving from MGS-1C and the salts added by employing the MSW simulant, according to **Table 4.16**. The tempering of MGS-1C with MGS-1 caused a reduction in the intensity of peaks associated with quartz and montmorillonite phases, which have not been assigned in the green body pattern.

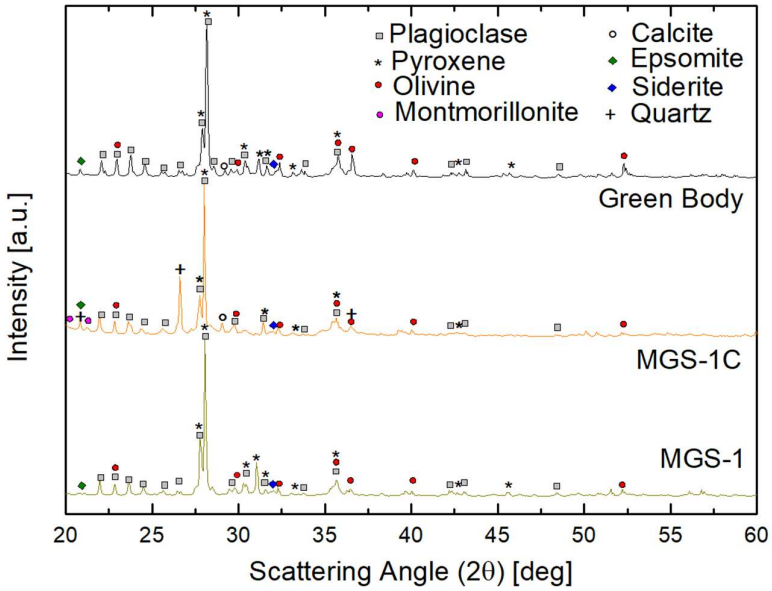

Figure 4.30 - XRD Patterns of the as received MGS-1 (olive line) and MGS-1C (orange line) powders and of the crushed LIS printed green body (black line).

Figure 4.31 collects a 2θ = 20°- 60° focus of the XRD spectra of LIS samples sintered in air (a) and CO_2 (b) atmospheres for the case of the optimal conditions 1190°C-3h and 1180°C-3h, and an intermediate condition 1170°C-3h. The XRD spectrum of the crushed green body has also been reported for the sake of comparison. For the case of the samples sintered in air at the intermediate routine of 1170°C-3h, the main observable differences with the green body are a rearrangement in the relative intensities of the plagioclase and pyroxene-associated peaks and the appearance of reflections ascribable to hematite and magnetite. This phenomenon is possibly related to a progressive crystallization of the vitreous phases present in the pristine simulants, especially ferrihydrite and basaltic glass, as well as to the decomposition of siderite. Along these rearrangements in the main phases, it is worth noticing the disappearance of all peaks associated with carbonates (Calcite and Siderite) and sulphates (Epsomite). This corroborates the results obtained in the TG analyses reported in **Figure 4.26a**, where mass drops associated with CO_2 and SO_2 degassing peaks in the mass spectroscopy signals suggested a decomposition of carbonates and sulphates starting at temperatures lower than 400°C and 800°C, respectively.

The main difference encountered between the condition 1170°C-3h and the optimized 1190°C-3h is the absence of hematite phase reflection and the higher intensities associated with magnetite. This

aspect agrees with the progressive pigmentation change of sintered samples observable in **Figure 4.29a**. The bright red colour of 1170°C-3h samples ascribable to hematite progressively fades towards darker brown-red starting from 1190°C-3h, suggesting a progressive depletion of such phase.

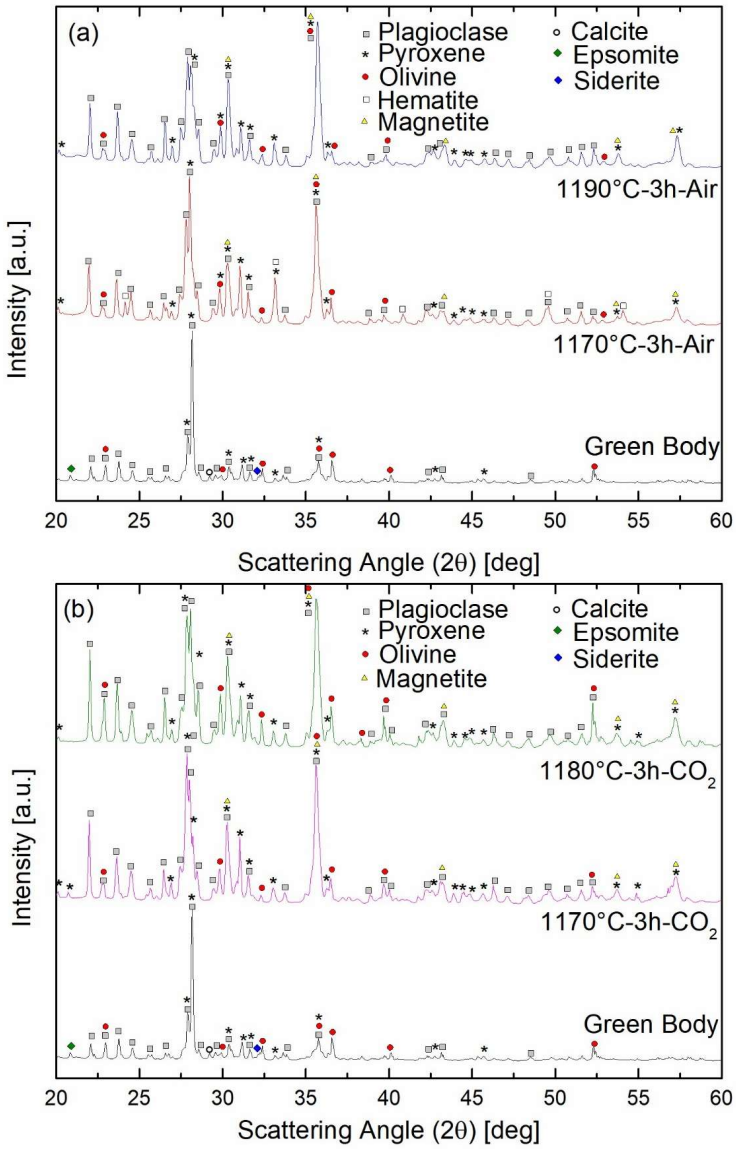

Figure 4.31 - 2θ = 20°- 60° focus of XRD patterns obtained for the crushed LIS printed green body (black line) and for (a) crushed LIS samples sintered at 1170°C-3h (red line) and at 1190°C-3h (blue line) in air atmosphere and (b) crushed LIS samples sintered at 1170°C-3h (magenta line) and at 1180°C-3h (green line) in simulated Martian atmosphere.

Figure 4.31b suggests that a rather similar behaviour with respect to the case of air sintering is encountered when operating in a CO_2 atmosphere. Siderite, Calcite and Epsomite phases are already lost in the 1170°-3h condition, for which a general rearrangement in pyroxene and plagioclase phase reflection intensities is also detectable. In this case, no hematite phase is detected, but only magnetite peaks are identifiable. At the optimized 1180°C-3h condition, a slight increase in the intensity of the olivine-related peaks was observed, along with a small decrease in pyroxene-related reflections. Observing **Figure 4.29b**, the much darker colour of the samples sintered at 1170°C-3h in the simulated Martian atmosphere, if compared to the ones sintered in air, is in agreement with the absence of hematite in the CO_2-sintered samples. This aspect was observed in previous literature **[100]**, suggesting that operating under low pressures (925 Pa) and CO_2 is able to generate reducing conditions, which favour the hematite to magnetite phase transition **[279]**. The occurrence of such a transition was also observed when exposing such iron oxides to other reducing gases, such as CO or H_2 **[279,280]**.

Heat conductivity was measured on the LIS 1190°C-3h air sintered and the LIS 1180°C-3h sample sintered under a simulated Martian atmosphere, yielding values in the range 0.77-0.53 W/mK and 0.80-0.56 W/mK, respectively, in the temperature range 100 K to 300 K, as reported in **Figure 4.32**. These values, collected in a temperature range resemblant of day-night conditions on Mars, are in line with data generally reported for earth concrete **[281]**.

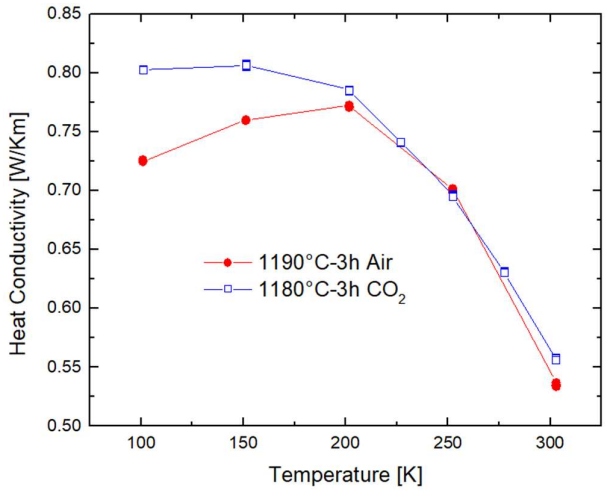

Figure 4.32 - Temperature dependence of the thermal conductivity of the LIS 1190°C-3h air sintered and the LIS 1180°C-3h sample sintered under simulated Martian atmosphere.

Table 4.18 compares the compressive strength of LIS and SC green bodies with the results of different wet additive manufacturing methods previously investigated. Most of the wet processed green bodies characterized in the literature exhibit a compressive strength higher than dry pressed samples **[106]**, underlining once more the importance of water and clays in the enhancement of particle rearrangement, agglomeration and formation of interparticle necks during drying, as described elsewhere **[106]**. Comparing the SC green bodies result with previous literature data reported in **Table 4.18**, a significant drop in compressive strength for the case of slip cast samples can be observed (-27%). Two factors can explain this outcome: firstly, the reduced clay content employed in this work (2.5 wt.%) compared to the one used in **Karl et al. 2020a [106]** (5 wt.%), secondly from the different dispersant, in the former case Martian Saltwater Simulant while in the latter deionized water enriched with 0.5 wt.% PC67. A halved clay content, while markedly reducing cracks during drying, is also responsible for the reduction of the beneficial effects postulated when wet processing this kind of material, i.e., clay swelling and ion dissolution-precipitation, believed to be responsible for the occurrence of strong bonds between unsintered particles.

Table 4.18 - Processing route and compressive strength of unfired samples produced using LIS and SC additive manufacturing methods, comparison with dry pressing.

Sample	Used dispersant	Used binder	Relative Density	Compressive strength
LIS **[This study]**	MSW	-	53.8%	0.93 ± 0.2 MPa
SC **[This study]**	MSW	-	60.4%	2.44 ± 0.46 MPa
SC **[106]**	DDW+ PC67	-	58.1%	3.34 ± 0.22 MPa
Dry pressed **[106]**	-	-	68.4%	1.64 ± 0.08 MPa
Hand build **[106]**	DDW+ PC67	-	62.4%	3.91 ± 0.23 MPa
Robocasting **[106]**	DDW+ PC67	-	63.4%	7.55 ± 1.33 MPa
LSD **[106]**	DDW+ PC67	Polymeric (5 wt.%)	61.7%	30.8 ± 2.47 MPa

In the case of LIS-printed green bodies, a further reduction of the green body compressive strength is ascribable to the low densification level achieved (53.8%): high porosities are well known to affect mechanical performances negatively. This outcome opens the possibility of further optimization studies of the LIS process aimed at obtaining higher relative densities in the unfired parts. Higher compressive strengths were reported for the case of samples obtained through robocasting or layerwise slurry deposition, albeit with the aid of a polymeric binder in the latter case **[106]**.

When evaluating the Weibull characteristic compressive strength of sintered samples reported in **Figure 4.33**, it is possible to observe that a gap in the measured property between LIS (~100 MPa) and SC (~165 MPa) samples sintered in air is maintained also after this process, reflecting the different densification level achieved between LIS and SC samples (77.8±3.1% vs. 84.2±0.9% respectively). However, when examining the results obtained for the samples processed in a simulated Martian atmosphere, it is evident that density is not the only controlling aspect of mechanical performance. Slightly lower Weibull characteristic compressive strengths of about 93 and 151 MPa were obtained for the LIS and SC samples, respectively, while the achieved densification level accounted for 82.1±3.3 (LIS) and 82.7±1.6% (SC). Most of the recorded differences are probably generated by the different printing process used to produce the green bodies, as well as the different phase evolution encountered during sintering in the different atmospheres. Sintered slip cast parts show a higher compressive strength compared to LIS printed parts, even in the case of comparable relative densities.

Even with relevant differences between LIS and SC samples, the techniques employed in this study allowed for the obtainment of superior properties with respect to most previous studies carried out on consolidated Martian regolith. For example, composites of 80 wt.% regolith - 20 wt.% polyethylene produced by **Sen et al. [233]** showed compressive strengths of about 40 MPa. Sulfur concretes were also produced by mixing 50 wt.% sulfur with JSC Mars-1A simulant at about 120°C, achieving a compressive strength above 50 MPa **[234]** or, in another case, mixing 30 wt.% sulfur with MGS-1 simulant and achieving a value of 27 MPa **[282]**. Similarly, geopolymers fabricated starting from Martian regolith simulants and various additives showed compressive strengths of 55.27 MPa **[283]** or 62.8 MPa **[284]**.

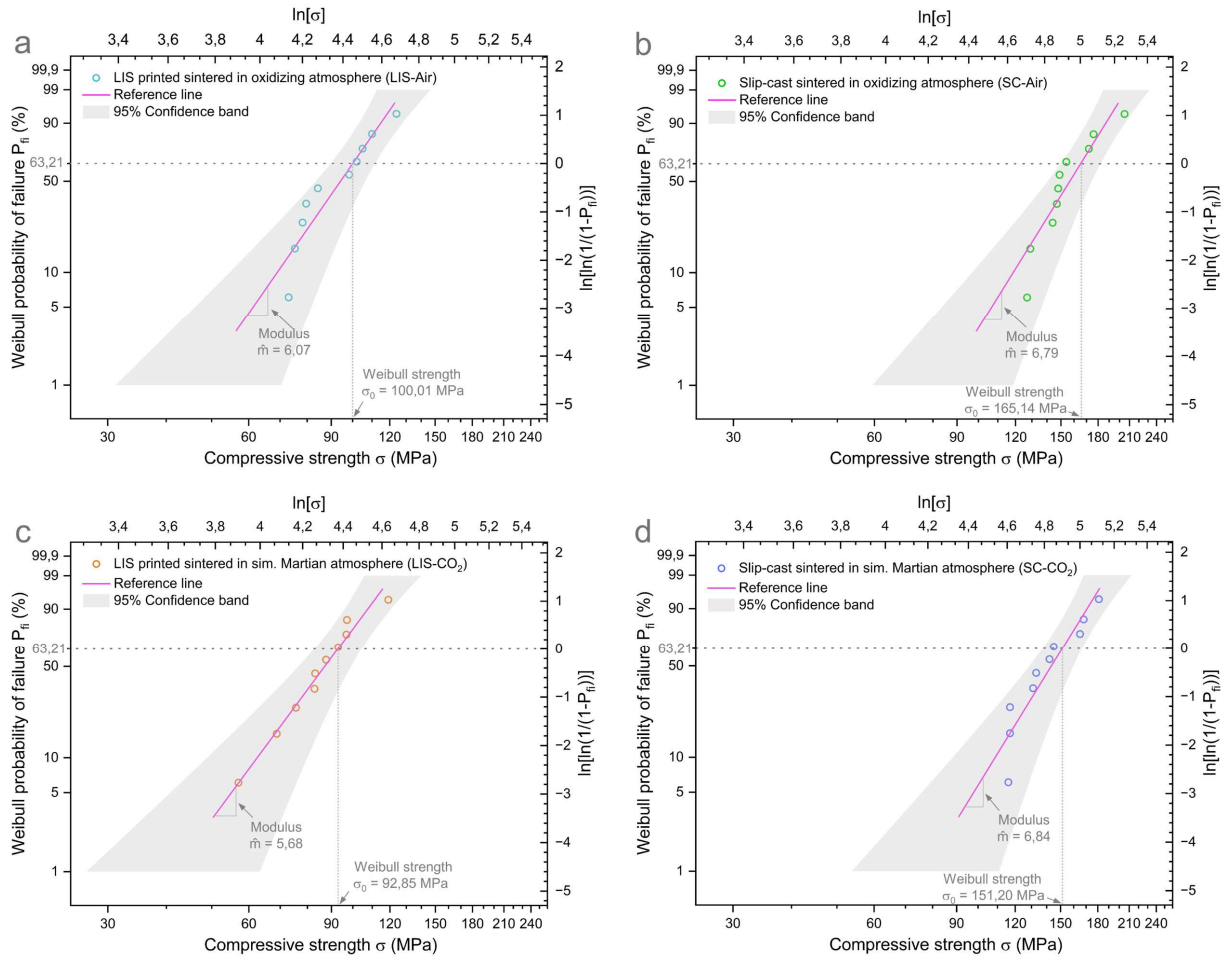

Figure 4.33 - Weibull fracture probability plots of the compressive strength measured for the cases of (a) LIS-AIR (LIS sample sintered in air at 1190°C-3h), (b) SC-AIR (SC sample sintered in air at 1190°C-3h), (c) LIS-CO_2 (LIS sample sintered in simulated Martian atmosphere at 1180°C-3h), (d) SC-CO_2 (SC sample sintered in simulated Martian atmosphere at 1180°C-3h).

Sintering of MGS-1 simulant enriched with about 5 wt.% polyvinyl alcohol at 1150°C led to values of about 40 MPa **[285]**. Recently, approaches aimed at maximizing the use of locally available materials have been pursued. Vibrational compaction of MGS-1, followed by sintering at 1150 and 1200 ◦C for 30 min, resulted in compressive strengths of ~27–77 MPa **[286]**. Cold sintered samples obtained by processing a 5wt.% clay containing a mixture of MGS-1 and MGS-1C at 400 MPa with 10M NaOH resulted in a value of 43 MPa, with an achieved consolidation level of 87.5%, higher if compared to the densities achieved in this study **[107]**. As reported in **Section 4.2**, recent attempts also employed

the Spark Plasma Sintering (SPS) technology, achieving very promising compressive strength values. **Min [112]** reported values of about 103 and 137 MPa after sintering MGS-1 and JEZ-1 Martian regolith simulants, respectively, while in the work described in **Section 4.2** values of about 310, 141, 152, and 198 MPa were obtained for JSC-Mars-1A, MMS, MGS-1 and JEZ-1 sintered simulants. It is worth reminding that even if the mechanical properties obtained in the previous Section are similar or higher than the ones achieved in the present one, this technology still appears unsuitable for the fabrication of complex shapes in one-step, even if promising efforts have recently been made in this regard **[83-86]**.

It is important to state that while higher compressive strength has been obtained in this study via conventional slip casting, the time, cost and automation advantages described above make LIS technology very promising in the framework of ISRU construction technologies. Moreover, since saltwater is possibly present on Mars' crust, its use as a dispersant in wet-based additive manufacturing technologies, is well suited in the framework of ISRU techniques.

The research activity described in this Section was mainly conducted during my period abroad at the Technische Universität Berlin, Germany. The obtained results are discussed in the following paper: **Casu, M.**, Bahr, J., Kleba-Ehrhardt, R., Mühler, T., Schwentenwein, M., Feyerherm, R., Orrù, R., Cao, G., Gurlo, A., & Karl, D., Sintering of wet-processed simulated Mars regolith slurries shaped using conventional and Laser-Induced Slip Casting (LIS)**.** *Icarus, submitted (2025)*

---

5. Concluding Remarks

This thesis work is aimed to study materials and related fabrication processes relevant to the space exploration and colonization framework. One specific focus was on the investigation of the aspects driving the synthesis, densification, mechanical properties and, especially, oxidation resistance of Ultra-High Temperature Ceramics based on multi component boride solid solutions. The second part of the Thesis was addressed to the development of technologies for the employment of *in-situ* available Martian regolith, with the target of future human presence on Mars. While UHTCs were synthetized via the SHS process, Martian regolith simulants available for the scientific community were employed for ISRU studies. The SPS consolidation technology was employed in both cases, while AM technologies were applied also for the processing of Martian simulants.

In the study described in **Section 3.1**, was focused to study the specific challenges both in processing and oxidation resistance deriving from the presence of VI group metals in HEBs. In detail, the solubilization of $(Mo,W)B_2$ phase was particularly difficult, and was achieved only when 1 wt.% graphite was employed as additive. The latter one was found to improve powder reactivity, which was only slightly enhanced by the use of finer W particles as synthesis precursor. Mo and W were responsible for the poor oxidation resistance at T<1200°C, making this system unsuitable for aerospace applications. This finding, which is in agreement with trends observed for VI group metal borides, can be associated to the high volatility of MoO_3 and WO_3 formed during the oxidation tests **[27]**. The introduction of SiC additive to the HEB allowed not only for an increase in the fracture toughness, with respect to the monolithic material, but also inhibited Mo and W oxides volatilization, thus improving the oxidation resistance.

Having identified quite clearly the detrimental role of VI metals on the oxidation resistance of multicomponent TMBs, the focus shifted to IV and V metals-based borides. In addition, due to the inherent complexity of quinary HEB, to establish the specific role played by each TMB constituent to make oxidation resistance of the resulting material better or worse, more simple binary formulations were investigated.

In this regard, $(Zr_{0.5}Hf_{0.5})B_2$, $(Zr_{0.5}Ta_{0.5})B_2$, $(Nb_{0.5}Hf_{0.5})B_2$ and $(Nb_{0.5}Ti_{0.5})B_2$ solid solutions were studied in detail in this Thesis. More severe SPS conditions were required when investigating the latter two ceramics with respect to the Zr-containing products, i.e. 2050 and 1850 °C, respectively.

This reflects the usual difficulties observed for Nb solubilization into HEB materials **[22,73,174]**. For all systems, the use of small amounts of graphite succeeded in the obtainment of the desired highly dense and single phase solid solution, except for the case of NTB, which was densified up to 93.6%. In terms of oxidation resistance, $(Zr_{0.5}Hf_{0.5})B_2$ and $(Zr_{0.5}Ta_{0.5})B_2$ systems behaved significantly better than Nb-containing ceramics. This can be ascribed to the detrimental phase transitions, associate to thermomechanical stresses, encountered by Nb-oxides at low temperatures (<1200°C). It is however interesting to notice how the substitution of 50 mol.% NbB_2 with either HfB_2 or TiB_2 resulted in improved oxidation resistance. In particular, the NTB system resists better than both its two individual constituents to the oxidation environment, due to the inhibition of phase transitions thanks to the formation of a stable mixed oxide phase, a phenomenon also occurring in literature for other compositions **[30,31]**. In the upcoming future, further effort can be made on the study of other binary systems, for example based on the lighter IV group metal boride, TiB_2. Special interest can be placed on Zr-based systems, to form ternary compositions such as $Zr_{0.33}Hf_{0.33}Ta_{0.33}B_2$ or $Zr_{0.33}Hf_{0.33}Ti_{0.33}B_2$. In this regard, work is on progress to better understand if the oxidation mechanisms observed for ZHB and ZTB can synergistically cooperate for improving oxidation resistance properties. As for Nb, other than being present as a constituent in the bulk of the borides, it could have an important role in slowing down the oxidation phenomena if used as a superficial coating, thanks to the stabilization of liquid boria observed by **Forster et al. [141]** for the case of Nb-coated ZrB_2.

To better identify the optimal conditions for SHS and SPS processes, two model-based studies validated with individual TMBs are presented in **Section 3.4** and **3.5**, respectively. The combination of the direct and the borothermal synthesis reactions was investigated in the former, thanks to a thermodynamic analysis aimed to maximize the use of cheap transition metal oxides as starting reactants rather than costly pure metal powders. Further extensions of this study will aim to the abatement of the oxide impurities still present in the synthesis products, and the extension of this approach to multicomponent systems. As for **Section 3.5**, the rheologic-based model developed for the SPS process proved to be able to properly describe the densification process of individual TMBs, and is expected to be, in the future, a useful tool for the individuation of the optimal densification conditions for different materials.

The SPS technique proved to be a useful tool also for processing different Martian regolith simulants. Indeed, MMS and JSC-Mars-1A powders were densified up to 97-100 % employing this technique.

The obtained sintered products proved to be interesting for the harvesting and conservation of solar energy, a useful feature on planet Mars. In the future, the optical performance of Martian regolith could be studied also in other settings compered than the one used in this work (latitude=0°, winter solstice at the northern hemisphere, local noon), for example observing how samples of JEZ-1 regolith, crafted to mimic Jezero delta's soil, would perform in the proximity of Jezero crater.

Other than showing promising optical properties, highly dense MMS and JSC-Mars-1A, along with DoE-optimized, spark plasma sintered MGS-1 and JEZ-1 simulants, presented mechanical properties (compressive strength, flexural strength and Vickers' hardness) superior to most literature results reported so far.

These findings make them suitable for structural applications on the red planet. As a drawback, the thermal input needed for their densification via standard SPS should be possibly reduced: One promising strategy is to take advantage of Cold Sintering techniques **[107,255-258]**. Moreover, for the obtainment of complex parts, while research is addressing SPS-3D printing combination **[83-86]**, an advanced technique based on traditional Slip-Casting, called Layerwise Induced Slip-Casting, was applied in **Section 4.3** to MGS-1, once mixed with a clay enriched MGS-1C simulant and wet processed with a Martian saltwater simulant. Pressureless sintering in air and simulated Martian atmosphere proved how good compressive strength properties can be obtained in both environments, with no impairing effect caused by the use of saltwater, instead of purified water, as dispersant. It would be also important to assess how the produced highly dense materials would perform in terms of radiation shielding, when employed as construction materials. Indeed, exposure to radiation is one of the issues related to a permanent human presence on Mars. Work is also in progress along this direction.

Based on the studied conducted in the present Thesis, it is apparent that the progress in space exploration and colonization requires the contribution of different scientific disciplines such as chemical and material engineering, physics, chemistry, etc. Indeed, experts on these and other fields have been involved in the present work. They all played a relevant and synergic role to provide important insights for the development of novel and efficient technologies capable to make human life multiplanetary possible in the foreseeable future.

List of Abbreviations

UHTC	Ultra-High Temperature Ceramic
TMB	Transition metal diboride
SHS	Self-propagating High-temperature Synthesis
SPS	Spark Plasma Sintering
ISRU	*In Situ* Resource Utilization
NASA	National Aeronautics and Space Administration
TM	Transition Metal
HEB	High Entropy Boride
BHR	BoroHydride Reduction
BR	Borothermal Reduction
BCR	Borocarbothermal Reduction
CR	Carbothermal Reduction
DR	Direct Reaction
RSPS	Reactive Spark Plasma Sintering
PLS	PressureLess Sintering
FS	Flash Sintering
ARM	Arc Melting
HP	Hot Pressing
FAST	Field Assisted Sintering
PECS	Pulsed Electric Current Sintering
EDM	Electronic Discharge Machining
MMS	Mars Mojave Simulant
JSC-Mars-1A	Johnson Space Centre Mars-1A
MGS-1	Mars Global Simulant
JEZ-1	JEZero delta simulant
MGS-1C	Mars Global hydrated Clay Simulant
MGS-1S	Mars Global polyhydrated Sulfate Simulant
BPR	Ball to Powders Ratio
HEB_W	$(Ti_{0.2}Zr_{0.2}Hf_{0.2}Mo_{0.2}W_{0.2})B_2$

HEBM	High-Energy Ball Milling
HEB_W_c_0C	SPS sintered $(Ti_{0.2}Zr_{0.2}Hf_{0.2}Mo_{0.2}W_{0.2})B_2$, coarser W precursor, without C
HEB_W_f_0C	SPS sintered $(Ti_{0.2}Zr_{0.2}Hf_{0.2}Mo_{0.2}W_{0.2})B_2$, finer W precursor, without C
HEB_W_c_1C	SPS sintered $(Ti_{0.2}Zr_{0.2}Hf_{0.2}Mo_{0.2}W_{0.2})B_2$, coarser W precursor, 1% C
HEB_W_f_1C	SPS sintered $(Ti_{0.2}Zr_{0.2}Hf_{0.2}Mo_{0.2}W_{0.2})B_2$, finer W precursor, 1% C
HEB_W_SiC	SPS sintered $(Ti_{0.2}Zr_{0.2}Hf_{0.2}Mo_{0.2}W_{0.2})B_2$, finer W precursor, 1% C, 20 vol.% SiC
SEM	Scanning Electron Microscope
HRSEM	High-Resolution Scanning Electron Microscope
XRD	X-ray Diffraction
EDX	Energy-Dispersive X-ray spectroscopy
COD	Crystallography Open Database
EU	European Union
ZHB	$(Zr_{0.5}Hf_{0.5})B_2$
ZTB	$(Zr_{0.5}Ta_{0.5})B_2$
TGA	ThermoGravimetric Analysis
DLR	German Aerospace Centre
NB	NbB_2
TB	TiB_2
HB	HfB_2
NTB	$(Nb_{0.5}Ti_{0.5})B_2$
NHB	$(Nb_{0.5}Hf_{0.5})B_2$
HR	Heating Rate
CNR-INO	
JSC@800-15	JSC-Mars-1A sample sintered at 800°C, 15 MPa
JSC@900-30	JSC-Mars-1A sample sintered at 900°C, 30 MPa
JSC@1000-30	JSC-Mars-1A sample sintered at 1000°C, 30 MPa
MMS@950-30	MMS sample sintered at 950°C, 30 MPa
MMS@1000-30	MMS sample sintered at 1000°C, 30 MPa
MMS@1050-30	MMS sample sintered at 1050°C, 30 MPa
DoE	Design of Experiment
SN	Signal-to-Noise

AM	Additive Manufacturing
LSD	Layerwise Slurry Deposition
SC	Slip Casting
LIS	Laser Induced Slip casting
MSW	Martian Saltwater Simulant
DDW	Double Deionized Water

List of Figures

Figure 1.1 - Melting temperature for elements and compounds from different families of materials showing that very few materials have melting temperatures above 3000 °C. Taken from **Fahrenholtz et al. [12]** 9

Figure 1.2 - Example of "cocktail effect": hardness values of HEB samples obtained by **Gild et al.**, compared to the average values of the related individual TMBs **[22]** 11

Figure 1.3 - Properties and characterization of regolith-based materials for construction on space. The moon is depicted, but the same consideration are valid also for Mars. Taken from **Zhou et al. [45]** 12

Figure 1.4 - Standard state Gibbs' free energy of formation as a function of temperature for the synthesis of ZrB_2, calculated from tabulated data **[58]**. Borothermal reaction: red solid line; borocarbothermal reaction: blue solid line; carbothermal reaction: green solid line; direct reaction: black solid line. 15

Figure 1.5 – Schematic of the SPS process. 19

Figure 1.6 – Geological features of planet Mars. (a) Planet topography reporting the main mission landing sites and (b), (c), (d) elemental distribution of Si, Fe, K as detected by the Gamma Ray Spectrometer Suite of 2001 Mars Odyssey mission. Adapted from Jet Propulsion Laboratory Image Gallery, NASA/JPL-Caltech (a), NASA/JPL/University of Arizona (b), (c), (d) **[89]**. 21

Figure 1.7 – Physical appearance and particle size distribution of numerous simulants available to a broad range of researchers. Taken from **Karl et al. [37]**. 22

Figure 2.1 – Schematic of the SHS apparatus used in this work (a). Schematic of the SHS reacting pellet during the combustion process (b). 25

Figure 2.2 – The SPS 515S apparatus used in this work. 27

Figure 3.1 - XRD pattern and Rietveld refinement of (a) SHS milled powders from coarser W reactants and corresponding bulk samples obtained by SPS (b) with no graphite, and (c) with 1 wt.% C. Experimental: red dots; Best Fit: dark solid line… 37

Figure 3.2 - SEM micrographs and corresponding EDX elemental maps of the 1h milled powders prepared by SHS from (a) coarse, and (b) fine W reactants. 38

Figure 3.3 - XRD pattern and related Rietveld refinement of (a) SHS 1 h milled product from finer W powders and corresponding bulk samples obtained by SPS (b) with no graphite, (c) with 1 wt.% C, (d) with 1 wt.% C and 20 vol.% SiC. Experimental: red dots… 39

Figure 3.4 - Cross sectional SEM micrographs and related EDX elemental maps of HEB_W samples obtained by SPS from SHS powder with no graphite addition: (a) coarser, (b) finer W powders, and with 1 wt% graphite addition: (c) coarser, and (d) finer W powders. 40

Figure 3.5 - Cross sectional SEM micrographs and related EDS elemental maps of HEB_W_f_1C_SiC sample obtained by SPS: (a) general, (b) detailed views, and (c)-(h) related EDX elemental maps. 41

Figure 3.6 - Comparison of weight changes per surface area of additive free and SiC containing HEB_W samples during oxidation tests carried out in air furnace as a function of temperature (isotherm duration=1h). 43

Figure 3.7 - XRD patterns of HEB_W (a) and HEB_W_SiC (b) samples after being heat treated in air furnace at different temperatures. 43

Figure 3.8 - Cross sectional SEM micrographs and related EDX elemental maps of SiC free samples after oxidation at (a) 800°C, (b) 1000°C, (c) 1200°C, and (d) HEB_W_SiC product heat treated in air furnace at 1200°C. 45

Figure 3.9 - XRD patterns of ZHB products: SHS powders (a), and SPS bulk samples obtained with no additive at T_D=1950 °C (b) and in presence of 1 wt.% graphite at T_D=1850 °C (c). Red dots are experimental data, the continuous lines are the calculated best fit. 53

Figure 3.10 - SEM micrographs and corresponding EDX elemental maps of (a) (Zr,Ta)B_2, and (b) (Zr,Hf)B_2 powders synthesized by SHS. 54

Figure 3.11 - Cross sectional SEM micrographs and corresponding EDX elemental maps of ZHB samples obtained by SPS at (a) T_D=1950 °C with no graphite, and at (b) T_D=1850 °C in presence of 1 wt.% graphite. 55

Figure 3.12 - XRD patterns of ZTB products: SHS powders (a), and SPS bulk samples obtained with no additive at T_D = 1950 °C (b) and in presence of 1 wt.% graphite at T_D 57

= 1850 °C (c). Red dots are experimental data, the continuous lines are the calculated best fit.

Figure 3.13 - Cross sectional SEM micrographs and related EDX elemental maps of ZTB samples obtained by SPS at (a) T_D = 1950 °C with no graphite, and at (b) T_D = 1850 °C in presence of 1 wt.% graphite. 58

Figure 3.14 - Specific weight changes during (a) TGA oxidation test in air of ZHB samples, (b) TGA oxidation test in air of ZTB samples and (c) oxidation tests in air furnace for both ZTB and ZHB samples produced in this work by SPS (T_D=1850 °C, 1 wt.% C) as a function of temperature. Literature data of TGA results of individual diborides, i.e. HfB_2 (ρ=98.8 %) **[154]**, ZrB_2 (ρ=98.5%) **[16]**, and TaB_2 (ρ=93.9%) **[16]** are also reported for comparison in graph (a) and (b). 61

Figure 3.15 - XRD patterns of (a) ZHB, and (b) ZTB samples' surface after being heat treated in air furnace at different temperatures. 63

Figure 3.16 - ZHB sample after heat treatment in air furnace at 1200 °C: (a) cross sectional SEM micrograph, (b) O, (c) Zr, (d) Hf elemental maps. 64

Figure 3.17 - ZTB sample after heat treatment in air furnace at 1200 °C: (a) cross sectional SEM micrograph, (b) O, (c) Zr, (d) Ta elemental maps. 65

Figure 3.18 - XRD patterns and related Rietveld profiles of NB samples: (a) SHS powders, SPS products obtained at T_D=1950°C with (b) no graphite, and (c) after the addition of 1 wt.% C. Experimental data (black dots)... 71

Figure 3.19 - XRD patterns and related Rietveld profiles of TB samples: (a) SHS powders, SPS products obtained at T_D=1950°C with (b) no graphite, and (c) after the addition of 1 wt.% C. Experimental data (black dots)... 71

Figure 3.20 - XRD patterns and related Rietveld profiles of HB samples: (a) SHS powders, SPS products obtained at T_D=1950°C with (b) no graphite, and (c) after the addition of 1 wt.% C. Experimental data (black dots)… 72

Figure 3.21 - SEM micrographs and associated EDX metal maps of (a) NB, (b) TB, (c) HB, (d) B, and (e) NTB powders prepared by SHS. 73

Figure 3.22 - SEM micrographs and associated EDX metal maps of individual diborides produced by SPS: NB obtained at 1950°C/20min/20MPa with no graphite (a) and with 1 wt.% C (b); TB prepared at 1950°C/20min/20MPa with no graphite (c) and with 1 75

wt.% C (d); HB produced at 1950°C/20min/20MPa with no graphite (e) and with 1 wt.% C (f). EDX analysis spectra performed on the pores (marked with a yellow asterisk) of the NB (g), TB (h) and HB (i) samples obtained by SPS at 1950°C/20min with no graphite addition.

Figure 3.23 - XRD patterns and related Rietveld profiles of NHB (a) and NTB (b) powders produced by SHS. Experimental data (black dots)… 78

Figure 3.24 - XRD patterns and related Rietveld profiles of NHB samples produced by SPS, in presence of 1wt.% graphite, at different sintering temperatures and dwelling times. Experimental data (black dots)… 80

Figure 3.25 - XRD patterns and related Rietveld profiles of NTB samples produced by SPS, in presence of 1wt.% graphite, at different sintering temperatures and dwelling times. Experimental data (black dots)… 81

Figure 3.26 - XRD patterns and related Rietveld profiles of NHB (2050°C/40min) (a) and NTB (2050°C/20min) (b) samples produced by SPS with no graphite. Experimental data (black dots)… 82

Figure 3.27 - SEM micrographs and associated EDX metal maps of NHB products obtained by SPS at 2050°C/40min/20MPa: with no graphite (a) and with 1 wt.%C (b). 83

Figure 3.28 - SEM micrographs at different magnitudes and associated EDS metal maps of NTB products obtained by SPS at 2050°C/20min/20MPa: with no graphite (a) and with 1 wt.%C (b). 84

Figure 3.29 - Specific weight changes during (a) TGA oxidation test in air and (b) after 1h in air furnace at 600, 800, 1000 and 1200 °C for the NTB, NB, TB samples produced in this work via SHS-SPS. (c) Oxide layer thickness of samples subjected to oxidation tests at different temperatures in air furnace. NB (green line and dots), TB (orange line and dots) and NTB (blue line and dots) 87

Figure 3.30 - Specific weight changes during (a) TGA oxidation test in air and (b) after 1h in air furnace at 600, 800, 1000 and 1200 °C for the NHB, NB, HB samples produced in this work via SHS-SPS. (c) Oxide layer thickness of samples subjected to oxidation tests at different temperatures in air furnace. NB (green line and dots), HB (ochre line and dots) and NHB (magenta line and dots) 88

Figure 3.31 - Optical images showing the changes of (a) individual, and (b) binary diboride samples fabricated in this work after oxidation experiments in air furnace at different temperatures. 89

Figure 3.32 - XRD patterns relative to the surface of individual diborides samples after being heat treated in air furnace at different temperatures: NB (a), TB (b), HB (c). Patterns of NB_ox_800, NB_ox_1000, and NB_ox_1200 systems are related to the oxide layers separated during the test from the corresponding samples (see **Figure 3.31a**)… 92

Figure 3.33 - XRD patterns relative to the surface of binary diborides samples after being heat treated in air furnace at different temperatures: NTB (a), and NHB (b). Patterns of NHB_ox_1000, and NHB_ox_1200 systems are related to the oxide layers separated during the test from the corresponding samples (see **Figure 3.31**)… 93

Figure 3.34 - Cross sectional SEM micrographs and corresponding EDS elemental maps of samples after receiving 1h heat treatment in air furnace under the highest temperature condition where no separation of the formed oxide layer was observed: NB (600°C), TB (1200°C), HB (1200°C), NTB (1200°C), and NHB (800°C). 95

Figure 3.35 – B_2O_3 phase diagram calculated according to Eq. (8). 103

Figure 3.36 – Calculated adiabatic temperatures as a function of Z and pressure for TiB_2 (a), ZrB_2 (b), and HfB_2 (c). 103

Figure 3.37 – Front propagation velocity measured as a function of Z for the case of TiB_2. 104

Figure 3.38 - XRD patterns of TiB_2 (a), ZrB_2 (b), HfB_2 (c) systems for the complete direct synthesis, and the last combination for which the reaction self-propagated with and without prior BM. 106

Figure 3.39 - XRD patterns of TiB_2 observed 1 day and 28 days after synthesis (a), and 1 day and 28 days after the leaching process (b). 107

Figure 3.40 - Schematic representation of the two-stage viscoplastic model of densification. a) Conceptual decomposition of the powder compact into two idealized bodies: Body (1) represents the initial stage with rigid particles dispersed in a continuous void network, while Body (2) models the subsequent deformable porous medium consisting of a continuous solid matrix with voids. b) Rheological elements 112

governing densification: the slider simulates particle rearrangement via a stress-dependent ideal plastic threshold (activated when the equivalent stress σ_{eq} exceeds the yield strength σ_Y), while the dashpot describes viscous deformation, governed by an apparent viscosity $\mu(\dot{\varepsilon}, \rho, T)$ dependent on strain rate, porosity, and temperature. c) Mechanical analog of the full model: Element (1) accounts for particle rearrangement while Element (2) reproduces the densification of the continuous porous matrix through viscous flow. The two elements act in series and are subjected to the same applied uniaxial stress σ_{app}.

Figure 3.41 - Comparison between experimental and simulated porosity time profiles for a) HfB_2, b) NbB_2, and c) TiB_2 samples during SPS. Experimental data (black open circles)… 119

Figure 3.42 - Evolution of stress-related quantities during SPS at σ_{app} = 20 MPa, t_H = 600 s, t_D = 1200 s, and T_D = 1950 °C for: a) HfB_2, b) NbB_2, and c) TiB_2 … 122

Figure 3.43 - a) Simulated strain rate during densification by SPS of transition metal diborides (σ_{app} = 20 MPa; t_H = 600 s; T_D = 1950 °C); b) effect of applied pressure on strain rates time evolution for HfB_2; c) effect of applied pressure on porosity time evolution for HfB_2; d) effect of shear viscosity activation energy on strain rates time evolution for TiB_2; e) effect of shear viscosity activation energy on porosity time evolution for TiB_2. 125

Figure 3.44 - Estimation of (porosity independent) shear viscosity η^* based on the experimental (smoothed) porosity time profiles during the isothermal period of densification reported in the inset. 128

Figure 3.45 - Simulated apparent viscosity μ during densification of transition metal diborides (σ_{app} = 20 MPa; t_H = 600 s; T_D = 1950 °C). 130

Figure 3.46 - Calculated zero-rate shear viscosity η^0 (porosity and strain-rate independent) of transition metal diborides as a function of temperature. 131

Figure 3.47 - Simulated (lines) of shear viscosity η^* of dense (pore less) transition metal diborides at 1950 °C as a function of the equivalent strain rate. Points represent the shear viscosity η^* at the same temperature as the estimate based on (smoothed) experimental data related to the isothermal period (see **Figure 3.44**). 133

Figure 3.48 - Comparison between experimental data taken from the literature and model outcomes: a) final relative density of HfB_2 samples as a function of the dwell temperature, T_D (HR = 100 °C/min; t_D = 10 min; σ_{app} = 50 MPa) – data from **Venugopal et al. [200]** and **Dubey et al. [201]**; b) final calculated relative density of NbB_2 samples versus the experimental one. Operating conditions are as follows: **Akin et al. [165]**: HR = 2 °C/min; T_D = 1750 °C, t_D = 5 min, σ_{app} = 50 MPa; This work (slightly modified conditions with respect to those in **Section 3.3**): HR = 185 °C/min; T_D = 1850 °C, t_D = 20 min, σ_{app} = 20 MPa; **Demirskyi et al., 2017 [163]**: HR = 110 °C/min; T_D = 1950 °C, t_D = 10 min, σ_{app} = 80 MPa; **Demirskyi et al., 2019 [169]**: HR = 110 °C/min; T_D = 1900 °C, t_D = 10 min, σ_{app} = 80 MPa; c) final relative density of TiB_2 samples as a function of the dwell time, t_D (HR = 50 °C/min; T_D = 1500 °C; σ_{app} = 50 MPa) – data from **Balcı et al. [202]**; d) final relative density of TiB_2 samples as a function of the applied pressure, σ_{app} (HR = 50 °C/min; T_D = 1500 °C; t_D = 15 min) – data from **Balcı et al. [202]**. Numbers in brackets indicate the difference (percentage) between the calculated and the experimental relative densities. 136

Figure 3.49 - Simulated effect of operating conditions on densification of transition metal diborides: a) porosity time profile up to 12 h (σ_{app} = 20 MPa; t_H = 600 s; T_D = 1950 °C); b) HfB_2 porosity time profile for different values of the applied pressure, σ_{app}; c) final relative density as function of the dwell temperature (σ_{app} = 20 MPa; t_H = 600 s; t_D = 1200 s). Dashed line in Figure c) gives the 99% relative density. 138

Figure 4.1 - (a) Weight change (%) of JSC-Mars-1A (before and after being heat treated for 2h at 700°C) and MMS simulants during TGA experiment under dynamic conditions. (b) Weight change (%) at room temperature in air of heat treated (700°C, 2h) JSC-Mars-1A simulant. 148

Figure 4.2 - XRD patterns of (a) pristine MMS and (b) JSC-Mars-1A (pristine and heat treated) simulants. 150

Figure 4.3 - SPS outputs (sample shrinkage, gas pressure inside the sintering chamber) and the corresponding temperature time profile recorded during the consolidation of JSC-Mars-1A (preliminarily heat treated) and pristine MMS regolith powders for the 153

case of T_D=1000°C, P=15 MPa. Filled and empty symbols refer to JSC-Mars-1A and MMS, respectively.

Figure 4.4 - Effect of the dwell temperature, at different mechanical pressure levels, on the density of bulk samples obtained by SPS from (a) JSC-Mars-1A (preliminarily heat treated) and (b) pristine MMS regolith simulants. 154

Figure 4.5 - XRD patterns of JSC-Mars-1A bulk samples obtained by SPS at T_D= 800, 900, and 1000°C. The XRD pattern of initial (heat-treated) simulant is also shown, for comparison. 156

Figure 4.6 - Phase content changes, as determined by Rietveld analysis from XRD patterns (**Figure 4.5**), of JSC-Mars-1A regolith samples after heat treatment at 700°C and during SPS at T_D= 800, 900, and 1000°C with respect to the pristine simulant. 157

Figure 4.7 - XRD patterns of MMS regolith samples: pristine simulant, and corresponding bulk samples obtained by SPS at T_D= 950, 1000, and 1050°C. 158

Figure 4.8 - Phase content changes, as determined by Rietveld analysis from XRD patterns (**Figure 4.7**), of MMS regolith samples during SPS at T_D= 950, 1000, and 1050°C with respect to the pristine simulant. 159

Figure 4.9 - SEM micrograph of SPS samples obtained from the two regolith simulants. JSC-Mars-1A: (a) JSC@800-15, (b) JSC@900-30, and (c) JSC@1000-30; MMS: (a) MMS@950-30, (b) MMS@1000-30, and (c) MMS@1050-30. 160

Figure 4.10 - Reflectance spectra of the simulants in powder form. (a) Spectral range 0.4-2.2 μm, to allow the comparison with **Allen et al. [215]** and **Peters et al. [90]**; (b) Full range 0.19-16.0 μm investigated in this work. 162

Figure 4.11 - Reflectance spectra of the sintered ceramics obtained from (a) the JSC-Mars-1 simulant and (b) the MMS simulant. The spectrum of the corresponding powders (the annealed one, in case of JSC-Mars-1 simulant) is also indicated for comparison. 163

Figure 4.12 - Total emittance calculated from normal hemispherical reflectance spectra for JSC-Mars-1A (a) and MMS (b) samples (Eqs. (25), (26), (28)). 167

Figure 4.13 - Consolidation of MGS-1 simulant by SPS (T_D=1200°C, t_D=5min, P=35MPa): (a) temperature (blue line) and sample displacement (red line) time profile; (b) evidence of the formation of a molten phase (red arrow) in the resulting sample. 177

Figure 4.14 - TGA curves reporting weight changes (%) of as received simulants up to 800°C. The behaviour of JSC-Mars-1A and JEZ-1 simulants after being heat treated for 2h at 700°C are also shown. 181

Figure 4.15 - Weight gain (%) of JSC-Mars-1A and JEZ-1 simulants following their heat treatment (700°C, 2h). 182

Figure 4.16 - Effect of T_D, t_D, P on the densification and energy consumption during SPS test according to the Taguchi method. Mean of SN Ratios for (a) MGS-1 density, (b) MGS-1 energy consumption, (c) JEZ-1 density, (d) JEZ-1 energy consumption 184

Figure 4.17 - XRD patterns of pristine, heat-treated and sintered JSC-Mars-1A samples (**Table 4.12**). (a) Extensive view with Rietveld refinement: experimental data (black dots), calculated intensity (red solid line) and amorphous content (green solid line). (b) Detailed view indicating crystalline phases detected. 187

Figure 4.18 - XRD patterns of pristine, and sintered MMS samples (**Table 4.12**). a) Extensive view with Rietveld refinement: experimental data (black dots), calculated intensity (red solid line) and amorphous content (green solid line). (b) Detailed view indicating crystalline phases detected. 187

Figure 4.19 - XRD patterns of pristine, and sintered MGS-1 samples (**Table 4.12**). a) Extensive view with Rietveld refinement: experimental data (black dots), calculated intensity (red solid line) and amorphous content (green solid line). (b) Detailed view indicating crystalline phases detected. 188

Figure 4.20 - XRD patterns of pristine, heat-treated and sintered JEZ-1 samples (**Table 4.12**). (a) Extensive view with Rietveld refinement: experimental data (black dots), calculated intensity (red solid line) and amorphous content (green solid line). (b) Detailed view indicating crystalline phases detected. 189

Figure 4.21 - SEM micrographs and corresponding EDX maps of the most representative elemental constituents of bulk samples obtained under the optimized SPS conditions (**Table 4.11**) from Martian regolith simulants: (a) JSC-Mars-1A, (b) MMS, (c) MGS-1, and (d) JEZ-1. 192

Figure 4.22 - Mechanical properties evaluated for the 4 regolith simulants sintered at their tailored optimal conditions. (a) Compressive strength, (b) Flexural strength, and (c) Vickers Hardness. 195

Figure 4.23 - Illustration of the LIS process, inspired by **Lüchtenborg et al. [270].** a) The first layer of slurry is deposited in the build platform by the doctor blade. b) The laser locally dries the slurry, producing the first layer of the green body c) A new layer of slurry is deposited. d) The laser locally dries the second layer of slurry. e) The excess slurry is drained f) The printed green body remains. 199

Figure 4.24 - Viscosity and shear rate over shear stress for different slurries: comparison of 60-45 wt.% water, 50 wt.% saltwater content and Al_2O_3 reference slurry. 208

Figure 4.25 - LIS parts (80x80x5 mm) printed according to configuration A (a) and configuration B (b) starting from MSW slurry. The part printed according to configuration A was photographed while still in the build platform, when cracks (highlighted with red circles) started to appear. 209

Figure 4.26 - Weight loss and evolved gases during the TG analyses in air. (a) Comparison between LIS-printed green bodies prepared with DDW and MSW. (b) Comparison of TG analyses in air and N_2 for the case of LIS-printed green bodies prepared with MSW. 211

Figure 4.27 - Sintering test results in terms of (a) relative density and (b) 10 minutes of water adsorption and linear sintering shrinkage in an air atmosphere. The green box evidences the optimal condition. 212

Figure 4.28 - Sintering test results in terms of (a) relative density and (b) 10 minutes of water absorption and linear sintering shrinkage in the simulated Martian atmosphere. The green box evidences the optimal condition. 213

Figure 4.29 - Samples sintered under different conditions in (a) air and (b) simulated Martian atmosphere. The images were produced by combining photos of individual samples (due to different perspectives in these photos and slightly varying green body sizes, the heights were adapted to match the observed linear sintering shrinkages). 215

Figure 4.30 - XRD Patterns of the as received MGS-1 (olive line) and MGS-1C (orange line) powders and of the crushed LIS printed green body (black line). 216

Figure 4.31 - 2θ = 20°- 60° focus of XRD patterns obtained for the crushed LIS printed green body (black line) and for (a) crushed LIS samples sintered at 1170°C-3h (red line) and at 1190°C-3h (blue line) in air atmosphere and (b) crushed LIS samples sintered at 217

1170°C-3h (magenta line) and at 1180°C-3h (green line) in simulated Martian atmosphere.

Figure 4.32 - Temperature dependence of the thermal conductivity of the LIS 1190°C-3h air sintered and the LIS 1180°C-3h sample sintered under simulated Martian atmosphere. 218

Figure 4.33 - Weibull fracture probability plots of the compressive strength measured for the cases of (a) LIS-AIR (LIS sample sintered in air at 1190°C-3h), (b) SC-AIR (SC sample sintered in air at 1190°C-3h), (c) LIS-CO_2 (LIS sample sintered in simulated Martian atmosphere at 1180°C-3h), (d) SC-CO_2 (SC sample sintered in simulated Martian atmosphere at 1180°C-3h). 221

List of Tables

Table 1.1 – Enthalpy of formation and adiabatic combustion temperature of different IV and V group TMBs. 16

Table 2.1 – Ultra High Temperature Ceramics precursors or additives employed in this work (n.r.: not reported by the producer). 26

Table 2.2 - Main oxide constituents (wt.%) of JSC Mars-1A, MMS, MGS-1, JEZ-1 simulants compared to average data collected on actual Martian regolith (in italics) on Gale crater **[114]**, Meridiani planum and Gusev crater **[115,116]**). (n.r.: not reported). 29

Table 3.1 - Density, composition, and mechanical properties of the bulk $(Ti_{0.2}Zr_{0.2}Hf_{0.2}Mo_{0.2}W_{0.2})B_2$-based products obtained in this work by SPS from coarser and finer W powders, with no graphite or in presence of 1wt.% of this additive. The corresponding values reported in the literature for the same HEB formulation are also included. BR: Borothermal reduction; BCR: Boro-Carbothermal Reduction; HEBM: High-Energy Ball Milling; PLS: Pressureless Sintering; RSPS: Reactive SPS; ρ_t= theoretical density of HEB; n.q.: not quantified; n.r.: not reported. 33

Table 3.2 - Mechanical properties of bulk ZHB and ZTB samples produced by SPS in this work in presence and with no graphite addition. The corresponding processing conditions and density values are also reported. EC: Evans and Charles; LF: Lawn and Fuller; EW: Evans and Wilshaw; L: Lankford. n. d.: not determined. 60

Table 3.3 - Characteristics of SHS powders and related SPS products obtained in this work for the preparation of bulk single-phase NbB_2, TiB_2, HfB_2, NTB, and NHB at different conditions 74

Table 3.4 - Mechanical properties of bulk NB (ρ_r =92.2±1.0%), TB (ρ_r =98.9±0.9 %), HB (ρ_r =97.2±1.3%), NTB (ρ_r =93.6±0.8%), and NHB (ρ_r =97.4±0.2%) samples produced by SPS in this work. EC: Evans and Charles; LF: Lawn and Fuller; EW: Evans and Wilshaw; L: Lankford; n.d.: not determined. 85

Table 3.5 - Fitted parameters for the thermodynamic analysis (n.d.: not determined) 101

Table 3.6 - Initial values of some model variables. 116

Table 3.7 - Summary of model parameters. 117

Table 4.1 - Particle size parameters of Martian regolith simulants used to obtain bulk samples by SPS 149

Table 4.2 - Phase composition of pristine MMS and JSC-MARS-1A simulants obtained by Rietveld refinement (n.d.: not detected). 151

Table 4.3 - Phase composition of sintered JSC-Mars-1A and MMS simulants estimated by Rietveld refinement (n.d.: not detected). 157

Table 4.4 - Average values and standard deviation of surface porosity measured by image analysis on the bulk JSC-Mars-1A and MMS samples obtained by SPS at different conditions. 160

Table 4.5 - Average values and standard deviation of roughness parameters measured on the bulk JSC-Mars-1A and MMS samples obtained at different SPS conditions. 161

Table 4.6 - Solar absorptance values calculated from Eqs. (25), (27). 165

Table 4.7 - Literature values of thermal conductivity of some regolith simulants and comparison with terrestrial basalt rocks. 168

Table 4.8 - Examples of research studies involving the processing of different Martian regolith simulants and the mechanical characterization of the resulting bulk samples in terms of compressive and flexural strength. When missing, relative densities were calculated from the measured absolute values; n.r.: not reported. 172-173

Table 4.9 – Summary of phase composition of pristine MMS and JSC-MARS-1A simulants obtained by Rietveld refinement (see **Section 4.1**) and pristine MGS-1 **[93]** and JEZ-1 simulants **[94]**. 175

Table 4.10 - (a) Sintering parameters and their levels selected for screening of MGS-1 and JEZ-1. (b) Sintering optimization treatments prescribed by the Taguchi method 178

Table 4.11 - Particle size parameters of Martian regolith powders used to obtain bulk samples by SPS. 183

Table 4.12 - Optimized SPS parameters and corresponding relative density values of samples used for the evaluation of mechanical properties. The theoretical density of initial powders to be processed by SPS (i.e. pristine MMS and MGS-1, and heat-treated 185

JEZ-1 and JSC-Mars-1A) was used for the calculation of relative density of resulting bulk samples.

Table 4.13 - Phase composition (wt.%) of regolith simulants determined with Rietveld Refinement from XRD analysis. 190

Table 4.14 - Oxide constituents (wt.%) of MGS-1 and MGS-1C simulants and the MGS-1/16 mixture employed in this work. Producer values as well as values obtained via XRF on the same batches used in this work have been taken from **Karl et al. [106] and references therein**. The calculated MGS-1/16 mixture values refer to the latter. 200

Table 4.15 - Phase composition (wt.%) of MGS-1 **[273]** and MGS-1C **[274]**simulants and the MGS-1/16 mixture employed in this work (n.r.: not reported). 201

Table 4.16 - Mars saltwater simulant (MSW) composition (1 L solution) **[266]**. 202

Table 4.17 - Investigated parameters for the LIS process. Values reported in italics identify a parameter that was varied and optimized for the obtainment of the LIS printed part. 205

Table 4.18 - Processing route and compressive strength of unfired samples produced using LIS and SC additive manufacturing methods, comparison with dry pressing. 219

References

[1] Macdonald, M., & Badescu, V. (Eds.). (2014). *The International Handbook of Space Technology*. Springer Berlin Heidelberg. https://doi.org/10.1007/978-3-642-41101-4

[2] Vernile, A. (2018). *The Rise of Private Actors in the Space Sector*. Springer International Publishing. https://doi.org/10.1007/978-3-319-73802-4

[3] Meurisse, A., & Carpenter, J. (2020). Past, present and future rationale for space resource utilisation. *Planetary and Space Science*, *182*, 104853. https://doi.org/10.1016/j.pss.2020.104853

[4] Padture, N. P. (2016). Advanced structural ceramics in aerospace propulsion. *Nature Materials*, *15*(8), 804–809. https://doi.org/10.1038/nmat4687

[5] Fahrenholtz, W. G., & Hilmas, G. E. (2017). Ultra-high temperature ceramics: Materials for extreme environments. *Scripta Materialia*, *129*, 94–99. https://doi.org/10.1016/j.scriptamat.2016.10.018

[6] NASA. *Space Shuttle*. https://www.nasa.gov/space-shuttle/ (Accessed 25th September 2025)

[7] SpaceX. *Falcon 9, First Orbital Class Rocket Capable of Reflight*. https://www.spacex.com/vehicles/falcon-9 (Accessed 25th September 2025)

[8] SpaceX. *Falcon Heavy, Over 5 millions lbs of thrust*. https://www.spacex.com/vehicles/falcon-heavy (Accessed 25th September 2025)

[9] SpaceX. *Starship, Service to Earth Orbit, Moon, Mars and Beyond*. https://www.spacex.com/vehicles/starship (Accessed 25th September 2025)

[10] ESA. *Enabling & Support, Themis*. https://www.esa.int/Enabling_Support/Space_Transportation/Themis (Accessed 25th September 2025)

[11] Huang, A., & NASA. *Thermal Protection Materials Branch – Reusable Materials*. https://www.nasa.gov/general/thermal-protection-materials-branch-reusable-materials/ (Accessed 25th September 2025)

[12] Fahrenholtz, W. G., Hilmas, G. E., Talmy, I. G., & Zaykoski, J. A. (2007). Refractory Diborides of Zirconium and Hafnium. *Journal of the American Ceramic Society*, *90*(5), 1347–1364. https://doi.org/10.1111/j.1551-2916.2007.01583.x

[13] Hillig, W. B. (1986). Prospects for Ultra-High-Temperature Ceramic Composites. In *Tailoring Multiphase and Composite Ceramics* (pp. 697–712). Springer US. https://doi.org/10.1007/978-1-4613-2233-7_55

[14] Opeka, M. M., Talmy, I. G., Wuchina, E. J., Zaykoski, J. A., & Causey, S. J. (1999). Mechanical, Thermal, and Oxidation Properties of Refractory Hafnium and zirconium Compounds. *Journal of the European Ceramic Society*, *19*(13–14), 2405–2414. https://doi.org/10.1016/S0955-2219(99)00129-6

[15] Zhang, X., Luo, X., Han, J., Li, J., & Han, W. (2008). Electronic structure, elasticity and hardness of diborides of zirconium and hafnium: First principles calculations. *Computational Materials Science*, *44*(2), 411–421. https://doi.org/10.1016/j.commatsci.2008.04.002

[16] Licheri, R., Musa, C., Orrù, R., Cao, G., Sciti, D., & Silvestroni, L. (2016). Bulk monolithic zirconium and tantalum diborides by reactive and non-reactive spark plasma sintering. *Journal of Alloys and Compounds*, *663*, 351–359. https://doi.org/10.1016/J.JALLCOM.2015.12.096

[17] Musa, C., Licheri, R., Orrù, R., & Cao, G. (2014). Synthesis, Sintering, and Oxidative Behavior of HfB_2–$HfSi_2$ Ceramics. *Industrial & Engineering Chemistry Research*, *53*(22), 9101–9108. https://doi.org/10.1021/ie4032692

[18] Guo, S., Hu, C., & Kagawa, Y. (2011). Mechanochemical Processing of Nanocrystalline Zirconium Diboride Powder. *Journal of the American Ceramic Society*, *94*(11), 3643–3647. https://doi.org/10.1111/j.1551-2916.2011.04825.x

[19] López-Arenal, J., Moshtaghioun, B. M., Gómez-García, D., & Ortiz, A. L. (2024). Affordable spark plasma sintering of superhard Al-doped ZrB_2 nanoceramics from ZrH_2, B, and Al mechanically activated by shaker milling. *Ceramics International*, *50*(9), 15856–15866. https://doi.org/10.1016/J.CERAMINT.2024.02.065

[20] Basu, B., Raju, G. B., & Suri, A. K. (2006). Processing and properties of monolithic TiB_2 based materials. *International Materials Reviews*, *51*(6), 352–374. https://doi.org/10.1179/174328006X102529

[21] Zhang, X., Li, W., Tian, H., Liu, J., Li, C., Dong, H., Chen, J., Song, M., Chen, B., Sheng, H., Wang, S., Zhang, D., & Zhang, H. (2021). Ultra-incompressible High-Entropy Diborides. *The Journal of Physical Chemistry Letters*, *12*(12), 3106–3113. https://doi.org/10.1021/acs.jpclett.1c00399

[22] Gild, J., Zhang, Y., Harrington, T., Jiang, S., Hu, T., Quinn, M. C., Mellor, W. M., Zhou, N., Vecchio, K., & Luo, J. (2016). High-Entropy Metal Diborides: A New Class of High-Entropy Materials and a New Type of Ultrahigh Temperature Ceramics. *Scientific Reports*, *6*(1), 37946. https://doi.org/10.1038/srep37946

[23] Barbarossa, S., Orrù, R., Garroni, S., Licheri, R., & Cao, G. (2021). Ultra high temperature high-entropy borides: Effect of graphite addition on oxides removal and densification behaviour. *Ceramics International*, *47*(5), 6220–6231. https://doi.org/10.1016/j.ceramint.2020.10.200

[24] Barbarossa, S., Orrù, R., Cannillo, V., Iacomini, A., Garroni, S., Murgia, M., & Cao, G. (2021). Fabrication and Characterization of Quinary High Entropy-Ultra-High Temperature Diborides. *Ceramics*, *4*(2), 108–120. https://doi.org/10.3390/ceramics4020010

[25] Tallarita, G., Licheri, R., Garroni, S., Barbarossa, S., Orrù, R., & Cao, G. (2020). High-entropy transition metal diborides by reactive and non-reactive spark plasma sintering: A comparative investigation. *Journal of the European Ceramic Society*, *40*(4), 942–952. https://doi.org/10.1016/J.JEURCERAMSOC.2019.10.031

[26] Monteverde, F., Saraga, F., Gaboardi, M., Feng, L., Hilmas, G., & Fahrenholtz, W. (2022). Quantitative inspection of grain-scale chemical inhomogeneities in high-entropy AlB_2-type transition metal diborides. *Journal of the American Ceramic Society*, *105*(11), 6910–6923. https://doi.org/10.1111/jace.18619

[27] Backman, L., & Opila, E. J. (2019). Thermodynamic assessment of the group IV, V and VI oxides for the design of oxidation resistant multi-principal component materials. *Journal of the European Ceramic Society*, *39*(5), 1796–1802. https://doi.org/10.1016/j.jeurceramsoc.2018.11.004

[28] Backman, L., Gild, J., Luo, J., & Opila, E. J. (2020). Part I: Theoretical predictions of preferential oxidation in refractory high entropy materials. *Acta Materialia*, *197*, 20–27. https://doi.org/10.1016/J.ACTAMAT.2020.07.003

[29] Backman, L., Gild, J., Luo, J., & Opila, E. J. (2020). Part II: Experimental verification of computationally predicted preferential oxidation of refractory high entropy ultra-high temperature ceramics. *Acta Materialia*, *197*, 81–90. https://doi.org/10.1016/j.actamat.2020.07.004

[30] Butler, T. M., Chaput, K. J., Dietrich, J. R., & Senkov, O. N. (2017). High temperature oxidation behaviors of equimolar NbTiZrV and NbTiZrCr refractory complex concentrated alloys (RCCAs). *Journal of Alloys and Compounds*, *729*, 1004–1019. https://doi.org/10.1016/j.jallcom.2017.09.164

[31] Müller, F., Gorr, B., Christ, H.-J., Müller, J., Butz, B., Chen, H., Kauffmann, A., & Heilmaier, M. (2019). On the oxidation mechanism of refractory high entropy alloys. *Corrosion Science*, *159*, 108161. https://doi.org/10.1016/j.corsci.2019.108161

[32] Smith, M., Craig, D., Herrmann, N., Mahoney, E., Krezel, J., McIntyre, N., & Goodliff, K. (2020). The Artemis Program: An Overview of NASA's Activities to Return Humans to the Moon. *2020 IEEE Aerospace Conference*, 1–10. https://doi.org/10.1109/AERO47225.2020.9172323

[33] SpaceX, Mars and Beyond: the road to making humanity multiplanetary, https://www.spacex.com/humanspaceflight/mars/, (Accessed 25th September 2025)

[34] Vago, J., Witasse, O., Svedhem, H., Baglioni, P., Haldemann, A., Gianfiglio, G., Blancquaert, T., McCoy, D., & de Groot, R. (2015). ESA ExoMars program: The next step in exploring Mars. *Solar System Research*, *49*(7), 518–528. https://doi.org/10.1134/S0038094615070199

[35] Farley, K. A., Williford, K. H., Stack, K. M., Bhartia, R., Chen, A., de la Torre, M., Hand, K., Goreva, Y., Herd, C. D. K., Hueso, R., Liu, Y., Maki, J. N., Martinez, G., Moeller, R. C., Nelessen, A., Newman, C. E., Nunes, D., Ponce, A., Spanovich, N., … Wiens, R. C. (2020). Mars 2020 Mission Overview. *Space Science Reviews*, *216*(8), 142. https://doi.org/10.1007/s11214-020-00762-y

[36] Zou, Y., Zhu, Y., Bai, Y., Wang, L., Jia, Y., Shen, W., Fan, Y., Liu, Y., Wang, C., Zhang, A., Yu, G., Dong, J., Shu, R., He, Z., Zhang, T., Du, A., Fan, M., Yang, J., Zhou, B., … Peng, Y. (2021). Scientific objectives and payloads of Tianwen-1, China's first Mars exploration mission. *Advances in Space Research*, *67*(2), 812–823. https://doi.org/10.1016/J.ASR.2020.11.005

[37] Karl, D., Cannon, K. M., & Gurlo, A. (2022). Review of space resources processing for Mars missions: Martian simulants, regolith bonding concepts and additive manufacturing. *Open Ceramics*, *9*, 100216. https://doi.org/10.1016/j.oceram.2021.100216

[38] NASA, Using space-based resources for deep space exploration, https://www.nasa.gov/overview-in-situ-resource-utilization, (Accessed 25th September 2025)

[39] Starr, S. O., & Muscatello, A. C. (2020). Mars in situ resource utilization: a review. *Planetary and Space Science*, *182*, 104824. https://doi.org/10.1016/J.PSS.2019.104824

[40] Sanders, G. B., Duke M. (2005). Capability road map (CRM) 13: in-situ resource utilization (ISRU), in: NASA Capability Roadmaps Executive Summary, Willcoxon, R., Thronson, H., Varsi, G., Mueller, R., Regenie, V., Inman, T., et al. (Eds.), https://ntrs.nasa.gov/citations/20050204002 (Accessed 25th September 2025)

[41] Williams, D.R. (2015). A crewed mission to Mars, https://nssdc.gsfc.nasa.gov/planetary/mars/marsprof.html, (Accessed 09th May 2025)

[42] NASA Mars architecture steering group, Drake, B.G. (Ed.) (2009), Human Exploration of Mars Design Reference Architecture 5.0, http://www.nasa.gov/pdf/373665main_NASA-SP-2009-566.pdf (Accessed 25th September 2025)

[43] NASA, Artemis III, https://www.nasa.gov/mission/artemis-iii/, (Accessed 25th September 2025)

[44] Naser, M. Z. (2019). Extraterrestrial construction materials. *Progress in Materials Science*, *105*, 100577. https://doi.org/10.1016/j.pmatsci.2019.100577

[45] Zhou, C., Gao, Y., Zhou, Y., She, W., Shi, Y., Ding, L., & Miao, C. (2024). Properties and Characteristics of Regolith-Based Materials for Extraterrestrial Construction. *Engineering*, *37*, 159–181. https://doi.org/10.1016/j.eng.2023.11.019

[46] Costa, N., Bonetto, A., Ferretti, P., Casarotto, B., Massironi, M., Altieri, F., Nava, J., & Favero, M. (2024). Analytical data on three Martian simulants. *Data in Brief*, *57*, 111099. https://doi.org/10.1016/j.dib.2024.111099

[47] Fahrenholtz, W. G., Binner, J., & Zou, J. (2016). Synthesis of ultra-refractory transition metal diboride compounds. *Journal of Materials Research*, *31*(18), 2757–2772. https://doi.org/10.1557/jmr.2016.210

[48] Guo, W., Zhang, G., You, Y., Wu, S., & Lin, H. (2014). TiB_2 Powders Synthesis by Borothermal Reduction in TiO_2 Under Vacuum. *Journal of the American Ceramic Society*, *97*(5), 1359–1362. https://doi.org/10.1111/jace.12908

[49] Yeh, C. L., & Wang, H. J. (2011). Combustion synthesis of vanadium borides. *Journal of Alloys and Compounds*, *509*(7), 3257–3261. https://doi.org/10.1016/j.jallcom.2010.12.004

[50] Yeh, C. L., & Wang, H. J. (2011). A comparative study on combustion synthesis of Ta–B compounds. *Ceramics International*, *37*(5), 1569–1573. https://doi.org/10.1016/j.ceramint.2011.01.024

[51] Musa, C., Licheri, R., Orrù, R., Cao, G., Balbo, A., Zanotto, F., Mercatelli, L., & Sani, E. (2018). Optical characterization of hafnium boride and hafnium carbide-based ceramics for solar energy receivers. *Solar Energy*, *169*, 111–119. https://doi.org/10.1016/j.solener.2018.04.036

[52] Sani, E., Mercatelli, L., Meucci, M., Balbo, A., Musa, C., Licheri, R., Orrù, R., & Cao, G. (2016). Optical properties of dense zirconium and tantalum diborides for solar thermal absorbers. *Renewable Energy*, *91*, 340–346. https://doi.org/10.1016/j.renene.2016.01.068

[53] Belisario, J., Mondal, S., Khakpour, I., Franco Hernandez, A., Durygin, A., & Cheng, Z. (2021). Synthesis and flash sintering of $(Hf_{1-x}Zr_x)B_2$ solid solution powders. *Journal of the European Ceramic Society*, *41*(4), 2215–2225. https://doi.org/10.1016/j.jeurceramsoc.2020.12.015

[54] Dorner, A. N., Werbach, K., Hilmas, G. E., & Fahrenholtz, W. G. (2021). Effect of tantalum solid solution additions on the mechanical behavior of ZrB_2. *Journal of the European Ceramic Society*, *41*(6), 3219–3226. https://doi.org/10.1016/j.jeurceramsoc.2020.12.049

[55] Zou, J., Huang, S., Vanmeensel, K., Zhang, G., Vleugels, J., & van der Biest, O. (2013). Spark Plasma Sintering of Superhard B_4C–ZrB_2 Ceramics by Carbide Boronizing. *Journal of the American Ceramic Society*, *96*(4), 1055–1059. https://doi.org/10.1111/jace.12284

[56] Zou, J., Liu, J., Zhao, J., Zhang, G.-J., Huang, S., Qian, B., Vleugels, J., van der Biest, O., & Shen, J. Z. (2014). A top-down approach to densify ZrB_2–SiC–BN composites with deeper homogeneity and improved reliability. *Chemical Engineering Journal*, *249*, 93–101. https://doi.org/10.1016/j.cej.2014.03.089

[57] Yan, Y., Huang, Z., Dong, S., & Jiang, D. (2006). New Route to Synthesize Ultra-Fine Zirconium Diboride Powders Using Inorganic–Organic Hybrid Precursors. *Journal of the American Ceramic Society*, *89*(11), 3585–3588. https://doi.org/10.1111/j.1551-2916.2006.01269.x

[58] Barin, I. (1995). *Thermochemical Data of Pure Substances*. Wiley. https://doi.org/10.1002/9783527619825

[59] Moshtaghioun, B. M., Crespo, R. C., Cumbrera, F. L., Gómez-García, D., Fernández, M. G., Rodríguez, M. A., & Moreno, R. (2026). Mechanical performance of sub-stoichiometric titanium carbide ceramics synthesized by a hybrid SHS and SPS methodology. *Journal of the European Ceramic Society*, *46*(1), 117748. https://doi.org/10.1016/j.jeurceramsoc.2025.117748

[60] López-Arenal, J., Moshtaghioun, B. M., Zhukova, I., Cumbrera, F. L., Gómez-García, D., García Fernández, M., Rodríguez, M. A., & Moreno, R. (2025). Fabrication of solid-solution $Ti_{1-y}Al_yC_{1-x}$ ceramics: Theoretical and experimental approach to structural stability. *Journal of the European Ceramic Society*, *45*(5), 117158. https://doi.org/10.1016/j.jeurceramsoc.2024.117158

[61] Musa, C., Licheri, R., Montinaro, S., Orrù, R., & Cao, G. (2017). Tantalum carbide products from chemically-activated combustion synthesis reactions. *Ceramics International*, *43*(15), 12844–12850. https://doi.org/10.1016/j.ceramint.2017.06.175

[62] Yi, H. C., Guigné, J. Y., Woodger, T. C., & Moore, J. J. (1998). Combustion synthesis of HfB_2-Al composites. *Metallurgical and Materials Transactions B*, *29*(4), 877–887. https://doi.org/10.1007/s11663-998-0147-2

[63] Munir, Z. A., & Anselmi-Tamburini, U. (1989). Self-propagating exothermic reactions: The synthesis of high-temperature materials by combustion. *Materials Science Reports*, *3*(7–8), 277–365. https://doi.org/10.1016/0920-2307(89)90001-7

[64] Shanghai Metals Market, Price results for Titanium, https://www.metal.com/search?keyword=titanium&type=price, (Accessed 3rd September 2025)

[65] Chamberlain, A. L., Fahrenholtz, W. G., & Hilmas, G. E. (2009). Reactive hot pressing of zirconium diboride. *Journal of the European Ceramic Society*, *29*(16), 3401–3408. https://doi.org/10.1016/j.jeurceramsoc.2009.07.006

[66] Wu, W.-W., Zhang, G.-J., & Sakka, Y. (2013). Nanocrystalline ZrB_2 powders prepared by mechanical alloying. *Journal of Asian Ceramic Societies*, *1*(3), 304–307. https://doi.org/10.1016/j.jascer.2013.08.002

[67] Ran, S., van der Biest, O., & Vleugels, J. (2010). ZrB_2–SiC composites prepared by reactive pulsed electric current sintering. *Journal of the European Ceramic Society*, *30*(12), 2633–2642. https://doi.org/10.1016/j.jeurceramsoc.2010.05.012

[68] Ojalvo, C., Zamora, V., Guiberteau, F., & Ortiz, A. L. (2025). Reactive spark plasma sintering of ultrahard wear-resistant boron carbide-SiC-TaB_2 composites from B_4C with $TaSi_2$ aids. *Journal of the European Ceramic Society*, *45*(15), 117626. https://doi.org/10.1016/j.jeurceramsoc.2025.117626

[69] Pakhomova, E., Cao, G., Orrù, R., Garroni, S., Ferro, P., & Licheri, R. (2024). High-Entropy Diborides—Silicon Carbide Composites by Reactive and Non-Reactive Spark Plasma Sintering: A Comparative Study. *Materials*, *17*(3), 718. https://doi.org/10.3390/ma17030718

[70] Orrù, R., & Cao, G. (2013). Comparison of Reactive and Non-Reactive Spark Plasma Sintering Routes for the Fabrication of Monolithic and Composite Ultra High Temperature Ceramics (UHTC) Materials. *Materials*, *6*(5), 1566–1583. https://doi.org/10.3390/ma6051566

[71] Ye, S., Zhu, J., Li, P., Li, M., Yan, N., & Wang, H. (2023). Study on microstructure, mechanical properties and thermal performance of single-phase (Ti,Zr,Hf)B_2 solid solution. *Materials Today Communications*, *34*, 105228. https://doi.org/10.1016/j.mtcomm.2022.105228

[72] Zhang, Y., Guo, W.-M., Jiang, Z.-B., Zhu, Q.-Q., Sun, S.-K., You, Y., Plucknett, K., & Lin, H.-T. (2019). Dense high-entropy boride ceramics with ultra-high hardness. *Scripta Materialia*, *164*, 135–139. https://doi.org/10.1016/j.scriptamat.2019.01.021

[73] Feng, L., Fahrenholtz, W. G., Hilmas, G. E., & Monteverde, F. (2021). Effect of Nb content on the phase composition, densification, microstructure, and mechanical properties of high-entropy boride ceramics. *Journal of the European Ceramic Society*, *41*(1), 92–100. https://doi.org/10.1016/j.jeurceramsoc.2020.08.058

[74] Barbarossa, S., Orrù, R., Cao, G., Balbo, A., Zanotto, F., & Sani, E. (2023). Optical properties of bulk high-entropy diborides for solar energy applications. *Journal of Alloys and Compounds*, *935*, 167965. https://doi.org/10.1016/j.jallcom.2022.167965

[75] Mazo, I., Molinari, A., & Sglavo, V. M. (2022). Electrical resistance flash sintering of tungsten carbide. *Materials & Design*, *213*, 110330. https://doi.org/10.1016/j.matdes.2021.110330

[76] Failla, S., Galizia, P., Fu, S., Grasso, S., & Sciti, D. (2020). Formation of high entropy metal diborides using arc-melting and combinatorial approach to study quinary and quaternary solid solutions. *Journal of the European Ceramic Society*, *40*(3), 588–593. https://doi.org/10.1016/j.jeurceramsoc.2019.10.051

[77] Orrù, R., Licheri, R., Locci, A. M., Cincotti, A., & Cao, G. (2009). Consolidation/synthesis of materials by electric current activated/assisted sintering. *Materials Science and Engineering: R: Reports*, *63*(4–6), 127–287. https://doi.org/10.1016/j.mser.2008.09.003

[78] Cao, G., Estournes, C., Garay, J., & Orrù, R. (Eds.). (2019). *Spark Plasma Sintering, current status, new developments and challenges*. Elsevier. https://doi.org/10.1016/C2018-0-02428-7

[79] Liu, J.-X., Shen, X.-Q., Wu, Y., Li, F., Liang, Y., & Zhang, G.-J. (2020). Mechanical properties of hot-pressed high-entropy diboride-based ceramics. *Journal of Advanced Ceramics*, *9*(4), 503–510. https://doi.org/10.1007/s40145-020-0383-8

[80] McClane, D. L., Fahrenholtz, W. G., & Hilmas, G. E. (2015). Thermal Properties of (Zr, TM)B_2 Solid Solutions with TM = Ta, Mo, Re, V, and Cr. *Journal of the American Ceramic Society*, *98*(2), 637–644. https://doi.org/10.1111/jace.13341

[81] Arati, D. S., Murthy Tammana, S. R. C., Sonber, J. K., Paul, B., Majumdar, S., & Tyagi, A. K. (2023). Studies on synthesis and densification of niobium diboride using carbothermic reduction and hot pressing. *International Journal of Refractory Metals and Hard Materials*, *112*, 106119. https://doi.org/10.1016/j.ijrmhm.2023.106119

[82] Musa, C., Licheri, R., Locci, A. M., Orrù, R., Cao, G., Rodriguez, M. A., & Jaworska, L. (2009). Energy efficiency during conventional and novel sintering processes: the case of Ti–Al_2O_3–TiC composites. *Journal of Cleaner Production*, *17*(9), 877–882. https://doi.org/10.1016/j.jclepro.2009.01.012

[83] le Cloarec, J., Marinel, S., Estournès, C., Folton, C., Dehmas, M., & Manière, C. (2024). Sacrificial ceramics powders mix for titanium alloys complex shapes production by hybridization of SPS and 3D printing. *Powder Technology*, *448*, 120324. https://doi.org/10.1016/j.powtec.2024.120324

[84] le Cloarec, J., Marinel, S., Estournès, C., Dehmas, M., Folton, C., & Manière, C. (2024). Stereolithography coupled with spark plasma sintering to produce Ti-6Al-4V complex shapes. *Journal of Manufacturing Processes*, *114*, 122–135. https://doi.org/10.1016/j.jmapro.2024.01.084

[85] Fregeac, A., Hurtault, M., Larignon, C., Beynet, Y., & Epherre, R. (2024, October 15). FAST/SPS: New Industrial Post-Process for Full Densification of 3D Complex Shape from Sinter Based Additive Manufacturing Technologies. *Euro PM2024 Proceedings*. https://doi.org/10.59499/EP246276973

[86] Sández-Gómez, Á., Ortiz, A. L., & Miranda, P. (2025). Production of complex microchanneled parts of ZrB_2-$MoSi_2$ ultra-high temperature ceramics by freeze casting and pressureless spark plasma sintering. *Journal of the European Ceramic Society*, *45*(2), 116966. https://doi.org/10.1016/j.jeurceramsoc.2024.116966

[87] Cannon, K. M., Britt, D. T., Smith, T. M., Fritsche, R. F., & Batcheldor, D. (2019). Mars global simulant MGS-1: A Rocknest-based open standard for basaltic martian regolith simulants. *Icarus*, *317*, 470–478. https://doi.org/10.1016/j.icarus.2018.08.019

[88] Wray, J. J. (2019). Diverse Surface Mineralogy of Mars from Hyperspectral Sensing. *IGARSS 2019 - 2019 IEEE International Geoscience and Remote Sensing Symposium*, 4908–4910. https://doi.org/10.1109/IGARSS.2019.8900545

[89] Jet Propulsion Laboratory (JPL), California Institute of Technology, *Image Gallery*, https://www.jpl.nasa.gov/images/, (Accessed 25th September 2025)

[90] Peters, G. H., Abbey, W., Bearman, G. H., Mungas, G. S., Smith, J. A., Anderson, R. C., Douglas, S., & Beegle, L. W. (2008). Mojave Mars simulant—Characterization of a new geologic Mars analog. *Icarus*, *197*(2), 470–479. https://doi.org/10.1016/j.icarus.2008.05.004

[91] Schindler, M., Michel, S., Batcheldor, D., & Hochella, M. F. (2019). A nanoscale study of the formation of Fe-(hydr)oxides in a volcanic regolith: Implications for the understanding of soil forming processes on Earth and Mars. *Geochimica et Cosmochimica Acta*, *264*, 43–66. https://doi.org/10.1016/j.gca.2019.08.008

[92] Orbitec, (2008), *JSC Mars-1A Martian regolith simulant material safety datasheet,* https://web.archive.org/web/20160331191710/http://orbitec.com/store/JSC_Mars-1A_Material_Safety_Datasheet.pdf, (Accessed 25th September 2025)

[93] Exolith Lab, now Space Resources Technologies, *MGS-1 Mars global simulant fact sheet 002-05-001-0621*, https://spaceresourcetech.com/collections/martian-simulants/products/mgs-1-mars-global-simulant, (Accessed 25th September 2025)

[94] Exolith Lab, now Space Resources Technologies, *JEZ-1 Jezero Delta simulant fact sheet 002-08-001-0621*, https://spaceresourcetech.com/collections/martian-simulants/products/jez-1-jezero-delta-simulant, (Accessed 25th September 2025)

[95] Exolith Lab, now Space Resources Technologies, University of Central Florida, USA, *Datasheet for MGS-1C Clay ISRU*, https://sciences.ucf.edu/class/simulant_mgs1c, (Accessed 25th September 2025)

[96] Exolith Lab, now Space Resources Technologies, *Mars Global Polyhydrated Sulfate (MGS-1S) Martian Regolith Simulant*, https://spaceresourcetech.com/collections/martian-simulants/products/mgs-1s-sulfate-isru, (Accessed 25th September 2025)

[97] Liu, Y., Shen, T., Lv, X., Zhang, G., Wang, C., Gu, J., Zhang, X., Wang, Q., Chen, X., Quan, X., & Yao, W. (2023). Investigation on a lunar energy storage and conversion system based on the in-situ resources utilization. *Energy*, *268*, 126681. https://doi.org/10.1016/j.energy.2023.126681

[98] Tillotson, B. (1991, September 4). Regolith thermal energy storage for lunar nighttime power. *Conference on Advanced SEI Technologies*. https://doi.org/10.2514/6.1991-3420

[99] Karl, D., Kamutzki, F., Zocca, A., Goerke, O., Guenster, J., & Gurlo, A. (2018). Towards the colonization of Mars by in-situ resource utilization: Slip cast ceramics from Martian soil simulant. *PLOS ONE*, *13*(10), e0204025. https://doi.org/10.1371/journal.pone.0204025

[100] Karl, D., Kamutzki, F., Lima, P., Gili, A., Duminy, T., Zocca, A., Günster, J., & Gurlo, A. (2020). Sintering of ceramics for clay in situ resource utilization on Mars. *Open Ceramics*, *3*, 100008. https://doi.org/10.1016/j.oceram.2020.100008

[101] Corrias, G., Licheri, R., Orru, R., & Cao, G. (2011). Self-Propagating High-Temperature Synthesis Reactions for ISRU and ISFR Applications. *Eurasian Chemico-Technological Journal*, *13*(3–4), 137–148. https://doi.org/10.18321/ectj77

[102] Corrias, G., Licheri, R., Orrù, R., & Cao, G. (2012). Self-propagating high-temperature reactions for the fabrication of Lunar and Martian physical assets. *Acta Astronautica*, *70*, 69–76. https://doi.org/10.1016/j.actaastro.2011.07.022

[103] Concas, A., Corrias, G., Orru, R., Licheri, R., Pisu, M., & Cao, G. (2012). Remarks on ISRU and ISFR Technologies for Manned Missions on Moon and Mars. *Eurasian Chemico-Technological Journal*, *14*(3), 243–248. https://doi.org/10.18321/ectj120

[104] Chow, B. J., Chen, T., Zhong, Y., & Qiao, Y. (2017). Direct Formation of Structural Components Using a Martian Soil Simulant. *Scientific Reports*, *7*(1), 1151. https://doi.org/10.1038/s41598-017-01157-w

[105] Hintze, P. E., & Quintana, S. (2013). Building a Lunar or Martian Launch Pad with In Situ Materials: Recent Laboratory and Field Studies. *Journal of Aerospace Engineering*, *26*(1), 134–142. https://doi.org/10.1061/(ASCE)AS.1943-5525.0000205

[106] Karl, D., Duminy, T., Lima, P., Kamutzki, F., Gili, A., Zocca, A., Günster, J., & Gurlo, A. (2020). Clay in situ resource utilization with Mars global simulant slurries for additive manufacturing and traditional shaping of unfired green bodies. *Acta Astronautica*, *174*, 241–253. https://doi.org/10.1016/j.actaastro.2020.04.064

[107] Karacasulu, L., Karl, D., Gurlo, A., & Vakifahmetoglu, C. (2023). Cold sintering as a promising ISRU technique: A case study of Mars regolith simulant. *Icarus*, *389*, 115270. https://doi.org/10.1016/j.icarus.2022.115270

[108] Licheri, R., Orrù, R., Sani, E., Dell'Oro, A., & Cao, G. (2022). Spark plasma sintering and optical characterization of lunar regolith simulant. *Acta Astronautica*, *201*, 164–171. https://doi.org/10.1016/j.actaastro.2022.09.016

[109] Zhang, X., Gholami, S., Khedmati, M., Cui, B., Kim, Y.-R., Kim, Y.-J., Shin, H.-S., & Lee, J. (2021). Spark plasma sintering of a lunar regolith simulant: effects of parameters on microstructure evolution, phase transformation, and mechanical properties. *Ceramics International*, *47*(4), 5209–5220. https://doi.org/10.1016/j.ceramint.2020.10.100

[110] Phuah, X. L., Wang, H., Zhang, B., Cho, J., Zhang, X., & Wang, H. (2020). Ceramic Material Processing Towards Future Space Habitat: Electric Current-Assisted Sintering of Lunar Regolith Simulant. *Materials*, *13*(18), 4128. https://doi.org/10.3390/ma13184128

[111] Han, W., Zhou, Y., Dang, F., Zhou, C., & Ding, L. (2024). Spark plasma sintering of HUST-1 lunar regolith simulant and its thermal shock resistance properties. *Advances in Space Research*, *73*(3), 1992–2003. https://doi.org/10.1016/j.asr.2023.11.027

[112] Min, T. J. (2022). *Manufacturing Construction Materials on Mars, A feasibility study on the use of Spark Plasma Sintering (SPS) for bulk manufacturing of a viable ISRU Mars construction material using regolith simulant*. https://resolver.tudelft.nl/uuid:ed1f6110-c7f6-4103-b115-8b1675329c91 (Accessed 1st October 2025)

[113] Hoekman, G. W. H. (2022). *Creating structural material from Martian Regolith using spark plasma sintering, Understanding the effect of additives and the possibility to lower the energy requirement*. https://resolver.tudelft.nl/uuid:c69a5167-8782-43ae-923d-16a20ce10d52 (Accessed 1st October 2025)

[114] O'Connell-Cooper, C. D., Spray, J. G., Thompson, L. M., Gellert, R., Berger, J. A., Boyd, N. I., Desouza, E. D., Perrett, G. M., Schmidt, M., & VanBommel, S. J. (2017). APXS-derived chemistry of the Bagnold dune sands: Comparisons with Gale Crater soils and the global Martian average. *Journal of Geophysical Research: Planets*, *122*(12), 2623–2643. https://doi.org/10.1002/2017JE005268

[115] Yen, A. S., Mittlefehldt, D. W., McLennan, S. M., Gellert, R., Bell, J. F., McSween, H. Y., Ming, D. W., McCoy, T. J., Morris, R. v., Golombek, M., Economou, T., Madsen, M. B., Wdowiak, T., Clark, B. C., Jolliff, B. L., Schröder, C., Brückner, J., Zipfel, J., & Squyres, S. W. (2006). Nickel on Mars: Constraints on meteoritic material at the surface. *Journal of Geophysical Research: Planets*, *111*(E12). https://doi.org/10.1029/2006JE002797

[116] Achilles, C. N., Downs, R. T., Ming, D. W., Rampe, E. B., Morris, R. v., Treiman, A. H., Morrison, S. M., Blake, D. F., Vaniman, D. T., Ewing, R. C., Chipera, S. J., Yen, A. S., Bristow, T. F., Ehlmann, B. L., Gellert, R., Hazen, R. M., Fendrich, K. v., Craig, P. I., Grotzinger, J. P., … Morookian, J. M. (2017). Mineralogy of an active eolian sediment from the Namib dune, Gale crater, Mars. *Journal of Geophysical Research: Planets*, *122*(11), 2344–2361. https://doi.org/10.1002/2017JE005262

[117] Zhang, Y., Sun, S.-K., Zhang, W., You, Y., Guo, W.-M., Chen, Z.-W., Yuan, J.-H., & Lin, H.-T. (2020). Improved densification and hardness of high-entropy diboride ceramics from fine powders synthesized via borothermal reduction process. *Ceramics International*, *46*(9), 14299–14303. https://doi.org/10.1016/j.ceramint.2020.02.214

[118] Gild, J., Wright, A., Quiambao-Tomko, K., Qin, M., Tomko, J. A., Shafkat bin Hoque, M., Braun, J. L., Bloomfield, B., Martinez, D., Harrington, T., Vecchio, K., Hopkins, P. E., & Luo, J. (2020). Thermal conductivity and hardness of three single-phase high-entropy metal diborides fabricated by borocarbothermal reduction and spark plasma sintering. *Ceramics International*, *46*(5), 6906–6913. https://doi.org/10.1016/j.ceramint.2019.11.186

[119] Smith, S. M., Fahrenholtz, W. G., & Hilmas, G. E. (2023). Pressureless sintering of high-entropy boride ceramics. *Journal of the European Ceramic Society*, *43*(12), 5168–5173. https://doi.org/10.1016/j.jeurceramsoc.2023.04.050

[120] Qin, M., Gild, J., Wang, H., Harrington, T., Vecchio, K. S., & Luo, J. (2020). Dissolving and stabilizing soft WB_2 and MoB_2 phases into high-entropy borides via boron-metals reactive sintering to attain higher hardness. *Journal of the European Ceramic Society*, *40*(12), 4348–4353. https://doi.org/10.1016/j.jeurceramsoc.2020.03.063

[121] Gaboardi, M., Monteverde, F., Saraga, F., Aquilanti, G., Feng, L., Fahrenholtz, W., & Hilmas, G. (2022). Local structure in high-entropy transition metal diborides. *Acta Materialia*, *239*, 118294. https://doi.org/10.1016/j.actamat.2022.118294

[122] Guo, R., Li, Z., Li, L., Liu, Y., Zheng, R., & Ma, C. (2022). Microstructures and oxidation mechanisms of $(Zr_{0.2}Hf_{0.2}Ta_{0.2}Nb_{0.2}Ti_{0.2})B_2$ high-entropy ceramic. *Journal of the European Ceramic Society*, *42*(5), 2127–2134. https://doi.org/10.1016/j.jeurceramsoc.2021.12.036

[123] Murchie, A. C., Watts, J. L., Fahrenholtz, W. G., & Hilmas, G. E. (2022). Room-temperature mechanical properties of a high-entropy diboride. *International Journal of Applied Ceramic Technology*, *19*(4), 2293–2299. https://doi.org/10.1111/ijac.14026

[124] Zhang, Y., Jiang, Z.-B., Sun, S.-K., Guo, W.-M., Chen, Q.-S., Qiu, J.-X., Plucknett, K., & Lin, H.-T. (2019). Microstructure and mechanical properties of high-entropy borides derived from boro/carbothermal reduction. *Journal of the European Ceramic Society*, *39*(13), 3920–3924. https://doi.org/10.1016/j.jeurceramsoc.2019.05.017

[125] Shen, X.-Q., Liu, J.-X., Li, F., & Zhang, G.-J. (2019). Preparation and characterization of diboride-based high entropy $(Ti_{0.2}Zr_{0.2}Hf_{0.2}Nb_{0.2}Ta_{0.2})B_2$–SiC particulate composites. *Ceramics International*, *45*(18), 24508–24514. https://doi.org/10.1016/j.ceramint.2019.08.178

[126] Zhang, Y., Sun, S.-K., Guo, W.-M., Xu, L., Zhang, W., & Lin, H.-T. (2021). Optimal preparation of high-entropy boride-silicon carbide ceramics. *Journal of Advanced Ceramics*, *10*(1), 173–180. https://doi.org/10.1007/s40145-020-0418-1

[127] Gong, Y., Yang, Z., Wei, X., Song, S., & Ma, S. (2022). Synthesis and electromagnetic wave absorbing properties of high-entropy metal diboride-silicon carbide composite powders. *Journal of Materials Science*, *57*(20), 9218–9230. https://doi.org/10.1007/s10853-022-07238-0

[128] Cheng, Y., Zhou, L., Liu, J., Tan, Y., & Zhang, G. (2023). Grain growth inhibition by sluggish diffusion and Zener pinning in high-entropy diboride ceramics. *Journal of the American Ceramic Society*, *106*(8), 4997–5004. https://doi.org/10.1111/jace.19128

[129] Shackelford, J. F., & Alexander, W. (Eds.). (2000). *CRC Materials Science and Engineering Handbook*. CRC Press. https://doi.org/10.1201/9781420038408

[130] Matthews, F. L., & Rawlings, R. D. (2008). *Composite materials : engineering and science*. Woodhead Publishing/CRC Press.

[131] Lutterotti, L., Ceccato, R., Dal Maschio, R., & Pagani, E. (1998). Quantitative Analysis of Silicate Glass in Ceramic Materials by the Rietveld Method. *Materials Science Forum*, *278–281*, 87–92. https://doi.org/10.4028/www.scientific.net/MSF.278-281.87

[132] Ponton, C. B., & Rawlings, R. D. (1989). Vickers indentation fracture toughness test Part 1 Review of literature and formulation of standardised indentation toughness equations. *Materials Science and Technology*, *5*(9), 865–872. https://doi.org/10.1179/mst.1989.5.9.865

[133] Ponton, C. B., & Rawlings, R. D. (1989). Vickers indentation fracture toughness test Part 2 Application and critical evaluation of standardised indentation toughness equations. *Materials Science and Technology*, *5*(10), 961–976. https://doi.org/10.1179/mst.1989.5.10.961

[134] Parthasarathy, T. A., Rapp, R. A., Opeka, M., & Cinibulk, M. K. (2012). Modeling Oxidation Kinetics of SiC-Containing Refractory Diborides. *Journal of the American Ceramic Society*, *95*(1), 338–349. https://doi.org/10.1111/j.1551-2916.2011.04927.x

[135] Mogilevsky, P., & Cinibulk, M. K. (2024). Oxidation kinetics of silicon carbide-containing refractory diborides, I: Revised model. *Journal of the American Ceramic Society*, *107*(2), 1274–1301. https://doi.org/10.1111/jace.19471

[136] Golla, B. R., Mukhopadhyay, A., Basu, B., & Thimmappa, S. K. (2020). Review on ultra-high temperature boride ceramics. *Progress in Materials Science*, *111*, 100651. https://doi.org/10.1016/j.pmatsci.2020.100651

[137] Sciti, D., Guicciardi, S., & Nygren, M. (2008). Densification and Mechanical Behavior of HfC and HfB_2 Fabricated by Spark Plasma Sintering. *Journal of the American Ceramic Society*, *91*(5), 1433–1440. https://doi.org/10.1111/j.1551-2916.2007.02248.x

[138] Parthasarathy, T. A., Rapp, R. A., Opeka, M., & Kerans, R. J. (2007). A model for the oxidation of ZrB_2, HfB_2 and TiB_2. *Acta Materialia*, *55*(17), 5999–6010. https://doi.org/10.1016/j.actamat.2007.07.027

[139] Parthasarathy, T. A., Rapp, R. A., Opeka, M., & Kerans, R. J. (2009). Effects of Phase Change and Oxygen Permeability in Oxide Scales on Oxidation Kinetics of ZrB_2 and HfB_2. *Journal of the American Ceramic Society*, *92*(5), 1079–1086. https://doi.org/10.1111/j.1551-2916.2009.03031.x

[140] Sciti, D., Medri, V., & Silvestroni, L. (2010). Oxidation behaviour of HfB_2–15 vol.% $TaSi_2$ at low, intermediate and high temperatures. *Scripta Materialia*, *63*(6), 601–604. https://doi.org/10.1016/j.scriptamat.2010.05.050

[141] Förster, J. E., Fahrenholtz, W. G., Hilmas, G. E., & Naraparaju, R. (2024). Hafnium oxide coating to improve the oxidation behavior of Zirconium Diboride. *Journal of the European Ceramic Society*, *44*(15), 116774. https://doi.org/10.1016/J.JEURCERAMSOC.2024.116774

[142] European Commission, Directorate-General for Internal Market, Industry, Entrepreneurship and SMEs, Grohol, M., Veeh, C. (2023). *Study on the critical raw materials for the EU 2023: final report*. https://data.europa.eu/doi/10.2873/725585, (Accessed 25th September 2025)

[143] Saklatvala, E. (2025, March 31). The niche minerals now surging in price as defence spending booms. *Financial Times*. https://www.ft.com/content/e56cd163-d934-4e13-ae00-0a5ddfc8514c, (Accessed 25th September 2025)

[144] Shanghai Metals Market. *Price results for Zirconium*. https://www.metal.com/search?keyword=zirconium&type=price (Accessed 3rd September 2025)

[145] Inoue, R., Arai, Y., Kubota, Y., Kogo, Y., & Goto, K. (2018). Oxidation of ZrB_2 and its composites: a review. *Journal of Materials Science*, *53*(21), 14885–14906. https://doi.org/10.1007/s10853-018-2601-0

[146] Hu, P., Guolin, W., & Wang, Z. (2009). Oxidation mechanism and resistance of ZrB_2–SiC composites. *Corrosion Science*, *51*(11), 2724–2732. https://doi.org/10.1016/j.corsci.2009.07.005

[147] Fahrenholtz, W. G. (2005). The ZrB_2 Volatility Diagram. *Journal of the American Ceramic Society*, *88*(12), 3509–3512. https://doi.org/10.1111/j.1551-2916.2005.00599.x

[148] Hsain, H. A., Lee, Y., Materano, M., Mittmann, T., Payne, A., Mikolajick, T., Schroeder, U., Parsons, G. N., & Jones, J. L. (2022). Many routes to ferroelectric HfO_2: A review of current deposition methods. *Journal of Vacuum Science & Technology A*, *40*(1). https://doi.org/10.1116/6.0001317

[149] Sitler, S. J., Raja, K. S., & Charit, I. (2017). ZrB_2-HfB_2 solid solutions as electrode materials for hydrogen reaction in acidic and basic solutions. *Materials Letters*, *188*, 239–243. https://doi.org/10.1016/j.matlet.2016.10.122

[150] Sitler, S. J., Raja, K. S., & Charit, I. (2017). Hot corrosion behavior of ZrB_2-HfB_2 solid solutions in KCl and K_2SO_4 at 1500 °C. *Ceramics International*, *43*(18), 17071–17085. https://doi.org/10.1016/j.ceramint.2017.09.122

[151] Vorotilo, S., Sidnov, K., Kurbatkina, V. v., Loginov, P. A., Patsera, E. I., Sviridova, T. A., Lobova, T. A., Levashov, E. A., & Klechkovskaya, V. v. (2022). Super-hardening and localized plastic deformation behaviors in ZrB_2 –TaB_2 ceramics. *Journal of Alloys and Compounds*, *901*, 163368. https://doi.org/10.1016/J.JALLCOM.2021.163368

[152] Otani, S., Aizawa, T., & Kieda, N. (2009). Solid solution ranges of zirconium diboride with other refractory diborides: HfB_2, TiB_2, TaB_2, NbB_2, VB_2 and CrB_2. *Journal of Alloys and Compounds*, *475*(1–2), 273–275. https://doi.org/10.1016/j.jallcom.2008.08.023

[153] Dorner, A. N., Monteverde, F., Fahrenholtz, W. G., & Hilmas, G. E. (2022). Solid-state formation mechanisms of core–shell microstructures in (Zr,Ta)B_2 ceramics. *Journal of the American Ceramic Society*, *105*(5), 3147–3152. https://doi.org/10.1111/jace.18363

[154] Musa, C., Orrù, R., Sciti, D., Silvestroni, L., & Cao, G. (2013). Synthesis, consolidation and characterization of monolithic and SiC whiskers reinforced HfB_2 ceramics. *Journal of the European Ceramic Society*, *33*(3), 603–614. https://doi.org/10.1016/j.jeurceramsoc.2012.10.004

[155] Oliver, W. C., & Pharr, G. M. (1992). An improved technique for determining hardness and elastic modulus using load and displacement sensing indentation experiments. *Journal of Materials Research*, *7*(6), 1564–1583. https://doi.org/10.1557/JMR.1992.1564

[156] Barbarossa, S., Murgia, M., Orrù, R., & Cao, G. (2021). Processing Conditions Optimization for the Synthesis and Consolidation of High-Entropy Diborides. *Eurasian Chemico-Technological Journal*, *23*(3), 213–220. https://doi.org/10.18321/ectj1104

[157] Mishra, S. K., Das, S., & Pathak, L. C. (2004). Defect structures in zirconium diboride powder prepared by self-propagating high-temperature synthesis. *Materials Science and Engineering: A*, *364*(1–2), 249–255. https://doi.org/10.1016/j.msea.2003.08.021

[158] Licheri, R., Orrù, R., Musa, C., & Cao, G. (2008). Combination of SHS and SPS Techniques for fabrication of fully dense ZrB_2-ZrC-SiC composites. *Materials Letters*, *62*(3), 432–435. https://doi.org/10.1016/j.matlet.2007.05.066

[159] Wen, T., Ye, B., Liu, H., Ning, S., Wang, C., & Chu, Y. (2020). Formation criterion for binary metal diboride solid solutions established through combinatorial methods. *Journal of the American Ceramic Society*, *103*(5), 3338–3348. https://doi.org/10.1111/jace.16983

[160] Luo, P., Wu, X., Xiao, W., Zhang, F., Wang, Y., Huang, D., & Du, Y. (2022). Phase equilibria in the ZrO_2 –Ta $_2O_5$ –Nb_2O_5 system: Experimental studies and thermodynamic modeling. *Journal of the American Ceramic Society*, *105*(1), 668–686. https://doi.org/10.1111/jace.18079

[161] Förster, J. E., Fahrenholtz, W. G., Hilmas, G. E., & Naraparaju, R. (2023). Oxidation behavior of Nb-coated zirconium diboride. *Journal of the European Ceramic Society*, *43*(12), 5174–5182. https://doi.org/10.1016/j.jeurceramsoc.2023.04.029

[162] Sairam, K., Sonber, J. K., Murthy, T. S. R. Ch., Subramanian, C., Fotedar, R. K., & Hubli, R. C. (2014). Reaction spark plasma sintering of niobium diboride. *International Journal of Refractory Metals and Hard Materials*, *43*, 259–262. https://doi.org/10.1016/j.ijrmhm.2013.12.011

[163] Demirskyi, D., Solodkyi, I., Nishimura, T., Sakka, Y., & Vasylkiv, O. (2017). High-temperature strength and plastic deformation behavior of niobium diboride consolidated by spark plasma sintering. *Journal of the American Ceramic Society*, *100*(11), 5295–5305. https://doi.org/10.1111/jace.15048

[164] Maity, T. N., Biswas, K., & Basu, B. (2018). Critical role of ZrO_2 on densification and microstructure development in spark plasma sintered NbB_2. *Acta Materialia*, *152*, 215–228. https://doi.org/10.1016/j.actamat.2018.03.049

[165] Akin, I., Ocak, B. C., Sahin, F., & Goller, G. (2019). Effects of *SiC* and *SiC* -GNP additions on the mechanical properties and oxidation behavior of NbB_2. *Journal of Asian Ceramic Societies*, *7*(2), 170–182. https://doi.org/10.1080/21870764.2019.1595929

[166] Shanghai Metals Market. *Price results for Niobium*. https://www.metal.com/search?keyword=niobium&type=price, (Accessed 3rd September 2025)

[167] Shanghai Metals Market. *Price results for Tantalum*. https://www.metal.com/search?keyword=tantalum&type=price, (Accessed 3rd September 2025)

[168] Kurbatkina, V. v., Patsera, E. I., Sviridova, T. A., Kochetov, N. A., & Levashov, E. A. (2023). Combustion Synthesis and Characterization of Ultra-High-Temperature NbB_2–HfB_2 Solid Solutions. *International Journal of Self-Propagating High-Temperature Synthesis*, *32*(4), 313–325. https://doi.org/10.3103/S1061386223040143

[169] Demirskyi, D., Solodkyi, I., Nishimura, T., & Vasylkiv, O. O. (2019). Fracture and property relationships in the double diboride ceramic composites by spark plasma sintering of TiB_2 and NbB_2. *Journal of the American Ceramic Society*, *102*(7), 4259–4271. https://doi.org/10.1111/jace.16276

[170] Kaplan Akarsu, M., & Akin, I. (2023). Production and characterization of spark plasma sintered (Ti,Nb)B_2 solid solutions with graphene nanoplatelets and hexagonal boron nitride. *Ceramics International*, *49*(4), 5582–5594. https://doi.org/10.1016/j.ceramint.2022.10.155

[171] Munro, R. G. (2000). Material properties of titanium diboride. *Journal of Research of the National Institute of Standards and Technology*, *105*(5), 709. https://doi.org/10.6028/jres.105.057

[172] Huang, B., Chen, S., Yao, Z., Zhang, M., Jing, Y., Li, B., & Xiong, W. (2015). Study of carbothermal synthesis of TiB_2 assisted by extended high-energy milling. *Powder Technology*, *275*, 69–76. https://doi.org/10.1016/j.powtec.2014.12.025

[173] Gild, J., Kaufmann, K., Vecchio, K., & Luo, J. (2019). Reactive flash spark plasma sintering of high-entropy ultrahigh temperature ceramics. *Scripta Materialia*, *170*, 106–110. https://doi.org/10.1016/j.scriptamat.2019.05.039

[174] Monteverde, F., Saraga, F., & Gaboardi, M. (2020). Compositional disorder and sintering of entropy stabilized (Hf,Nb,Ta,Ti,Zr)B_2 solid solution powders. *Journal of the European Ceramic Society*, *40*(12), 3807–3814. https://doi.org/10.1016/j.jeurceramsoc.2020.04.026

[175] Ma, J., Du, Y., Wu, M., Li, G., Feng, Z., Guo, M., Sun, Y., Song, W., Lin, M., & Guo, X. (2009). A simple inorganic-solvent-thermal route to nanocrystalline niobium diboride. *Journal of Alloys and Compounds*, *468*(1–2), 473–476. https://doi.org/10.1016/j.jallcom.2008.01.021

[176] Nico, C., Monteiro, T., & Graça, M. P. F. (2016). Niobium oxides and niobates physical properties: Review and prospects. *Progress in Materials Science*, *80*, 1–37. https://doi.org/10.1016/j.pmatsci.2016.02.001

[177] Liu, C., Luo, P., Feng, Y., Gong, W., & Zhang, F. (2023). Phase equilibria in the TiO_2–Nb_2O_5 system: New experiments and thermodynamic modeling. *Ceramics International*, *49*(18), 30471–30480. https://doi.org/10.1016/j.ceramint.2023.06.311

[178] Griffith, K. J., Senyshyn, A., & Grey, C. P. (2017). Structural Stability from Crystallographic Shear in TiO_2–Nb_2O_5 Phases: Cation Ordering and Lithiation Behavior of $TiNb_{24}O_{62}$. *Inorganic Chemistry*, *56*(7), 4002–4010. https://doi.org/10.1021/acs.inorgchem.6b03154

[179] Herklotz, A., Grove, K. M., Bowen, M. S., Quade, R. M., Tippey, K. E., & Cann, D. P. (2024). Insights into the $Hf_nNb_2O_{2n5}$ homologous phases from experimental, first-principle, and force-field studies. *Journal of the American Ceramic Society*, *107*(10), 6554–6561. https://doi.org/10.1111/jace.19949

[180] Wu, K.-H., Wang, Y., Yu-Jiang, Zhang, G.-H., Jiao, S.-Q., & Chou, K.-C. (2019). Low temperature synthesis of titanium diboride nanosheets by molten salt–assisted borothermal reduction of TiO_2. *Journal of Nanoparticle Research*, *21*(5), 103. https://doi.org/10.1007/s11051-019-4560-z

[181] Kolios, G., Frauhammer, J., & Eigenberger, G. (2002). Efficient reactor concepts for coupling of endothermic and exothermic reactions. *Chemical Engineering Science*, *57*(9), 1505–1510. https://doi.org/10.1016/S0009-2509(02)00022-2

[182] Perry, R. H. ., & Green, D. W. . (2008). *Perry's chemical engineers' handbook*. 8th ed. McGraw-Hill.

[183] Olevsky, E. A. (1998). Theory of sintering: from discrete to continuum. *Materials Science and Engineering: Reports*, *23*(2), 41–100. https://doi.org/10.1016/S0927-796X(98)00009-6

[184] Olevsky, E. A., Tikare, V., & Garino, T. (2006). Multi-Scale Study of Sintering: A Review. *Journal of the American Ceramic Society*, *89*(6), 1914–1922. https://doi.org/10.1111/j.1551-2916.2006.01054.x

[185] van der Laan, A., Epherre, R., Chevallier, G., Beynet, Y., Weibel, A., & Estournès, C. (2021). Fully coupled electrothermal and mechanical simulation of the production of complex shapes by spark plasma sintering. *Journal of the European Ceramic Society*, *41*(7), 4252–4263. https://doi.org/10.1016/j.jeurceramsoc.2021.02.010

[186] van der Laan, A., Epherre, R., & Estournès, C. (2022). Numerical approach for the determination of multi-mechanisms of the densification of TiAl by spark plasma sintering. *Intermetallics*, *141*, 107435. https://doi.org/10.1016/j.intermet.2021.107435

[187] Diatta, J. S., Couder, C., Harnois, C., Marinel, S., & Manière, C. (2023). Modeling spark plasma sintering of zirconia with prediction of final stage high densification rate. *Materials Letters*, *337*, 133930. https://doi.org/10.1016/j.matlet.2023.133930

[188] Manière, C., Diatta, J. S., Harnois, C., Couder, C., Bilot, C., & Marinel, S. (2023). Pressure assisted sintering stress exponent assessment methods: Accuracy analysis and effect of sintering stress. *Mechanics of Materials*, *181*, 104664. https://doi.org/10.1016/j.mechmat.2023.104664

[189] McWilliams, B., Yu, J., & Zavaliangos, A. (2015). Fully coupled thermal–electric-sintering simulation of electric field assisted sintering of net-shape compacts. *Journal of Materials Science*, *50*(2), 519–530. https://doi.org/10.1007/s10853-014-8463-1

[190] Trzaska, Z., Bonnefont, G., Fantozzi, G., & Monchoux, J.-P. (2017). Comparison of densification kinetics of a TiAl powder by spark plasma sintering and hot pressing. *Acta Materialia*, *135*, 1–13. https://doi.org/10.1016/j.actamat.2017.06.004

[191] Cincotti, A., Locci, A. M., Orrù, R., & Cao, G. (2007). Modeling of SPS apparatus: Temperature, current and strain distribution with no powders. *AIChE Journal*, *53*(3), 703–719. https://doi.org/10.1002/aic.11102

[192] Sobotka, Z. . (1984). *Rheology of materials and engineering structures*. Elseview ; Distribution for the U.S.A. and Canada, Elsevier Science Pub. Co.

[193] Mackenzie, J. K., & Shuttleworth, R. (1949). A Phenomenological Theory of Sintering. *Proceedings of the Physical Society. Section B*, *62*(12), 833–852. https://doi.org/10.1088/0370-1301/62/12/310

[194] Kingery, W. D., & Berg, M. (1955). Study of the Initial Stages of Sintering Solids by Viscous Flow, Evaporation-Condensation, and Self-Diffusion. *Journal of Applied Physics*, *26*(10), 1205–1212. https://doi.org/10.1063/1.1721874

[195] Scherer, G. W. (1977). Sintering of Low-Density Glasses: I, Theory. *Journal of the American Ceramic Society*, *60*(5–6), 236–239. https://doi.org/10.1111/j.1151-2916.1977.tb14114.x

[196] Du, X., Zhang, Z., Wang, Y., Wang, J., Wang, W., Wang, H., & Fu, Z. (2015). Hot-Pressing Kinetics and Densification Mechanisms of Boron Carbide. *Journal of the American Ceramic Society*, *98*(5), 1400–1406. https://doi.org/10.1111/jace.13483

[197] Maksimov, R. N., Shitov, V. A., & Yurovskikh, A. S. (2018). Effect of rate-controlled sintering on characteristics of hot isostatically pressed transparent Yb-doped Lu2O3 ceramics. *Materials Letters*, *211*, 208–211. https://doi.org/10.1016/j.matlet.2017.10.013

[198] Bradbury, W. L., & Olevsky, E. A. (2010). Production of SiC–C composites by free-pressureless spark plasma sintering (FPSPS). *Scripta Materialia*, *63*(1), 77–80. https://doi.org/10.1016/j.scriptamat.2010.03.009

[199] Yamanoglu, R. (2019). Pressureless Spark Plasma Sintering: A Perspective from Conventional Sintering to Accelerated Sintering Without Pressure. *Powder Metallurgy and Metal Ceramics*, *57*(9–10), 513–525. https://doi.org/10.1007/s11106-019-00010-1

[200] Venugopal, S., Paul, A., Vaidhyanathan, B., Binner, J. G. P., Heaton, A., & Brown, P. M. (2014). Synthesis and spark plasma sintering of sub-micron HfB_2: Effect of various carbon sources. *Journal of the European Ceramic Society*, *34*(6), 1471–1479. https://doi.org/10.1016/j.jeurceramsoc.2013.12.025

[201] Dubey, S., Shiven, P., & Balani, K. (2025). Intermediate and final stage sintering kinetics of spark plasma sintered hafnium diboride. *Ceramics International*, *51*(12), 15475–15482. https://doi.org/10.1016/j.ceramint.2025.01.384

[202] Balcı, Ö., Ağaoğulları, D., Muhaffel, F., Öveçoğlu, M. L., Çimenoğlu, H., & Duman, İ. (2016). Effect of sintering techniques on the microstructure and mechanical properties of niobium borides. *Journal of the European Ceramic Society*, *36*(13), 3113–3123. https://doi.org/10.1016/j.jeurceramsoc.2016.05.014

[203] Sani, E., Meucci, M., Mercatelli, L., Balbo, A., Musa, C., Licheri, R., Orrù, R., & Cao, G. (2017). Titanium diboride ceramics for solar thermal absorbers. *Solar Energy Materials and Solar Cells*, *169*, 313–319. https://doi.org/10.1016/j.solmat.2017.05.038

[204] Liu, Z., Wang, J., Wang, Z., Yan, T., Cheng, K., Xu, J., & Qin, J. (2023). Numerical analysis on lunar heat storage system: Multi-objective optimization, heat storage capacity, and thermal insulation performance. *Journal of Energy Storage*, *59*, 106508. https://doi.org/10.1016/j.est.2022.106508

[205] Fleith, P., Cowley, A., Canals Pou, A., Valle Lozano, A., Frank, R., López Córdoba, P., & González-Cinca, R. (2020). In-situ approach for thermal energy storage and thermoelectricity generation on the Moon: Modelling and simulation. *Planetary and Space Science*, *181*, 104789. https://doi.org/10.1016/j.pss.2019.104789

[206] Palos, M. F., Serra, P., Fereres, S., Stephenson, K., & González-Cinca, R. (2020). Lunar ISRU energy storage and electricity generation. *Acta Astronautica*, *170*, 412–420. https://doi.org/10.1016/j.actaastro.2020.02.005

[207] Sizemore, H. G., & Mellon, M. T. (2008). Laboratory characterization of the structural properties controlling dynamical gas transport in Mars-analog soils. *Icarus*, *197*(2), 606–620. https://doi.org/10.1016/j.icarus.2008.05.013

[208] Altomare, A., Cuocci, C., Giacovazzo, C., Moliterni, A., & Rizzi, R. (2008). *QUALX* : a computer program for qualitative analysis using powder diffraction data. *Journal of Applied Crystallography*, *41*(4), 815–817. https://doi.org/10.1107/S0021889808016956

[209] Gražulis, S., Chateigner, D., Downs, R. T., Yokochi, A. F. T., Quirós, M., Lutterotti, L., Manakova, E., Butkus, J., Moeck, P., & le Bail, A. (2009). Crystallography Open Database – an open-access collection of crystal structures. *Journal of Applied Crystallography*, *42*(4), 726–729. https://doi.org/10.1107/S0021889809016690

[210] *ASTM E490-00a. Standard Solar Constant and Zero Air Mass Solar Spectral Irradiance Tables*. (2019). ASTM International.

[211] Wamelink, G. W. W., Frissel, J. Y., Krijnen, W. H. J., Verwoert, M. R., & Goedhart, P. W. (2014). Can Plants Grow on Mars and the Moon: A Growth Experiment on Mars and Moon Soil Simulants. *PLoS ONE*, *9*(8), e103138. https://doi.org/10.1371/journal.pone.0103138

[212] Glavin, D. P., Freissinet, C., Miller, K. E., Eigenbrode, J. L., Brunner, A. E., Buch, A., Sutter, B., Archer, P. D., Atreya, S. K., Brinckerhoff, W. B., Cabane, M., Coll, P., Conrad, P. G., Coscia, D., Dworkin, J. P., Franz, H. B., Grotzinger, J. P., Leshin, L. A., Martin, M. G., … Mahaffy, P. R. (2013). Evidence for perchlorates and the origin of chlorinated hydrocarbons detected by SAM at the Rocknest aeolian deposit in Gale Crater. *Journal of Geophysical Research: Planets*, *118*(10), 1955–1973. https://doi.org/10.1002/jgre.20144

[213] Leshin, L. A., Mahaffy, P. R., Webster, C. R., Cabane, M., Coll, P., Conrad, P. G., Archer, P. D., Atreya, S. K., Brunner, A. E., Buch, A., Eigenbrode, J. L., Flesch, G. J., Franz, H. B., Freissinet, C., Glavin, D. P., McAdam, A. C., Miller, K. E., Ming, D. W., Morris, R. v., … Moores, J. E. (2013). Volatile, Isotope, and Organic Analysis of Martian Fines with the Mars Curiosity Rover. *Science*, *341*(6153). https://doi.org/10.1126/science.1238937

[214] Clark, J. V., Archer, P. D., Gruener, J. E., Ming, D. W., Tu, V. M., Niles, P. B., & Mertzman, S. A. (2020). JSC-Rocknest: A large-scale Mojave Mars Simulant (MMS) based soil simulant for in-situ resource utilization water-extraction studies. *Icarus*, *351*, 113936. https://doi.org/10.1016/j.icarus.2020.113936

[215] Allen, C. C., Morris, R. V., Lindstrom, D. J., Lindstrom, M. M., & Lockwood, J. P. (1997, March 29). JSC Mars-1: Martian regolith simulant. *Lunar and Planetary Institute Conference Abstracts* . https://www.lpi.usra.edu/meetings/LPSC98/pdf/1690.pdf (Accessed 1st October 2025)

[216] Martikainen, J., Muñoz, O., Jardiel, T., Gómez Martín, J. C., Peiteado, M., Willame, Y., Penttilä, A., Muinonen, K., Wurm, G., & Becker, T. (2023). Optical Constants of Martian Dust Analogs at UV–Visible–Near-infrared Wavelengths. *The Astrophysical Journal Supplement Series*, *268*(2), 47. https://doi.org/10.3847/1538-4365/acf0be

[217] Sani, E., Mercatelli, L., Meucci, M., Balbo, A., Silvestroni, L., & Sciti, D. (2016). Compositional dependence of optical properties of zirconium, hafnium and tantalum carbides for solar absorber applications. *Solar Energy*, *131*, 199–207. https://doi.org/10.1016/j.solener.2016.02.045

[218] Sani, E., Sciti, D., Silvestroni, L., Bellucci, A., Orlando, S., & Trucchi, D. M. (2020). Tailoring optical properties of surfaces in wide spectral ranges by multi-scale femtosecond-laser texturing: A case-study for TaB_2 ceramics. *Optical Materials*, *109*, 110347. https://doi.org/10.1016/j.optmat.2020.110347

[219] NASA. *Mars Facts*. https://science.nasa.gov/mars/facts/ (Accessed 1st October 2025)

[220] Appelbaum, J., & Landis, G. A. (1993). Photovoltaic arrays for Martian surface power. *Acta Astronautica*, *30*, 127–142. https://doi.org/10.1016/0094-5765(93)90105-6

[221] Appelbaum, J., & Flood, D. J. (1990). Solar radiation on Mars. *Solar Energy*, *45*(6), 353–363. https://doi.org/10.1016/0038-092X(90)90156-7

[222] Lemmon, M. T., Wolff, M. J., Bell, J. F., Smith, M. D., Cantor, B. A., & Smith, P. H. (2015). Dust aerosol, clouds, and the atmospheric optical depth record over 5 Mars years of the Mars Exploration Rover mission. *Icarus*, *251*, 96–111. https://doi.org/10.1016/j.icarus.2014.03.029

[223] Lemmon, M. T., Guzewich, S. D., Battalio, J. M., Malin, M. C., Vicente-Retortillo, A., Zorzano, M.-P., Martín-Torres, J., Sullivan, R., Maki, J. N., Smith, M. D., & Bell, J. F. (2024). The Mars Science Laboratory record of optical depth measurements via solar imaging. *Icarus*, *408*, 115821. https://doi.org/10.1016/j.icarus.2023.115821

[224] Lemmon, M. T., Smith, M. D., Viudez-Moreiras, D., de la Torre-Juarez, M., Vicente-Retortillo, A., Munguira, A., Sanchez-Lavega, A., Hueso, R., Martinez, G., Chide, B., Sullivan, R., Toledo, D., Tamppari, L., Bertrand, T., Bell, J. F., Newman, C., Baker, M., Banfield, D., Rodriguez-Manfredi, J. A., … Apestigue, V. (2022). Dust, Sand, and Winds Within an Active Martian Storm in Jezero Crater. *Geophysical Research Letters*, *49*(17). https://doi.org/10.1029/2022GL100126

[225] Vicente-Retortillo, Á., Valero, F., Vázquez, L., & Martínez, G. M. (2015). A model to calculate solar radiation fluxes on the Martian surface. *Journal of Space Weather and Space Climate*, *5*, A33. https://doi.org/10.1051/swsc/2015035

[226] Alberghini, M., Morciano, M., Bergamasco, L., Fasano, M., Lavagna, L., Humbert, G., Sani, E., Pavese, M., Chiavazzo, E., & Asinari, P. (2019). Coffee-based colloids for direct solar absorption. *Scientific Reports*, *9*(1), 4701. https://doi.org/10.1038/s41598-019-39032-5

[227] Presley, M. A., & Craddock, R. A. (2006). Thermal conductivity measurements of particulate materials: 3. Natural samples and mixtures of particle sizes. *Journal of Geophysical Research: Planets*, *111*(E9). https://doi.org/10.1029/2006JE002706

[228] Seiferlin, K., Ehrenfreund, P., Garry, J., Gunderson, K., Hütter, E., Kargl, G., Maturilli, A., & Merrison, J. P. (2008). Simulating Martian regolith in the laboratory. *Planetary and Space Science*, *56*(15), 2009–2025. https://doi.org/10.1016/j.pss.2008.09.017

[229] Nagihara, S., Ngo, P., & Grott, M. (2022). Thermal Properties of the Mojave Mars Regolith Simulant in Mars-Like Atmospheric Conditions. *International Journal of Thermophysics*, *43*(7), 98. https://doi.org/10.1007/s10765-022-03023-y

[230] Grott, M., Spohn, T., Knollenberg, J., Krause, C., Hudson, T. L., Piqueux, S., Müller, N., Golombek, M., Vrettos, C., Marteau, E., Nagihara, S., Morgan, P., Murphy, J. P., Siegler, M., King, S. D., Smrekar, S. E., & Banerdt, W. B. (2021). Thermal Conductivity of the Martian Soil at the InSight Landing Site From HP^3 Active Heating Experiments. *Journal of Geophysical Research: Planets*, *126*(7). https://doi.org/10.1029/2021JE006861

[231] Deng, Y., Li, F., Zhou, S., Tao, X., Zhou, Q., & Feng, Q. (2025). Integrated optimization of Martian regolith Sintering: Tailoring microstructure and performance in a mineralogically replicated simulant. *Acta Astronautica*, *237*, 224–235. https://doi.org/10.1016/j.actaastro.2025.08.038

[232] Goulas, A., Harris, R. A., & Friel, R. J. (2016). Additive manufacturing of physical assets by using ceramic multicomponent extra-terrestrial materials. *Additive Manufacturing*, *10*, 36–42. https://doi.org/10.1016/j.addma.2016.02.002

[233] Sen, S., Carranza, S., & Pillay, S. (2010). Multifunctional Martian habitat composite material synthesized from in situ resources. *Advances in Space Research*, *46*(5), 582–592. https://doi.org/10.1016/j.asr.2010.04.009

[234] Wan, L., Wendner, R., & Cusatis, G. (2016). A novel material for in situ construction on Mars: experiments and numerical simulations. *Construction and Building Materials*, *120*, 222–231. https://doi.org/10.1016/j.conbuildmat.2016.05.046

[235] Caprio, L., Demir, A. G., Previtali, B., & Colosimo, B. M. (2020). Determining the feasible conditions for processing lunar regolith simulant via laser powder bed fusion. *Additive Manufacturing*, *32*, 101029. https://doi.org/10.1016/j.addma.2019.101029

[236] Llamas, H. J., Aplin, K. L., & Berthoud, L. (2022). Effectiveness of Martian regolith as a radiation shield. *Planetary and Space Science*, *218*, 105517. https://doi.org/10.1016/j.pss.2022.105517

[237] NASA. *Mars Fact Sheet*. https://nssdc.gsfc.nasa.gov/planetary/factsheet/marsfact (Accessed 1st October 2025)

[238] Zhang, X., Khedmati, M., Kim, Y., Shin, H., Lee, J., Kim, Y., & Cui, B. (2020). Microstructure evolution during spark plasma sintering of FJS-1 lunar soil simulant. *Journal of the American Ceramic Society*, *103*(2), 899–911. https://doi.org/10.1111/jace.16808

[239] Taguchi, G. (1986). *Introduction to quality engineering : designing quality into products and processes*. Asian Productivity Organization.

[240] Minitab Support. *Taguchi Designs*. https://support.minitab.com/en-us/minitab/help-and-how-to/statistical-modeling/doe/supporting-topics/taguchi-designs/taguchi-designs/ (Accessed 1st October 2025)

[241] *ASTM C1161-18. Test Method for Flexural Strength of Advanced Ceramics at Ambient Temperature*. (2023). ASTM International. https://doi.org/10.1520/C1161-18R23

[242] *ASTM E384. Test Method for Microindentation Hardness of Materials*. (2022). ASTM International. https://doi.org/10.1520/E0384-22

[243] Tian, L., Tahmasebi, A., & Yu, J. (2014). An experimental study on thermal decomposition behavior of magnesite. *Journal of Thermal Analysis and Calorimetry*, *118*(3), 1577–1584. https://doi.org/10.1007/s10973-014-4068-9

[244] Huang, C.-L., Weng, M.-H., Lion, C.-T., & Wu, C.-C. (2000). Low temperature sintering and microwave dielectric properties of $Ba_2Ti_9O_{20}$ ceramics using glass additions. *Materials Research Bulletin*, *35*(14–15), 2445–2456. https://doi.org/10.1016/S0025-5408(00)00432-3

[245] de la Iglesia, P. G., García-Moreno, O., Menéndez, J. L., de Aza, A. H., Álvarez-Clemares, I., & Torrecillas, R. (2018). Microstructural development and mechanical performance of mullite-alumina and hibonite-alumina ceramics with controlled addition of a glass phase. *Ceramics International*, *44*(2), 2292–2299. https://doi.org/10.1016/j.ceramint.2017.10.192

[246] Silva, L. B. da, Blaese, D., Peres, A. P. da S., Costa, A. C. S. da, & Acchar, W. (2020). Effect of the addition of glasses as sintering aids on microstructure and properties of nanoalumina. *Matéria (Rio de Janeiro)*, *25*(1). https://doi.org/10.1590/s1517-707620200001.0910

[247] Bellucci, D., Desogus, L., Montinaro, S., Orrù, R., Cao, G., & Cannillo, V. (2017). Innovative hydroxyapatite/bioactive glass composites processed by spark plasma sintering for bone tissue repair. *Journal of the European Ceramic Society*, *37*(4), 1723–1733. https://doi.org/10.1016/j.jeurceramsoc.2016.11.012

[248] Luginina, M., Angioni, D., Montinaro, S., Orrù, R., Cao, G., Sergi, R., Bellucci, D., & Cannillo, V. (2020). Hydroxyapatite/bioactive glass functionally graded materials (FGM) for bone tissue engineering. *Journal of the European Ceramic Society*, *40*(13), 4623–4634. https://doi.org/10.1016/j.jeurceramsoc.2020.05.061

[249] Farries, K. W., Visintin, P., Smith, S. T., & van Eyk, P. (2021). Sintered or melted regolith for lunar construction: state-of-the-art review and future research directions. *Construction and Building Materials*, *296*, 123627. https://doi.org/10.1016/j.conbuildmat.2021.123627

[250] Kharaziha, M., & Fathi, M. H. (2010). Improvement of mechanical properties and biocompatibility of forsterite bioceramic addressed to bone tissue engineering materials. *Journal of the Mechanical Behavior of Biomedical Materials*, *3*(7), 530–537. https://doi.org/10.1016/j.jmbbm.2010.06.003

[251] Hassanzadeh-Tabrizi, S. A. (2017). Spark plasma sintering of forsterite nanopowder and mechanical properties of sintered materials. *Ceramics International*, *43*(17), 15714–15718. https://doi.org/10.1016/j.ceramint.2017.08.132

[252] Whitney, D. L., Broz, M., & Cook, R. F. (2007). Hardness, toughness, and modulus of some common metamorphic minerals. *American Mineralogist*, *92*(2–3), 281–288. https://doi.org/10.2138/am.2007.2212

[253] Huang, Z. H., Gandais, M., & Gaboriaud, R.-J. (1985). Microhardness of feldspar single crystals (Or_{98} and An_{58}) as a function of temperature. *Bulletin de Minéralogie*, *108*(6), 835–841. https://doi.org/10.3406/bulmi.1985.7902

[254] Dorner, D., & Stöckhert, B. (2004). Plastic flow strength of jadeite and diopside investigated by microindentation hardness tests. *Tectonophysics*, *379*(1–4), 227–238. https://doi.org/10.1016/j.tecto.2003.11.008

[255] Denis, Y., Philippot, G., Roitero, E., Goglio, G., Suchomel, M. R., Chung, U. C., Hérisson de Beauvoir, T., Reveron, H., Chevalier, J., Estournès, C., & Elissalde, C. (2025). Cold sintering of zirconia and yttria-stabilized zirconia from reactive hydroxides precursors. *Journal of the European Ceramic Society*, *45*(16), 117650. https://doi.org/10.1016/J.JEURCERAMSOC.2025.117650

[256] Grasso, S., Biesuz, M., Zoli, L., Taveri, G., Duff, A. I., Ke, D., Jiang, A., & Reece, M. J. (2020). A review of cold sintering processes. *Advances in Applied Ceramics*, *119*(3), 115–143. https://doi.org/10.1080/17436753.2019.1706825

[257] Hérisson de Beauvoir, T., & Estournès, C. (2021). Translucent γ-AlOOH and γ-Al_2O_3 glass-ceramics using the cold sintering process. *Scripta Materialia*, *194*, 113650. https://doi.org/10.1016/J.SCRIPTAMAT.2020.113650

[258] Elissalde, C., Hérisson de Beauvoir, T., Chung, U. C., Martin, E., Denis, Y., de Landtsheer, J., Suchomel, M. R., Goglio, G., Philippot, G., & Estournès, C. (2024). Densification of zirconia-based

ceramics by non-conventional sintering processes and chemical pathways. *Ceramics International*, *50*(19), 37385–37394. https://doi.org/10.1016/J.CERAMINT.2024.06.155

[259] Ehlmann, B. L., & Edwards, C. S. (2014). Mineralogy of the Martian Surface. *Annual Review of Earth and Planetary Sciences*, *42*(1), 291–315. https://doi.org/10.1146/annurev-earth-060313-055024

[260] Bramson, A. M., Byrne, S., Putzig, N. E., Sutton, S., Plaut, J. J., Brothers, T. C., & Holt, J. W. (2015). Widespread excess ice in Arcadia Planitia, Mars. *Geophysical Research Letters*, *42*(16), 6566–6574. https://doi.org/10.1002/2015GL064844

[261] Archer, P. D., Franz, H. B., Sutter, B., Arevalo, R. D., Coll, P., Eigenbrode, J. L., Glavin, D. P., Jones, J. J., Leshin, L. A., Mahaffy, P. R., McAdam, A. C., McKay, C. P., Ming, D. W., Morris, R. v., Navarro-González, R., Niles, P. B., Pavlov, A., Squyres, S. W., Stern, J. C., … Wray, J. J. (2014). Abundances and implications of volatile-bearing species from evolved gas analysis of the Rocknest aeolian deposit, Gale Crater, Mars. *Journal of Geophysical Research: Planets*, *119*(1), 237–254. https://doi.org/10.1002/2013JE004493

[262] McEwen, A. S., Dundas, C. M., Mattson, S. S., Toigo, A. D., Ojha, L., Wray, J. J., Chojnacki, M., Byrne, S., Murchie, S. L., & Thomas, N. (2014). Recurring slope lineae in equatorial regions of Mars. *Nature Geoscience*, *7*(1), 53–58. https://doi.org/10.1038/ngeo2014

[263] Rennó, N. O., Bos, B. J., Catling, D., Clark, B. C., Drube, L., Fisher, D., Goetz, W., Hviid, S. F., Keller, H. U., Kok, J. F., Kounaves, S. P., Leer, K., Lemmon, M., Madsen, M. B., Markiewicz, W. J., Marshall, J., McKay, C., Mehta, M., Smith, M., … Young, S. M. M. (2009). Possible physical and thermodynamical evidence for liquid water at the Phoenix landing site. *Journal of Geophysical Research: Planets*, *114*(E1). https://doi.org/10.1029/2009JE003362

[264] Martín-Torres, F. J., Zorzano, M.-P., Valentín-Serrano, P., Harri, A.-M., Genzer, M., Kemppinen, O., Rivera-Valentin, E. G., Jun, I., Wray, J., Bo Madsen, M., Goetz, W., McEwen, A. S., Hardgrove, C., Renno, N., Chevrier, V. F., Mischna, M., Navarro-González, R., Martínez-Frías, J., Conrad, P., … Vaniman, D. (2015). Transient liquid water and water activity at Gale crater on Mars. *Nature Geoscience*, *8*(5), 357–361. https://doi.org/10.1038/ngeo2412

[265] Nuding, D. L., Davis, R. D., Gough, R. v., & Tolbert, M. A. (2015). The aqueous stability of a Mars salt analog: Instant Mars. *Journal of Geophysical Research: Planets*, *120*(3), 588–598. https://doi.org/10.1002/2014JE004722

[266] Linne, D., Moses, R., Sanders, G., Kleinhenz, J., & Mueller, R. (2019). *Mars ISRU & Civil Engineering Current Thinking and Approaches, Presentation to the International Mars Exploration Working Group (IMEWG)*. https://ntrs.nasa.gov/citations/20200000010 (Accessed 1st October 2025)

[267] Buchner, C., Pawelke, R. H., Schlauf, T., Reissner, A., & Makaya, A. (2018). A new planetary structure fabrication process using phosphoric acid. *Acta Astronautica*, *143*, 272–284. https://doi.org/10.1016/j.actaastro.2017.11.045

[268] Warren, P., Raju, N., Ebrahimi, H., Krsmanovic, M., Raghavan, S., Kapat, J., & Ghosh, R. (2022). Effect of sintering temperature on microstructure and mechanical properties of molded Martian and Lunar regolith. *Ceramics International*, *48*(23), 35825–35833. https://doi.org/10.1016/j.ceramint.2022.07.329

[269] Zocca, A., & Günster, J. (2024). Towards a debinding-free additive manufacturing of ceramics: A development perspective of water-based LSD and LIS technologies. *Open Ceramics*, *19*, 100632. https://doi.org/10.1016/j.oceram.2024.100632

[270] Lüchtenborg, J., Mühler, T., Léonard, F., & Günster, J. (2017). Laser-Induced Slip Casting (LIS) – a New Additive Manufacturing Process for Dense Ceramics Demonstrated with Si3N4. *Journal of Ceramic Science and Technology*, *8*(4), 531–540. https://doi.org/https://doi.org/10.4416/JCST2017-00091

[271] Günster, J., Heinrich, J., & Mühler, T. (2018). *Method for Laser-Induced Additive Production of a Green Body by Means of Slip Casting* (Patent US20180141235A1).

[272] Malaiškienė, J., & Mačiulaitis, R. (2013). Frost Resistant Ceramics Produced from Local Raw Materials and Wastes. *Procedia Engineering*, *57*, 739–745. https://doi.org/10.1016/j.proeng.2013.04.093

[273] Exolith Lab, Now Space Resource Technologies. *Datasheet for MGS-1 Mars Global Simulant,* University of Central Florida, USA. https://sciences.ucf.edu/class/simulant_marsglobal (Accessed 1st October 2025)

[274] Exolith Lab, Now Space Resource Technologies. *Datasheet for MGS-1C Clay ISRU,* University of Central Florida, USA. https://sciences.ucf.edu/class/simulant_mgs1c (Accessed 1st October 2025)

[275] Dhupe, A. P., & Gokarn, A. N. (1990). Studies in the thermal decomposition of natural siderites in the presence of air. *International Journal of Mineral Processing*, *28*(3–4), 209–220. https://doi.org/10.1016/0301-7516(90)90043-X

[276] Karunadasa, K. S. P., Manoratne, C. H., Pitawala, H. M. T. G. A., & Rajapakse, R. M. G. (2019). Thermal decomposition of calcium carbonate (calcite polymorph) as examined by in-situ high-temperature X-ray powder diffraction. *Journal of Physics and Chemistry of Solids*, *134*, 21–28. https://doi.org/10.1016/j.jpcs.2019.05.023

[277] Souza, B., Souza, R., Santos, I., & Brocchi, E. (2020). MgSO4 carbothermic reductive decomposition to produce a highly reactive MgO powder. *Journal of Materials Research and Technology*, *9*(2), 1847–1855. https://doi.org/10.1016/j.jmrt.2019.12.017

[278] Scheidema, M. N., & Taskinen, P. (2011). Decomposition Thermodynamics of Magnesium Sulfate. *Industrial & Engineering Chemistry Research*, *50*(16), 9550–9556. https://doi.org/10.1021/ie102554f

[279] Oh, J., & Noh, D. (2017). The reduction kinetics of hematite particles in H_2 and CO atmospheres. *Fuel*, *196*, 144–153. https://doi.org/10.1016/j.fuel.2016.10.125

[280] Ponomar, V. P., Brik, O. B., Cherevko, Yu. I., & Ovsienko, V. V. (2019). Kinetics of hematite to magnetite transformation by gaseous reduction at low concentration of carbon monoxide. *Chemical Engineering Research and Design*, *148*, 393–402. https://doi.org/10.1016/j.cherd.2019.06.019

[281] Asadi, I., Shafigh, P., Abu Hassan, Z. F. bin, & Mahyuddin, N. B. (2018). Thermal conductivity of concrete – A review. *Journal of Building Engineering*, *20*, 81–93. https://doi.org/10.1016/j.jobe.2018.07.002

[282] K., S., Sinha, P., & Chaunsali, P. (2024). Development of waterless extra-terrestrial concrete using Martian regolith. *Advances in Space Research*, *73*(1), 933–944. https://doi.org/10.1016/j.asr.2023.07.036

[283] Song, L., Lei, W., Zhu, X., Luo, L., & Wang, Q. (2024). Microstructural and mechanical properties of high-strength geopolymer based on Martian soil simulant. *Vacuum*, *230*, 113753. https://doi.org/10.1016/j.vacuum.2024.113753

[284] Shao, R., Wu, C., & Li, J. (2025). Engineering cement-free high-performance Martian concrete with enhanced in-situ utilization of soil simulant: Curing across −20 °C–40 °C and CO_2-rich environments. *Journal of Environmental Management*, *375*, 124426. https://doi.org/10.1016/j.jenvman.2025.124426

[285] Gupta, N., Dawara, V., Kumar, A., & Viswanathan, K. (2024). Synthetic space bricks from lunar and Martian regolith via sintering. *Advances in Space Research*, *74*(8), 3902–3915. https://doi.org/10.1016/j.asr.2024.06.045

[286] Grossman, K. (2018). *Regolith-Based Construction Materials for Lunar and Martian Colonies*. https://stars.library.ucf.edu/etd/6165 (Accessed 1st October 2025)

[287] Hill, R. (2009). *The mathematical theory of plasticity*. Clarendon Press.

[288] Mendelson, A. (1968). *Plasticity : theory and application*. R.E. Krieger Pub. Co.

[289] Aryanpour, G., Mashl, S., & Warke, V. (2013). Elastoplastic–viscoplastic modelling of metal powder compaction: application to hot isostatic pressing. *Powder Metallurgy*, *56*(1), 14–23. https://doi.org/10.1179/1743290112Y.0000000027

[290] van Nguyen, C., Deng, Y., Bezold, A., & Broeckmann, C. (2017). A combined model to simulate the powder densification and shape changes during hot isostatic pressing. *Computer Methods in Applied Mechanics and Engineering*, *315*, 302–315. https://doi.org/10.1016/j.cma.2016.10.033

[291] Kohar, C. P., Martin, É., Connolly, D. S., Patil, S., Krutz, N., Wei, D., & Inal, K. (2019). A new and efficient thermo-elasto-viscoplastic numerical implementation for implicit finite element simulations of powder metals: An application to hot isostatic pressing. *International Journal of Mechanical Sciences*, *155*, 222–234. https://doi.org/10.1016/j.ijmecsci.2019.01.046

[292] Khun, H. A., & Downey C. L. (1971). Deformation characteristics and plasticity theory of sintered powder materials. *International Journal of Powder Metallurgy*, *7*(1), 15–25.

[293] Green, R. J. (1972). A plasticity theory for porous solids. *International Journal of Mechanical Sciences*, *14*(4), 215–224. https://doi.org/10.1016/0020-7403(72)90063-X

[294] Abouaf, M., Chenot, J. L., Raisson, G., & Bauduin, P. (1988). Finite element simulation of hot isostatic pressing of metal powders. *International Journal for Numerical Methods in Engineering*, *25*(1), 191–212. https://doi.org/10.1002/nme.1620250116

[295] Arnol'd, V. I. . (1989). *Mathematical methods of classical mechanics*. Springer.

[296] Benaarbia, A., Rouse, J. P., & Sun, W. (2018). A thermodynamically-based viscoelastic-viscoplastic model for the high temperature cyclic behaviour of 9–12% Cr steels. *International Journal of Plasticity*, *107*, 100–121. https://doi.org/10.1016/j.ijplas.2018.03.015

[297] Bird, R. Byron., Armstrong, R. C., & Hassager, O. (1987). *Dynamics of polymeric liquids. Vol. 1, Fluid mechanics*. Wiley.

[298] Locci, A. M., Orrù, R., & Cao, G. (2020). Modeling of Electric Current Assisted Sintering: An extended fluid-like approach for the description of powders rheological behavior. *Chemical Engineering Research and Design*, *154*, 283–302. https://doi.org/10.1016/j.cherd.2019.12.001

[299] Hendrickx, P., Milligan, J., & Brochu, M. (2015). Consideration of particle rearrangement during the modeling of spark plasma densification of Al–Mg alloy powders. *Scripta Materialia*, *102*, 7–10. https://doi.org/10.1016/j.scriptamat.2015.01.003

Appendices

A. Rietveld Analysis Results

A.a. Obtainment of W- and Mo-containing High Entropy Boride and SiC-reinforced composite.

Table A1 -. Phases and quantitative phase analysis results of the $(Ti_{0.2}Zr_{0.2}Hf_{0.2}Mo_{0.2}W_{0.2})B_2$ products obtained by (a) SHS (R-factor Rwp = 2.72%) from coarser W powders, and after SPS (T_D= 1950°C) (b) without (R-factor Rwp = 9.44%) and (c) in presence of 1 wt.% graphite (R-factor Rwp = 8.74%).

Table A1(a)

SHS product							
Phase	**wt.%**	**a (Å)**	**c (Å)**	**Symmetry**	**Space Group**	**Crystallite size (Å)**	**Microstrain**
$(Ti_{0.2}Zr_{0.2}Hf_{0.2}Mo_{0.2}W_{0.2})B_2$	12	3.0561	3.2929	Hexagonal	P6/mmm	752	$3.39*10^{-3}$
$(Mo_{0.5}Ti_{0.5})B_2$	27	3.0561	3.2937	Hexagonal	P6/mmm	988	$3.38*10^{-3}$
$(Hf_{0.5}Ti_{0.5})B_2$	18	3.1095	3.4297	Hexagonal	P6/mmm	1332	$7.80*10^{-3}$
$(Ti_{0.5}Zr_{0.5})$ B2	15	3.1124	3.4342	Hexagonal	P6/mmm	985	$7.56*10^{-3}$
TiB_2	11	3.0468	3.2588	Hexagonal	P6/mmm	991	$3.65*10^{-3}$
WB_2	7	2.9881	13.8928	Hexagonal	P63/mmc	881	$1.58*10^{-3}$

277

WB_4	5	5.2868	6.1780	Hexagonal	P63/mmc	1782	$2.89 *10^{-3}$
HfB_2	3	3.1414	3.4747	Hexagonal	P6/mmm	1541	$6.58*10^{-4}$
ZrB_2	2	3.1699	3.5270	Hexagonal	P6/mmm	1987	$1.38*10^{-4}$

Table A1(b)

SPS product (*0 wt.% graphite)*

Phase	**wt.%**	**a (Å)**	**c (Å)**	**Symmetry**	**Space Group**	**Crystallite size (Å)**	**Microstrain**
$(Ti_{0.2}Zr_{0.2}Hf_{0.2}Mo_{0.2}W_{0.2})B_2$	89	3.0876	3.3560	Hexagonal	P6/mmm	>2000	$2.14*10^{-3}$
$(W,Mo)B_2$	9	3.0341	3.0652	Hexagonal	P6/mmm	1131	$4.16*10^{-4}$
TiO_2	2	3.6999	9.5359	Tetragonal	I41/amd:1	1066	$8.03 *10^{-3}$

Table A1(c)

SPS product (*1 wt.% graphite)*

Phase	**wt.%**	**a (Å)**	**c (Å)**	**Symmetry**	**Space Group**	**Crystallite size (Å)**	**Microstrain**
$(Ti_{0.2}Zr_{0.2}Hf_{0.2}Mo_{0.2}W_{0.2})B_2$	>99	3.0852	3.3553	Hexagonal	P6/mmm	>2000	$2.52*10^{-3}$
$(W,Mo)B_2$	<1	3.0545	3.0585	Hexagonal	P6/mmm	990	$4.20*10^{-3}$

278

Table A2. Phases and quantitative phase analysis results of the $(Ti_{0.2}Zr_{0.2}Hf_{0.2}Mo_{0.2}W_{0.2})B_2$ products obtained by (a) SHS (R-factor Rwp = 6.52%) from finer W powders, and after SPS (T_D= 1950°C) (b) without (R-factor Rwp = 10.24%) and (c) in presence of 1 wt.% graphite (R-factor Rwp = 8.74%).

Table A2(a)

SHS product								
Phase	**wt.%**	**a (Å)**	**b (Å)**	**c (Å)**	**Symmetry**	**Space Group**	**Crystallite size (Å)**	**Microstrain**
$(Ti_{0.2}Zr_{0.2}Hf_{0.2}Mo_{0.2}W_{0.2})B_2$	17	3.0668	-	3.3568	Hexagonal	P6/mmm	1145	$7.93*10^{-4}$
$(Ti_{0.5}Zr_{0.5})B_2$	13	3.1080	-	3.4071	Hexagonal	P6/mmm	1550	$3.50*10^{-3}$
$(Hf_{0.5}Zr_{0.5})B_2$	13	3.1224	-	3.4472	Hexagonal	P6/mmm	1764	$5.03*10^{-3}$
$(Hf_{0.5}Ti_{0.5})B_2$	6	3.0662	-	3.4235	Hexagonal	P6/mmm	1902	$2.17*10^{-3}$
TiB_2	25	3.0531	-	3.2587	Hexagonal	P6/mmm	1644	$1.72*10^{-3}$
HfB_2	8	3.1475	-	3.4828	Hexagonal	P6/mmm	1956	$4.52*10^{-4}$
WB_2	5	2.9925	-	13.9240	Hexagonal	P63/mmc	1224	$9.39*10^{-4}$
ZrB_2	4	3.1717	-	3.5339	Hexagonal	P6/mmm	>2000	$1.39*10^{-4}$
WB_4	3	5.2117	-	6.3417	Hexagonal	P63/mmc	>2000	$2.77*10^{-3}$
Mo	2	3.1487	-		Cubic	Im-3m	1613	$1.56*10^{-4}$
$Mo_2B_{4.026}$	2	3.0039	-	20.9447	Trigonal	R-3m:H	1133	$4.96*10^{-3}$
$Mo_{0.875}Zr_{0.125}$	1	3.1699	-		Cubic	Im-3m	>2000	$2.08*10^{-4}$

279

MoO_2	1	5.6282	4.8646	5.6946	Monoclinic	P21/c:b1	>2000	2.28*10.4

Table A2(b)

SPS product (*0 wt.% graphite)*

Phase	wt.%	a (Å)	c (Å)	Symmetry	Space Group	Crystallite size (Å)	Microstrain
$(Ti_{0.2}Zr_{0.2}Hf_{0.2}Mo_{0.2}W_{0.2})B_2$	100	3.0889	3.3582	Hexagonal	P6/mmm	>2000	1.67*10-3

Table A2(c)

SPS product (*1 wt.% graphite)*

Phase	wt.%	a (Å)	c (Å)	Symmetry	Space Group	Crystallite size (Å)	Microstrain
$(Ti_{0.2}Zr_{0.2}Hf_{0.2}Mo_{0.2}W_{0.2})B_2$	100	3.0860	3.3533	Hexagonal	P6/mmm	>2000	9.56*10-4

280

Table A3. Phases and quantitative phase analysis results of the $(Ti_{0.2}Zr_{0.2}Hf_{0.2}Mo_{0.2}W_{0.2})B_2$– SiC product obtained by SPS (R-factor Rwp=9.23%).

SPS product (1wt.% graphite, 20 vol.%SiC)							
Phase	**wt.%**	**a (Å)**	**c (Å)**	**Symmetry**	**Space Group**	**Crystallite size (Å)**	**Microstrain**
$(Ti_{0.2}Zr_{0.2}Hf_{0.2}Mo_{0.2}W_{0.2})B_2$	93	3.0929	3.3646	Hexagonal	P6/mmm	1316	7.58 E-4
SiC	7	3.0809	15.1197	Hexagonal	P63mc	623	9.91 E-4

A.b Synthesis and sintering of ZrB_2-based solid solutions

Table A4 - Quantitative phase analysis results of ZHB SHS (Rwp=10.1%), SPS without (T_D= 1950°C) (Rwp = 9.8%) and with 1 wt.% graphite (T_D= 1850°C) (Rwp=8.5%).

Table A4(a)

SHS product							
Phase	**%**	**a (Å)**	**c (Å)**	**Symmetry**	**Space Group**	**Crystallite size (Å)**	**Microstrain**
$(Zr_{0.5}Hf_{0.5})B_2$	21.3	3.1590	3.5160	Hexagonal	P6/mmm	1780	2.90 E-4
HfB_2	31.2	3.1470	3.4830	Hexagonal	P6/mmm	1430	5.89 E-4
ZrB_2	43.0	3.1660	3.5233	Hexagonal	P6/mmm	>2000	8.51 E-4
Zr	4.5	3.2265	5.1363	Hexagonal	P63/mmc	300	1.81 E-4

281

Table A4(b)

SPS product (*0 wt.% graphite, T_D= 1950°C)*

Phase	**%**	**a (Å)**	**b (Å)**	**c (Å)**	**beta (°)**	**Symmetry**	**Space Group**	**Crystallite size (Å)**	**Microstrain**
$(Zr_{0.5}Hf_{0.5})B_2$	85.5	3.1575	-	3.5043	-	Hexagonal	P6/mmm	1136	1.38 E-4
ZrO_2	1.1	3.6854	-	5.2950	-	Tetragonal	P42/nmc:1	1925	2.48 E-3
ZrO_2	7.0	5.1064	-	--	-	Cubic	Fm-3m	253	6.88 E-5
HfO_2	6.4	5.1371	5.2012	5.2474	98.6723	Monoclinic	P21/c:b1	182	6.52 E-4

Table A4(c)

SPS product (*1 wt.% graphite, T_D= 1850°C)*

Phase	**%**	**a (Å)**	**c (Å)**	**Symmetry**	**Space Group**	**Crystallite size (Å)**	**Microstrain**
$(Zr_{0.5}Hf_{0.5})B_2$	96.6	3.1573	3.5053	Hexagonal	P6/mmm	1070	3.60 E-4
ZrO_2	2.1	3.7167	5.2228	Tetragonal	P42/nmc:1	1010	2.99 E-3
ZrC	0.6	4.7770	-	Cubic	Fm-3m	1100	9.17 E-4
C	0.7	2.3472	6.7238	Hexagonal	P63mn	1000	7.3 E-3

282

Table A5 - Phases and quantitative phase analysis results of the $(Zr_{0.5}Ta_{0.5})B_2$ products obtained by SHS (R-factor Rwp = 9.6%), and after SPS without (T_D= 1950°C) (R-factor Rwp = 8.4%) and in presence of 1 wt.% graphite (T_D= 1850°C) (R-factor Rwp = 7.3%).

Table A5(a)

SHS product							
Phase	**%**	**a (Å)**	**c (Å)**	**Symmetry**	**Space Group**	**Crystallite size (Å)**	**Microstrain**
$(Zr_{0.26}Ta_{0.74})B_2$	20.6	3.1438	3.4504	Hexagonal	P6/mmm	835	7.07 E-3
$(Zr_{0.35}Ta_{0.65})B_2$	10.4	3.1117	3.3446	Hexagonal	P6/mmm	819	7.75 E-3
$(Zr_{0.08}Ta_{0.92})B_2$	32.6	3.0923	3.2864	Hexagonal	P6/mmm	780	3.95 E-3
TaB_2	16.7	3.0869	3.2599	Hexagonal	P6/mmm	>2000	1.74 E-4
ZrB_2	19.4	3.1679	3.5276	Hexagonal	P6/mmm	>2000	1.19 E-4

283

Table A5(b)

SPS product (*0 wt.% graphite, T_D= 1950°C)*

Phase	%	a (Å)	b (Å)	c (Å)	beta (°)	Symmetry	Space Group	Crystallite size (Å)	Microstrain
$(Zr_{0.5}Ta_{0.5})B_2$	82.8	3.1267	-	3.4108	-	Hexagonal	P6/mmm	687	1.72 E-3
ZrO_2	4.5	3.6372	-	5.2731	-	Tetragonal	P42/nmc:1	777	3.51 E-3
ZrO_2	6.6	5.1616	5.3229	5.4682	97.25	Monoclinic	P21/c:b1	831	3.79 E-3
TaO_2	4.9	13.5317	-	6.1494	-	Tetragonal	I41/a:1	291	5.88 E-3

Table A5(c)

SPS product (*1 wt.% graphite, T_D= 1850°C)*

Phase	%	a (Å)	c (Å)	Symmetry	Space Group	Crystallite size (Å)	Microstrain
$(Zr_{0.5}Ta_{0.5})B_2$	97.2	3.1207	3.4135	Hexagonal	P6/mmm	799	1.80 E-3
ZrO_2	2.8	3.6489	5.2309	Tetragonal	P42/nmc:1	1380	6.66 E-3

284

A.c Synthesis and sintering of NbB_2-based solid solutions

Table A6 - Phases and quantitative phase analysis results of the NB products obtained by SHS (R-factor Rwp=14.9%) and SPS (1950°C, 20 min, 20MPa) without (R-factor Rwp=16.2%) and in presence of 1 wt.% graphite (R-factor Rwp=10.9%)

Table A6(a)

SHS powders

Phase	%	a (Å)	b (Å)	c (Å)	β (°)	Symmetry	Space Group	Crystallite size (Å)	Microstrain	Unit cell volume (Å³)
NbB_2	>99.9	3.1048	-	3.2968	-	Hexagonal	P6/mmm	533	$1.5 \cdot 10^{-3}$	27.5219

Table A6(b)

SPS product (*0 wt.% graphite*)

Phase	%	a (Å)	b (Å)	c (Å)	β (°)	Symmetry	Space Group	Crystallite size (Å)	Microstrain	Unit cell volume (Å³)
NbB_2	>99.9	3.1078	-	3.2991	-	Hexagonal	P6/mmm	1171	$7.1 \cdot 10^{-4}$	27.5943

Table A6(c)

SPS product (*1 wt.% graphite*)

Phase	%	a (Å)	b (Å)	c (Å)	β (°)	Symmetry	Space Group	Crystallite size (Å)	Microstrain	Unit cell volume (Å³)
NbB_2	>99.9	3.1052	-	3.2993	-	Hexagonal	P6/mmm	1325	$7.4 \cdot 10^{-4}$	27.5498

285

Table A7 - Phases and quantitative phase analysis results of the TB products obtained by SHS (R-factor Rwp=14.5%) and SPS (1950°C, 20 min, 20MPa) without (R-factor Rwp=10.8%) and in presence of 1 wt.% graphite (R-factor Rwp=11.1%)

Table A7(a)

SHS powders

Phase	**%**	**a (Å)**	**b (Å)**	**c (Å)**	**β (°)**	**Symmetry**	**Space Group**	**Crystallite size (Å)**	**Microstrain**	**Unit cell volume (Å³)**
TiB_2	98.4	3.0316	-	3.2304	-	Hexagonal	P6/mmm	877	$4.8 \cdot 10^{-5}$	25.7109
$TiBO_3$	1.6	4.7184	-	14.8554	-	Trigonal	R-3c:H	790	$1.9 \cdot 10^{-3}$	286.4208

Table A7(b)

SPS product (*0 wt.% graphite*)

Phase	**%**	**a (Å)**	**b (Å)**	**c (Å)**	**β (°)**	**Symmetry**	**Space Group**	**Crystallite size (Å)**	**Microstrain**	**Unit cell volume (Å³)**
TiB_2	98.6	3.0307	-	3.2309	-	Hexagonal	P6/mmm	>2000	$3.8 \cdot 10^{-4}$	25.6997
$TiBO_3$	1.4	4.7133	-	14.8392	-	Trigonal	R-3c:H	1482	$3.2 \cdot 10^{-3}$	285.4903

286

Table A7(c)

SPS product (*1 wt.% graphite*)

Phase	%	a (Å)	b (Å)	c (Å)	β (°)	Symmetry	Space Group	Crystallite size (Å)	Microstrain	Unit cell volume (Å^3)
TiB_2	98.7	3.0286	-	3.2322	-	Hexagonal	P6/mmm	>2000	$4.3 \cdot 10^{-4}$	25.6744
TiC	1.3	4.2970	-	-	-	Cubic	Fm-3m	614	$2.6 \cdot 10^{-4}$	79.3407

Table A8 - Phases and quantitative phase analysis results of the HB products obtained by SHS (R-factor Rwp=11.0%) and SPS (1950°C, 20 min, 20MPa) without (R-factor Rwp=13.7%) and in presence of 1 wt.% graphite (R-factor Rwp=13.1%)

Table A8(a)

SHS powders

Phase	%	a (Å)	b (Å)	c (Å)	β (°)	Symmetry	Space Group	Crystallite size (Å)	Microstrain	Unit cell volume (Å^3)
HfB_2	99.3	3.1440	-	3.4776	-	Hexagonal	P6/mmm	518	$1.6 \cdot 10^{-3}$	29.7689
HfO_2	0.6	5.1663	5.2800	5.2925	99.66	Monoclinic	P21/c:b1	840	$8.5 \cdot 10^{-4}$	142.3221

287

Table A8(b)

SPS product (*0 wt.% graphite*)

Phase	%	a (Å)	b (Å)	c (Å)	β (°)	Symmetry	Space Group	Crystallite size (Å)	Microstrain	Unit cell volume (Å^3)
HfB_2	95.9	3.1418	-	3.4756	-	Hexagonal	P6/mmm	1547	$3.8 \cdot 10^{-4}$	29.7101
HfO_2	4.1	5.1232	5.1768	5.2902	99.19	Monoclinic	P21/c:b1	940	$1.9 \cdot 10^{-3}$	138.5046

Table A8(c)

SPS product (*1 wt.% graphite*)

Phase	%	a (Å)	b (Å)	c (Å)	β (°)	Symmetry	Space Group	Crystallite size (Å)	Microstrain	Unit cell volume (Å^3)
HfB_2	96.9	3.1417	-	3.4783	-	Hexagonal	P6/mmm	1360	$5.0 \cdot 10^{-4}$	29.7313
HfC	3.1	4.6281	-	-	-	Cubic	Fm-3m	1243	$1.3 \cdot 10^{-3}$	99.1307

Table A9 - Phases and quantitative phase analysis results of the (Nb,Hf)B_2 products obtained by SHS (R-factor Rwp=7.6%) and SPS (20MPa) in presence of 1 wt.% graphite (T_D=1850 °C, 40min, R-factor Rwp=10.8%), (T_D=1950 °C, 40min, R-factor Rwp=9.9%), (T_D=2050 °C, 20min, R-factor Rwp=9.5%), (T_D=2050 °C, 30min, R-factor Rwp=9.0%), (T_D=2050 °C, 40min, R-factor Rwp=14.0%) and without graphite (T_D=2050 °C, 40min, R-factor Rwp=13.5%).

Table A9(a)

SHS powders

Phase	**%**	**a (Å)**	**b (Å)**	**c (Å)**	**β (°)**	**Symmetry**	**Space Group**	**Crystallite size (Å)**	**Microstrain**	**Unit cell volume (Å^3)**
$(Nb_{0.5}Hf_{0.5})B_2$	53.1	3.1274	-	3.4189	-	Hexagonal	P6/mmm	317	$3.9\cdot10^{-3}$	28.9590
HfB_2	27.6	3.1335	-	3.4641	-	Hexagonal	P6/mmm	919	$3.2\cdot10^{-3}$	28.6061
NbB_2	18.7	3.1157	-	3.2793	-	Hexagonal	P6/mmm	708	$2.9\cdot10^{-3}$	27.5691
HfO_2	0.6	5.2086	5.0672	5.4799	100.2	Monoclinic	P21/c:b1	1010	$1.0\cdot10^{-3}$	142.3453

289

Table A9(b)

SPS product (1850°C, 40 min, *1 wt.% graphite*)

Phase	%	a (Å)	b (Å)	c (Å)	β (°)	Symmetry	Space Group	Crystallite size (Å)	Microstrain	Unit cell volume (Å³)
Hf-rich $(Nb,Hf)B_2$	84.5	3.1233	-	3.4153	-	Hexagonal	P6/mmm	635	$8.2 \cdot 10^{-4}$	28.8527
HfB_2	4.4	3.1309	-	3.4592	-	Hexagonal	P6/mmm	>2000	$2.1 \cdot 10^{-3}$	29.3660
Nb-rich $(Nb,Hf)B_2$	10.7	3.1242	-	3.2995	-	Hexagonal	P6/mmm	1076	$3.4 \cdot 10^{-3}$	27.8905
$(Nb_{0.5}Hf_{0.5})C$	0.4	4.4340	-	-	-	Cubic	Fm-3m	700	$2.6 \cdot 10^{-3}$	87.1740

Table A9(c)

SPS product (1950°C, 40 min, *1 wt.% graphite*)

Phase	%	a (Å)	b (Å)	c (Å)	β (°)	Symmetry	Space Group	Crystallite size (Å)	Microstrain	Unit cell volume (Å³)
Hf-rich $(Nb,Hf)B_2$	88.6	3.1226	-	3.4150	-	Hexagonal	P6/mmm	680	$8.1 \cdot 10^{-4}$	28.8373
Nb-rich $(Nb,Hf)B_2$	11.3	3.1240	-	3.3127	-	Hexagonal	P6/mmm	1261	$4.0 \cdot 10^{-3}$	27.9985

290

Table A9(d)

SPS product (2050°C, 20min, 1 *wt.% graphite*)

Phase	%	a (Å)	b (Å)	c (Å)	β (°)	Symmetry	Space Group	Crystallite size (Å)	Microstrain	Unit cell volume (Å^3)
Hf-rich (Nb,Hf)B_2	88.4	3.1213	-	3.4063	-	Hexagonal	P6/mmm	890	$9.1 \cdot 10^{-4}$	28.7399
Nb-rich (Nb,Hf)B_2	10.6	3.1216	-	3.3656	-	Hexagonal	P6/mmm	1476	$4.7 \cdot 10^{-3}$	28.4019
($Nb_{0.5}Hf_{0.5}$)C	1.0	4.5767	-	-	-	Cubic	Fm-3m	1000	$1.6 \cdot 10^{-3}$	95.8644

Table A9(e)

SPS product (2050°C, 30min, 1 *wt.% graphite*)

Phase	%	a (Å)	b (Å)	c (Å)	β (°)	Symmetry	Space Group	Crystallite size (Å)	Microstrain	Unit cell volume (Å^3)
Hf-rich (Nb,Hf)B_2	89.0	3.1217	-	3.4093	-	Hexagonal	P6/mmm	885	$8.1 \cdot 10^{-4}$	28.7725
Nb-rich (Nb,Hf)B_2	11.0	3.1250	-	3.3100	-	Hexagonal	P6/mmm	1256	$3.7 \cdot 10^{-3}$	27.9936

291

Table A9(f)

SPS product (2050°C, 40 min, *0.% graphite*)

Phase	%	a (Å)	b (Å)	c (Å)	β (°)	Symmetry	Space Group	Crystallite size (Å)	Microstrain	Unit cell volume (Å^3)
$(Nb_{0.5}Hf_{0.5})B_2$	78.5	3.1228	-	3.4145	-	Hexagonal	P6/mmm	1080	$1.3 \cdot 10^{-3}$	28.8367
NbB_2	20.2	3.1216	-	3.3306	-	Hexagonal	P6/mmm	1012	$5.8 \cdot 10^{-3}$	28.1065
HfO_2	1.3	5.1244	5.1462	5.2840	99.1	Monoclinic	P21/c:b1	992	$4.7 \cdot 10^{-3}$	137.5915

Table A10 - Phases and quantitative phase analysis results of the (Nb,Ti)B_2 products obtained by SHS (R-factor Rwp=11.1%) and SPS (20MPa) in presence of 1 wt.% graphite (T_D=1950 °C, 40min, R-factor Rwp=8.1%), (T_D=2050 °C, 10min, R-factor Rwp=12.5%), (T_D=2050 °C, 20min, R-factor Rwp=15.3%), (T_D=2050 °C, 40min, R-factor Rwp=12.1%) and without graphite (T_D=2050 °C, 20min, R-factor Rwp=13.8%).

Table A10(a)

SHS powders

Phase	%	a (Å)	b (Å)	c (Å)	β (°)	Symmetry	Space Group	Crystallite size (Å)	Microstrain	Unit cell volume (Å^3)
$(Nb_{0.5}Ti_{0.5})B_2$	62.9	3.0674	-	3.2693	-	Hexagonal	P6/mmm	1222	$4.1 \cdot 10^{-3}$	26.6395
NbB_2	23.6	3.1004	-	3.2976	-	Hexagonal	P6/mmm	576	$2.0 \cdot 10^{-3}$	27.4514
TiB_2	13.5	3.0371	-	3.2369	-	Hexagonal	P6/mmm	807	$1.4 \cdot 10^{-3}$	25.8570

Table A10(b)

SPS product (T_D=1950°C, 40 min, *1 wt.% graphite*)

Phase	**%**	**a (Å)**	**b (Å)**	**c (Å)**	**β (°)**	**Symmetry**	**Space Group**	**Crystallite size (Å)**	**Microstrain**	**Unit cell volume (Å³)**
Ti-rich $(Nb,Ti)B_2$	90.8	3.0680	-	3.2736	-	Hexagonal	P6/mmm	1435	$1.3 \cdot 10^{-3}$	26.6850
Nb-rich $(Nb,Ti)B_2$	8.7	3.0861	-	3.2937	-	Hexagonal	P6/mmm	1013	$2.3 \cdot 10^{-3}$	27.1666
NbC	0.4	4.4300	-	-	-	Cubic	Fm-3m	999	$1.5 \cdot 10^{-4}$	86.9383

Table A10(c)

SPS product (T_D=2050°C, 10 min, 1 *wt.% graphite*)

Phase	**%**	**a (Å)**	**b (Å)**	**c (Å)**	**β (°)**	**Symmetry**	**Space Group**	**Crystallite size (Å)**	**Microstrain**	**Unit cell volume (Å³)**
Ti-rich $(Nb,Ti)B_2$	98.1	3.0694	-	3.2728	-	Hexagonal	P6/mmm	>2000	$4.5 \cdot 10^{-4}$	26.7028
Nb-rich $(Nb,Ti)B_2$	1.8	3.0990	-	3.2741	-	Hexagonal	P6/mmm	972	$7.7 \cdot 10^{-4}$	27.2311
NbC	0.1	4.4280	-	-	-	Cubic	Fm-3m	1000	$3.2 \cdot 10^{-3}$	86.82061

293

Table A10(d)

SPS product (T_D=2050°C, 20 min, *1 wt.% graphite*)

Phase	%	a (Å)	b (Å)	c (Å)	β (°)	Symmetry	Space Group	Crystallite size (Å)	Microstrain	Unit cell volume (Å^3)
$(Nb_{0.5}Ti_{0.5})B_2$	>99.9	3.0707	-	3.2750	-	Hexagonal	P6/mmm	1643	$4.7 \cdot 10^{-4}$	26.7434

Table A10(e)

SPS product (T_D=2050°C, 40 min, *1 wt.% graphite*)

Phase	%	a (Å)	b (Å)	c (Å)	β (°)	Symmetry	Space Group	Crystallite size (Å)	Microstrain	Unit cell volume (Å^3)
$(Nb_{0.5}Ti_{0.5})B_2$	>99.9	3.0679	-	3.2735	-	Hexagonal	P6/mmm	>2000	$5.0 \cdot 10^{-4}$	26.6824

Table A10(f)

SPS product (T_D=2050°C, 20 min, *0 wt.% graphite*)

Phase	%	a (Å)	b (Å)	c (Å)	β (°)	Symmetry	Space Group	Crystallite size (Å)	Microstrain	Unit cell volume (Å^3)
Ti-rich $(Nb,Ti)B_2$	92.7	3.0665	-	3.2701	-	Hexagonal	P6/mmm	1221	$1.2 \cdot 10^{-3}$	26.6304
Nb-rich $(Nb,Ti)B_2$	7.3	3.0843	-	3.2832	-	Hexagonal	P6/mmm	788	$3.1 \cdot 10^{-3}$	27.0484

294

A.d Processing of Martian regoliths for their application as solar energy absorbers on Mars

Table A11 -Crystallite size parameters estimated by Rietveld method for JSC-Mars-1A and MMS, prior to and post SPS. Data in Angstrom (Å).

JSC-Mars-1A					
	Pristine	**Heat Treated @700**	**SPS @800-15**	**SPS @900-30**	**SPS @1000-30**
Magnetite (S.G.: Fd-3m)	1460	1470	1470	1490	1790
Andesine (S.G.: P-1)	1825	>2000	>2000	>2000	>2000
Olivine (S.G.: Pbnm)	725	800	800	850	900
Pyroxene (S.G.: C2/c)	980	1100	>2000	>2000	>2000

MMS				
	Pristine	**SPS @950-30**	**SPS @1000-30**	**SPS @1050-30**
Augite (S.G.: C2/c)	>2000	>2000	>2000	>2000
Andesine (S.G.: P-1)	>2000	>2000	>2000	>2000
Bytownite (S.G.: P-1)	1920	1920	1980	2000
Fe_2CoO_4 (S.G.: Fd-3m)	880	920	950	950
Ortoclase (S.G.: C2/m)	720	1090	>2000	>2000
Pigeonite (S.G.: $P2_1/c$)	620	700	770	770
Montmorillonite (S.G.: C2/m)	140	-	-	-
Olivine (S.G.: Pbnm)	1030	1110	1350	1780

295

Table A12. Comparison between microstrain (r.m.s) estimated by the Rietveld method for the JSC-Mars-1A and MMS simulants, pre and post SPS.

JSC-Mars-1A					
	Pristine	**Heat Treated @700**	**SPS @800-15**	**SPS @900-30**	**SPS @1000-30**
Magnetite (S.G.: Fd-3m)	2.30E-04	9.80E-04	9.70E-04	9.70E-03	4.50E-03
Andesine (S.G.: P-1)	1.70E-03	6.00E-04	6.00E-04	6.00E-04	9.00E-04
Olivine (S.G.: Pbnm)	2.90E-03	2.60E-04	2.60E-04	2.60E-04	3.00E-04
Pyroxene (S.G.: C2/c)	2.00E-03	3.20E-03	3.20E-03	3.20E-03	1.70E-04

MMS				
	Pristine	**SPS @950-30**	**SPS @1000-30**	**SPS @1050-30**
Augite (S.G.: C2/c)	8.20E-04	6.00E-04	8.90E-04	6.00E-04
Andesine (S.G.: P-1)	7.60E-04	7.60E-04	7.60E-04	7.60E-04
Bytownite (S.G.: P-1)	2.30E-03	5.20E-04	1.90E-03	1.80E-03
Fe2CoO4 (S.G.: Fd-3m)	5.50E-03	1.60E-03	1.50E-03	1.60E-03
Ortoclase (S.G.: C2/m)	7.90E-04	7.90E-04	2.40E-04	1.30E-03
Pigeonite (S.G.: $P2_1/c$)	2.00E-03	6.00E-03	3.00E-03	3.30E-03
Montmorillonite (S.G.: C2/m)	5.00E-04	-	-	-
Olivine (S.G.: Pbnm)	7.90E-04	7.90E-04	2.40E-04	1.30E-03

296

Table A13. Lattice parameters estimated by the Rietveld Method for the JSC-Mars-1A simulant, prior to and post SPS.

JSC-Pristine							
	a (Å)	**b (Å)**	**c (Å)**	**α (°)**	**β (°)**	**γ (°)**	**V (Å^3)**
Magnetite (S.G.: Fd-3m)	8.3928	8.3928	8.3928	-	-	-	591.2
Andesine (S.G.: P-1)	8.1835	12.8945	7.1177	93.4	116.1	90.4	751.1
Olivine (S.G.: Pbnm)	4.7054	10.0867	6.1042	-	-	-	289.7
Pyroxene (S.G.: C2/c)	9.7606	8.8681	5.3143	-	106.9	-	460

JSC-HT							
	a (Å)	**b (Å)**	**c (Å)**	**α (°)**	**β (°)**	**γ (°)**	**V (Å^3)**
Magnetite (S.G.: Fd-3m)	8.3687	8.3687	8.3687	-	-	-	586.1
Andesine (S.G.: P-1)	8.1829	12.8812	7.1187	93.4	116.2	90.4	750.4
Olivine (S.G.: Pbnm)	4.7047	10.7176	6.2169	-	-	-	313.5
Pyroxene (S.G.: C2/c)	9.8028	8.8409	5.3785	-	107.1	-	466.1

297

JSC@800-15							
	a (Å)	**b (Å)**	**c (Å)**	**α (°)**	**β (°)**	**γ (°)**	**V (Å^3)**
Magnetite (S.G.: Fd-3m)	8.3622	8.3622	8.3622	-	-	-	584.7
Andesine (S.G.: P-1)	8.1771	12.888	7.1165	93.4	116.2	90.4	750
Olivine (S.G.: Pbnm)	4.7121	10.7098	6.2136	-	-	-	313.6
Pyroxene (S.G.: C2/c)	9.8009	8.8321	5.3786	-	106.9	-	465.6

JSC @900-30							
	a (Å)	**b (Å)**	**c (Å)**	**α (°)**	**β (°)**	**γ (°)**	**V (Å^3)**
Magnetite (S.G.: Fd-3m)	8.3622	8.3622	8.3622	-	-	-	584.7
Andesine (S.G.: P-1)	8.1771	12.8881	7.1165	93.4	116.2	90.3	750
Olivine (S.G.: Pbnm)	4.7121	10.7098	6.21362	-	-	-	313.6
Pyroxene (S.G.: C2/c)	9.8009	8.8321	5.3786	-	106.9	-	465.6

JSC@1000-30							
	a (Å)	**b (Å)**	**c (Å)**	**α (°)**	**β (°)**	**γ (°)**	**V (Å^3)**
Magnetite (S.G.: Fd-3m)	8.4002	8.4002	8.4002	-	-	-	592.7
Andesine (S.G.: P-1)	8.1735	12.8918	7.1074	93.4	116.2	90.3	748.9

298

Olivine (S.G.: Pbnm)	4.5993	10.7227	6.2569	-	-	-	308.6
Pyroxene (S.G.: C2/c)	9.8488	8.836	5.3537	-	106.9	-	465.9

Table A14. Lattice parameters estimated by the Rietveld Method for the MMS simulant, prior to and post SPS.

	MMS-Pristine						
	a (Å)	**b (Å)**	**c (Å)**	**α (°)**	**β (°)**	**γ (°)**	**V (Å^3)**
Andesine (S.G.: P-1)	8.1807	12.8753	7.1128	93.4	116.1	90.3	749.2
Augite (S.G.: C2/c)	9.7532	8.9254	5.269	-	106.4	-	458.7
Pigeonite (S.G.: P21/c)	9.6634	8.9606	5.3523	-	108.8	-	463.5
Olivine (S.G.: Pbnm)	4.3924	10.3394	5.9937	-	-	-	272.2
Ortoclase (S.G.: C2/m)	8.6988	12.942	6.5812	-	115.2	-	740.9
Bytownite (S.G.: P-1)	7.2165	11.7629	11.7151	80.6	98.7	58.7	994.5
Fe_2CoO_4 (S.G.: Fd-3m)	9.0705	9.0705	9.0705	-	-	-	746.3
Montmorillonite (S.G.: C2/m)	5.1750	9.0960	16.35	-	107.59	-	769.6

299

MMS@950-30							
	a (Å)	**b (Å)**	**c (Å)**	**α (°)**	**β (°)**	**γ (°)**	**V (Å^3)**
Andesine (S.G.: P-1)	8.1801	12.884	7.1118	93.5	116.2	90.3	749.5
Augite (S.G.: C2/c)	9.769	8.9214	5.2672	-	106.4	-	459.1
Pigeonite (S.G.: P21/c)	9.6314	8.9407	5.228	-	108.6	-	450.2
Olivine (S.G.: Pbnm)	4.711	10.1375	6.2945	-	-	-	300.6
Ortoclase (S.G.: C2/m)	8.6531	12.8682	6.777	-	115.1	-	754.6
Bytownite (S.G.: P-1)	7.226	11.8826	11.7587	80.2	97.4	57.5	1009.6
Fe_2CoO_4 (S.G.: Fd-3m)	8.4067	8.4067	8.4067	-	-	-	594.1

MMS@1000-30							
	a (Å)	**b (Å)**	**c (Å)**	**α (°)**	**β (°)**	**γ (°)**	**V (Å^3)**
Andesine (S.G.: P-1)	8.1767	12.887	7.1094	93.4	116.1	90.3	749.1
Augite (S.G.: C2/c)	9.7549	8.9351	5.2723	-	106.4	-	459.5
Pigeonite (S.G.: P21/c)	9.6473	8.9153	5.2356	-	108.6	-	450.3
Olivine (S.G.: Pbnm)	4.7428	10.1791	6.262	-	-	-	302.3
Ortoclase (S.G.: C2/m)	8.6003	12.8718	6.7644	-	114.7	-	748.8
Bytownite (S.G.: P-1)	7.2255	11.8476	11.7544	80.0	96.8	58.1	1006.2

300

Fe_2CoO_4 (S.G.: Fd-3m)	8.4002	8.4002	8.4002	-	-	-	592.7

	MMS@1050-30						
	a (Å)	**b (Å)**	**c (Å)**	**α (°)**	**β (°)**	**γ (°)**	**V ($Å^3$)**
Andesine (S.G.: P-1)	8.1776	12.8848	7.1102	93.4	116.1	90.3	749.2
Augite (S.G.: C2/c)	9.7533	8.9293	5.2683	-	106.4	-	458.8
Pigeonite (S.G.: P21/c)	9.6463	8.9317	5.2349	-	108.6	-	451.0
Olivine (S.G.: Pbnm)	4.7081	10.1636	6.2679	-	-	-	299.9
Ortoclase (S.G.: C2/m)	8.6164	12.8516	6.7581	-	114.7	-	748.4
Bytownite (S.G.: P-1)	7.2272	11.8609	11.76	80.0	96.8	58.1	1008.1
Fe_2CoO_4 (S.G.: Fd-3m)	8.3900	8.3900	8.3900	-	-	-	590.6

301

B. Phase diagrams adapted from literature

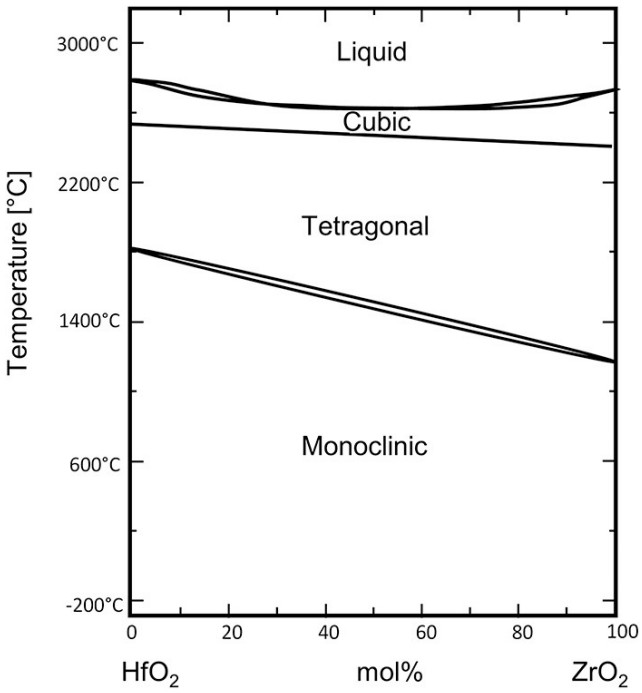

Figure B1 – HfO_2-ZrO_2 phase diagram, taken from **Hsain et al. and references therein [148]**.

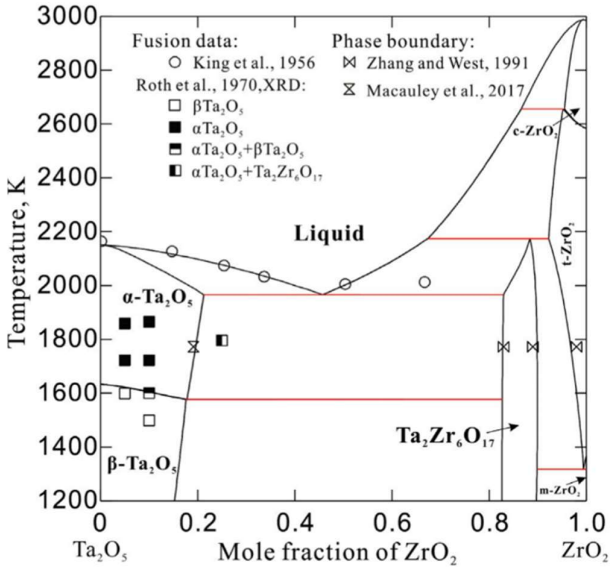

Figure B2 - Calculated ZrO_2-Ta_2O_5 phase diagram, correlated with selected experimental data, adapted from **Luo et al. [160]**.

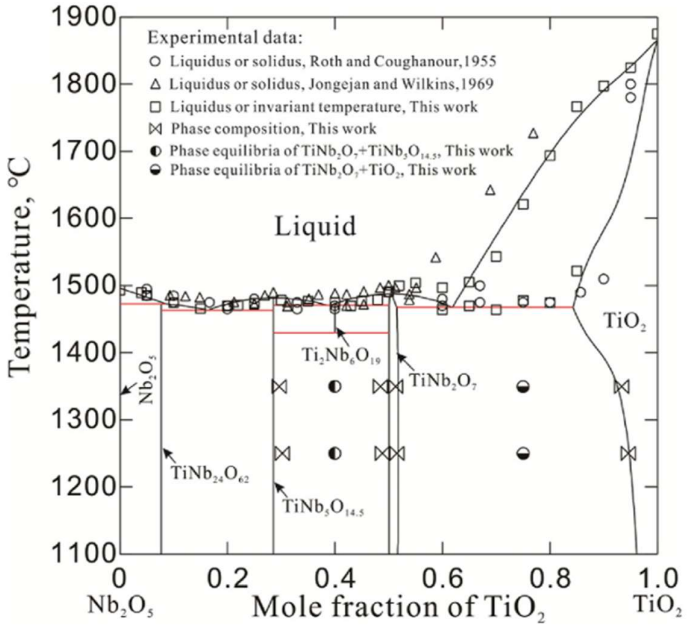

Figure B3 - Calculated Nb_2O_5-TiO_2 phase diagram, correlated of selected experimental data, adapted from **Liu et al. [177]**.

C. Details of the constitutive model of pressure-assisted powder consolidation by Spark Plasma Sintering applied to transition metal diborides

C.a Plastic deformation of Body (1)

Let us assume that Body (1) behaves as a perfectly plastic porous body (elasticity is neglected). Under the same assumptions illustrated in the previous paragraph (pressing in a rigid die), the variation of the plastic strain tensor components can be expressed by the flow rule **[287,288]**:

$$d\varepsilon_{ij}^{P} = d\Lambda \frac{\partial \Psi^{P}}{\partial \sigma_{ij}} \tag{C1}$$

where Ψ^{P} is the plastic potential, σ_{ij} are the Cauchy stress tensor components, and Λ is the plastic multiplier. By assuming an associated flow rule, the plastic potential equals the yield function F **[289-291]** such that

$$d\varepsilon_{ij}^{P} = d\Lambda \frac{\partial F}{\partial \sigma_{ij}} \tag{C2}$$

The yield function is given by the following expression **[289-291]**:

$$F = \sigma_{eq}\left(\sigma_{ij}, \rho\right) - \sigma_{Y}(\rho, T) \tag{C3}$$

where T is the temperature. The equivalent stress σ_{eq} is defined as follows **[292-294]**:

$$\sigma_{eq} = [A(\rho)J_2 + B(\rho)I_1^2]^{1/2} \tag{C4}$$

where $A(\rho)$ and $B(\rho)$ are empirical constants depending on relative density ρ. J_2 is the second invariant of the deviatoric Cauchy stress tensor:

$$J_2 = \frac{1}{2}\sigma'_{ij}\sigma'_{ij} \tag{C5}$$

while I_1 is the first invariant of the Cauchy stress tensor:

$$I_1 = tr(\boldsymbol{\sigma}) \tag{C6}$$

where $tr(\boldsymbol{\sigma})$ indicates the trace of the tensor, and σ'_{ij} are the deviatoric Cauchy tensor components defined as:

$$\sigma'_{ij} = \sigma_{ij} - \frac{I_1}{3}\delta_{ij} \tag{C7}$$

where δ_{ij} represents the Kronecker delta.

As defined by Eq. (C3), F is a function of the variables σ_{ij}, ρ, and T. The consistency condition can be then written down as follows:

$$dF = \frac{\partial F}{\partial \sigma_{ij}}d\sigma_{ij} + \frac{\partial F}{\partial \rho}d\rho + \frac{\partial F}{\partial T}dT = 0 \tag{C8}$$

The mass conservation principle (continuity equation) leads to:

$$d\rho = -\rho\, tr(d\boldsymbol{\varepsilon}^P) \tag{C9}$$

which using Eq. (C2) can be written as follows:

$$d\rho = -\rho d\Lambda\, tr\left(\frac{\partial F}{\partial \sigma_{ij}}\right) \tag{C10}$$

Inserting Eq. (C10) into Eq. (C8)

$$\frac{\partial F}{\partial \sigma_{ij}}d\sigma_{ij} - \frac{\partial F}{\partial \rho}\rho\, d\Lambda\, tr\left(\frac{\partial F}{\partial \sigma_{ij}}\right) + \frac{\partial F}{\partial T}dT = 0 \tag{C11}$$

and solving for $d\Lambda$ yields:

$$d\Lambda = \frac{\frac{\partial F}{\partial \sigma_{ij}} d\sigma_{ij} + \frac{\partial F}{\partial T} dT}{\rho \frac{\partial F}{\partial \rho}\ tr\left(\frac{\partial F}{\partial \sigma_{ij}}\right)} \tag{C12}$$

Substituting Eq. (C12) into Eq. (C2), it can be obtained that

$$d\varepsilon_{ij}^{P} = \frac{\left(\frac{\partial F}{\partial \sigma_{ij}}\right)^{2} d\sigma_{ij} + \left(\frac{\partial F}{\partial \sigma_{ij}}\right)\frac{\partial F}{\partial T} dT}{\rho \frac{\partial F}{\partial \rho}\ tr\left(\frac{\partial F}{\partial \sigma_{ij}}\right)} \tag{C13}$$

It is also that (see Eq.(C3))

$$\frac{\partial F}{\partial \sigma_{ij}} = \frac{\partial}{\partial \sigma_{ij}}\left(\sigma_{eq} - \sigma_{Y}\right) = \frac{\partial \sigma_{eq}}{\partial \sigma_{ij}} \tag{C14}$$

$$\frac{\partial F}{\partial \rho} = \frac{\partial}{\partial \rho}\left(\sigma_{eq} - \sigma_{Y}\right) = \frac{\partial \sigma_{eq}}{\partial \rho} - \frac{\partial \sigma_{Y}}{\partial \rho} \tag{C15}$$

$$\frac{\partial F}{\partial T} = \frac{\partial}{\partial T}\left(\sigma_{eq} - \sigma_{Y}\right) = -\frac{\partial \sigma_{Y}}{\partial T} \tag{C16}$$

Then Eq. (C13) becomes:

$$d\varepsilon_{ij}^{P} = \frac{\left(\frac{\partial \sigma_{eq}}{\partial \sigma_{ij}}\right)^{2} d\sigma_{ij} - \left(\frac{\partial \sigma_{eq}}{\partial \sigma_{ij}}\right)\frac{\partial \sigma_{Y}}{\partial T} dT}{\rho\left(\frac{\partial \sigma_{eq}}{\partial \rho} - \frac{\partial \sigma_{Y}}{\partial \rho}\right)\ tr\left(\frac{\partial \sigma_{eq}}{\partial \sigma_{ij}}\right)} \tag{C17}$$

Recalling Eq. (C4), it can be derived that

$$\frac{\partial \sigma_{eq}}{\partial \sigma_{ij}} = \frac{1}{2\sigma_{eq}}\left[A\sigma_{ij} - \left(\frac{1}{3}A - 2B\right) I_{1}\delta_{ij}\right] \tag{C18}$$

For the sake of shorter notation let us define

$$\Sigma_{ij} = A\sigma_{ij} - \left(\frac{1}{3}A - 2B\right) I_1 \delta_{ij} \tag{C19}$$

such that Eq. (C17) can be re-written as:

$$d\varepsilon_{ij}^{P} = \frac{\frac{1}{2\sigma_{eq}}\left(\Sigma_{ij}\right)^2 d\sigma_{ij} - \Sigma_{ij}\frac{\partial \sigma_Y}{\partial T}dT}{\rho\left(\frac{\partial \sigma_{eq}}{\partial \rho} - \frac{\partial \sigma_Y}{\partial \rho}\right) tr(\boldsymbol{\Sigma})} \tag{C20}$$

Conveying the trace of tensor $\boldsymbol{\Sigma}$ in cylindrical coordinates gives

$$tr(\boldsymbol{\Sigma}) = 6BI_1 \tag{C21}$$

and substituting Eq. (C21) into Eq. (C20) yields:

$$d\varepsilon_{ij}^{P} = \frac{\frac{1}{2\sigma_{eq}}\left(\Sigma_{ij}\right)^2 d\sigma_{ij} - \Sigma_{ij}\frac{\partial \sigma_Y}{\partial T}dT}{6\rho\left(\frac{\partial \sigma_{eq}}{\partial \rho} - \frac{\partial \sigma_Y}{\partial \rho}\right) BI_1} \tag{C22}$$

According to the assumption of densification taking place in a rigid cylindrical die, it follows that $\varepsilon_{rr}^{P} = \varepsilon_{\vartheta\vartheta}^{P} = 0$. Then, applying Eq. (C22) to the unique non-null component of the strain tensor and expressing Eq. (C22) in terms of temporal variation, the first term on the r.h.s of Eq. (24) is obtained:

$$\frac{d\varepsilon_{zz,1}^{P}}{dt} = \dot{\varepsilon}_{zz,1}^{P} = \frac{\frac{1}{2\sigma_{eq}}\left(\Sigma_{zz}\right)^2 \frac{d\sigma_{zz}}{dt} - \Sigma_{zz}\frac{\partial \sigma_Y}{\partial T}\frac{dT}{dt}}{6\rho\left(\frac{\partial \sigma_{eq}}{\partial \rho} - \frac{\partial \sigma_Y}{\partial \rho}\right) BI_1} \tag{C23}$$

where it can be clearly seen that the dynamics of the plastic deformation of Element 1 is determined by the temporal variations of the applied stress σ_{zz} and temperature T.

To solve Eq. (C23) the value of I_1 is needed. In the case of cylindrical coordinates, the first invariant is given by:

$$I_1 = \sigma_{rr} + \sigma_{\vartheta\vartheta} + \sigma_{zz} \tag{C24}$$

where σ_{rr} and $\sigma_{\vartheta\vartheta}$ are the radial and the hoop stresses, respectively, generated inside the sample by the application of the external load σ_{zz}. By introducing the contact pressure p exerted by the sample to the die internal wall, under the adopted simplifying assumptions (see Eq. (21a)), it follows that

$$\sigma_{rr} = \sigma_{\vartheta\vartheta} = -p \tag{C25}$$

Accordingly,

$$I_1 = \sigma_{zz} - 2p \tag{C26}$$

To find the stress p, Eq. (C23) is applied to the null components of the plastic strain tensor:

$$0 = \frac{\frac{1}{2\sigma_{eq}}(\Sigma_{\alpha\alpha})^2 \frac{d\sigma_{\alpha\alpha}}{dt} - \Sigma_{\alpha\alpha}\frac{\partial\sigma_Y}{\partial T}\frac{dT}{dt}}{6\rho\left(\frac{\partial\sigma_{eq}}{\partial\rho} - \frac{\partial\sigma_Y}{\partial\rho}\right)6BI_1} \tag{C27}$$

where subscript α can be either r or ϑ, respectively. Eq. (C27) is verified if

$$\frac{1}{2\sigma_{eq}}(\Sigma_{\alpha\alpha})^2 \frac{d\sigma_{\alpha\alpha}}{dt} - \Sigma_{\alpha\alpha}\frac{\partial\sigma_Y}{\partial T}\frac{dT}{dt} = 0 \tag{C28}$$

Eq. (C28) should be verified whatever the operating conditions (i.e., $\frac{dT}{dt}$, $\frac{d\sigma_{\alpha\alpha}}{dt}$) and yield strength temperature dependence (i.e., $\frac{\partial\sigma_Y}{\partial T}$) are. Taking the special case of isothermal compression and constant stress components leads to the condition

$$\Sigma_{\alpha\alpha} = 0 \tag{C29}$$

Recalling Eqs. (C19) and (C26) yields

$$p = -\frac{\left(\frac{1}{3}A - 2B\right)}{\left(\frac{1}{3}A + 4B\right)}\sigma_{zz} \quad \text{(C30)}$$

C.b Plastic deformation of Body (2)

To establish a thermodynamically consistent formulation of the stress-strain rate constitutive law, a dissipation potential-based approach inspired by the procedure introduced by Olevsky is adopted **[183]**. Within this framework, the constitutive relationship governing the dashpot element is derived ensuring convexity and compliance with the second law of thermodynamics. In parallel, it is shown that the viscoplastic potential that defines the yield function associated with the slider is dual to the selected dissipation potential, meaning that they describe complementary aspects of the material response. This duality highlights the internal consistency of the model and provides further justification for the combined use of slider and dashpot elements to capture the distinct mechanisms active during pressure-assisted sintering.

C.c Derivation of stress–strain rate relation

To describe the viscoplastic behavior of the Bingham fluid modeled by a rheological element consisting of a slider and a dashpot in parallel (as illustrated in **Figure 3.40**), the following dissipation potential is defined:

$$\Phi\left(\dot{\varepsilon}_{ij}\right) = 2\eta\dot{\gamma}^2 + \frac{1}{2}\kappa\, tr(\dot{\boldsymbol{\varepsilon}})^2 + (1-\theta)\frac{\sigma_Y^2}{6\eta^*} \quad \text{(C31)}$$

where $\dot{\gamma}$ is the second invariant of the strain rate tensor deviator $\dot{\boldsymbol{\varepsilon}}'$ and $\theta = 1 - \rho$ represents the sample porosity.

The first term of Eq. (C31) represents the viscous deformation of Body (2) (**Figure 3.40**) while its compressibility is expressed by the second term. The last one makes the porous material behaving as a Bingham fluid whose deformation occurs if the applied equivalent stress σ_{eq} exceeds the yield

strength of the (pore-free) material, $\sigma_{Y,2}$. The shear (η) and bulk (κ) viscosities of the compacting (porous) sample can be expressed as follows **[183]**:

$$\eta = \varphi\eta^* \tag{C32}$$

$$\kappa = \psi\kappa^* = 2\psi\eta^* \tag{C33}$$

where φ and ψ are functions of the sample porosity (see **Table C1**), and η^* and κ^* are the shear and bulk viscosity of the dense (pore-free) matrix material, respectively.

The stress-strain rate relationship can be obtained as:

$$\sigma_{ij} = \frac{\partial \Phi}{\partial \dot{\varepsilon}_{ij}} \tag{C34}$$

$$\sigma_{ij} = 2\eta\dot{\varepsilon}'_{ij} + \kappa tr(\dot{\boldsymbol{\varepsilon}})\delta_{ij} \tag{C35}$$

Recalling that

$$\sigma_{ij} = \sigma'_{ij} + \frac{1}{3}tr(\boldsymbol{\sigma})\delta_{ij} \tag{C36}$$

and comparing Eqs. (C35) and (C36) results that

$$\sigma'_{ij} = 2\eta\dot{\varepsilon}'_{ij} \tag{C37}$$

$$\frac{1}{3}tr(\boldsymbol{\sigma}) = \kappa tr(\dot{\boldsymbol{\varepsilon}}) \tag{C38}$$

Expressing Eq. (C35) in terms of the strain rate tensor instead of its deviator yields

$$\sigma_{ij} = 2\eta\dot{\varepsilon}_{ij} + \left(\kappa - \frac{2}{3}\eta\right)tr(\dot{\boldsymbol{\varepsilon}})\delta_{ij} \tag{C39}$$

C.d Duality between dissipation Φ and viscoplastic Ψ potentials

The thermodynamic consistency of the model is further supported by showing that the dissipation potential introduced in the previous section to define the response of Element 2 to the applied load

is dual to the viscoplastic potential governing the sliders, thereby linking in a consistent way the stress–strain rate relationship (C39) with the yield criterion adopted in **Section 3.5.2.1**.

Assigned the dissipation potential $\Phi(\dot{\varepsilon}_{ij})$ defined by Eq. (C31), the viscoplastic potential $\Psi(\sigma_{ij})$ is given by the following Legendre-Fenchel transform **[295,296]**:

$$\Psi(\sigma_{ij}) = \sup_{\dot{\varepsilon}_{ij}} \{\dot{\varepsilon}_{ij}\sigma_{ij} - \Phi(\dot{\varepsilon}_{ij})\} \tag{C40}$$

and substituting Eq. (C31) into Eq. (C40) leads to

$$\Psi(\sigma_{ij}) = \sup_{\dot{\varepsilon}_{ij}} \left\{\dot{\varepsilon}_{ij}\sigma_{ij} - \eta\dot{\varepsilon}'_{ij}\dot{\varepsilon}'_{ij} - \frac{1}{2}\kappa tr(\dot{\boldsymbol{\varepsilon}})^2 - (1-\theta)\frac{\sigma_Y^2}{6\eta^*}\right\} \tag{C41}$$

Decomposing the stress and strain rate tensors and recalling that tensors $\boldsymbol{\sigma}'$ and $\boldsymbol{\varepsilon}'$ are traceless, Eq. (C41) is expressed as follows:

$$\Psi(\sigma_{ij}) = \sup_{\dot{\varepsilon}'_{ij}} \left\{\sigma'_{ij}\dot{\varepsilon}'_{ij} + \frac{1}{3}tr(\dot{\boldsymbol{\varepsilon}})tr(\boldsymbol{\sigma}) - \eta\dot{\varepsilon}'_{ij}\dot{\varepsilon}'_{ij} - \frac{1}{2}\kappa tr(\dot{\boldsymbol{\varepsilon}})^2 - (1-\theta)\frac{\sigma_Y^2}{6\eta^*}\right\} \tag{C42}$$

Eq. (C42) can be separated into two independent maximizations:

$$\Psi(\sigma_{ij}) = \sup_{\dot{\varepsilon}'_{ij}}\{\sigma'_{ij}\dot{\varepsilon}'_{ij} - \eta\dot{\varepsilon}'_{ij}\dot{\varepsilon}'_{ij}\} + \sup_{e}\left\{\frac{1}{3}tr(\boldsymbol{\sigma})\, tr(\dot{\boldsymbol{\varepsilon}}) \; - \frac{1}{2}\kappa tr(\dot{\boldsymbol{\varepsilon}})^2 - (1-\theta)\frac{\sigma_Y^2}{6\eta^*}\right\} \tag{C43}$$

Maximation of first term

$$\frac{\partial}{\partial\dot{\varepsilon}'_{ij}}\left(\sigma'_{ij}\dot{\varepsilon}'_{ij} - \eta\dot{\varepsilon}'_{ij}\dot{\varepsilon}'_{ij}\right) = 0 \tag{C44}$$

$$\dot{\varepsilon}'_{ij} = \frac{\sigma'_{ij}}{2\eta} \tag{C45}$$

and substituting Eq. (C45) into the first term of Eq. (C43) yields

$$\sup_{\dot{\varepsilon}'_{ij}}\left\{\sigma'_{ij}\dot{\varepsilon}'_{ij}-\eta\dot{\varepsilon}'_{ij}\dot{\varepsilon}'_{ij}\right\}=\frac{\sigma'_{ij}\sigma'_{ij}}{4\eta} \tag{C46}$$

Calculating the supremum expressed by the second term of Eq. (C43)

$$\frac{\partial}{\partial e}\left(\frac{1}{3}tr(\boldsymbol{\sigma})\,tr(\dot{\boldsymbol{\varepsilon}})\;-\frac{1}{2}\kappa tr(\dot{\boldsymbol{\varepsilon}})^2-(1-\theta)\frac{\sigma_Y^2}{6\eta^*}\right)=0 \tag{C47}$$

$$tr(\dot{\boldsymbol{\varepsilon}})=\frac{tr(\boldsymbol{\sigma})}{3\kappa} \tag{C48}$$

Substituting Eq. (C43) into the second term of Eq. (C43) results in

$$\sup_{e}\left\{\frac{1}{3}tr(\boldsymbol{\sigma})\,tr(\dot{\boldsymbol{\varepsilon}})\;-\frac{1}{2}\kappa tr(\dot{\boldsymbol{\varepsilon}})^2-(1-\theta)\frac{\sigma_Y^2}{6\eta^*}\right\}=\frac{1}{18\kappa}\left(tr(\boldsymbol{\sigma})\right)^2\;-(1-\theta)\frac{\sigma_Y^2}{6\eta^*} \tag{C49}$$

Summing up Eqs. (C46) and (C49), the expression of the viscoplastic potential can be obtained:

$$\Psi\left(\sigma_{ij}\right)=\frac{1}{2\eta}J_2+\frac{1}{18\kappa}I_1^2-(1-\theta)\frac{\sigma_Y^2}{6\eta^*} \tag{C50}$$

Inserting Eqs. (C32) and (C33), rearranging and recalling Eq. (C4) leads to the following final form of Ψ:

$$\Psi\left(\sigma_{ij}\right)=\frac{(1-\theta)}{6\eta^*}\left(\sigma_{eq}^2-\sigma_Y^2\right) \tag{C51}$$

By equating to zero Eq. (C51), the yield function F adopted in **Section 3.5.2.1** is attained. Notably, if $\theta\to 0$ the Von Mises definition of equivalent stress ($\sigma_{eq}=\sqrt{3J_2}$) and the corresponding yield criterion can be derived.

C.e Application to uniaxial pressing in a rigid cylindrical die and material viscosity functionality

The stress–strain rate relationship derived in **Section 3.5.2.1** is now applied to the case of uniaxial pressure-assisted sintering in a rigid cylindrical die, corresponding to the experimental setup used in this study. Applying Eq. (C39) under the already mentioned simplifying assumptions, the following expression for the stress and strain rate relationship is obtained:

$$\frac{d\varepsilon_{zz}^{VP}}{dt} = \dot{\varepsilon}_{zz} = \frac{\sigma_{zz}}{\mu} \tag{C52}$$

that computes the second contribution appearing on the r.h.s. of Eq. (24). The apparent viscosity μ of the densifying sample introduced in Eq. (C52) is defined as

$$\mu = \kappa + \frac{4}{3}\eta \tag{C53}$$

This property quantifies the total viscous resistance of the porous compact to densification. It integrates the effects of both shape-preserving and volume-reducing deformations, thus providing a meaningful macroscopic indicator of sinterability under combined thermomechanical loading.

As for the evolving thermomechanical conditions during densification, the material viscosity μ must be expressed as a function of temperature, porosity, and equivalent strain rate. In particular, the latter dependence is captured using the Bird–Carreau model, which allows a continuous transition between Newtonian and shear-thinning behavior without imposing a priori a linear or non-linear behavior **[297,298]**. By also considering Eqs. (C32) and (C33), the apparent viscosity of the consolidating sample can be comprehensively expressed as follows:

$$\mu(T, \theta, \dot{\varepsilon}_{zz}) = \eta^0(T)\frac{4}{3}\left(\varphi + \frac{3}{2}\psi\right)[1 + \lambda(T)W]^{m-1} \tag{C54}$$

where m is the strain-rate sensitivity coefficient and W is the equivalent strain rate defined by

$$W = f(\theta)|\dot{\varepsilon}_{zz}| \tag{C55}$$

$$f(\theta) = \sqrt{\frac{\frac{4}{9}\varphi + \frac{2}{3}\psi}{(1-\theta)}} \tag{C56}$$

The first factor in Eq. (C54), η^0, represents the zero-shear rate viscosity of dense (pore-free) material whose temperature dependence is taken as

$$\eta^0 = a^0 exp\left(\frac{Q_\eta}{RT}\right) \tag{C57}$$

Finally, the parameter λ, which appears in Eq. (C54), characterizes the strain-rate time scale at which the material transitions from Newtonian (linear) to shear-thinning (nonlinear) behavior. Physically, it can be interpreted as a material-specific relaxation time: the characteristic timescale over which the microstructure can respond viscously to applied stress. When the inverse of the equivalent strain rate (W^{-1}) is large compared to λ, the material deforms linearly; as the strain rate increases and becomes comparable to or exceeds λ^{-1}, nonlinear effects become significant. During pressure-assisted sintering, this transition is influenced by temperature, porosity evolution, and particle interactions, making λ a key parameter that bridges microscopic flow mechanisms and macroscopic deformation behavior. For the sake of simplicity, in this work only the temperature dependence is accounted for through the following relation **[298]**:

$$\lambda(T) = \lambda^0 T^{\left(\frac{m}{m-1}\right)} exp\left(\frac{Q_\eta}{RT}\right) \tag{C58}$$

C.f Constitutive parameter dependencies

The rheological behavior of the TMB powder during densification is governed not only by its mechanical structure but also by the evolution of key material properties, such as shear viscosity, bulk viscosity, and yield strength, as functions of temperature, porosity, and strain rate. The constitutive relationships adopted here to describe these dependencies are essential for accurately describing the nonlinear viscoplastic response of the system under varying SPS conditions. For clarity, all functional forms, auxiliary relations, and dependencies are summarized in **Table C1.** It is worth mentioning that, in this work, the yield strength σ_Y is taken as a function of temperature only, while lumping the porosity effect on the equivalent stress (see Eq. (C4)) **[292,293]**.

Table C1- Summary of constitutive dependencies for temperature-, porosity-, and strain rate-sensitive model parameters used in this work.

Quantity	Functionality	Reference
$\sigma_{eq}(\theta)$	$[A(\theta)J_2 + B(\theta)I_1^2]^{1/2}$	**[294]**
$A(\theta)$	$\frac{3}{(1-\theta)\varphi}$	**This work**
$B(\theta)$	$\frac{1}{6(1-\theta)\psi}$	**This work**
$\varphi(\theta)$	$(1-\theta)^2$	**[183]**
$\psi(\theta)$	$\frac{(1-\theta)^3}{\theta}$	**This work**
$\sigma_Y(T)$	$\sigma_Y^{\infty} + (\sigma_Y^0 - \sigma_Y^{\infty})\left[1 + exp\left(\frac{T-A_T}{B_T}\right)\right]^{-1}$	**[299]**
$\frac{\partial \sigma_{eq}}{\partial \theta}$	$\frac{1}{2\sigma_{eq}}\left(\frac{\partial A}{\partial \theta}J_2 + \frac{\partial B}{\partial \theta}I_1^2 + \frac{\partial J_2}{\partial \theta}A + 2BI_1\frac{\partial I_1}{\partial \theta}\right)$	**This work**
$\frac{\partial A}{\partial \theta}$	$\frac{9}{(1-\theta)^4}$	**This work**
$\frac{\partial B}{\partial \theta}$	$\frac{1}{6}\frac{3\theta+1}{(1-\theta)^5}$	**This work**
$\frac{\partial J_2}{\partial \theta}$	$\frac{2}{3}(p-\sigma_{app})\frac{\partial p}{\partial \theta}$	**This work**
$\frac{\partial I_1}{\partial \theta}$	$-2\frac{\partial p}{\partial \theta}$	**This work**
$\frac{\partial p}{\partial \theta}$	$\frac{2p}{\left(\frac{1}{9}A^2 + \frac{2}{3}AB - 8B^2\right)}\left(B\frac{dA}{d\theta} - A\frac{dB}{d\theta}\right)$	**This work**
$\frac{\partial \sigma_Y}{\partial \theta}$	0	**This work**
$\frac{\partial \sigma_Y}{\partial T}$	$-\frac{(\sigma_Y^0 - \sigma_Y^{\infty})\,exp\left(\frac{T-A_T}{B_T}\right)}{B_T\left[1 + exp\left(\frac{T-A_T}{B_T}\right)\right]^2}$	**This work**
$\frac{d\sigma_{zz}}{dt}$	0	**This work**
$\frac{dT}{dt}$	see experimental details reported in the text	**This work**

Figure C1 graphically illustrates the selected temperature-dependent evolution of the yield strength σ_Y associated with the slider elements in the proposed rheological model. The curve shows the smooth transition from the low-temperature asymptotic value σ_Y^0 to the high-temperature asymptotic value σ_Y^∞, thus elucidating the effect of temperature on the particle rearrangement (Body (1)) or material matrix thermal softening (Body (2)).

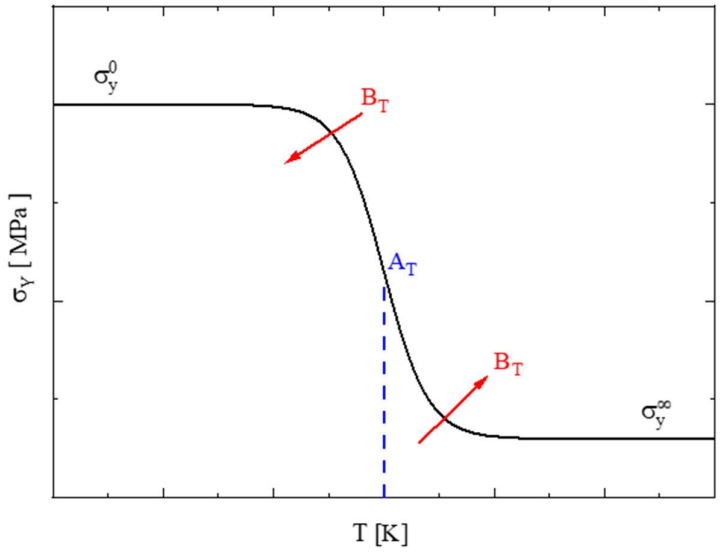

Figure C1 - Temperature-dependent yield strength σ_Y used in the proposed model. The curve captures the transition from the low-temperature yield strength σ_Y^0 to the high-temperature asymptotic value σ_Y^∞, following a sigmoidal decay. The parameters A_T and B_T define the temperature at which the transition occurs and sharpness of this transition, respectively. This behavior reflects the thermally activated particle interaction (Body (1)) or the continuous matrix softening (Body (2)) and plays a central role in regulating the onset of the different mechanisms within the rheological model shown in **Figure 3.40**.

This transition is controlled by two parameters: A_T, which defines the midpoint temperature of the shift, and B_T, which characterizes the shift steepness. At low temperatures ($T \ll A_T$), σ_Y approaches σ_Y^0 representing the high resistance to plastic rearrangement (body (1)) or to material deformation when atomic mobility is limited (Body (2)). At high temperatures ($T \gg A_T$), the yield strength

decreases toward σ_Y^{∞}, reflecting the enhanced packability of the particle network (Body (1)) or the material deformability (Body (2)) as the temperature increases. The sigmoidal shape of the curve allows a smooth albeit remarkable transition, consistent with the onset of the significant thermal activation typically observed during sintering of TMBs. In particular, as far as the slider of Element 1 is concerned, this function ensures that such model component is only active within a limited temperature range during early heating while it automatically deactivates as temperature rises and the material behavior becomes dominated by viscous deformation.